PhD Thesis

2023

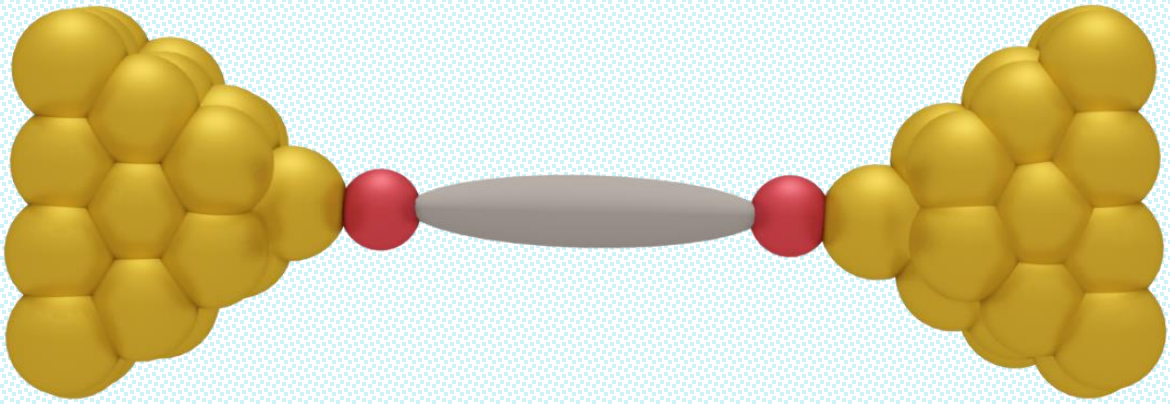

Influence Of Molecular Orientation On The Electronic Transport Of A Metal-Molecule-Metal Junction

Biswajit Pabi

S. N. Bose National Centre for Basic Sciences

Dedicated to Baba (বাবা) and Maa (মা)…

Acknowledgements

First and foremost, I would like to express my heartfelt gratitude to my Ph.D. supervisor, *Dr. Atindra Nath Pal*, for his invaluable assistance in carrying out my research, as well as his patience, insightful discussion and humble guidance. He gave me the chance to begin my research career in such a beautiful direction, and for that I am incredibly grateful. He has always inspired me to put forth my best effort and pushed me to independently consider the research strategy. I learned the fundamentals of research from designing the research plan to carrying out the idea and presenting it in a scientific manner from him. His invaluable suggestions and comments influenced me greatly in pursuing my research in a more efficient manner. When I begin writing this paragraph, there is one incident that I would like to share. The experimental setup that we had developed in our lab was destroyed as a result of my hand falling to the floor and when I informed him of it. "*Don't worry, it's a part of life*" he quickly replied, making me feel more comfortable sharing any problems with him. I am extremely grateful for his evergreen inspiration, encouragement, and mental support; without his help it would not be possible to introduce my thesis. Aside from academics, he always insists to spend time in the playground.

I am highly obliged to *Prof. Oren Tal, Weizmann Institute of Science*, for his unconditional help at any instant. It's always a pleasure to discuss with him. I am always fascinated by his approach to understanding experimental results and his attitude towards interpreting microscopic phenomena. His experimental setup, received on lien, enabled me to complete my doctoral research on time. I am also grateful to *Prof. Priya Mahadevan, S. N. Bose National Centre for Basic Sciences* (*SNBNCBS*), for the fruitful discussions and insightful comments that have helped me a lot to understand and interpret the experimental findings. I am also thankful to *Dr. Ayelet Vilan, Weizmann Institute of Science*, who provided me with numerous MATLAB programming suggestions. I am also grateful to *Dr. Arijit Halder*, *S. N. Bose National Centre for Basic Sciences* (*SNBNCBS*), for assisting me in fitting the complex DIDV spectra using the TLS model. I am also glad to have so many energetic and enthusiastic collaborators during my journey: *Debayan Mondal*, *Prof. Priya Mahadevan*, *Stepan Marek*, *Dr. Richard Korytar*, *Jakub Sabesta*, *Adwitiya Pal*, *Puja Kumari*, *Dr. Arunabha Thakur*, *Dr. Soumya Jyoti Ray*, *Tal Klein*, *Prof. Oren Tal*, *Aishwarya Ghosh* and *Prof. Tanusri Saha Dasgupta*. *Debayan* is classmate from my home institute who assisted me greatly in completing the work together.

I am grateful to the *S. N. Bose National Centre for Basic Sciences* (*SNBNCBS*), *Kolkata* for providing a lush green campus with an excellent research environment. I am extremely grateful to *Department of science and Technology, Government of India*, for the financial support (*Inspire award code: IF170934*) during the tenure of my research work.

I would to like to thank the present and past lab mates of quantum transport and devices lab: *Subhadip da, Rafiqul, Shubhrasish, Riju, Taniya, Soumili, Tausif, Buddhadeb da, Shubhankar, Gaurab, Sujoy da, Obai da* and *Dayal* for their delightful company and the support in various ways. All of them are very cooperative to maintain a good research environment inside the laboratory. I was one from the first group of students of this lab, which began with four members: *Subhadip da, Rafiqul, Shubhrasish* and myself. We four were actively involved in building this lab from the ground up. Our lab now has numerous setups, a plethora of accessories, and more members that mesmerized me. We four spend a lot of quality time together, both academically and socially. Despite being our only senior, *Subhadip da* allowed us to share friendship rather than a senior-junior relationship, which motivated our enormous effort to make him couple. *Rafiqul,* we call him as *Rafi,* helped me a lot to figure out the LABVIEW programming and instrument communication. My friendship with *Shubhrasish* (I used to call him *Shubhra*) began during my undergraduate studies, and we spent 11 years together in the same College, University, and PhD laboratory. Our journey has left me with many unforgettable memories that I will cherish forever. *Riju,* our tech-man, has been a junior for a long time and has had to put up with a lot of leg pulling.

I am grateful to all of my colleagues at the SNB centre. Special thanks to *Piya di*, *Didhithi* (*Maa*), *Debayan, Subrata da, Dipika di, Dipanjan da, Sankar da, Sudipta da, Supriyo da, Mehebub da, Keshab da, Koushik da, Arnab da, Amrita, Jayanta, Dhrubojyoti, Sanuja* and *Biswajit (Panda)* for their amazing company. Moreover, encouragement from *Riya* is really invaluable. A large number of people on the football and cricket fields make my day more colorful and memorable. *Piya di* and *Subrata da* is like a personal guide who always gives me useful advice for both academic and personal problems. I also want to thank every staff members including cleaners, gardeners, and mess staff for making my stay memorable here. Special thanks to *Swarup* da and *Nibedita* mam for his unwavering support regarding the fellowship and contingency grant arrangements.

I am especially grateful to *Subhasish Sir, Partha sir, Rita di, Bubai da, Sudhir babu, Late Surojit Sir, Debasish sir* (*D.B. sir*), *Tanmoy sir* (*T.B. sir*), and *SKP sir*. I am also thankful to my

master's thesis supervisor *Prof. Partha Mitra* and he is like my family member who support me in all sorts of possibilities. It would have been impossible to begin this wonderful journey without their constant support from the beginning of my life and their constant encouragement has helped the shape who I am today.

I want to show my gratitude to my friends Sumanta, Sukalyan, Raktim, Sukanya, Arghya, *Raju*, *Bratati*, *Siddhartha*, *Chandi*, *Anjan Da*, *Tubai da*, *Kalyan da*, *Subhasish da*, *Kushal*, *Soumya*, *Banti*, *Rimpa* who are very supportive and helped me in every possible way. I always love their company. Meanwhile, I lost one of my gem from the above list, Late *Sk Samsuddoza*. Still, I feel the loss, and your contribution is indescribable, and I believe, you are always available to me.

Finally, I want to express my gratitude to baba, maa (*Dayamay Pabi* & *Mita Pabi*), didi (*Piu Pabi Mondal*), brother in law (*Bappa Mondal*), Jethu (Santi Pabi) and dadu (*Sunil Kundu*) for their sacrifice, moral support, love, affection, and guidance. One more little member of my family is my niece *Ishika Mondal* who have a lot of complain against me for not giving time to her and used to tell that "*PhD e tomar sob*". Didi and Maa always treats me as a friend, and I can share anytime any difficulties either personal or professional with them. Lastly, I find myself blessed to have dadu in my life.

Biswajit Pabi

S. N. Bose National Centre for Basic Sciences, Kolkata

Contents

Abstract

Understanding electronic transport in atomic-sized devices is critically important for both fundamental reasons and electronic applications at such a small length scale. Present thesis explores two important aspects in this field. Firstly, the contributions of molecular structure and orientation to the formation and charge transport characteristics of single molecular junction were investigated in mechanically controllable break junction platform. Secondly, we looked into the formation of impurity induced atomic/molecular chain through electronic transport measurements.

The study of two isomers of bipyridine molecular junctions (Au/4,4′-bipyridine/Au and Au/ 2,2′-bipyridine /Au) reveals distinct evolution during stretching caused by the difference in Au-N bond strengths due to steric effect, establishing a close relationship between metal-molecule contact formation and molecule orientation. The significance of spatial orientation is further manifested by investigating the transport mechanism of ferrocene molecule connected to Au electrodes at ambient conditions. We observed a significant high conductance for Au/Ferrocene/Au single molecular junction (~ one quarter of a conductance quantum), which is further explained via resonant transport mechanism due to a strong hybridization between the metal electrodes and the molecule orienting perpendicular to the electrode axis. Whereas, parallel orientation exhibits a low conducting off-resonant mechanism. Furthermore, when ferrocene is terminated with two anchoring groups (**-NH_2**) and (**-CN**), it exhibits perpendicular conformational characteristics as well as features at low conductance due to bonding with the chemical anchors. When the same ferrocene junction is examined at 4.2K, 77K, and 300K, a striking influence of temperature on the formation of junction is observed, demonstrating an increase in the number of stable conformations with the reduction of temperature. The key factor influencing the formation (i.e., the metal-molecule coupling) is the temperature-dependent rotational dynamics of Cp rings which destabilized the parallel configuration at 300K. Considering other possibility, the mechanical gating response of a ferrocene molecular junction connected between Ag electrodes is studied which indicate that gating efficiency can be tuned by modifying the spatial distribution of frontier molecular orbitals. Apart from that, investigation of copper (Cu) and aluminum (Al) atomic junctions in hydrogen environment enables the formation of Cu atomic chain with conductance value in the tunneling regime in contrast to Al junction, implying the role of frontier molecular orbitals in the realization of impurity assisted atomic chain. Overall, reported findings are expected to establish a set of general principles for the design of atomic scale devices with new electronic functionality.

সারাংশ

বাস্তবসম্মত পারমাণবিক-আকারের যন্ত্রের মধ্যে ইলেকট্রনের পরিবহন বোঝা মৌলিক কারণে এবং এই ধরনের ছোট দৈর্ঘ্যের স্কেলে বৈদ্যুতিক যন্ত্র প্রস্তুত করা, উভয়ের জন্যই খুব গুরুত্বপূর্ণ। বর্তমান গবেষণামূলক প্রবন্ধে মূলত দুটি গুরুত্বপূর্ণ দিকের উপর আলোকপাত করা হয়েছে । প্রথমত, যান্ত্রিকভাবে নিয়ন্ত্রণযোগ্য প্ল্যাটফর্মে গঠিত পারমাণবিক-আকারের সংযোগে (ধাতু-অণুর), আধান পরিবহন বৈশিষ্ট্য এবং সংযোগের প্রস্তুতিতে অনুর গঠন এবং অভিযোজনের অবদানকে তুলে ধরা হয়েছে ।দ্বিতীয়ত, আমরা ইলেকট্রনের পরিবহন পরিমাপের মাধ্যমে বাহ্যিক অপদ্রব্যের সাহায্যে সৃষ্ট পারমাণবিক/আণবিক শৃঙ্খলের দিকে নজর দিয়েছি।

বাইপাইরিডিন-এর দুটি আইসোমারের সহিত গোল্ডের সংযোগকে (Au/4,4′-bipyridine/Au এবং Au/ 2,2′-bipyridine /Au) প্রসারিত করে আমাদের গবেষণা প্রকাশ করে যে স্টেরিক প্রভাবের দরুন Au-N বন্ডের শক্তিতে যে পার্থক্য তৈরী হয় তা সংযোগের বিবর্তনেও পার্থক্য তৈরী করে। তাছাড়াও, ধাতু-অণু সংযোগ স্থাপন এবং অণুর অভিযোজনের মধ্যে একটি ঘনিষ্ঠ সম্পর্ক প্রতিষ্ঠা করে। অনুর স্থানীয় অভিযোজনর গুরুত্ব আরো দৃঢ়ভাবে প্রকাশিত হয় গোল্ড-ফেরোসিনে অনুর সংযোগস্থলে ইলেকট্রনের পরিবহন পরীক্ষা করে। ফেরোসিন অনুর লম্ব অভিযোজন, ধাতু-অনুর সহযোগস্থলে দৃঢ় সংকরণ তৈরী করে এবং ইলেকট্রনের অনুরণিত পরিবহন ব্যবস্থা স্থাপন করে যা পরীক্ষামূলকভাবে নির্ধারিত বিভব নির্ভরশীল উচ্চ পরিবাহিতা (~ কন্ডাক্টেন্স কোয়ান্টামের এক চতুর্থাংশ) সম্পন্ন গোল্ড -ফেরোসিন অনুর সংযোগস্থল কে প্রমান করে। অন্যদিকে, সমান্তরাল অভিযোজন কম পরিবাহিতা সম্পন্ন বন্ধ অনুরণিত পদ্ধতি প্রদর্শন করে। আবার ফেরোসিনের সাথে দুটি রাসায়নিক গ্রুপ কে (**-NH_2** এবং **-CN**) যুক্ত করলে, এটি লম্ব অভিযোজনের জন্য সৃষ্ট উচ্চ পরিবাহিতা সম্পন্ন গঠনমূলক বৈশিষ্ঠের পাশাপাশি রাসায়নিক গ্রপের সাথে বন্ধনের কারণে কম পরিবাহিতা সম্পন্ন বৈশিষ্ঠীও প্রকাশ করে। গোল্ড-ফেরোসিনের একই সংযোগস্থলকে ৪.২ k , ৭৭ k, ৩০০ k তাপমাত্রায় পরীক্ষা করা হয় এবং সংযোগ গঠনে তাপমাত্রার এক আকষর্ষনীয় প্রভাব লক্ষ করা যায় : তাপমাত্রা হ্রাসের সাথে সাথে স্থিতিশীল সংযোগ গঠনের সম্ভবনা বৃদ্ধি পাই । এক্ষেত্রে দেখা যায়, তাপমাত্রার সাথে গঠনকে (অর্থাৎ ধাতু-অণু সংযোগ) প্রভাবিত করার অন্যতম উপাদান হল ফেরোসিনের Cp রিংগুলির তাপমাত্রা-নির্ভর ঘূর্ণন গতিবিদ্যা যা ৩০০ k- তাপমাত্রায় সমান্তরাল অভিযোজনকে সম্পূর্ণভাবে অস্থিতিশীল করে তোলে। এছাড়াও এই প্রবন্ধে ধাতু – অনু সংযোগের অন্যান্য সম্ববনাকেও বিবেচনা করা হয় , সিলভার বিদ্যুদ্বাহকের মধ্যে সংযুক্ত ফেরোসিনের একটি আণবিক সংযোগের যান্ত্রিক গেটিং প্রতিক্রিয়া অধ্যয়ন করা হয়, যা ইঙ্গিত দেয় যে সীমান্তের আণবিক কাক্ষিকের স্থানীয় বন্টনকে পরিবর্তন করে গেটিং দক্ষতার সমন্বয় করা যেতে পারে। পরবর্তীকালে, হাইড্রোজেন পরিবেশে তামা (Cu) এবং অ্যালুমিনিয়ামের (Al) পারমাণবিক সংযোগগুলির উপর পারমাণবিক শৃঙ্খল সংক্রান্ত আমাদের তদন্ত নির্দেশ করে যে তামা মৃদু তড়িৎবাহী সম্পন্ন পারমাণবিক শৃঙ্খল গঠন করতে সক্ষম হলেও, অ্যালুমিনিয়াম হাইড্রোজেন পরিবেশে অপ্রভাবিত থাকে এবং এই তদন্ত অপদ্রব্য সহায়তাপ্রাপ্ত পারমাণবিক শৃঙ্খল উপলব্ধির ক্ষেত্রে সীমান্তের আণবিক কাক্ষিকের ভূমিকা বোঝায়। সামগ্রিকভাবে, জ্ঞাপিত ফলাফলগুলি নতুন বৈদ্যুতিন কার্যকারিতা সহ পারমাণবিক-আকারের যন্ত্র প্রস্তুতির জন্য মৌলিক নীতি-নির্ধারণে সহায়তা করবে বলে আশা করা যায়।

List of Publications

Included in the thesis

1. **Biswajit Pabi**, Debayan Mondal, Priya Mahadevan*, and Atindra Nath Pal*. "Probing metal-molecule contact at the atomic scale via conductance jumps". *Physical Review B (Letter),* 104(12), 2021.
2. **Biswajit Pabi***, and Atindra Nath Pal*. "An experimental set-up to probe the quantum transport through a single atomic/molecular junction at room temperature". *Pramana,* 97(1), 2022.
3. **Biswajit Pabi**, Jakub Šabesta, Richard Korytár, Oren Tal and Atindra Nath Pal*. "Structural regulation of mechanical gating in molecular junctions". *Nano Letters,* 23(9), 2023.
4. **Biswajit Pabi**, Štepán Marek, Adwitiya Pal, Puja Kumari, Soumya Jyoti Ray, Arunabha Thakur, Richard Korytár, and Atindra Nath Pal*. "Resonant transport in a highly conducting single molecular junction via metal-metal covalent bond". (Under review)
5. **Biswajit Pabi**, Debayan Mondal. Tal Klein, Adwitiya Pal, Arunabha Thakur, Priya Mahadevan* and Atindra Nath Pal*. "Temperature sensitive molecular conformation in Au/ferrocene/Au junction". (To be submitted soon)
6. **Biswajit Pabi**, Debayan Mondal, Priya Mahadevan*, and Atindra Nath Pal*. "Formation of copper atomic chain in hydrogen atmosphere". (Under Preparation)

Not included in the thesis

7. Aishwaryo Ghosh[#], **Biswajit Pabi**[#], Atindra Nath Pal* and Tanusri Saha Dasgupta*. "Machine-learning prediction on formation of atomic gold wires by mechanically controlled break junction". (Under review) [# contributed equally]
8. **Biswajit Pabi**, Tal Klein, Adwitiya Pal, Arunabha Thakur and Atindra Nath Pal*. "Unusual evolution and molecule assisted chain formation in Au/ferrocene/Au junctions". (Under Preparation)

List of figures

List of tables

List of abbreviations

STMBJ	Scanning tunneling microscope break junction
HOMO	Highest occupied molecular orbital
LUMO	Lowest unoccupied molecular orbital
MCBJ	Mechanically controllable break junction
D.C.	Direct current
DAQ	Data acquisition
MATLAB	Matrix laboratory
LABVIEW	Laboratory Virtual Instrument Engineering Workbench
A.C.	Alternating current
1D	One dimensional
2D	Two dimensional
3D	Three dimensional
4,4'-BPY	4,4'-Bipyridine
2,2'-BPY	2,2'-Bipyridine
DFT	Density-functional theory
MD	Molecular dynamics
J2C	Jump to molecular contact
DPP	Diketopyrrolopyrrole
FC	Ferrocene
DCM	Dichloromethane
2DCH	Two dimensional cross-correlation histogram
FC-NH_2	1,1′-bis(aminomethyl)ferrocene
FC-CN	1,1′-dicyanoferrocene
Cp	Cyclopentadienyl
TVS	Transition voltage spectroscopy
FN	Fowler-Nordheim plot
IETS	Inelastic electron tunneling spectroscopy
VITLS	Vibrationally induced two level systems
TLS	Two level systems

List of symbols

L_{φ}	Phase coherence length
l	Elastic mean free path
$f_{\alpha}(E)$	Fermi distribution function
E	Energy
K_B	Boltzmann constant
T_{α}, T	Temperature
μ	Chemical potential
$\hbar$	Reduced Planck constant
h	Planck constant
k_l	Longitudinal wave vector
m	Mass
N	Number of channels
$\hat{a}^{\dagger}, \hat{b}^{\dagger}$	Creation operator
$\hat{a}, \hat{b}$	Annihilation operator
$\hat{S}$	Scattering matrix
$\hat{r}, \hat{r}'$	Parameter to describe reflection of electron
$\hat{t}, \hat{t}'$	Parameter to describe transmission of electron
e, q	Charge of electron
E_F	Fermi level
$T_n(E)$	Transmission coefficients
G	Conductance
$I-V$	Current-Voltage
ϵ_0, ϵ	Molecular energy level
$\Gamma_L, \Gamma_R, \Gamma$	Coupling parameters
t	Hopping parameter
r	Attenuation factor
$\Delta d, \Delta$	Interelectrode separation
Δh	Displacement of the piezo

u	Length of the weak spot
t	Thickness of the substrate
$G_{Junction}$	Conductance of the junction
$V_{Junction}$	Voltage drop across the junction
V_{Bias}	Applied bias voltage
V_{R_s}	Voltage drop across the series resistance
$V_p \ or \ V_{piezo}$	Voltage at the piezo
G_0	Quantum of conductance
c	Calibration constant
ϕ	Work function
R, R_0	Resistance
$C_{m,n}$	Correlation parameter
Au	Gold
Pt	Platinum
Cu	Copper
Ag	Silver
Ir	Iridium
Ni	Nickel
W	Tungsten
Fe	Iron
-SH	Thiol
$-NH_2$	Amine
-PY	Pyridyl
-CN	Nitrile
-NC	Isonitrile
-COOH	Carboxylic acid
$-SnMe_3$	Trimethyltin
C60	Fullerene
dI/dV	Differential conductance
V_{trans}	Transition voltage

φ	Barrier height
A	Area
m_e	Electron effective mass
d	Barrier width
η	Asymmetry of coupling
β	Decay constant
H_2,	Hydrogen
O_2	Oxygen
N_2	Nitrogen
H_2O	Water
D_2	Deuterium
Pd	Palladium
Co	Cobalt
Al	Aluminum
σ_0, σ_1	Conductance
n_0, n_1	Occupation number
ν_0,ν_1	Inverse relaxation time
ρ_F	Density of states
γ_0,γ_1	Coupling parameter
N	Asymmetry Parameter
Δ	Energy difference

Chapter 1 | Introduction

This chapter demonstrate the overall introduction of the thesis, as well as an overview of each chapter.

Control and manipulation at the atomistic level is the perquisite to extend the further miniaturization of electronic circuits and this concept was primarily suggested by Physicist Richard Feynman in his famous lecture –

"There's Plenty of Room at the Bottom: An Invitation to Enter a New Field of Physics"

at the annual American Physical Society meeting on 29th December, 1959 at Caltech[1]. Decades later, the community of "*Molecular electronics*" adopted this revolutionary idea to realize the technological applications, which was pioneered by Aviram and Ratner's celebrated paper on "*Molecular Rectifier*" in 1974[2]. Since then, the basic goal in that direction is to establish a fundamental understanding of charge transport mechanism through the molecules with a deep focus in mind to explore the potential application in future. Immense interest in molecular electronics arises due to the smallest possible size of the molecules in contrast to conventional micro fabricated components. For instance, the latest commercial device size ranges in few nanometer scale, whereas, the diameter of a benzene ring is $0.28\ nm$[3]. More importantly, physics at that limit is completely dominated by quantum mechanical phenomena and cannot be described by the classical laws, which on the other hand can be a source of endless new physical phenomena by accounting great versatility of optical, mechanical and thermal properties of synthetic molecules.

The basic components of molecular electronics is the single molecule-electrode or many molecules-electrode junction and research groups across the world aimed to control and measure the charge transport through it. Molecular junction is generally classified into two types: ensemble molecular junctions or single molecular junction. My interest relies on the latter type which is attributed to few or single molecule captured between two nanoelectrodes whereas the former is based on many molecules. Next, obvious question is how to wire a molecule between the metallic leads, because achieving gap size $\sim 10\ nm$ using conventional lithography process is practically challenging and size of a molecule lies in the sub nanometer range. However, difficulties are partially circumvented and corresponding experimental techniques have been developed based on the electro-mechanical methods which ensures dynamic control of the junction at sub-angstrom resolution. Two most commonly used experimental methods are mechanically controllable break junction (MCBJ)[4–6] and scanning tunneling microscope break junction (STMBJ)[7,8] technique and in my doctoral course, I use the former technique to fabricate and examine the single molecular

junction. Particular description related to the principle and fine details of the MCBJ technique is depicted in **Chapter 3**.

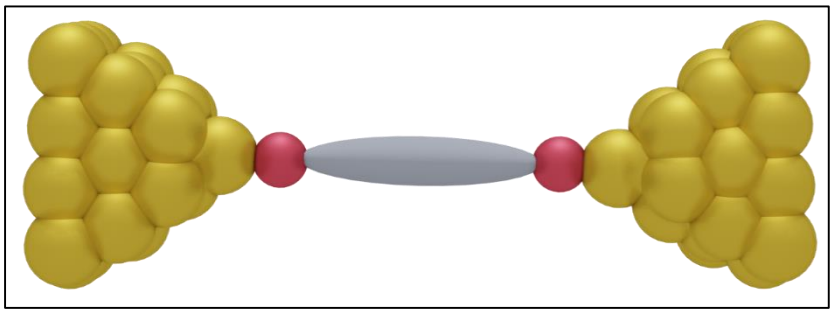

Figure 1.1 *Schematic of a single molecular junction, where a molecule is attached to the sharp metallic tips.*

Three essential ingredients of single molecular junction are metal-molecule interface, metallic electrode and molecular backbone[9–11] where molecule inside the junction serve as both functional and interfacial element. A typical single molecular junction with a molecule encapsulated between two sharp atomic tips is schematically shown in **Figure 1.1** where the interface is donated by red balls. Generally, extent of the hybridization and energy difference between the frontier molecular and metallic orbitals, the local density of states of the electrodes at the Fermi level and the degree of π-conjugation inside the molecule profoundly affects the charge transfer and functionality of the junction[9,12,13]. Within the junction, energy levels of the molecules are renormalized and broadened due to coupling with the metallic leads at the metal-molecule interface. This interface is one of the key parameters to control the charge transfer to or from the molecules. Furthermore, interfaces make a significant impact to achieve a physically stable configuration. Considering language of chemistry, several anchoring groups (for instance: **-SH**, **-NH_2**, **-CN**, **-PY,** **-NC**, **-C60**, **-COOH** and so on)[6,7,21,8,14–20] are employed as an interfacial element which essentially binds the molecular backbone and metallic electrodes. However, presence of such linker agents adversely affect the electronic coupling in most of the cases[22] and interface without anchoring groups i.e., direct coupling[12,23–27] have also been attempted, which on the other side suffers lack of mechanical stability. Thus, optimization towards the efficient mechanical and electronic coupling at the interface is still a subject of interest, considering potentiality of several electrodes (both metal and nonmetal) and synthetic chemistry[9]. Another great opportunity to manipulate the performance of the junction rests on the central molecular part which has two distinctive subcomponents- main backbone and substituents. Main backbone is the pathway through which charge flows like π bond in phenyl rings and substituents are the chemical moiety attached to the main backbone, which can

modify both the electronic coupling and conformation. Substitute mediated conformation for biphenyl molecules reveals a pronounced effect on the conductance value[15,28–30] and hint a strong relationship between the molecular conformation and conductance. Moreover, conformation is a difference maker[9–11] to realize the quantum interference phenomena which describes the interference of de-Broglie waves propagating through the several molecular orbitals of a single molecular junction. Interference can be either constructive or destructive type which enhances or suppresses the conductance, thus, choice of suitable interference pathways of a molecular junction offer a possible route to realize a large ON/OFF ratios for molecular scale devices. Nevertheless, the importance of molecular orientation on the characteristics operation of single molecular junction are studied to some extent, an extensive mapping on the orientation-property correlations for single molecular junction is still limited. In that perspective, primary focus of my thesis is to explore and understand the role of spatial orientation of molecule on the evolution and charge transport characteristics of the junction. This thesis is divided into ten chapters and an overview of each chapters is summarized as follows-

In ***chapter 2***, a brief introduction of the theoretical modelling to describe the charge transport through single atomic or molecular junction is demonstrated. Flow of electrons through atomic conductor is completely ballistic in nature and conductance is quantized in contrast to diffusive phenomena. Most famous theoretical formalism to explain the conductance quantization of ballistic contact is the Landauer's formalism of scattering approach which is outlined briefly[31–33] . In case of molecular junction, electronic transport is more complicated due to involvement of multiple atoms of different species and a single level resonant tunneling model for coherent transport through molecular junction is presented in that chapter. Furthermore, a toy model based on the resonant tunneling is discussed to explain the Fano like resonance in molecular junction, appearing due to quantum interference of electronic waves.

Chapter 3 deals with the experimental technique along with the development of our experimental arrangements to fabricate the single molecular junction and corresponding data analysis tools. To execute the reported study in that thesis, wire notched mechanically controllable break junction (MCBJ) technique is employed which operates on the three point bending mechanism[34]. A short note on the history and principle of MCBJ technique is stated comprising with the finer details of our experimental arrangements and electronic circuit diagrams. Additionally, characterization of our experimental set up using an atomic junction (gold) and a

well-studied molecular junction (4,4'-Bipyridine) are presented together with an extensive description of each data analysis tools.

Chapter 4 demonstrates the probing of metal-molecule contact formation at the atomic scale by studying the formation and the post rupture evolution of two isomers of bipyridine molecules (4,4'-Bipyridine and 2,2'-Bipyridine) connected via gold electrodes at room temperature. While both molecules form molecular junctions during the breaking of the junction, corresponding closing event show the formation of molecular junctions unambiguously for 4,4'-Bipyridine via a conductance jump from the tunneling regime, referred to as "jump to molecular contact," being absent for 2,2'-Bipyridine. Combining statistical analysis of the data, molecular dynamics and first-principles calculations, we establish that contact formation is strongly connected with the orientation of molecule as well as how the junction is broken during the breaking process.

Chapter 5 illustrates the realization of highly conducting molecular junction based on the near resonant transport mechanism in an organometallic molecule. Electronic transport measurements by directly connecting a ferrocene to Au electrodes exhibits a highly conducting feature at the ambient condition. A similar experiment was repeated for ferrocene terminated with amine (**-NH_2**) and cyano (**-CN**) anchors, where an extended low conductance features along with the high conductance feature like pristine ferrocene are observed. Theoretical calculation indicate that two different orientations of ferrocene (perpendicular and parallel to the electrode axis) are energetically favorable inside the junction which may lead to two different conductance values (high and low). A detailed statistical analysis of the data along with transport calculations suggests the near resonant transport mechanism in the perpendicular conformation with a strong hybridization between the Au electrodes and Fe atom (covalent like bonding) of ferrocene is responsible for the high conductance feature. Whereas, broad low conducting feature attributes to the multiple geometry due to coupling with the anchoring arms. Through this study, the decisive role of molecular orientation to the charge transport behavior of a three dimensional organometallic molecule is depicted. Furthermore, modification of conformation (perpendicular to parallel) of ferrocene is found to alter the transport mechanism from resonant to non-resonant under the considered bias window.

Chapter 6 continues to study the ferrocene molecular junction by investigating the effect of temperature on the molecular conformation. Single molecular conductance measurements at $4.2\,K$, $77\,K$, and $300\,K$ provides an interesting outcome: reduction of temperature leads to

enhancement of stable molecular conformation to be executed in the form of junction. Density functional theory (DFT) based calculation enables that stable perpendicular or parallel orientation of ferrocene, identified from the previous study, is developed due to coupling of Au electrodes with Fe atom or π bond of Cp rings of ferrocene. Surprisingly, another exciting fact of ferrocene is ascertained from the Molecular dynamics (MD) simulation. While Cp rings of ferrocene are rotated freely at $300\ K$, reduction of temperature freezes the Cp rings. This rotating Cp rings at $300\ K$ do not allow the formation of chemical bond between Au and the π orbitals in the parallel configuration, whereas static rings at low temperature opens the possibility of this conformation and perpendicular conformation is typically unaffected by the temperature. Thus, both parallel and perpendicular orientation of ferrocene is likely to be the possible conformations at low temperature in contrast to room temperature where only perpendicular configuration remains, in line with the experimentally determined accessibility of more conformation with the reduction of temperature. Combing experimental observations and theoretical calculation, sticking influence of temperature on the formation of ferrocene molecular junction is presented.

In ***chapter 7***, continuing ferrocene as a molecular component other possibilities of the single molecule junctions are explored on silver/ferrocene junction. In contrast to silicon-based transistors, single molecule junctions can be gated by simple mechanical means. Specifically, charge can be transferred between the junction's electrodes and its molecular bridge when the interelectrode separation is modified, leading to variations in the electronic transport properties of the junction. While this effect has been studied extensively, the influence of the molecule orientation on mechanical gating has not been addressed which is the central motivation of this chapter. Experimentally recorded differential conductance spectra along with the transition voltage spectroscopy (TVS) of silver/ferrocene molecular junction express that same junction can experience either clear mechanical gating or none. This effect is attributed to the orientation of the molecule inside the junction, proposed by the theoretical calculations. Two distinct stable configurations with parallel and perpendicular orientation of ferrocene with respect to the electrode axis are theoretically confirmed for silver/ferrocene junction, similar to the previous study on gold/ferrocene. When the molecule is oriented in parallel to the junction axis, mechanical gating is seen, however, for the perpendicular molecular orientation a similar effect cannot be found. The mechanical gating response for the parallel molecule configuration and the absence of this effect for the perpendicular configuration can be ascribed to the orientation of the molecular orbitals that

dominate transport with respect to the electrodes, and their coupling to the frontier electrode states. These findings emphasize the importance of geometry and local orbital structure of molecule in the context of charge transfer across metal-molecule interfaces.

Chapter 8 focuses on impurity induced metal atomic chain formation, another important aspect of single molecular electronics and our specific interest is to probe the configuration having conductance value in the tunneling conductance regime. Atomic chain is the thinnest possible metallic wire, consists of an array of metal atoms arranged linearly, which is regularly observed in break junction experiments. While spontaneous formation of atomic chain for late 5d transition metals (e.g., Au, Pt, Ir) are easily achievable, 3d and 4d metals (e.g., Cu, Ag) demands foreign impurities to form stable one-dimensional chain[35–41]. Primarily these metals were shown to form chains in presence of various impurities like oxygen (O_2), hydrogen (H_2), water (H_2O), deuterium (D_2)[42–49]. Conductance of this impurity assisted metallic chain belongs to high conductance regime($\geq\ 0.1\ G_0$, G_0 being the quantum of conductance). However, plausibility of configuration with conductance value $<\ 0.1\ G_0$ cannot be excluded and this possibility is investigated for copper and aluminum metallic junction by inserting hydrogen molecules. In presence of hydrogen, distinct evolution between copper and aluminum junction is evident from single molecular conductance measurements. Statistical analysis of data ensures the hydrogen decorated copper atomic chain with conductance value down to $0.001\ G_0$, which is completely absent for aluminum. Participation of hydrogen to these low conducting configurations is further verified from the characteristics vibrational signatures of the inelastic electron tunneling spectroscopy (IETS). Intrinsic frontier orbitals of aluminum and copper might play a crucial role for this contrary response. Thus, our observation demonstrates the opportunity to fabricate low conducting metal atomic chain with the help of external molecules in conjugation with a primary understanding of the contribution of the continuum states of metallic electrodes to form nearly insulating metallic wire.

Finally, the thesis is concluded by giving a conclusion and outlook of the executed study in ***chapter 9***.

An appendix chapter (***chapter 10***) is stitched before end, consisting of experimental results that have been performed during my doctoral course but not included in this thesis. Including all, I have carried out 55 single molecular conductance measurements, combining six different electrodes and ten types of molecules. To check the experimental history at a glance, a statistics

based on the related information including success and failure rate is given in the that chapter in the form of bar diagram.

Chapter 2 | Theoretical background

This chapter describes the charge transport across a single atomic and molecular junction using a theoretical modelling approach based on Landauer's scattering formalism. Furthermore, the key factors to tune the electrical characteristics of a single molecular junction are demonstrated.

2.1. What is ballistic transport?

Electrical conduction through macroscopic metallic wire is described by Ohm's law which demonstrates that current is proportional to the applied voltage and constant of proportionality is known as conductance. However, Ohm's law is not applicable to the atomic-sized conductors as it enters into the mesoscopic regime where quantum coherence plays a central role. It is important to mention that different length scales of mesoscopic systems are the key parameter to decide the transport mechanism and such length scales are determined by the scattering mechanisms[50]. For example, mesoscopic regime is said to dominate when $L < L_{\varphi}$, where L is the typical length of the sample and L_{φ} is called the phase coherence length. Phase coherence length is defined as the distance up to which information concerning the phase of the electronic wave remains conserved. Another important length scale is the elastic mean free path (l), roughly the distance between two elastic collisions with static impurities. Regime with $l \ll L$ is known as *diffusive* for which motion of the electron is considered as a random walk of step size l among the impurities. Another condition, $l > L$ leads to the *ballistic* regime where electron momentum is assumed to be constant and limited by the scattering with the boundaries of the sample. A schematic layout of diffusive and ballistic transport is displayed in **Figure 2.1**. Nowadays, advancement of nanotechnology techniques makes it possible to fabricate devices with characteristic dimensions smaller than the length scale of the diffusive scattering. An example of such a device include atomic or molecular junction where characteristic dimensions are the size of the several atomic units, relevant to this thesis. Under these conditions, transport is assumed to be governed by the ballistic phenomena: electrons are crossing without loss of momentum and phase.

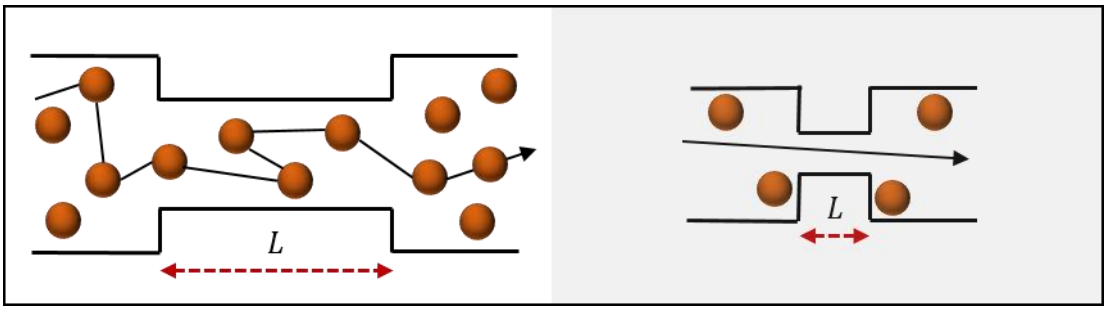

Figure 2.1 *Schematic illustration of diffusive (left) and ballistics transport (right).*

2.2. Conduction channels and Landauer's formalism of scattering approach:

The most popular theoretical formalism to describe coherent transport through nano-scale devices is the scattering approach, put forward by Rolf Landauer[33,50] in the late 1950's. Main idea of this approach is to relate the transport properties with the reflection and transmission probabilities for the carrier's incident on the sample[31,32].

Let us consider a mesoscopic sample connected to the two reservoirs, referred as left (L) and right (R) as shown in **Figure 2.2**. It is further assumed that reservoirs are so large that they can be characterized by a temperature $T_{L,R}$ and a chemical potential $\mu_{L,R}$. Distributions of the electrons inside the reservoirs obeys the Fermi distribution function

$$f_\alpha(E) = \frac{1}{1 + \exp {(E - \mu_\alpha)}/{K_B T_\alpha}} \qquad \alpha = L, R \tag{2.1}$$

Far from the sample, transverse and longitudinal motions of the electrons are assumed to be separable. Here, system is opened in the longitudinal direction and characterized by the continuous wave vector k_l. The longitudinal energy is thus $E_l = {\hbar^2 {k_l}^2}/{2m}$, whereas transverse motion is quantized due to confinement and described by the discrete index number n, corresponding to transverse energies $E_{L,R;n}$ (different for left and right reservoirs). These states are transverse quantum channels. Thus, total energy, $E = E_n + E_l$. Since E_l needs to be positive, for a given total energy(E), only a finite number of channels exists. The number of incoming channels are

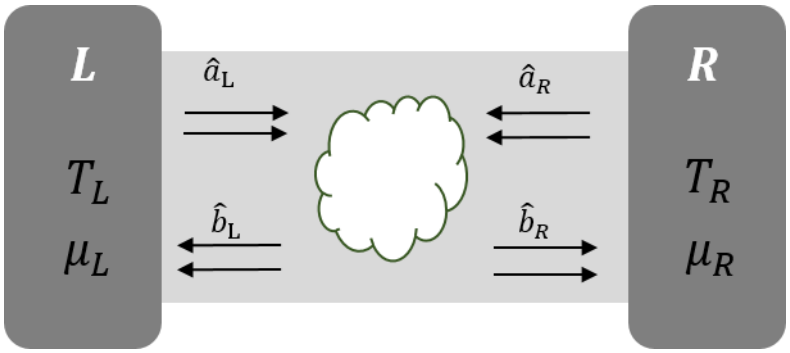

Figure 2.2 *Landauer formalism of scattering approach for ballistic transport. A rectangular ballistic conductor attached to infinite leads with a potential difference of $(\mu_L - \mu_R)$. A single scatter is located inside the conductor.*

denoted by $N_{L,R}(E)$ in the left and right lead, respectively. Further calculation is performed by introducing creation and annihilation operator of the electrons in the scattering states. Operators

$\hat{a}^{\dagger}_{\mathrm{L,R};n}(E)$ and $\hat{a}_{\mathrm{L,R};n}(E)$ create and annihilate electrons with total energy E, respectively, in the transverse channel n of each lead and $\hat{b}^{\dagger}_{L,R;n}(E)$, $\hat{b}_{L,R;n}(E)$, which in the same way, create and annihilate electrons in the outgoing states of each lead. The annihilation operators are related via the scattering matrix $\hat{S}$ that describes a barrier of an arbitrary shape.

$$\begin{pmatrix} \hat{b}_{L1} \\ \vdots \\ \hat{b}_{LN_L} \\ \hat{b}_{R1} \\ \vdots \\ \hat{b}_{RN_R} \end{pmatrix} = \hat{S} \begin{pmatrix} \hat{a}_{L1} \\ \vdots \\ \hat{a}_{LN_L} \\ \hat{a}_{R1} \\ \vdots \\ \hat{a}_{RN_R} \end{pmatrix} \tag{2.2}$$

The matrix $\hat{S}$ has dimensions of (N_L+N_R) × (N_L+N$_R$), such that its size and the matrix elements depend on the total energy E (determining the number of channels). It has a block structure:

$$\hat{S} = \begin{pmatrix} \hat{r} & \hat{t}' \\ \hat{t} & \hat{r}' \end{pmatrix} \tag{2.3}$$

where the square diagonal blocks $\hat{r}$ (size N_{L}×N_{L}) and $\hat{r}'$ (size N_{R}×N_R) describe electron reflection back from the left and right reservoirs respectively, and the off-diagonal rectangular blocks $\hat{t}$ (size N_R×N_{L}) and $\hat{t}'$ (size N_{L}×N_{R}) describe the electron transmission through the sample. The matrix $\hat{S}$ can be shown to be unitary, and symmetric under time reversal conditions. Using the above operators to describe the current, the following expression for the average current can be obtained:

$$I = \frac{e}{h}\int_{-\infty}^{\infty} dE\, Tr[\hat{t}^{\dagger}(E)\hat{t}(E)][f_{\mathrm{L}}(E) - f_{\mathrm{R}}(E)] \tag{2.4}$$

Here, the matrix $\hat{t}$ is the off-diagonal block of the scattering matrix, whose element: $t_{mn} = S_{R,L;mn}$ gives the probability amplitude for an electron wave in mode *n* on the left contact to be transmitted into mode *m* on the right of the contact. In the zero-temperature limit, and for a small applied voltage, **Equation (2.4)** gives a conductance of:

$$G = \frac{e^2}{h} Tr[\hat{t}^{\dagger}(E_F)\hat{t}(E_F)] \tag{2.5}$$

Equation (2.5) shows the relation between the scattering matrix evaluated at the Fermi energy and the conductance. The matrix $\hat{t}^{\dagger}\,\hat{t}$ can be diagonalized and it has a real set of eigenvalues, which are the transition coefficients $T_n(E)$, each of them between zero and one. The corresponding eigen functions are the eigen channels or conduction channels. In this natural basis, **Equation (2.4)** becomes:

$$I = \frac{e}{h}\sum_{n}\int_{-\infty}^{\infty} dE\, T_n(E)[f_{\mathrm{L}}(E) - f_{\mathrm{R}}(E)] \tag{2.6}$$

and the conductance, after adding a factor of two due to spin degeneracy, is

$$G = \frac{2e^2}{h}\sum_{n=1}^{N} T_n = G_0 \sum_{n=1}^{N} T_n \tag{2.7}$$

This is known as the multi-channel generalization for the Landauer formula. Here, the conductance is viewed to be carried by N independent conduction channels. Each conduction channel has a transmission probability of T_n . A fully open channel (T_n = 1) will conduct up to a value of $G_0 = (2e^2/h)$, which is known as the quantum of conductance. Note that the actual number of channels for an atomic junction is determined by the valence orbital structure of the atoms[51].

2.3. Coherent transport through molecular junction- Resonant tunneling model:

On the other hand, theoretical description of electrical conduction through molecular junctions is more complicated compared to atomic wires for various reasons[50]. The primary reason would be its complicated electronic structure, simply because it is composed of several atoms of different species. Secondly, weak interaction at the metal-molecule interface leads to the presence of correlation effects such as Coulomb blockade or the Kondo effect, which in turn play an important role for electronic transport. Furthermore, molecules possess internal degrees of freedom, in particular vibrations modes, which can be excited by the transport of electrons leading to a modification of the current-voltage $(I - V)$ characteristics. A molecule can also undergo conformational modification due to, for instance, the high electric fields applied in the contacts, mechanical stress, an external field (electromagnetic radiation) or the local environment (red-ox reactions).

Regarding the transport through the molecular junction, it is obvious that different molecular orbitals can participate simultaneously. However, there are many cases for which one level (HOMO or LUMO) lies closest to the Fermi level of the metal and hence dominates the transport in a certain voltage range. Such a situation can be described by the single level resonant tunneling model, depicted in **Figure 2.3a**. Level position is denoted by ϵ_0 with respect to the position of metallic Fermi levels. At finite bias, applied bias voltage can modulate the position of level, which is indicated by considering $\epsilon_0\ (V)$. The other key parameters of this model are the scattering rates

$\Gamma_{L,R}$ which describe the strength of the coupling to the metal electrodes (L, R). These parameters have dimensions of energy and it determine the lifetime or broadening of the resonant level.

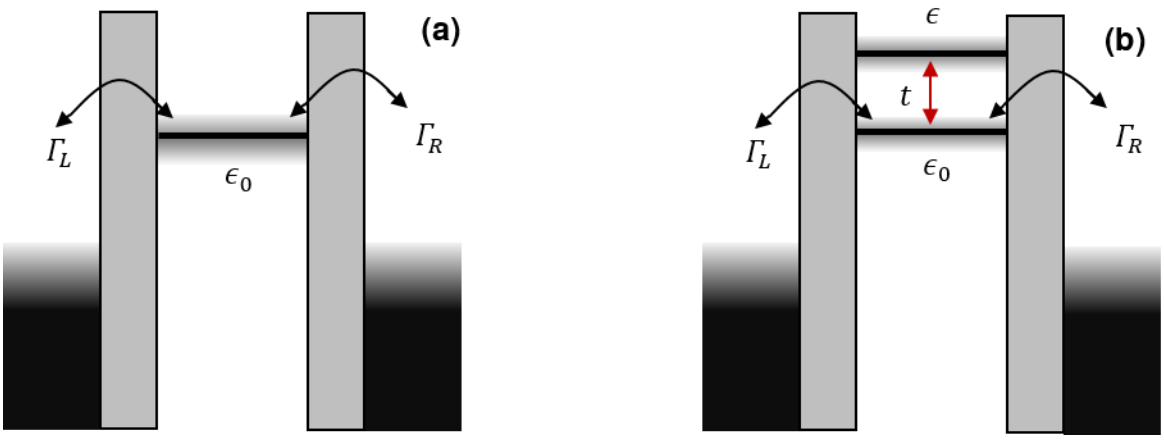

Figure 2.3 (a) *Level scheme of a molecular junction where the transport is dominated by a single level, ϵ_0.* ***(b)*** *Same scheme with two- level model to explain the physics of Fano resonance. Compared to the previous model, here, an additional level ϵ is introduced which is coupled to resonant level ϵ_0 via hopping parameter t, but not to the leads.*

Following the spirit of Landauer's approach, $I-V$ characteristics of this model can be expressed as,

$$I = \frac{2e}{h}\int_{-\infty}^{+\infty} dE\, T(E,V)\left[f\left(E - {}^{eV}/_{2}\right) - f\left(E + {}^{eV}/_{2}\right)\right] \tag{2.8}$$

Above equation is similar to **Equation (2.6)** except the factor 2 which is due to the spin symmetry, $f(E)$ is the Fermi function and $T(E,V)$ is the energy and bias voltage dependent transmission coefficient, given by the Breit-Wigner formula,

$$T(E,V) = \frac{4\Gamma_L\Gamma_R}{[E-\epsilon_0(V)]^2 + [\Gamma_L+\Gamma_R]^2} \tag{2.9}$$

As stated earlier, strength of metal-molecule coupling[52] and energetic offset is thus a deciding factor for electronic transmission through molecular junction. For instance, transmission calculated for different values of ϵ_0 and (Γ_L/Γ_R) is presented in **Figure 2.4a-b**. It is obvious that decrease of energetic offset increases the zero-bias transmission at the metallic Fermi energy (**Figure 2.4a**). On the other hand, introduction of asymmetry reduces the corresponding zero bias transmission (**Figure 2.4b**). $\Gamma_L \neq \Gamma_R$ corresponds to the asymmetric coupling where a molecule is differently coupled to the alternate electrodes. Asymmetry in the coupling can be due to extrinsic

factors like asymmetric configuration of the molecule or intrinsic geometry of the molecule under consideration. This factor simply induces asymmetric charge distribution in the molecular orbitals which, in turn, leads to the dissimilar voltage drop at the interfaces. Thus, molecular orientation or geometry inside the junction is one of the key parameters to engineer the hybridization at the metal-molecular interface, which is the primary subject of this thesis.

2.3.1. Fano resonances

Coherent transport through molecular junctions is determined by Breit-Wigner resonances that appear from the different molecular orbitals. However, these are not the only transmission line shapes that can be expected in molecular junctions. Possibility of Fano like resonance due to quantum interference of electronic waves cannot be neglected[53–61]. In case of molecular junction, a Fano resonance can appear in the transmission due to interplay between extended molecular orbitals and states that are localized in a molecular side group, decoupled from the electrodes[56]. Toy model[56] based on the resonant tunneling model is schematically presented in **Figure 2.3b** to explain the Fano resonance. The main inclusion is the additional site (energy level) that represents the side group, not directly coupled to the electrodes. Level position of this addition site is denoted by ϵ and coupling to the resonant level (ϵ_0) is described by the hopping t. Calculation of zero bias transmission in this model provides the following expression,

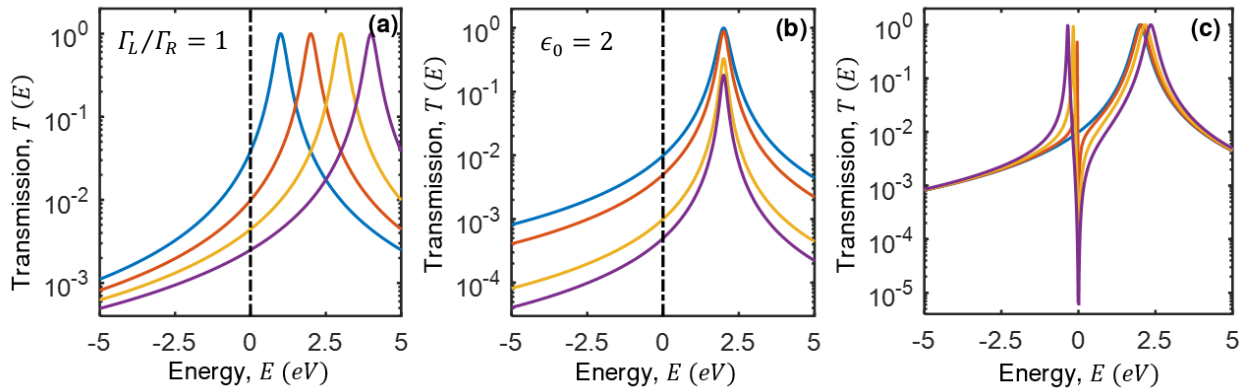

Figure 2.4 (a) *Zero bias transmission as a function of the energy for the model, schematically described in* ***Figure 2.3a*** *.Different curves correspond to different values of* $\epsilon_0 = 1.0\ eV$ *(blue),* $2.0\ eV$ *(orange),* $3.0\ eV$ *(yellow) and* $4.0\ eV$ *(violet) with* $\left(\Gamma_L/\Gamma_R\right) = 1$. ***(b)*** *Same as (a) where different curves correspond to different values of* $\left(\Gamma_L/\Gamma_R\right) = 1$ *(blue),* 2 *(orange),* 10 *(yellow) and* 20 *(violet) with* $\epsilon_0 = 2.0\ eV$. ***(c)*** *Zero-bias transmission as a function of the energy for the model, schematically presented in* ***Figure 2.3b*** *for* $\epsilon_0 = 2.0\ eV$, $\epsilon = 0.0\ eV$, $\Gamma_L = \Gamma_R = 0.1\ eV$ *and different values of the coupling:* $t =$ $0.0\ eV$ *(blue),* $0.3\ eV$ *(orange),* $0.6\ eV$ *(yellow) and* $0.9\ eV$ *(violet).*

$$T(E) = \frac{4\Gamma_L\Gamma_R}{[E - \epsilon_0 - {t^2}/{(E - \epsilon)}]^2 + (\Gamma_L + \Gamma_R)^2} \quad (2.10)$$

This equation takes the form of Breit-Wigner formula (**Equation (2.9)**) when coupling element vanishes($t = 0$). Key findings of this model are the presence of an anti resonance at $E = \epsilon$, appearing due to the destructive quantum interference of electronic waves. Apart from this anti resonance, transmission exhibits two maxima at $E = \epsilon_{\pm}$,

$$\epsilon_{\pm} = \frac{1}{2}\left\{(\epsilon + \epsilon_0) \pm \sqrt{(E - \epsilon_0)^2 + 4t^2}\right\} \quad (2.11)$$

In the weak coupling limit($t \ll (E - \epsilon_0)$), hybridization with side group leads to a peculiar asymmetric structure formed by a peak followed by a dip (anti resonance), which is the fingerprint of Fano resonance. Such feature is evident from the calculated transmission as shown in **Figure 2.4c,** for different values of t and is absent when $t = 0$. However, this peculiar fingerprint needs to be located in the vicinity of the metallic Fermi energy to achieve a significant impact on the transport characteristics[53,54].

Chapter 3 | Experimental methods and data analysis tools

This chapter covers the experimental technique (Mechanically controllable break junction) to fabricate single molecular junctions, including its principle, a brief history, and finer details of our indigenously developed experimental arrangements. Characterization of our experimental set up using an atomic junction (gold) and a well-studied molecular junction (4,4'-Bipyridine) are presented including a detailed description of each data analysis tool.

3.1. Method- Mechanically controllable break junction:

The present chapter deals with the experimental methods and data analysis tools, which would be used in the subsequent chapters. Our method of choice to fabricate the atomic or molecular junction is mechanically controllable break junction (MCBJ) technique. Excellent mechanical stability of this technique makes it widely accepted to study the dynamical response of the nanoscale junction. Historically the idea was first initialized by Moreland and Ekin in 1985 to study the vacuum tunneling between superconductors[62]. However, significant progress was made by Muller et al. in 1992 to check the quantum effects on the conductance behavior of a gold wire[5]. Later in 1997, Reed et al. used this technique to examine the charge transport properties of 1,4-Benzenedithiol molecular junctions[63].

Schematic layout of a mechanically controllable break junction set up based on the three-point bending configuration is shown in **Figure 3.1a**. Three important parts can easily be distinguished: a flexible substrate with a notched metallic wire on its top, a central pushing rod to give the upward force and two lateral counter support to rigidly hold the substrate. To prepare the MCBJ sample, a notch (weak spot) is prepared at the center of a macroscopic metallic wire using a surgical blade (Swan Morton), controlled by a Z positioner (Holmarc Opto-Mechatronics Ltd) as shown in **Figure 3.1b**. Metallic wire with the notch at its middle is then placed on top of a flexible substrate (phosphor bronze of thickness$\sim 1\ mm$), covered by a Kapton sheet for electrical insulation. An epoxy glue (Stycast 2850 FT with catalyst 9) is used at both sides of the notch to rigidly fix the wire (shown in the inset of **Figure 3.1b**). The substrate is then mounted in the home made three point bending configuration. Technical details of these set up are summarized in the next section. In case of a three point bending mechanism, bending the substrate leads to an increase of the strain in the wire, primarily concentrated at the weak spot. Such bending is achieved due to the upward motion of the central pushing rod. Further increase of the strain results in breaking of the wire, forming two freshly exposed atomistic electrodes. By relaxing the stretched substrate and employing fine control of the gap by means of a piezoelectric actuator (Piezomechanik Gmbh, Pst $150/2 \times 3/7$), atomic-size junctions can be formed and broken multiple times. Subsequently the nanogap between the two facing electrodes can be tuned with high accuracy during both bending and relaxing process, ideal for making a molecular junction connected via atomic tips. Molecules are introduced near the weak spot of the electrode using either an external vapor source[26,64] or employing a local cell for sublimation[65,66] or by means of self-assembly from solution[67]. After

successful formation of molecular junctions, charge transport properties are studied using an electrical circuit, described in the **Section 3.3**. Note that, small value of the attenuation factor [$r = \Delta d/\Delta h = (6ut/L^2)$, where t is the thickness of the substrate, u is the length of the weak spot and L is the length between the counter support of the three-point bending mechanism] defined as the ratio between interelectrode separation (Δd) and displacement of the piezo (Δh), makes it suitable to manipulate the conformation of the junction with a sub-angstrom resolution[34] and not only that, it provides excellent mechanical stability.

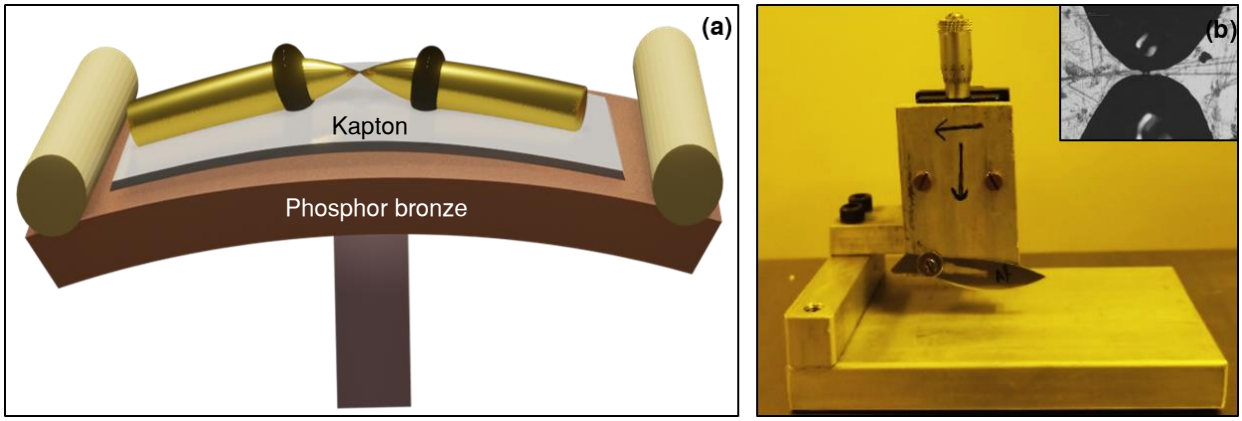

Figure 3.1 (a) *Schematic representation of the three-point bending configuration of the mechanically controllable break junction (MCBJ) technique.* ***(b)*** *'Wire notcher', designed to make the weak spot or notch in the wire by rolling the wire underneath the blade. Inset: a picture of the MCBJ sample with a notched gold wire where the two black spots are the epoxy (Stycast) that fixes the wire on top of the kapton foil.*

3.2. Technical details of the experimental set up:

Two experimental arrangements based on the MCBJ technique were developed in our lab as a part of my doctoral thesis. In this subsection, technical details of this setups are summarized. For simplicity, arrangements are named as "Room temperature MCBJ (set up-1)" and "MCBJ dipstick (set up-2)".

3.2.1. Room temperature MCBJ (set up-1)

Set up-1, shown in the **Figure 3.2**, is machined at the mechanical workshop of S. N. Bose. National Centre for Basic Sciences, Kolkata as per the design provided by us. Here, upward movement of the central rod is ensured from the combination of a Z positioner (Holmarc Opto-Mechatronics Ltd, India) and piezo stacks (Piezomechanik Gmbh, Germany, Pst 150/2 × 3/7) for rough and fine bending of the substrate, respectively. Set up is placed on top of a sponge (label 1 of **Figure 3.2a**)

inside a faraday cage (label 2 of **Figure 3.2a**) to reduce the external mechanical and electrical hazards. Moreover, the base of this set up is kept intentionally heavy to attain the desirable mechanical stability. After optimization of this set-up, we have been successful in performing the experiments at the ambient condition.

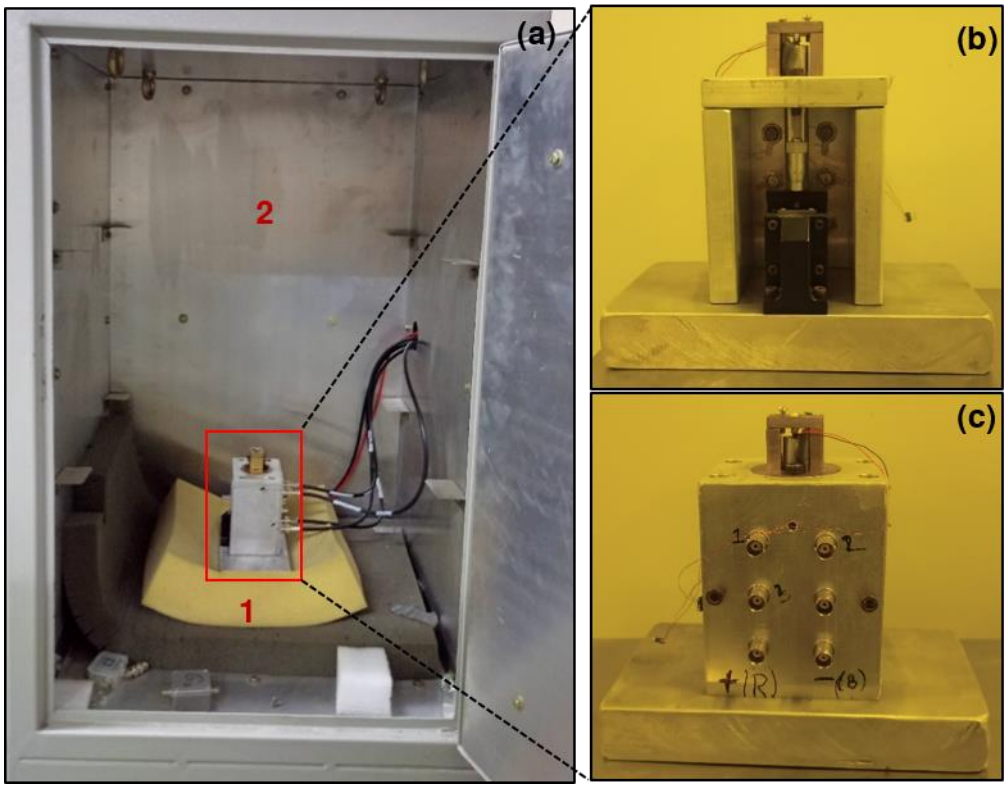

Figure 3.2 (a) *Experimental arrangements of room temperature MCBJ (set up-1), showing the sponge (1) and faraday cage (2) to reduce the external mechanical and electrical noise.* ***(b, c)*** *Rear view, front view of the home made three point bending configuration of the set up-1.*

3.2.2. MCBJ dipstick (set up-2)

MCBJ dipstick (set up-2) is machined at the *Excel Instruments, India* and in that case, fine details of the design are edited jointly by us and their team (based on the initial design of Prof. Oren Tal's lab, Weizmann Institute of Science, Israel). **Figure 3.3** shows the 3D view of the set up-2, sketched by the design department of the *Excel Instruments*. Electrical wiring and optimization of this setup for break junction experiments are completed in our lab. This system is designed primarily to perform experiments at cryogenic environments. MCBJ sample (substrate with a notched metallic wire) is loaded at the bottom of the stick and wired up to the top of the stick for necessary electrical measurements. Body of this stick consists of a long hollow pipe of length $\sim 110\ cm$ and $\sim 5\ cm$ in outer diameter which on the other hand serves as a Faraday cage. Pumping and electrical

measurements are performed from the chamber attached at the top of the stick and this part is not immersed in the cryogenic liquid (see **Figure 3.3b**). Electrical wires from the top to bottom are guided by different hollow pipes inside the stick. Bending of the substrate is obtained by a screw with fine pitch at the bottom, which is connected to a manually rotatable knob, attached to the top chamber via a vacuum feed through. However similar to set up-1, fine adjustment is achieved by a piezo electric actuator fixed at the bottom of the screw which allows breaking and making of the junction in sub-angstrom resolution. Until now, this set-up is capable of introducing foreign molecules in the gaseous form to the cold junction by using an in-situ molecule dozer. This is prepared by using thin metal capillary tube (shown in the **Figure 3.3c**) passing through the stick and equipped with an internal heating wire to avoid the premature condensation of the gas molecules. At the end of the capillary, it is like an "L" shape to insert molecules directly onto the notched part of the electrode. Prior to supply of the molecule, capillary tube is pumped for hours with a turbo molecular pump and often baked at $\sim 80 - 90^0\ C$ to get rid of any contamination. Continuous pumping of this capillary tube using a turbo molecular pump is necessary during the molecular insertion to prevent unwanted contamination.

Cryogenic vacuum and temperature stability are crucial to form stable atomic and molecular junction and hence, special attention was taken during the design and optimization of this stick.

(i) High vacuum

Stick is pumped to $\sim 10^{-6}\ mbar$ using turbo molecular pump prior to its insertion in the cryogenic liquid dewar (either N_2 or He). During the course of the pumping, repetitive bake out (at $\sim 80 - 90^0\ C$) is done to remove the contamination from the walls of the dipstick. It is necessary to continue the pumping until the reading of the pressure gauges saturates and it typically takes more than one day. Narrow capillary tube is evacuated separately using its internal heating provision to facilitate better cleaning. After attaining adequate pumping, the stick is immersed in the cryogenic liquid and the pump is disconnected soon after the cryogenic pumping takes over.

(ii) Thermal stability

To attain better thermal stability across the sample, it is important to thermally decouple the bottom part from the top chamber which is kept at the room temperature. Different efforts are tried, for instance, radiation shields (namely the metal plates) are placed inside the dipstick to support the inner pipes, which on the other hand, blocks thermal radiation from top chamber to the sample. One important step is the use of thermalization plates. The electrical wires from the top chamber

to the particular components (like piezo element, temperature sensors, and sample) at the bottom

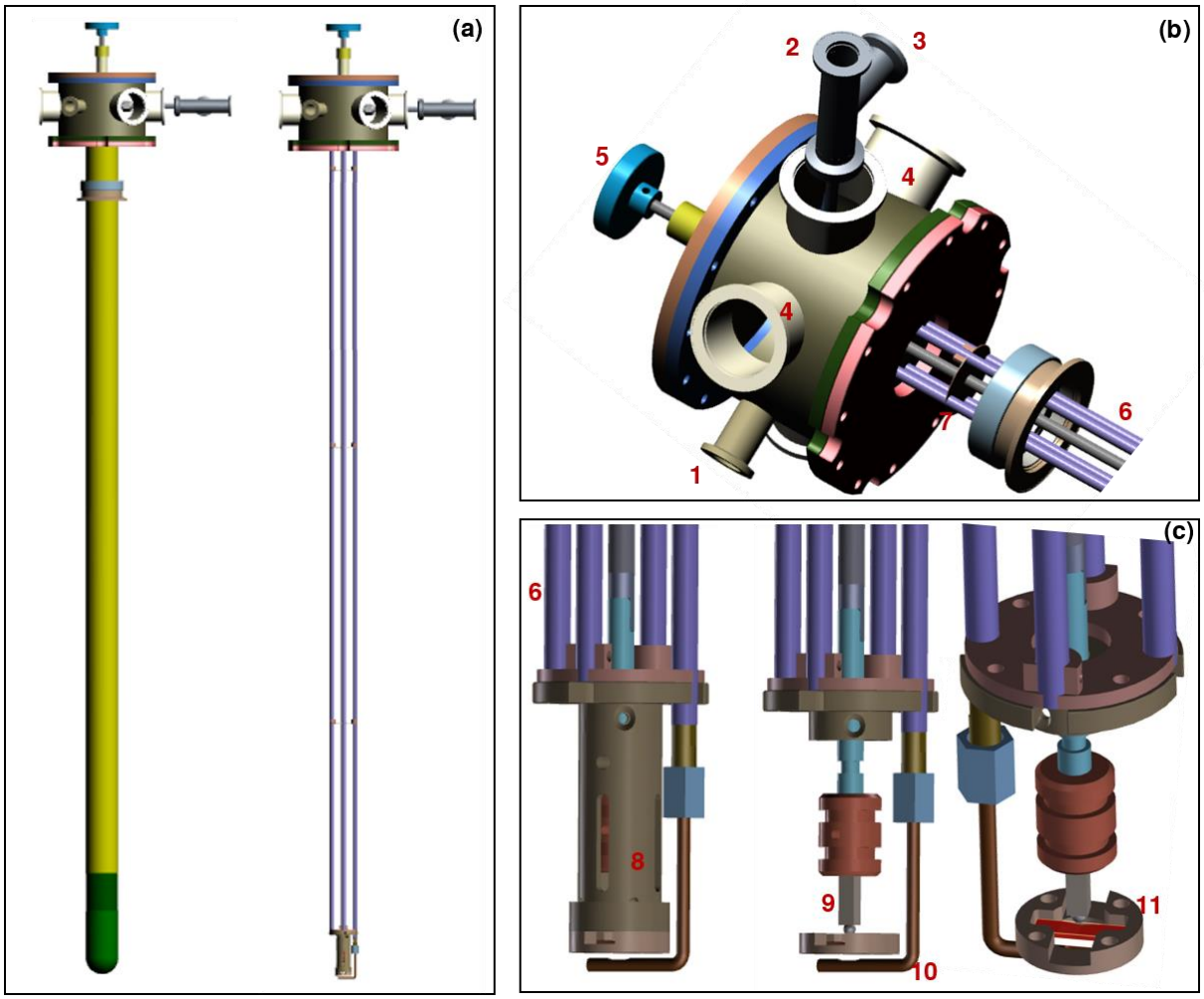

Figure 3.3 (a) *Sketch of the MCBJ dipstick (set up-2) with (left) and without outer jacket (right).* ***(b, c)*** *zoom in view of the top, bottom part of the stick. Number labels in different points of b, c demonstrates the following sections- 1. Pumping port for main stick, 2. Pumping port for capillary tube, 3. Port for capillary heating, 4. Port for Electrical connection (Piezo, conductance measurements and so on), 5. Knob for manual breaking of the samples, 6. Guided pipes of electrical wires, 7. Thermal radiation shield, 8. Thermalization plates of the electrical wires, 9. Piezo, 10. Capillary edges and 11. Sample.*

is connected via a thin copper plates, known as thermalization plates (shown in **Figure 3.3c**), instead of direct connection. To attain the bath temperature immediately, the thermalization plates are directly attached to the cryogenic bath via a metal jacket (using a cryogenic vacuum grease) which reduces thermal loss and ensures a good thermal stability. Moreover, all guiding pipes and outer jacket are made from thin wall stainless steel which has a low heat conductance. Another source of heat conduction is the capillary, being heated during the insertion of molecules.

However, capillary is thermally anchored to the cryogenic bath which confirms extremely fast cooling once molecule dozing is over. Stability of the temperature is verified from two independent sensors, placed- on the thermalization plate and on top of the substrate. Temperature of these two sensors is shown in the **Figure 3.4**. As such no noticeable difference between the temperatures are observed and during the experiment, the temperature sensor is kept on the thermalization plates to record the temperature.

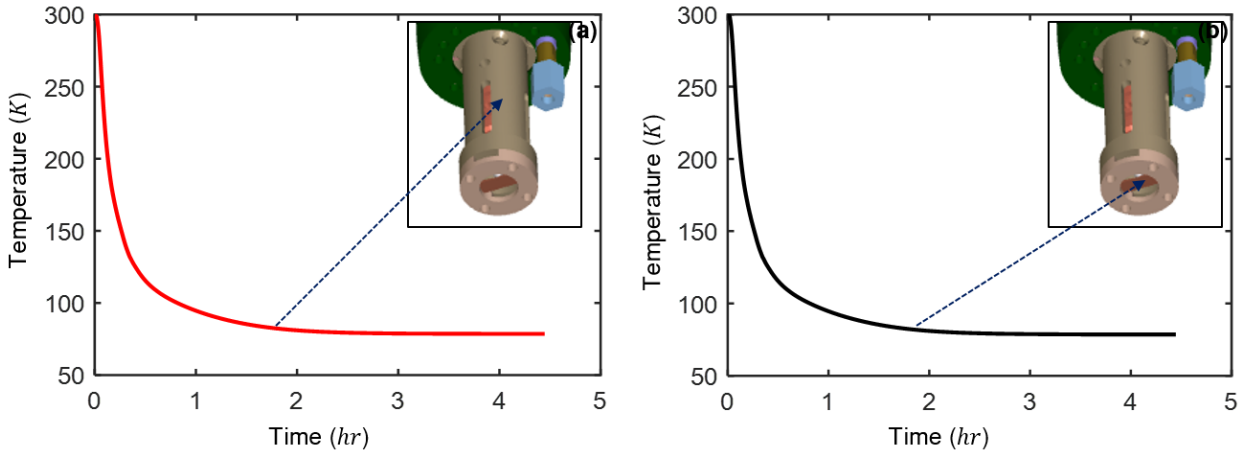

Figure 3.4 (a, b) *Temperature as a function of time for the sensors kept at the thermalization plates (a) and at the position of the sample (b). Inset: position of the sensors in the sketch.*

3.3. Electrical circuit diagram:

Electrical circuits used for biasing piezo stack, measuring d.c. conductance and differential conductance are schematically shown in **Figure 3.5 - Figure 3.7** and described briefly in the following section.

(i) Piezo bias circuit

A triangular waveform is applied to the piezoelectric element, from the output terminal of 24-bit (PCI 4461, National Instruments) data acquisition card (DAQ) via an amplifier (Piezomechanik Gmbh, Germany (SVR 150/1)), which essentially translates into a small displacement of atomic tips. The amplitude and frequency of this waveform are fixed by a custom designed LABVIEW interface. In each cycle of the waveform, conductance (G) of the junction is measured as a function of corresponding voltage at the piezo (V_p). Such a complete measurement cycle (G vs. V_p) is called conductance trace. This waveform is repeated multiple times to acquire large number of such conductance traces (let's say 10,000 or sometimes even more) to probe the most probable behavior of the junction by carrying out the statistical analysis, described in the next section.

(ii) D.C. conductance measurement circuit

For conductance measurements, a constant d.c. bias voltage (V) is applied to the junction via a $10:1$ divider (which improves the signal to noise ratio) from the output terminal of the data acquisition card (DAQ). Generated current (I) is amplified by a current to voltage preamplifier (SP 983, electronics lab, University of Basel) and the amplified signal is recorded at the input terminal of the same DAQ card. The d.c. conductance of the junction is thus the measured current divided by the applied voltage (I/V). This circuit can measure conductance over a large dynamic range ($\sim 20\ G_0$ to $10^{-4}\ G_0$ at a fixed bias of $100\ mV$) by keeping the preamplifier gain constant (typically $10^5\ V/A$). However, the DAQ card can measure the voltage upto $\pm\ 10\ V$ which limits the detection of the conductance lower than $\sim 10^{-4}\ G_0$ keeping the same dynamic range. The

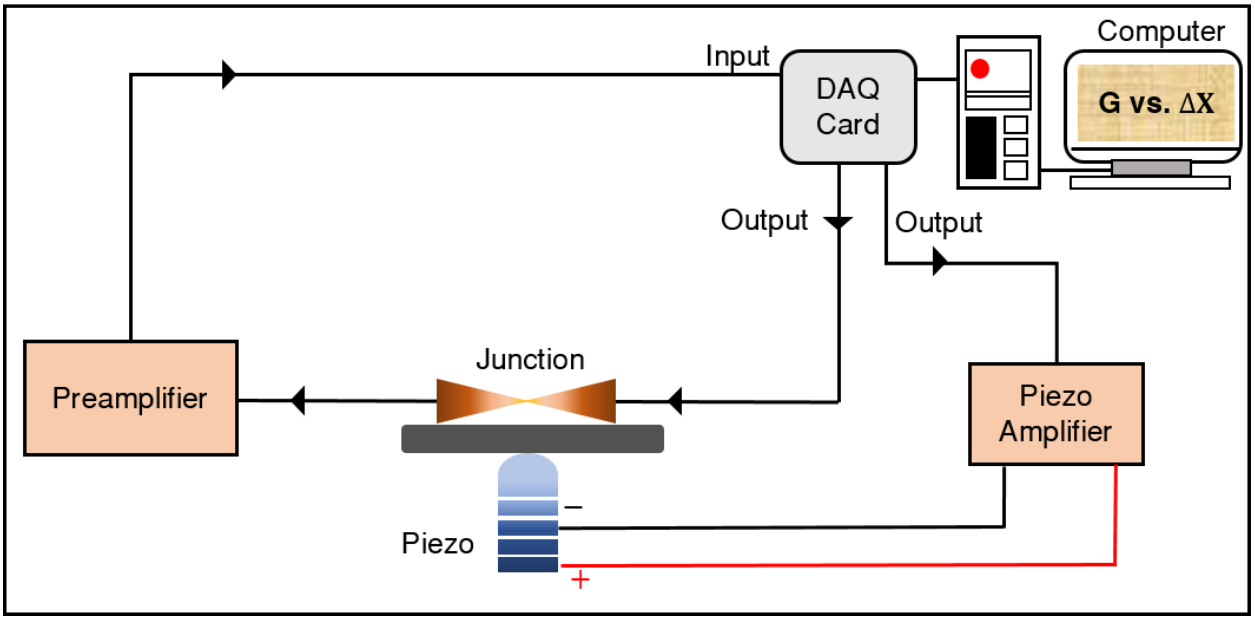

Figure 3.5 *Schematic of electronic circuit used to record the d.c. conductance of the atomic/molecular junction as a function of interelectrode separation or displacement.*

problem can be circumvented either by using a logarithmic preamplifier or by considering the circuit shown in **Figure 3.6**. In case of modified circuit, a resistance R_s ($50\ k\Omega$ for our experiments) is added in series to limit the current through the circuit[68]. Thus, when the conductance of the junction is higher, current is determined by the series resistance and for other limiting cases i.e., extremely low conducting junction (resistance$\sim G\Omega$), contribution of the series resistance is negligible and can be ignored. Conductance of the junction is thus obtained by measuring the current and the voltage drop across the junction following the equations:

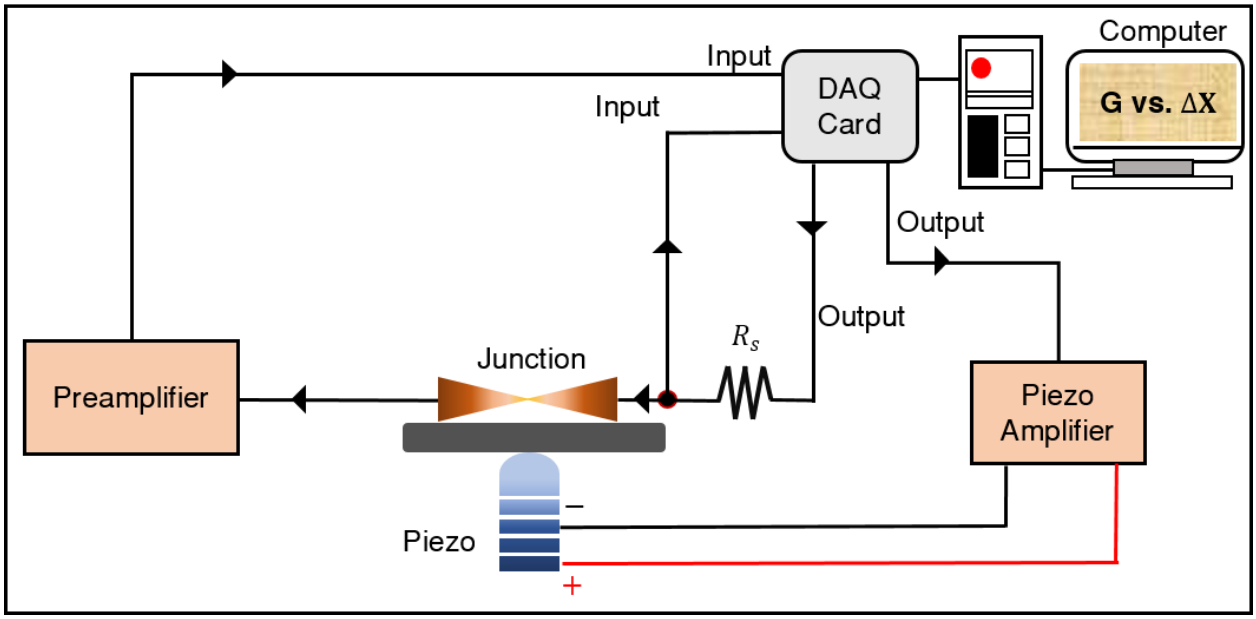

Figure 3.6 *Schematic of modified electronic circuit to improve the dynamic range of the dc conductance measurements (conductance vs. displacement).*

$$V_{Bias} = V_{R_s} + V_{Junction}$$

$$G_{Junction} = \frac{I}{V_{Junction}} = \frac{I}{(V_{Bias} - V_{R_s})} \qquad (3.1)$$

(V_{Bias} = Applied bias, V_{R_s} = Voltage drop across the series resistance, $V_{Junction}$ = Voltage drop across the junction, I = Current through the junction). An important consequence of this series resistance is that voltage drop across the junction which varies throughout the measurements, also needs to be measured simultaneously.

(iii) Differential conductance measurement circuit

To measure differential conductance (dI/dV) at a fixed d.c. bias voltage (V), we have used standard lock-in technique following the circuit shown in **Figure 3.7**. A reference sine signal from a lock-in amplifier (SR830) is added to the d.c. voltage (V) from the output terminal of the DAQ card and the total voltage is divided by 10: 1 to improve the signal to noise ratio. The a.c. response is probed by the same lock-in amplifier (SR830) and recorded by the DAQ card. The differential conductance spectra are obtained by dividing the alternating current signal (dI) with the applied alternating voltage bias (dV), as a function of a swiped d.c. voltage bias (V).

Note that, measurements and data acquisition are performed with the help of a custom written LABVIEW script.

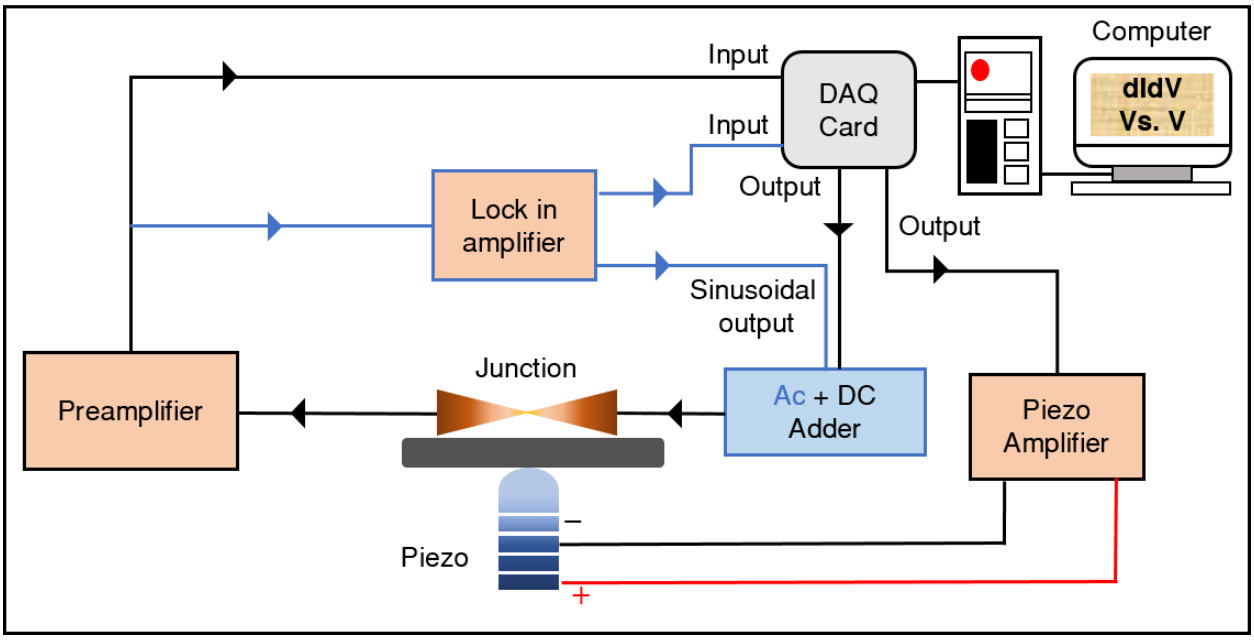

Figure 3.7 *Schematic of electronic circuit diagram used to measure the differential conductance of the atomic/molecular junction.*

3.4. Data analysis tools:

As described earlier, MCBJ set up is used to record the electrical conductance of the atomic or molecular junction as a function of interelectrode separation. For instance, experimentally obtained data is presented in the **Figure 3.8a** where upper panel is the evolution of the conductance during the sweep of the triangular waveform at the piezo, shown in the lower panel. Here, conductance is expressed in terms of quantum of conductance ($G_0 = 2e^2/h$). Amplitude of the triangular waveform is decided in such a way that it can drives the conductance from ~100 G_0 or even more to the lower limit of the experimental set up (noise level). The conductance traces measured at each cycle can be divided into two parts – pull or breaking traces and push or making traces. Part of the traces corresponding to the positively ramped triangular waveform is called the pull traces (**Figure 3.8b**, light blue) whereas negatively ramped section is known as push traces (**Figure 3.8b**, red). The pull traces demonstrate the gradual reduction in the minimal cross section of the junction as the electrodes are pulled away from each other. Likewise, the push trace describes the reformation of the contact as the tips crash back towards each other.

It is necessary to mention here that conductance is commonly expressed in terms of interelectrode separation or displacement (Å) by calibrating the inter-electrode gap size with the corresponding voltage applied at the piezo. Exponential dependence of the current on the vacuum gap is used to make a rough calibration of the gap size, following the previous reports[69].

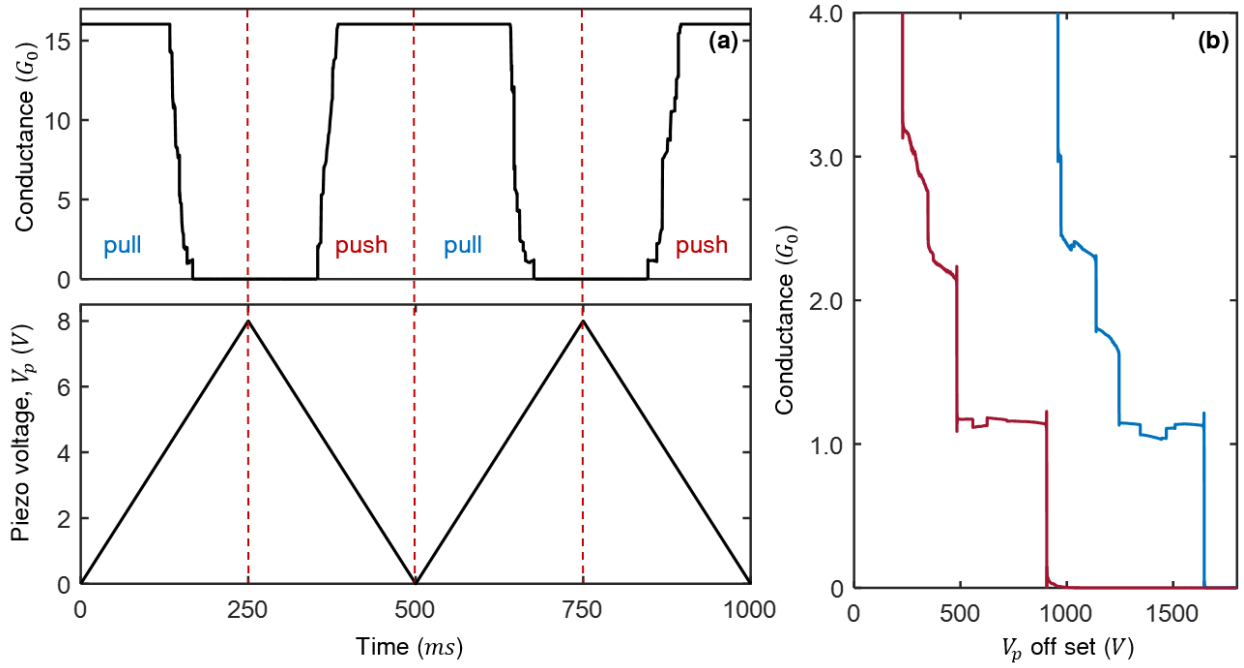

Figure 3.8 (a) *Acquisition of conductance traces for a gold (Au) atomic contact during consecutive breaking (pull) and making (push) in the break junction configuration. Bottom panel: Triangular waveform of the piezo voltage and Top panel: corresponding conductance of the junction.* ***(b)*** *A pull (blue) and push (red) trace of a single breaking-making cycle.*

Linear relation between the piezo expansion and inter-electrode gap size helps to define a simple calibration constant (c),

$$c = \frac{\Delta}{V_{piezo}} \tag{3.2}$$

Where Δ is the interelectrode separation and V_{piezo} is the voltage at the piezo. Tunneling current (I) between two electrodes which are separated by a distance Δ (provided that the applied voltage V_0 is smaller than the work function of the electrodes) can be expressed[70] as,

$$I\ (V_0) = kV_0 e^{-2\Delta\sqrt{2m\phi/\hbar^2}} \tag{3.3}$$

Where ϕ is the work function of the electrodes, m is mass of the electron, k is a constant related to the area of the electrode and to the electron density of states at the Fermi level and $\hbar$ is the reduced Planck constant. Resistance of the tunnel junction is thus,

$$R = R_0 e^{2\Delta\sqrt{2m\phi/\hbar^2}} \tag{3.4}$$

Combining **Equation (3.2)** and **Equation (3.4)**, we can write,

$$R = R_0 e^{2cV_{piezo}\sqrt{2m\phi/\hbar^2}} \tag{3.5}$$

Slope p, of the logarithmic resistance with respect to piezo voltage is thus,

$$p = \frac{\partial(lnR)}{\partial V_{piezo}} = \frac{\partial(2cV_{piezo}\sqrt{2m\phi/\hbar^2})}{\partial V_{piezo}} = \frac{\sqrt{2m\phi}}{\hbar}2c \tag{3.6}$$

Calibration constant, $$c = \frac{p * \hbar}{2\sqrt{2m\phi}} \tag{3.7}$$

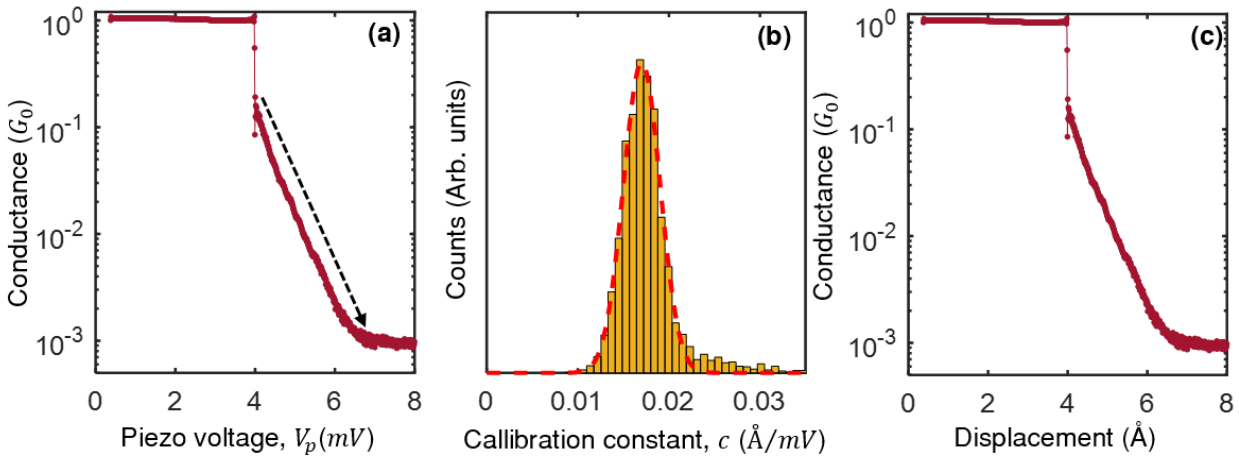

Figure 3.9 (a) *Push traces of gold atomic junction where conductance is presented in terms of piezo voltage (V_p). Region used for calculating the calibration constant is marked by the black dashed arrow.* ***(b)*** *Histogram of the calibration constants, obtained from* 10,000 *push traces of gold junction. Red dashedf line is the Gaussian fitting which provides the most possible calibration constant~* 0.018 Å/mV. ***(c)*** *Same as (a) after calibrating in terms of displacement (Å) using the calibration constant of (b).*

This expression is indeed very simple and clean electrodes follows an exponential behavior of the current (shown in **Figure 3.9a**) during stretching or relaxing of the atomic contact. Part of the traces to calculate the slope is marked by black dashed arrow (see **Figure 3.9a**). It would thus make a suitable method to calibrate the gap size. A histogram of calibration constant, shown in **Figure 3.9b**, is generated using the calculated slopes of push traces. From the histogram, most frequent c value is obtained by Gaussian fitting and is used further to calibrate. For reference, same trace after calibration is shown in **Figure 3.9c**. This calibration procedure is found to be consistent with other methods to obtain the interelectrode separation, including optical interferometry and Gunderlich oscillations, however, can be accurate within ~20% of error[69]. The major source of

inaccuracy in this method is coming from the value of work function considered, which is sensitive to the fine structural details of the tips[71] and also on the local environment[72].

So far, discussions have been limited to the different features of the conductance traces including calibration technique. However, in the following subsection, I will discuss the primary statistical analysis tools that have been used to analyze the experimentally acquired data. MATLAB scripts are used for these statistical analysis.

(i) Conductance histogram and conductance displacement histogram

Before going into details, necessity of the statistical analysis should be cleared. Conductance trace exhibits a series of plateaus (see left panel of **Figure 3.10a**), with the jumps in between, which corresponds to the stable configuration of the atomic contact where jumps are appearing due to the atomic rearrangements of the junction during stretching[73]. Experimentally, electrodes are always crashed up to few atoms to delete the memory from previous cycle before entering into the next cycle. In each cycle, junction evolves via series of elastic and plastic deformation leading to a unique configuration, which is beyond to probe experimentally. Hence, statistical analysis of large traces is important to study a large ensemble of possible structures. This has been performed by preparing conductance histogram[74] which presents distribution of conductance values collected from large number of traces. Consequently, when junction exhibits constant conductance values with respect to stretching (i.e., conductance plateaus), many values will add up to a small range of conductance and reflected as a peak in the histogram (middle panel of **Figure 3.10a-b**).Peaks in the histogram are usually fitted with either Gaussian or Lorentzian function to calculate the most probable conductance values.

However, conductance histogram provides only the conductance values, ignoring information related to the conductance in conjugation with interelectrode separation or displacement. Two dimensional (2D) conductance displacement histogram[16,75] is thus generated to check the correlation of conductance and displacement in a statistical manner. 2D conductance displacement histogram is constructed by following the way: first a conductance value is assigned for each traces as the origin of the displacement axis i.e., zero displacement point. Each point in the traces is then contributes to one of the 2D bins in the histogram, defined by conductance and displacement from the starting point. The resulting histogram (right panel of **Figure 3.10a-b**) can then be considered

as a stack of many traces, placed on top of each other and is helpful to determine the most common feature during stretching.

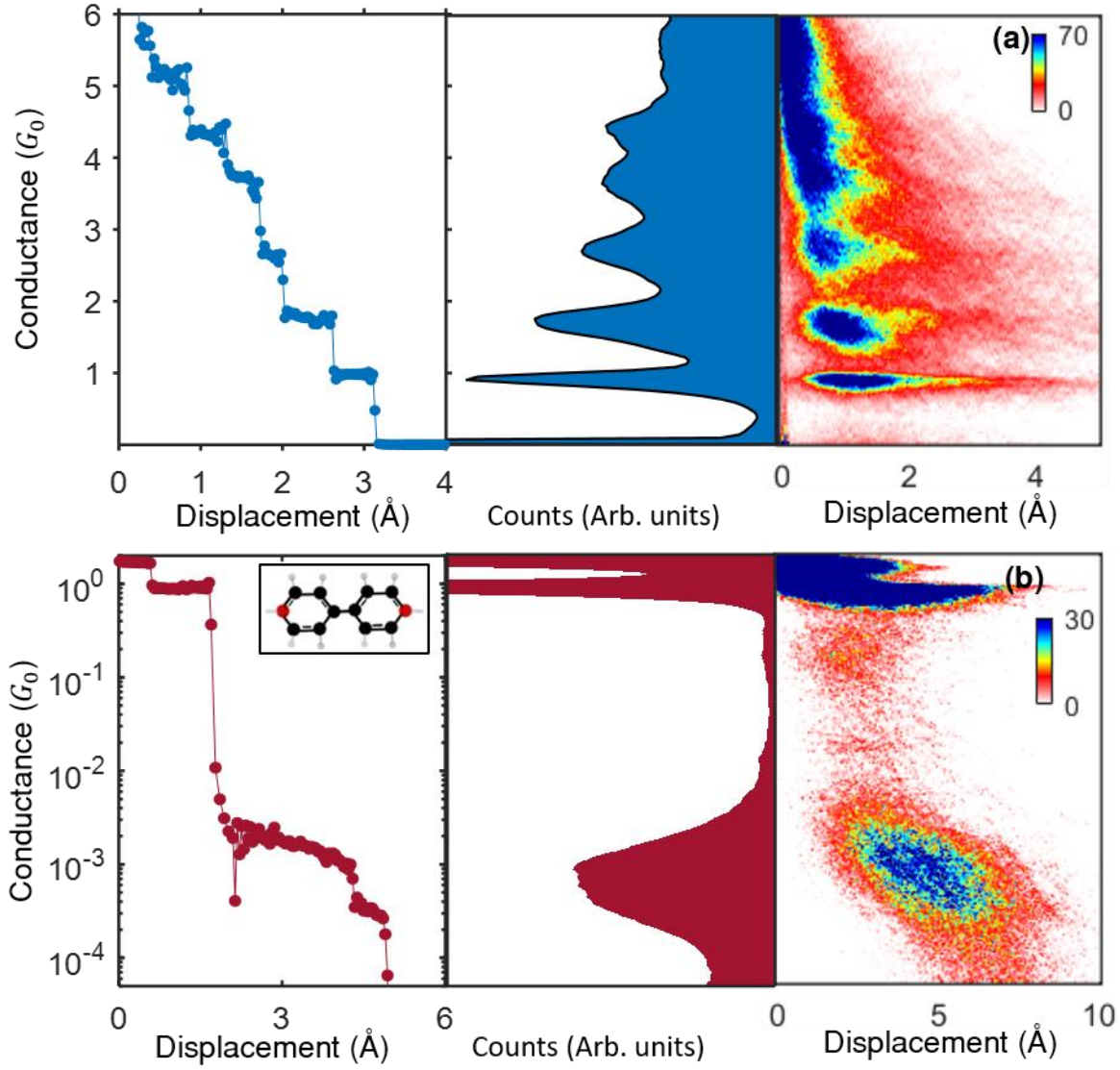

Figure 3.10 (a) *Characteristics conductance trace (left panel), conductance histogram (middle panel) and conductance displacement histogram (right panel) of gold atomic junction, measured at room temperature. Histograms are constructed from* 10,000 *consecutive pull traces using* 200 *bins and* 50 *bins respectively.* ***(b)*** *Similar characterization of gold/ 4,4'-bipyridine /gold molecular junction. Here histograms are prepared based on the* 5,000 *consecutive pull traces by logarithmic binning (*100 *and* 50 *bins per decade respectively). Inset of left panel depicts the chemical structure of molecule considered.*

An example of conductance traces, conductance histogram and conductance displacement histogram of atomic (Gold) and molecular (4,4'-bipyridine) junction is displayed in **Figure 3.10a** and **Figure 3.10b** respectively. Histograms are usually presented in linear scale for atomic junction

whereas for molecular junction, logarithmic binning is efficient because conductance of the single molecular contact lies well below 1 G_0 and can be as low as $< 10^{-6}\ G_0$[76]. In case of gold atomic junction, sharp peaks (middle panel of **Figure 3.10a**) and high density cloud (right panel of **Figure 3.10a**) at integer multiple of G_0 are clearly evident which is the characteristics signature of s-metal having single conduction channel. On the other hand for 4,4'-bipyridine molecules, slanted plateaus (left panel of **Figure 3.10b**) are appearing below 1 G_0 ($\sim 10^{-3} G_0$) which is accumulated as peaks (middle panel of **Figure 3.10b**) and data cloud (right panel of **Figure 3.10b**) in the corresponding histograms, in line with the previous reports [7,75,77].

(ii) Length histogram

Another important parameter is the length of the plateau, defined as the difference between two absolute displacement values, corresponding to a conductance G_i to a desired conductance value G_f. Histogram of these length is thus presents the distribution of plateau lengths, obtained from each traces. It is widely used to probe the chain formation phenomena of metal atomic junction. Atomic chain means the junction with two, three or even more atoms, arranged linearly and is formed during the spontaneous stretching of the junction at cryogenic environment. Length of the plateau is varied accordingly the number of atom involved in the junction which is reflected as equidistant peaks in length histogram, signature of chain formation. **Figure 3.11a** shows the length histogram of 1 G_0 plateau of gold atomic junction which exhibits a series of peaks with an average separation$\sim$ 2 Å. Length corresponding to each peak structure demonstrates the tendency

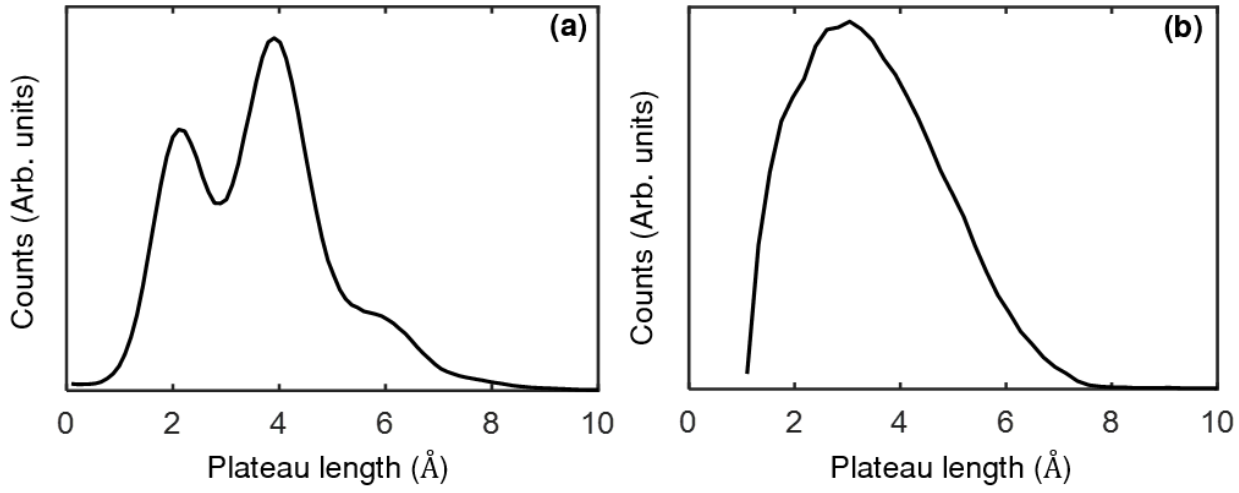

Figure 3.11 ***(a)*** *Length histogram of a gold atomic junction for plateaus with conductance value in the range* 0.5 G_0 *to* 1.5 G_0. ***(b)*** *Length histogram of 4,4'-bipyridine molecular junction considering plateaus with conductance in between* 0.0001 G_0 *to* 0.01 G_0.

of the atomic chain to break at that displacement values, in which a sufficient amount of stress is accumulated upon elongation of the chain. The relative separation between the peaks is of the order of the interatomic separation in gold, confirms that the chain is elongated by atomic units. Furthermore for molecular junction, most probable plateau length or stretching length of the molecular plateaus is calculated by Gaussian fitting of the histograms, which is an indicative of the stability of the junction[17]. For example, plateau length histogram of 4,4'-bipyridine molecular junction is shown in **Figure 3.11b**. Detailed analysis of length histogram helps to quantify the junction formation probability[78].

(*iii) Correlation Analysis*

Analysis described above suffers lack of information related to the evolution of the junction which has been solved by the introduction of correlation analysis. Correlation analysis, demonstrated by the Péter Makk et al.[79], is an extremely useful tool to detect several features of junction formation and evolution, which cannot be accessible using conventional conductance histogram. To obtain the statistical relation between different junction configurations having its characteristics conductance value, correlation parameter can be defined as,

$$C_{m,n} = \frac{< \delta N_m(r) * \delta N_n(r) >_r}{\sqrt{< [\delta N_m(r)]^2 >_r * < [\delta N_n(r)]^2 >_r}} \qquad (3.8)$$

Where $N_m(r)$ and $N_n(r)$ are the number of data points in the m^{th} and n^{th} bin of the given trace r. $\delta N_{m/n}(r) = N_{m/n}(r) - < N_{m/n}(r) >$ is the deviation from the mean value. Let's discuss the value of $C_{m,n}$ along with its physical significance-

(a) $C_{m,n} = 0$; Configurations are statistically independent.

(b) $C_{m,n} \neq 0$; Configurations are statistically dependent and type of dependency is determined by the sign of the function. Positive values of $C_{m,n}$ leads to the positive correlation and for these cases configurations either appear or disappear together. Negative value of the function indicate negative correlation and more than average counts in one configuration is supported by the less than average counts in another configuration. It may also be the situation that formation of one configuration resists the formation of other.

Similar function can also be used to understand the cross-correlation between the pull and its corresponding push traces[80]. This may help us to understand the post-rupture evolution of the junction and one can study the response of the junction after breaking (specifically whether

molecule attached to one of the electrode or diffuse away from the junction). The function is modified and described as,

$$C_{m,n} = \frac{< \delta N_m(r) * \delta N'_n(r) >_r}{\sqrt{< [\delta N_m(r)]^2 >_r * < [\delta N'_n(r)]^2 >_r}} \qquad (3.9)$$

Here *r* denotes the entire pull-push cycle, $N_m(r)$ is the number of data points in the m^{th} bin of the pull trace, whereas $N'_n(r)$ is the number of data points in the n^{th} bin of the push traces. In contrast to the former function, diagonal of the pull-push cross-correlation function is not unity. Using this method, a correlation map is drawn for arbitrary conductance pairs G_m and G_n. Two axis corresponds to the two conductance values and color illustrates the value of $C_{m,n}$. In that thesis, correlation analysis is used to study the post rupture evolution and pre-mature formation of 4,4'-bipyridine (**Figure 4.6b**, **Chapter 4**) and ferrocene molecule (**Figure 5.6e**, **Chapter 5**), attached to gold electrodes.

Chapter 4 | Effect of molecular structure on the metal-molecule contact formation

The formation and post-rupture evolution of two isomers of bipyridine molecules (4,4'-Bipyridine and 2,2'-Bipyridine) connected via gold electrodes are studied in this chapter to demonstrate the probing of metal-molecule contact formation at the atomic scale.

4.1. Introduction:

Surge towards the ultimate miniaturization has led to envisaged electronic components having characteristics dimensions in the nanometer scale. These elements could be molecules, and before putting them in a circuit, it is necessary to know how they would behave. While there have been tremendous advances made[81–84], contact formation at the microscopic level has not been straightforward. Considering metallic electrodes, examining the metal-metal contact formed in a break junction at liquid helium temperatures, one finds a regime in which one has quantum tunneling, followed by the formation of contacts. This transition from a tunneling transport regime to contact formation occurs, in most cases, via a sudden jump in the conductance, referred as jump to contact[85,86]. For instance, various metals like Au, Pt, Cu, and Ag exhibit a jump to contact, while there are others like Ir, Ni, and W without any signature of jump. Based on a controlled experiment involving an Au break junction, it was shown that the phenomena could be explained by a generic potential energy model with the elastic constant of the metal being the only free parameter[87]. However, formation of a metal-molecule bond is rather more complex and extremely sensitive to the binding groups and the geometry of the electrodes[8,17,88–93]. A jump to molecular contact was reported for several flat molecules through scanning tunneling microscopy based experiments at cryogenic temperatures[94–97]. It is believed that there exist two energetically close adsorption geometries with one of them bridging the junction via a soft phonon from the molecular side groups[95]. In the case of mechanically controllable break junctions, however, the shapes of the electrodes are not expected to remain in line while approaching each other, especially at room temperature[98]. This may lead to the formation of asymmetric junctions, which, in contrast to the breaking process, may not provide precise conductance of single molecular junctions. In recent break junction experiments with an organometallic compound, carried out in solution, a jump was observed in the conductance for making traces[99]. This was attributed to the formation of one-dimensional coordination polymers in those junctions. The knowledge about the role of metal-molecule interaction towards bond formation is rather limited and a general picture is still lacking. In the present chapter, we demonstrate the observation of jump to molecular contact in a single molecular junction by studying the charge transport of 4,4'-bipyridine (4,4'-BPY) and 2,2'-bipyridine (2,2'-BPY) molecule, attached to gold electrodes [chemical structures are shown in **Figure 4.1a** and **b**]. Through statistical analysis of conductance displacement traces, along with density functional

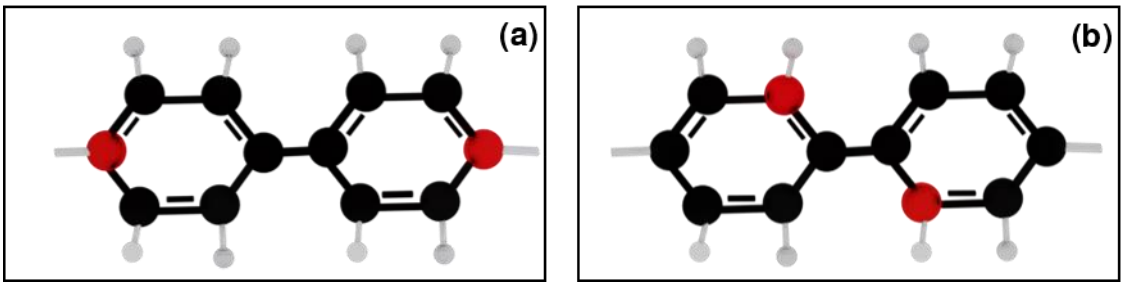

Figure 4.1 (a, b) *Chemical structure of the molecule used here: 4,4'-bipyridine [4,4'-BPY] (a) and 2, 2'-bipyridine [2,2'-BPY] (b).*

theory based calculations and ab initio molecular dynamics simulation, we provide the microscopic origin behind the metal-molecular contact formation. We find that molecular junctions form in the breaking traces for both the molecules. The surprising aspect is that 4,4'-BPY forms molecular junctions isotropically with conductance jumps in the making (push) traces also, an aspect that is absent for 2,2'-BPY. Our density functional theory (DFT) and molecular dynamics (MD) simulations reveal two important mechanisms for jump to molecular contact. Firstly, while the 2,2'-BPY prefers to lie flat on the Au surface, 4,4'-BPY has two stable minima—one with the molecule lying flat on the surface and the other with the molecule standing vertically, despite having a similar anchoring group involving nitrogen. This unusual aspect of the 4,4'-BPY emerges from the fact that the nitrogen forms a very strong bond in 4,4'-BPY[100] while the orientation on the Au surface in 2,2'-BPY does not allow a similar strong bond due to steric effects from the hydrogens attached to the carbon atoms. The possibility of having two stable energy conformations may lead to a jump to contact for 4,4'-BPY, similar to reference 95 . Additionally, we propose another mechanism, according to which, the observed jump to molecular contact in the case of 4,4'-BPY may arise from the fact that the molecule breaks by pulling a few gold atoms with it due to a strong Au-N bond compared to the Au-Au bond. Consequently, while making the contacts during the push loops, one does not have to worry about the directionality of the bonding. Through a statistical analysis of the experimental data the second mechanism was found to be the dominant one.

4.2. Results and discussions:

4.2.1. Conductance traces and histograms

Typical pull (blue) and push (red) conductance traces for both the molecules are shown in **Figure 4.2a-b**, respectively. During the junction breaking process (pull), well-developed molecular plateaus in the range of $10^{-3} - 10^{-4}\ G_0$ is noticed for both 4,4'-BPY and 2,2'-BPY. Push traces of

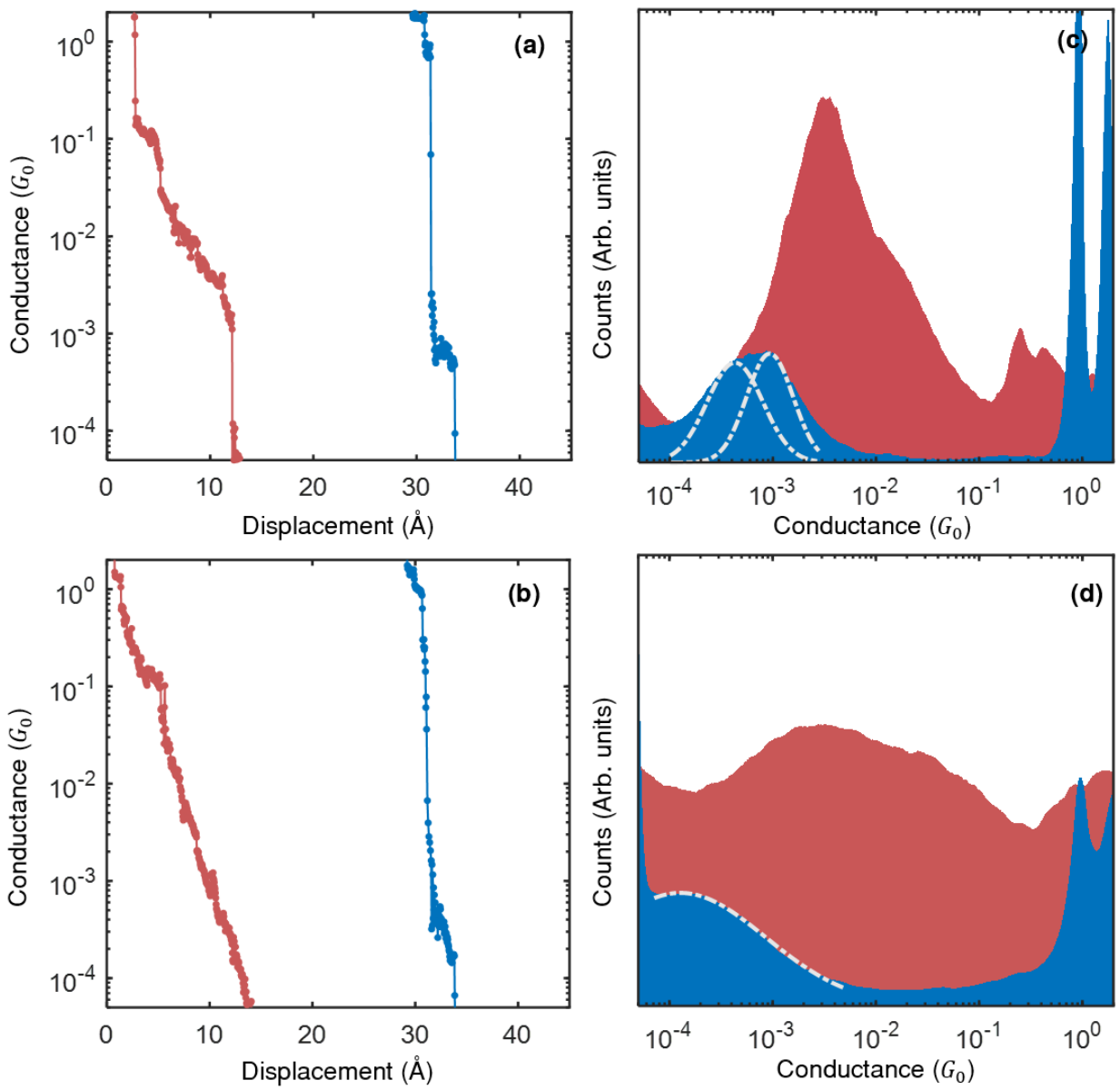

Figure 4.2(a, b) *Conductance displacement traces of 4,4'-BPY (a) and 2,2'-BPY (b) where blue (red) color denotes the pull (push) traces.* ***(c, d)*** *Logarithmically binned conductance histogram of 4,4'-BPY (c) and 2,2'-BPY (d) for pull and push traces, following the same colors. White dashed line depicts the Gaussian fitting to evaluate the most prevalent conductance value.*

4,4'-BPY, however, exhibit a plateau like feature which is longer and slanted compared to the pull traces, in line with the previous observations[101]. In the case of 2,2'-BPY, no such plateau was observed in push traces; instead, a continuous tunneling like behavior is observed. A closer look at the push traces for 4,4'-BPY reveals that atomic contacts of Au form via two jumps in the conductance: the first jump occurring from the background noise or tunneling to a conductance

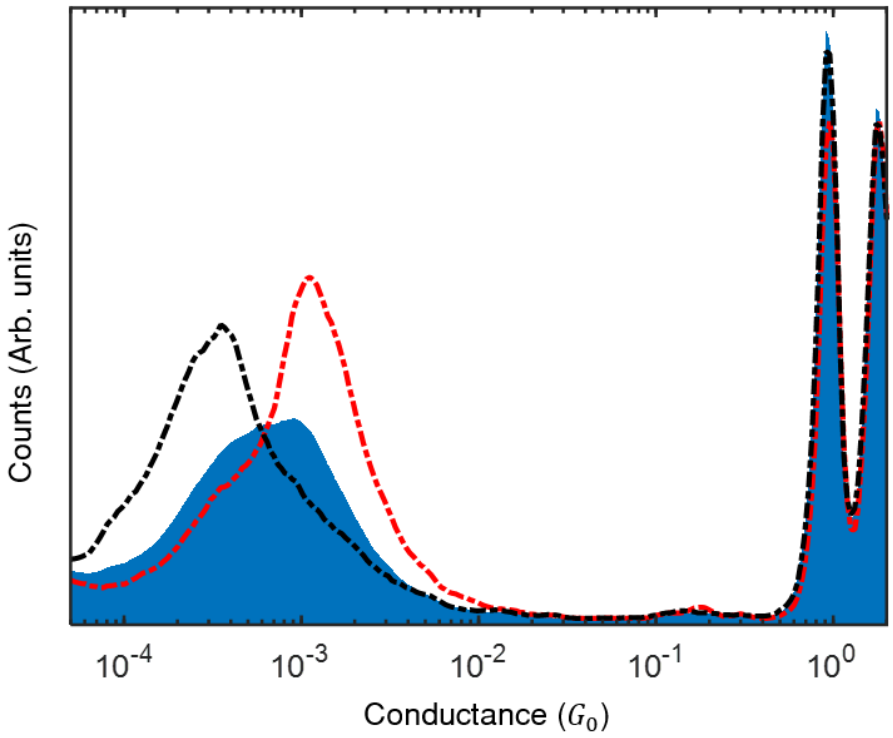

Figure 4.3 *Conditional conductance histogram of pull traces of 4,4'-BPY molecular junction where blue area plot is the histogram of all traces whereas red (black) dash dotted line represents the histogram of those traces with plateaus in the high (low) conductance region.*

value of $\sim 10^{-3} G_0$ and the second one from $\sim$ 0.1 G_0 to a few tenths of G_0. The first jump is referred to as "jump to molecular contact" (abbreviated as J2C) and the second jump corresponds to the formation of metallic contact. No such jump is observed in the case of 2,2'-BPY. In the following paragraphs we discuss more details about the origin of the J2C phenomena. Thousands of individual traces were collected, analyzed, and plotted as histograms to get a meaningful estimate of the molecular conductance from statistically independent junction configurations. **Figure 4.2c-d** displays the logarithmically binned normalized one-dimensional (1D) conductance histogram for 4,4'-BPY and 2,2'-BPY, following the same colors of pull and push traces. Histograms are constructed from 5000 (4,4'-BPY) and 8000 (2,2'-BPY) conductance traces without any data selection. For both the molecules, the pull histogram (blue) exhibits a clear peak around $1\ G_0$ corresponding to the Au atomic contact, followed by a prominent molecular conductance feature in the range of $5 \times 10^{-2}\ G_0$ to $5 \times 10^{-4}\ G_0$ (4,4'-BPY) and $1 \times 10^{-3}\ G_0$ to $1 \times 10^{-4}\ G_0$ (2,2'-BPY). For 4,4'-BPY, the conductance peak can be resolved into two separate peaks ($9.33 \pm 0.29 \times 10^{-4}$ and $4.28 \pm 0.07 \times 10^{-4}$), obtained by fitting Gaussian to the characteristic maxima, similar to the previous observation[75,77]. To point out the formational

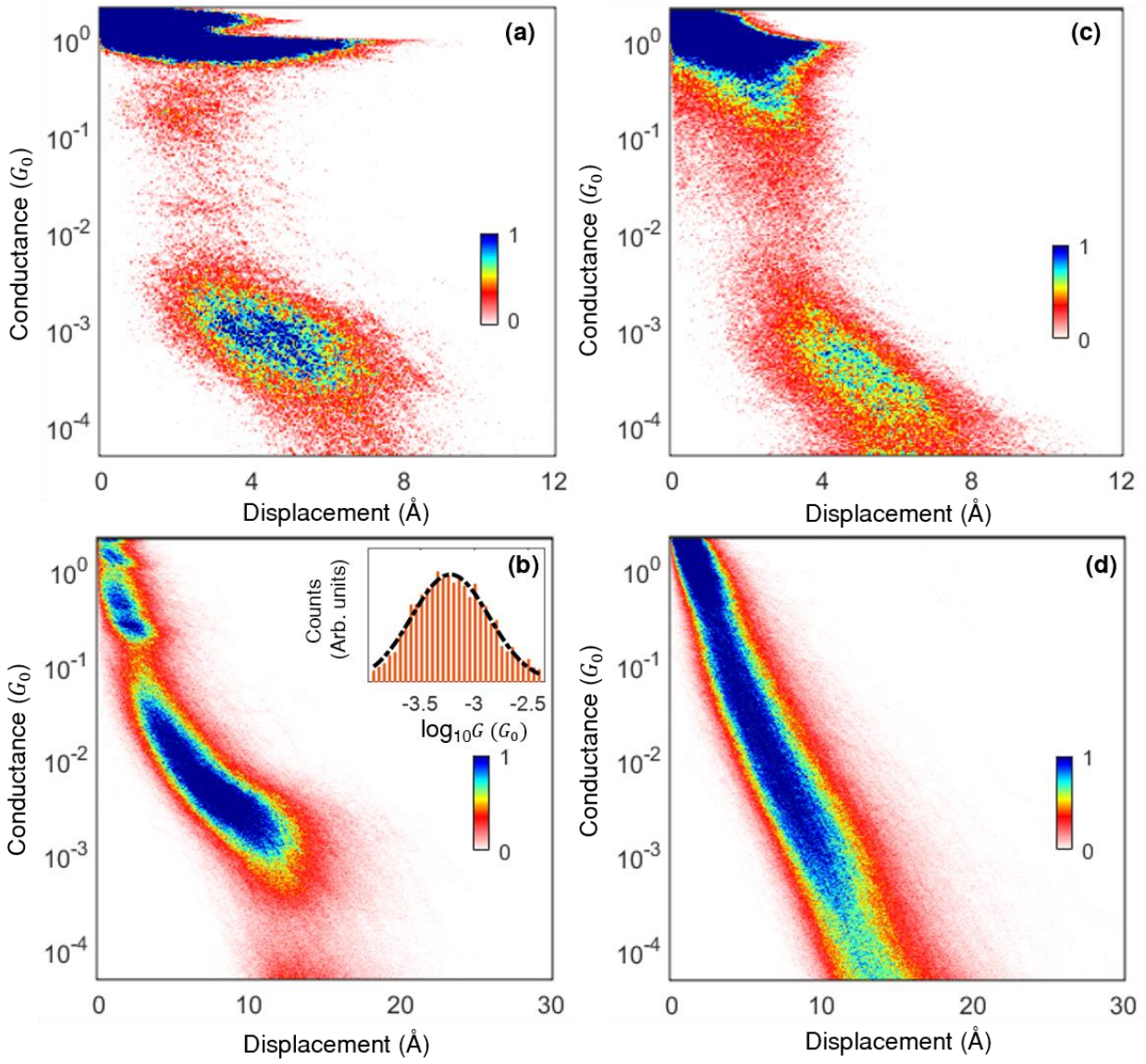

Figure 4.4 (a, b) *Conductance displacement histogram of pull, push traces of 4,4'-BPY. Inset of (b): Histogram of the conductance of the molecular contact formed after the jump.* 3750 *traces are used (see* ***Table 4.1*** *for details).* ***(c, d)*** *Similar characterization for 2,2'-BPY.*

dependency between these two peaks, conditional analysis is carried out and shown in **Figure 4.3**, where line plot is the conductance histogram of those traces having plateaus at either of two peak and area plot is same as **Figure 4.2c**. The relative intensity noticed in **Figure 4.3** validates the previous observation of negative correlation (plateau length wise) for 4,4'-BPY molecular junction [75,79]. Coming back to **Figure 4.2d**, most probable conductance for 2,2'-BPY was found to be $1.27 \pm 0.05 \times 10^{-4}\, G_0$. The push histogram (red) for 4,4'-BPY (**Figure 4.2c**) shows a clear conductance peak in the region (5×10^{-4} to $2 \times 10^{-1} G_0$), being higher than the pull

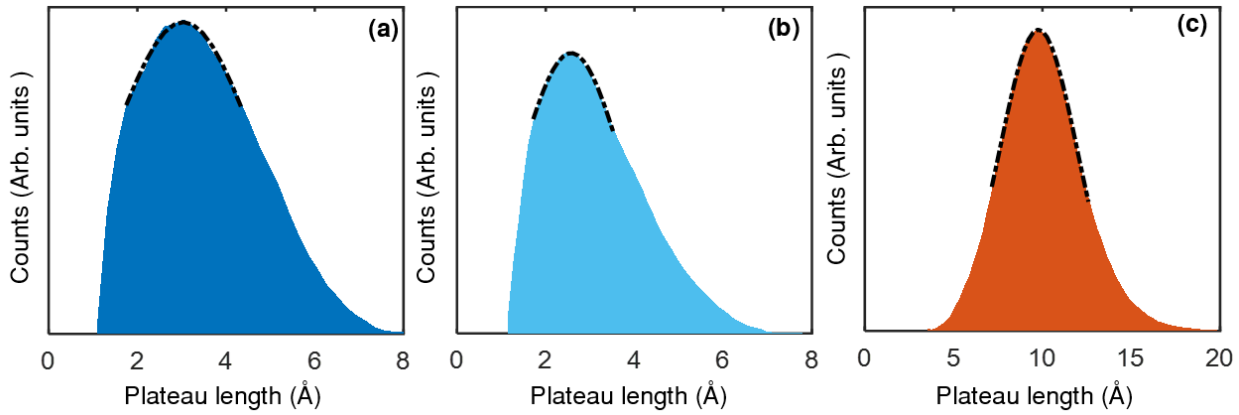

Figure 4.5 (a-c) *Plateau length histogram constructed by analyzing* 3352 *pull traces (a),* 5000 *push traces (c) of 4,4'-BPY molecular junction and* 3778 *pull traces (b) of 2,2'-BPY molecular junction. Black dash dotted line represents the Gaussian fitting to obtain most probable plateau length or stretching length.*

conductance, whereas, no such conductance peak is observed in the case of 2,2'-BPY. To understand the evolution of conductance during the formation processes and possible origin of the observed J2C in the case of 4,4'-BPY, we have taken into account conductance displacement histogram. **Figure 4.4** displays such 2D conductance displacement histogram for the pull data and push data of 4,4'-BPY and 2,2'-BPY. The plots were constructed from the same traces used in the 1D histogram, by aligning them at 2 G_0 and having 100 bins per decade. In case of conductance displacement histogram of pull traces (**Figure 4.4a, c**), high density data cloud is clearly evident in the characteristics region as expected from the corresponding traces and histogram. However, most intriguing aspect is the unambiguous formation of junction for 4,4'-BPY during the making process (push) with a conductance jump occurring mostly at $\sim 5.98 \pm 0.23 \times 10^{-4} G_0$, calculated from the Gaussian fit of the histogram of conductance values where jump to molecular contact takes place, shown in the inset of **Figure 4.4b**. This value bears a close resemblance to the conductance of Au/4,4'-BPY/Au junctions in the stretched configuration, reported earlier[75]. Jump to molecular contact is clearly absent for 2,2'-BPY (**Figure 4.4d**), where a continuous tunneling slope is observed from the noise background while closing the electrodes and no clear formation of molecular junction was noticed. Furthermore, by analyzing the length histogram (**Figure 4.5**), we see that 4,4'-BPY exhibits a longer and slanted conductance plateau in push with an average length of 9.77 ± 0.05 Å (**Figure 4.5c**), compared to the corresponding pull plateaus with an average plateau length of 3.03 ± 0.02 Å (**Figure 4.5a**). A similar analysis for 2,2'-BPY (pull) shows an average plateau length of 2.57 ± 0.01 Å (**Figure 4.5b**).

4.2.2. Correlation analysis

Now, a statistical correlation analysis of the conductance traces, as described in reference 79, has been used to distinguish various structural configurations. Using the same procedure, we have carried out a statistical correlation analysis between the pull and push traces [80] to find out if there is any possible correlation between them (see **Section 3.4** of **Chapter 3**; also see the references 79,80,102,103). **Figure 4.6b** shows the two-dimensional cross correlation plot for 4,4'-BPY, constructed from 10000 traces with 50 logarithmic bins per decade. The vertical axis belongs to the push traces and the horizontal to the corresponding pull traces. A clear positive correlation between the pull and corresponding push traces is observed, shown by a dark spot near the region where the pull and push peaks appear, as depicted by the black dash dotted lines. This is also evident from the conditional histogram of the corresponding pull (push) traces, shown by the black dash dotted line in **Figure 4.6a (Figure 4.6d)**. While selecting the push (pull) traces having a conductance plateau in the selected region between the black dash dotted lines, we observe a clear enhancement in the conductance peak of the pull (push) histogram. A positive correlation may indicate a structural memory effect[102] that any molecular junction in push is possible, mostly when a molecular junction is formed during the breaking process (pull). A similar positive correlation between pull and push traces was observed for the Au/CO/Au junction at cryogenic temperature[103]. It was concluded that the molecule is bound rigidly to the apex of one electrode and a similar single molecular configuration was reestablished during the making process. At room temperature, however, due to the enhanced surface diffusion, electrodes are flattened and a correlation between the breaking and making traces is uncommon. **Figure 4.6c** compares the correlation observed in push from eight different data sets from three different samples with a varying probability of molecular junction formation. A conditional analysis of eight statistically independent data sets indicates that J2C was observed for more than 80% of the cases whenever a molecular junction is formed during pull, establishing the fact that J2C is primarily associated with the formation of a molecular junction in pull (See **Table 4.1** for details).

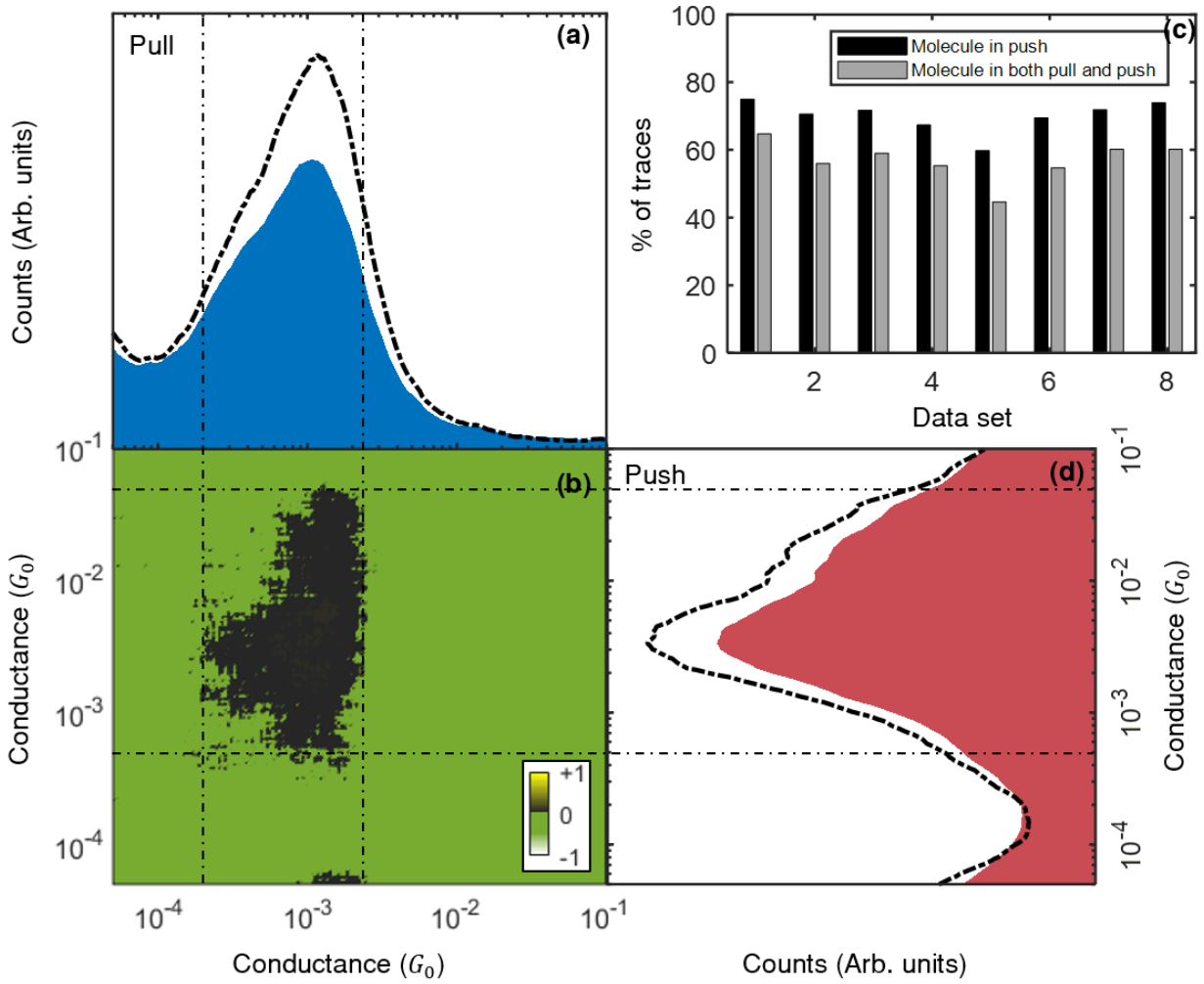

Figure 4.6 (a, d) *Conditional histogram of 4,4'-BPY for (a) pull and (d) push traces. The black dash dotted line represents the histogram of the selected pull (push) traces for which plateaus are formed in the corresponding push (pull) traces, respectively. The blue and red area graph represents the histogram of all traces, same as* ***Figure 4.2c****.* ***(b)*** *2D correlation histogram, indicating the correlation between the pull (horizontal axis) and push (vertical axis).* ***(c)*** *Bar diagram showing the percentage of traces forming a molecular junction in push via jump (black) and the percentage of traces having both molecules in the pull and push (gray) for eight different data sets.*

4.2.3. Theoretical calculations[1]

To simulate the experiment, we take two pyramidal gold electrodes and place the molecule 4,4'-BPY symmetrically between the electrodes. The optimized Au-molecule bond length was found to be 2.12 Å in the static calculation. Placing the molecule at this distance from the electrode led

[1] Theoretical calculation is performed by Debayan Mondal and Prof. Priya Mahadevan.

to an effective length (distance between two electrode tips) of 11.10 Å . The Au-Au bond lengths in the electrodes were set equal to the bond length of 2.65 Å found in the experimental structure. Molecular dynamics simulations were then carried out at a temperature of 300 K. After 200 iterations, we find that while the positions of the Au atoms in the electrode do not change, two

Table 4.1 *Details of the data of bar diagram (**Figure 4.6c**).*

Data set	Total number of traces (N_{Total})	Total number of traces (N_{jump}) with jump in *push* (% inside bracket)	Total number of traces (N_{mol}) having both jump in *push* and molecule in *pull* (% inside bracket)	N_{mol}/N_{jump}(%)
1	5000	3750 (75.00)	3236 (64.72)	86.29
2	2500	1765 (70.60)	1398 (55.92)	79.20
3	3500	2510 (71.71)	2066 (59.02)	82.31
4	3200	2155 (67.34)	1770 (55.31)	82.13
5	5000	2991 (59.82)	2232 (44.64)	74.62
6	10000	6946 (69.46)	5470 (54.70)	78.75
7	9000	6469 (71.87)	5418 (60.2)	83.75
8	10000	7396 (73.96)	6020 (60.2)	81.39

atoms from the electrode come closer to the molecule making shorter bonds. We have increased the effective length to several values as shown in **Figure 4.7a** and there are two aspects that emerge. An Au atom gets removed from the electrode and moves towards the molecule. Additionally the molecule is no longer symmetrically placed with respect to electrodes, and the distance of the molecule and one end of the electrode becomes shorter (on one side the length is 2.45 Å and on the other it is 2.55 Å). The converged effective length is now 12.20 Å (**Figure 4.7a**). If we increase the effective length further (13.00 Å), we still find that the Au atom moves towards the molecule (**Figure 4.7a**). A similar calculation was done for 2,2'-BPY. The N-Au bond length is found to be 2.24 Å where we optimized the structure at 0 K. When we increase the separation, the Au atom from the electrode is not detached as found for 4,4'-BPY (**Figure 4.7b**). In order to understand this further, we have examined the energy variations as we stretch the Au-Au bond of

a metal contact. The energy is found to vary continuously until a bond length of 3.20 Å (a stretch of 8.8 % in the bond length) (**Figure 4.7c**). At this point there is a discontinuous change in the bond length and a jump in the energy also. The energy variations now lie on a new curve and are again continuous. As the hopping interaction strength between any two atoms varies inversely with

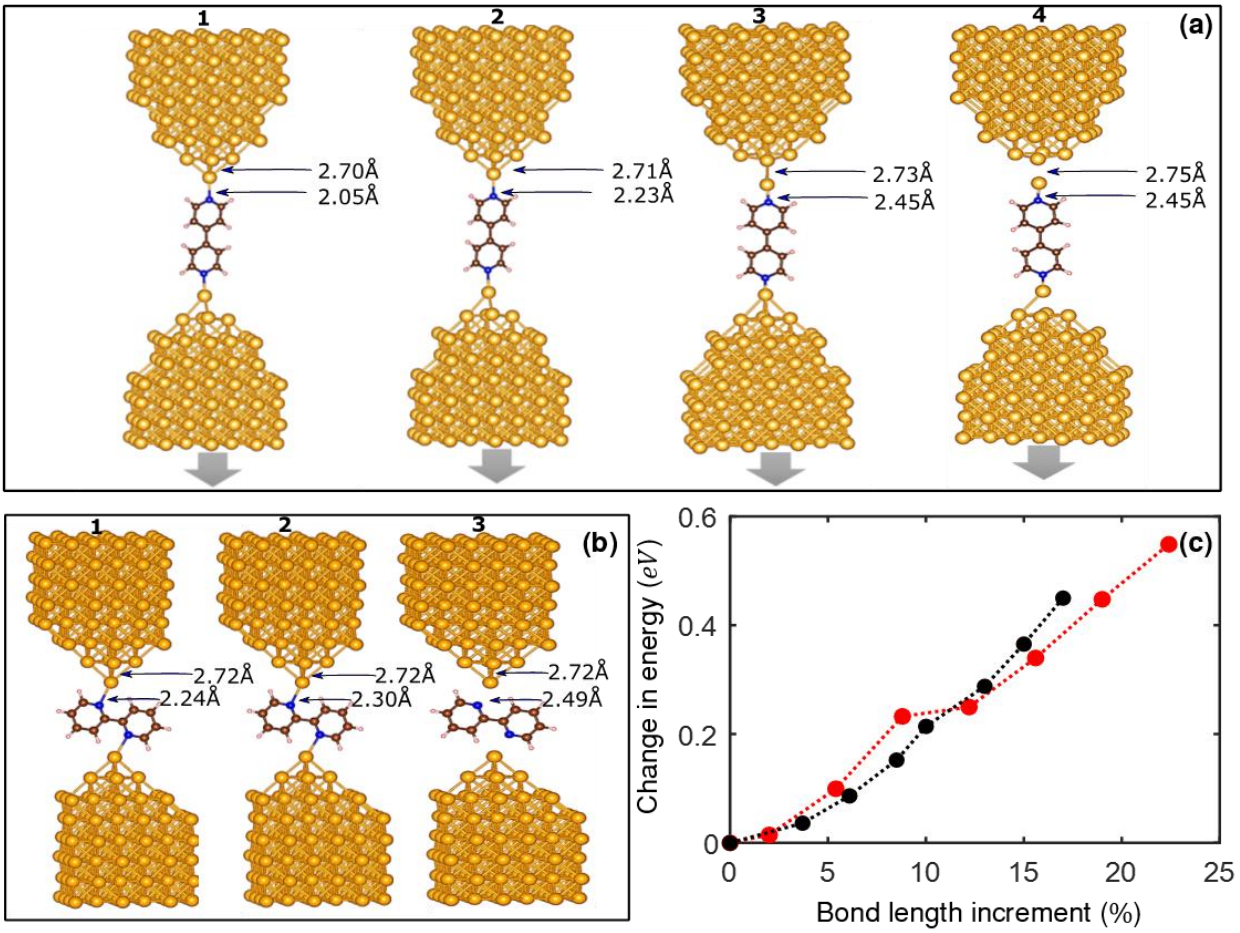

Figure 4.7 (a) *MD snapshot of molecular junction with 4,4'-BPY for effective length of electrode (1)* 11.10 Å, *(2)* 11.60 Å, *(3)* 12.20 Å, *and (4)* 12.45 Å. ***(b)*** *MD snapshot of molecular junction with 2,2'-BPY for effective length of electrode (1)* 6.65 Å, *(2)* 6.80 Å, *and (3)* 6.89 Å.***(c)*** *Change in total energy with respect to stretching of molecule-Au (black) and Au-Au atom (red) bond.*

their distance according to a power law, this jump in bond length would translate into a jump in the hopping interaction strength. This then leads to a jump in the conductance, and is consistent with experiments carried out with Au electrodes in which a jump to contact is observed[85–87]. When we went on to examine the variations in the energy of the molecule connected to an Au atom, on subjecting it to a similar elongation we found a continuous variation (**Figure 4.7c**). This suggests

that one should see only a monotonic variation in the conductivity in this case. This is, however, contrary to experiments where one has a jump to contact.

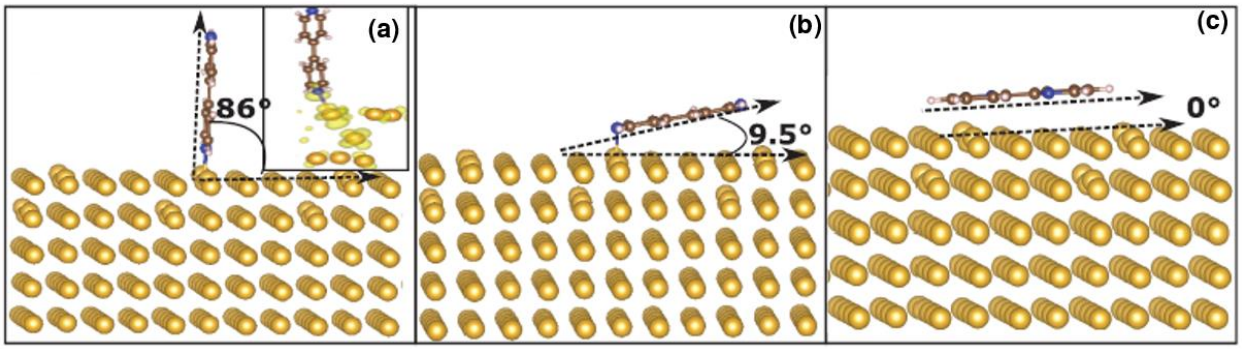

Figure 4.8 (a-c) *Complete optimized structure for vertically aligned and horizontally aligned orientations of the molecules shown in panels (a) and (b) for 4,4'-BPY and in panel (c) for 2,2'-BPY. Charge density of a state formed as a result of interactions between Au and the molecule is shown in the inset of panel (a).*

To shed more light on this, we have placed both molecules on gold surface and carried out static calculations for different orientations of both molecules at a fixed distance. These results suggest that there are two minima present for 4,4'-BPY on gold, while there is only one minima for the 2,2'-BPY. Allowing for a complete structural optimization in each case leads to the orientations of the molecules shown in panels **a** and **b** of **Figure 4.8** for 4,4'-BPY and what is shown in panel c for 2,2'-BPY. While in panel **a**, we find that the molecule prefers an orientation almost vertical to the surface, in **b** and **c** we find that the molecule likes to lie horizontal to the surface. The reason for this is easy to understand. In the horizontal position the molecule interacts through the carbon backbone with the Au surface. Hence for both molecules, this corresponds to a stable orientation. In the vertical orientation, 4,4'-BPY interacts strongly through the nitrogen with Au surface. This is evident from the charge density shown in the inset of **Figure 4.8a**, where one finds significant weight on several Au atoms beyond its nearest neighbor. In contrast the Au-N bond length is much longer for 2,2'-BPY and found to be 2.24 Å as the steric effects from the neighboring atoms do not allow the molecule to come closer to the Au surface. This leads to only one stable minima for 2,2'-BPY. The strong bonding interaction of the nitrogen in 4,4'-BPY that we find is extremely directional. This would therefore imply that in the push cycle, we would not have the desired reproducibility as only certain orientations would form strong bonds. However, as we saw in the MD simulations and also supported by an analysis of the charge density of the bonding state between 4,4'-BPY and the Au surface, we find the interaction between them to be strong enough

to pull one or more Au atoms out. This then leads to a contact between two Au atoms in the push cycle; needless to say, the bonding between Au atoms involves s orbitals and is isotropic (it does not need to attach back to its initial position, and can attach with any other gold atom)[85,104,105], and hence we have the reproducibility. From **Figure 4.6c** we observe that a jump to contact is observed in ~ 20 % cases despite not forming any molecular junction during pull. As we found that 4,4'-BPY has two stable orientations on the Au surface, a jump may occur between them via a soft phonon mode of the molecule during push[95].

4.3. Conclusion:

In conclusion, we have studied the formation and the post rupture evolution of molecular junctions at room temperature of two isomers of bipyridine (4,4'-BPY and 2,2'-BPY) having the same anchoring groups using MCBJ techniques. Transport measurements indicate the formation of a stable molecular junction during the breaking cycle for both of these molecules. During the making cycle, however, we see that 4,4'-BPY shows a clear formation of a molecular junction via a jump in the conductance from the tunneling regime, while a continuous quantum tunneling like behavior was observed for 2,2'-BPY. As such formations of molecular junctions via a jump in the conductance at room temperature are rare, we use DFT calculations as well as ab initio MD simulations to explain them. Two possible mechanisms have come out from our study. Firstly, 4,4'-BPY was found to have two possible conformations on the Au surface due to the formation of a strong Au-N bond, whereas, 2,2'-BPY prefers to lay flat on the Au surface. These two stable conformations of 4,4'-BPY may provide jump to contact while approaching the two electrodes. Secondly, we show that while breaking the Au/4,4'-BPY/Au junctions, primarily it is the Au-Au bond that is ruptured instead of the molecule-Au bond. As the Au atom attached to the molecule can bind isotropically with the other Au atoms of the electrodes, one has single molecular junctions formed during the making process via conductance jumps similar to what one has seen for Au-Au contacts. Statistical analysis of our experimental data indicates that the second mechanism is the most dominant one in our case. We provide an important insight, describing the role of metal-molecule interaction on the formation of chemical bonds, important for the development of molecular-scale electronics.

Chapter 5 | Low-bias resonant transport and orientation dependent conductance in Au/ferrocene/Au single molecular junction

This chapter describes the fabrication of highly conducting molecular junction based on the resonant transport mechanism of organometallic-based molecules via metal-metal covalent bond, as well as the significant role of molecular orientation in the transport mechanism of ferrocene molecular junction is demonstrated.

5.1. Introduction:

The central motivation of molecular electronics is to reduce the size of the conventional electronic components by taking advantage of the quantum mechanical phenomena at the atomic scale, along with the structural versatility of molecules. By adopting the revolutionary idea proposed by Aviram and Ratner[2], various experimental techniques[6,7,112–119,30,64,106–111] were developed to create single-molecule junctions, allowing access to electrical[76,120,121], chemical[122–126], mechanical[127–129], magnetic[81], thermal[83,130–132] and optical[133,134] properties. Typically, various anchoring groups such as thiol (**-SH**)[7,21,63], amine (**-NH₂**)[8,20], pyridyl (**-PY**)[7], nitrile (**-CN**)[15], isonitrile (**-NC**)[14,18], carboxylic acid (**-COOH**)[17], nitro (**-NO₂**)[135], trimethyltin (**-SnMe₃**)[136], fullerene(**C60**)[16,19] are used to connect organic molecules to the metal electrodes to achieve physically stable structure with reliable electronic coupling at the interface. Since the conductance of a single molecule junction is primarily sensitive to the degree of orbital hybridization and energy-offset between the frontier molecular orbitals and the Fermi level of the metal electrodes[12,13], the presence of these anchoring group adversely affects the conductance in most of the cases[137]. With the goal of achieving high conductance, molecular junctions were realized either via direct metal-carbon coupling through molecules like oligocene[24], benzene[23,25–27] , fullerene[12] or through direct Au-C covalent bonding in trimethyl tin ($SnMe_3$)-terminated polymethylene chains[136]. However, at ambient condition, the conductance remains far from the quantum of conductance ($G_0 = 2e^2/h \approx 77.6\ \mu S$) mostly due to the off-resonant transport mechanism[25,136,138], either through coherent tunneling or via hopping as a result of large energy off-set.

Recently, there are efforts to access the resonant transport regime in biphenyl-porphyrin oligomers (bp-ppo)[139], donor-acceptor oligomers based on DPP[121] and amine or thiomethyl terminated oligophenyls[140]. Notably, the resonance could be achieved only by applying a high source drain bias ($> 1.0\ V$) or through a gate voltage in a three-terminal configuration[141] at cryogenic temperature. At such a high bias the molecular junction could become unstable due to the Joule heating, or, the characteristics of the junction can be modified by the chemical reaction occurring due to the higher current density[142,143]. Also, considering the realistic difficulties in fabricating three terminal single molecular devices, it is indeed desirable to reduce the energy off-set by exploring other possibilities of chemical functionalization.

Here, we focus on ferrocene, a chemically stable molecule at ambient condition, as the primary

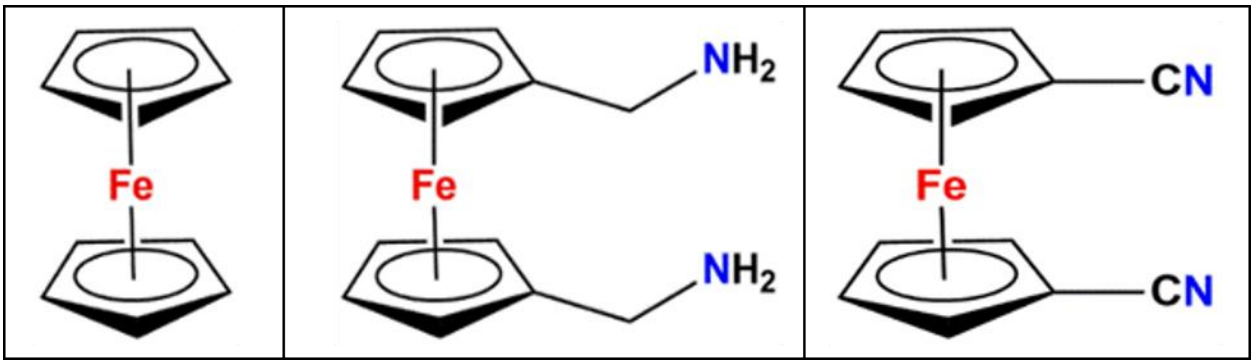

Figure 5.1 *Chemical structure of the considered molecules- ferrocene (left panel), 1,1'-bis(aminomethyl)ferrocene (middle panel) and 1,1'-dicyanoferrocene (right panel).*

component of a single molecular device[144–150] and corresponding structure is shown in **Figure 5.1** . The unique structure of metallocene having a central transition metal at the center was shown to provide near-ballistic spin transport while incorporated between silver electrodes at cryogenic environment[84]. Despite recent reports on ferrocene or its derivative in molecular junctions[146–148,151–153], the detailed transport mechanism of ferrocene based junction is still elusive. In this study, we demonstrate the charge transport characteristics of a single Au/ferrocene/Au junction via direct metal-molecule coupling, exhibiting a significantly high conductance (~ one quarter of the quantum of conductance) at ambient condition. Density functional theory-based transport calculations suggest that the frontier molecular orbitals (LUMO) lies in close proximity to the metallic Fermi level of the electrodes for a certain orientation of the molecule inside the junction, consequently, perfect transmission in the vicinity of Fermi energy and resonant transport through the molecule at small applied bias ($< 0.5V$) is achieved. Further experiment along with the theoretical calculation, considering ferrocene terminated with two anchoring groups (**-NH_2**) and (**-CN**) [chemical structure is shown in **Figure 5.1**], display the similar high conductance conformation in addition to the features at the low conductance value, arising due to bonding with the chemical anchors. In general, our study reveals a way to obtain the resonant transport at the low bias regime along with a deeper understanding on the role of the spatial orientation of organometallic molecules to the charge transport mechanism.

5.2. Results and discussions:

5.2.1. Conductance traces and histograms of ferrocene molecular junction

Typical conductance displacement breaking traces of ferrocene (abbreviated as FC) single molecular junction, connected to Au electrodes, is displayed in the left panel of **Figure 5.2**.

Conductance plateau at 1.0 G_0 ($G_0 = (2e^2/h)$ being the quantum of conductance) demonstrates the formation of single atomic contact, i.e., only one Au atom in the narrowest cross section. However, upon further stretching of the junction, the conductance decreases by several orders of magnitude which is termed as "jump out of contact"[154,155] and additional features start to appear below 1.0 G_0 till the noise level is reached. Almost flat conductance plateaus can be observed in the region $\sim 0.1 - 0.4\ G_0$ (**Figure 5.2**, left panel) following the post-rupture quantum tunneling features which confirm the successful formation of molecular junctions. Due to the pronounced thermal noise at room temperature, molecular plateaus are not always identical and vary from trace to trace. Thus, to get meaningful conductance value from statistically independent junction configurations, several thousands of traces are analyzed and represented as conductance histogram

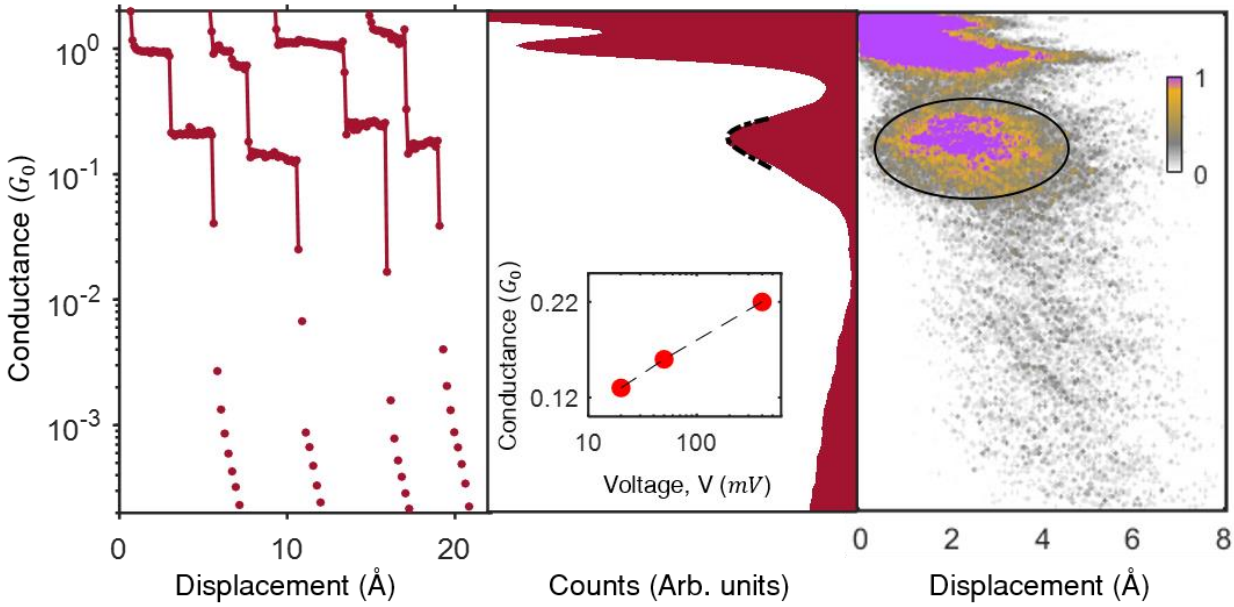

Figure 5.2 *Left panel: Conductance displacement breaking traces of Au/ferrocene/Au junction in semi-logarithmic scale, with traces shifted horizontally for clarity. Middle panel: One dimensional conductance histogram, constructed from* 1800 *molecular traces using* 35 *bins per decade. Black dash dotted line represents the Gaussian fitting of the corresponding molecular peak. Inset: conductance of the junction as a function of applied bias voltage. Right panel: Conductance displacement histogram of ferrocene molecular junctions based on the same* 1800 *molecular traces, constructed using logarithmic binning (*50 *bins per decade), where black circle shows the molecular plateaus.*

(1D histogram) in the middle panel of **Figure 5.2** (for bias voltage, $V_{bias} = 400\ mV$). Histogram is constructed using 35 bins per decade from 1800 molecular traces. Large counts at or around 1.0 G_0 appears due to repetitive formation of Au-atomic junction[73]. However, a well-defined conductance peak with maximum at $(2.20 \pm 0.03) \times 10^{-1}\ G_0$ is also evident from the histogram

and it corroborates the most probable conductance value of the Au/ferrocene/Au single molecular junction at room temperature. This peak is completely absent in control experiments with DCM

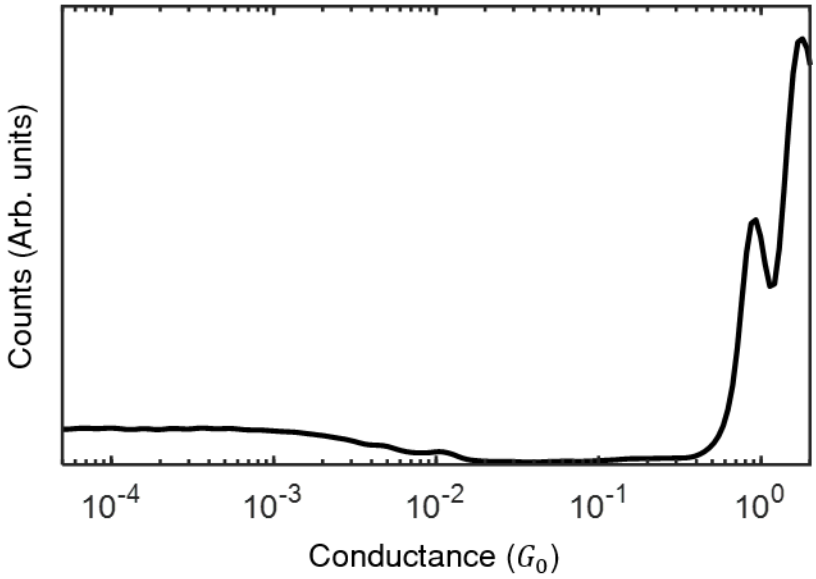

Figure 5.3 *Conductance histogram, constructed from* 3000 *conductance displacement traces, recorded for the junction exposed to dichloromethane (DCM) solvent during breaking. Characteristics molecular signature is absent here.*

(shown in **Figure 5.3**)[156]. The bias dependent measurement shows an enhancement of the conductance peak by almost a factor of 1.5 when the bias is increased from $20\,mV$ to $400\,mV$ (inset of **Figure 5.2**, middle panel; also see **Figure 5.4** for the histograms at 20 mV and 50 mV bias).To get more insight about the evolution of the junction during stretching, we constructed a 2D conductance displacement histogram in a semi logarithmic scale. The displacement or interelectrode separation was calibrated, following the method described in **Section 3.4** of **Chapter 3**[69]. Right panel of **Figure 5.2** shows the typical 2D histogram of FC, which is generated by compiling the same traces used in the 1D histogram with 80 bins per decade. High density data clouds at or above $1\,G_0$, represents the Au atomic junction. A second horizontal data cloud (marked with a black circle) is noticed from $3.00 \times 10^{-1}\,G_0$ to $8.00 \times 10^{-2}\,G_0$ and interestingly, conductance of the molecular plateaus does not change significantly with the increase of electrode separation, similar to the silver/Vanadocene junction reported by Pal et al[84].

5.2.2. Evolution of ferrocene molecular junction

The conductance histogram is now considered using traces with and without the molecular features (shown in the **Figure 5.5**). Histogram of the molecular traces reveals a shallow peak at ~1.2 G_0 in addition to the atomic peak at ~ 1.0 G_0, arising possibly due to the formation of precursor configuration prior to the atomic junction in line with the previous reports[80,88]. To get a clearer picture about the evolution of the junction, we divide the molecular traces into three different sub-

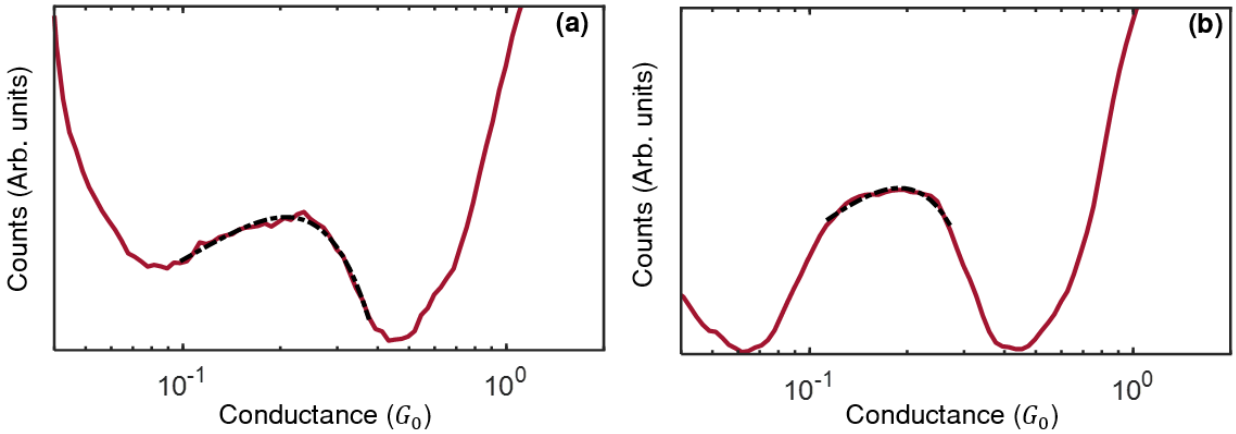

Figure 5.4 (a, b) *Conductance histogram of Au/ferrocene/Au junction in logarithmic scale for two different bias voltage* 20 *mV (a) and* 50 *mV (b) where black dash dotted line represents the Gaussian fitting of the corresponding molecular peak.*

categories based on the presence of plateaus at G_p, G_{Au} and G_m (Case-I), at G_p and G_m (Case-II), at G_{Au} and G_m (Case-III) (conductance values of G_p~1.2 G_0, G_{Au}~1.0 G_0 and G_m~0.2 G_0). Characteristic traces of three different sub categories are shown in **Figure 5.6a-c** with the inset revealing the possible junction geometries, where L and R denote the left and right electrodes with M as molecule. **Figure 5.6d** shows the conditional conductance histogram of the three categories and the pie chart (inset) showing the probability to find the different cases: Case-I [20%], Case-II [13%] and case-III [67%]. From the above analysis, it is obvious that precursor configuration is not a necessary condition to have the molecular junction. In fact, the most possible scenario [Case-III] does not even involve the precursor configuration. Similar precursor configuration was observed for diatomic[80,103] and organometallic[88] molecule-based junction which primarily occurs when the atomic contact lies in parallel to the molecular junction (shown schematically in the insets of **Figure 5.6a-c**). As a next step, we explore the statistical relationship of these configurations with the help of two dimensional cross-correlation histogram (2DCH) technique, described in **Chapter 3**[79]**.** Using this technique, a map is generated for arbitrary conductance pairs

G_i & G_j where the color-scale indicates the sign of the correlation among the conductance pairs (orange and blue represents the positive and negative correlation respectively). **Figure 5.6e** shows the 2D cross correlation map of ferrocene (FC) molecular junctions where horizontal and vertical axes correspond to the two conductance, G_i & G_j . Now we consider three different conductance regions: (a) R1- molecular conductance ($0.09 - 0.40\ G_0$); (b) R2 - single atomic conductance ($0.80 - 1.05\ G_0$) and (c) R3 – precursor conductance ($1.05 - 1.40\ G_0$). In line with the conditional analysis, a positive correlation between the precursor peak (R3) and the molecular peak (R1) is noticed, marked with the black rectangle in **Figure 5.6e**. However, the correlation between R1 and R2 is negative, marked by the white rectangle, similar to the observation of Ag/CO/Ag junction[80]. This observed negative

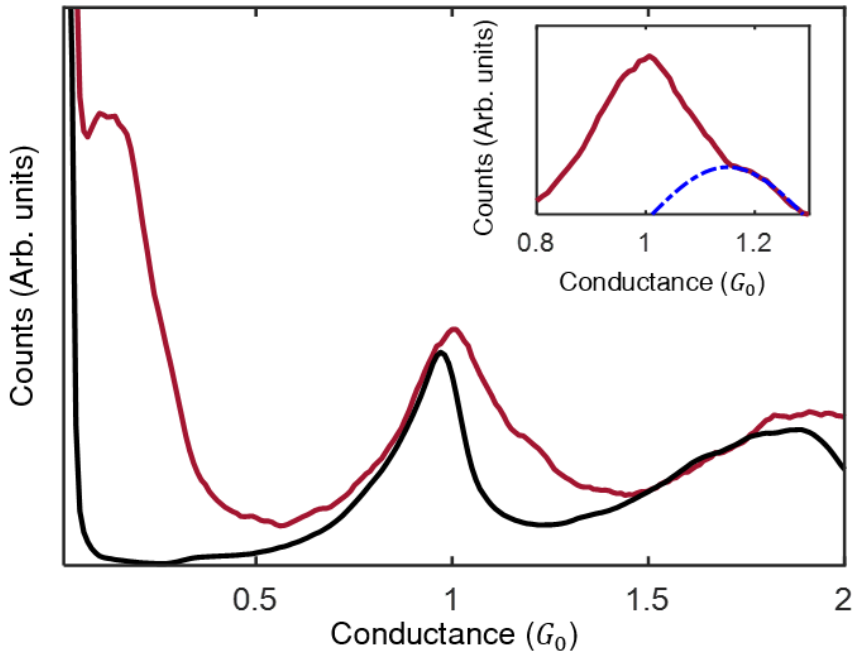

Figure 5.5 *Conductance histogram constructed from the conductance traces with (red) and without (black) molecular features. Inset: Zoomed view of the same histogram where blue dash dotted line presents the Gaussian fitting of the corresponding precursor peak.*

correlation is not an anti-correlation in the presence of these two configurations. Rather, the presence of one plateau restricts the occurrence of other in longer length, as evident from the conditional analysis shown in the **Figure 5.7**[79]. Overall, this combined analysis reestablishes the eventual formation of the precursor configuration in which molecule binds alongside to the atomic contact and opens additional channel which results in an increase of the conductance up to ~ 1.3 G_0.

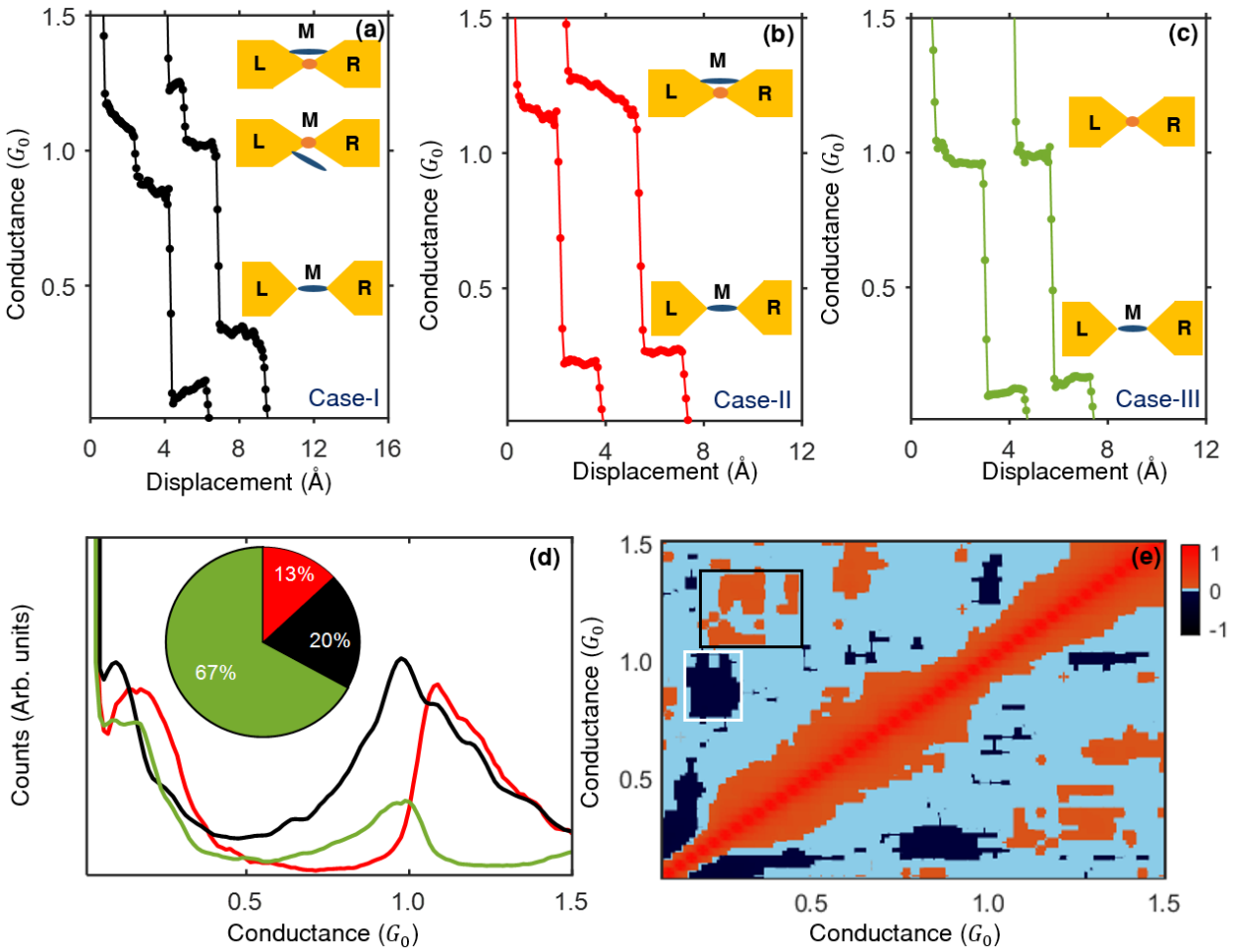

Figure 5.6 (a - c) *Sets of conductance traces with different combinations of plateaus during breaking the junction: 1. Case-I: Precursor, G_p~1.2 G_0, Atomic, G_{Au}~1.0 G_0 and Molecular, G_m ~0.2 G_0 (black), 2. Case-II: Precursor and Molecular (red), 3. Case-III: Atomic and Molecular (green). Inset: schematically presents the possible junction geometry where L, R and M denotes the left electrode, right electrode and molecule in between.* ***(d)*** *Conditional conductance histogram in linear scale, considering traces of case-I (black), II (red) and III (green) using* 200 *bins. Inset: Pie chart of percentage of traces contributing different cases.* ***(e)*** *2D correlation map of ferrocene molecular junctions for breaking conductance traces, where negative correlation (white rectangle) between the molecular region and atomic peak at* 1 G_0 *is clearly visible. Conductance of single-molecule configurations and precursor configuration is positively correlated (black rectangle).*

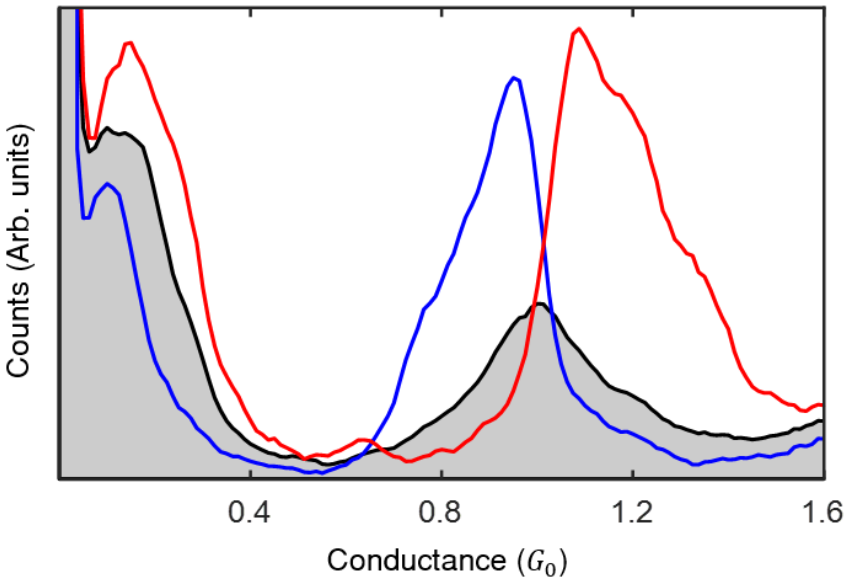

Figure 5.7 *Conditional histograms for selected traces with larger than average length in different regions: R1- molecular conductance region (red) and R2 - single atomic contacts region (blue). As a reference, the gray area graph shows the histogram for all traces.*

5.2.3. Effect of anchoring groups

We now focus on the influence of anchoring group on the conductance behavior of ferrocene molecular junction. Left panels of **Figure 5.8a-b**, respectively, show the conductance displacement breaking traces of amine-terminated ferrocene (1,1′-bis(aminomethyl)ferrocene, abbreviated as FC-NH_2) and cyano-terminated ferrocene (1,1′-dicyanoferrocene, abbreviated as FC-CN) single molecular junctions connected to Au electrodes. In contrast to FC, molecular plateaus of FC-NH_2 and FC-CN have a broad range of conductance values and subsequent plateaus can also appear in a single trace[148]. Transitions among these plateaus are not always sequential, their order completely arbitrary. Thus, introduction of anchoring group provides more conductance plateaus which signifies the multiple junction geometries. One-dimensional conductance histograms of FC- NH_2 and FC-CN molecular junctions are shown in the middle panels of **Figure 5.8a-b**. Histograms are constructed from 5000 molecular traces using 35 bins per decade. Closely looking into the histogram, well defined conductance peaks at $(3.57 \pm 0.09) \times 10^{-1} G_0$ and $(2.47 \pm 0.03) \times 10^{-1} G_0$ are observed for FC-NH_2 and FC-CN junctions. These conductance values agree well within a factor of two of the conductance peak of pristine FC and from now on, we address the high conductance peak as **H**. Additionally, FC-NH_2

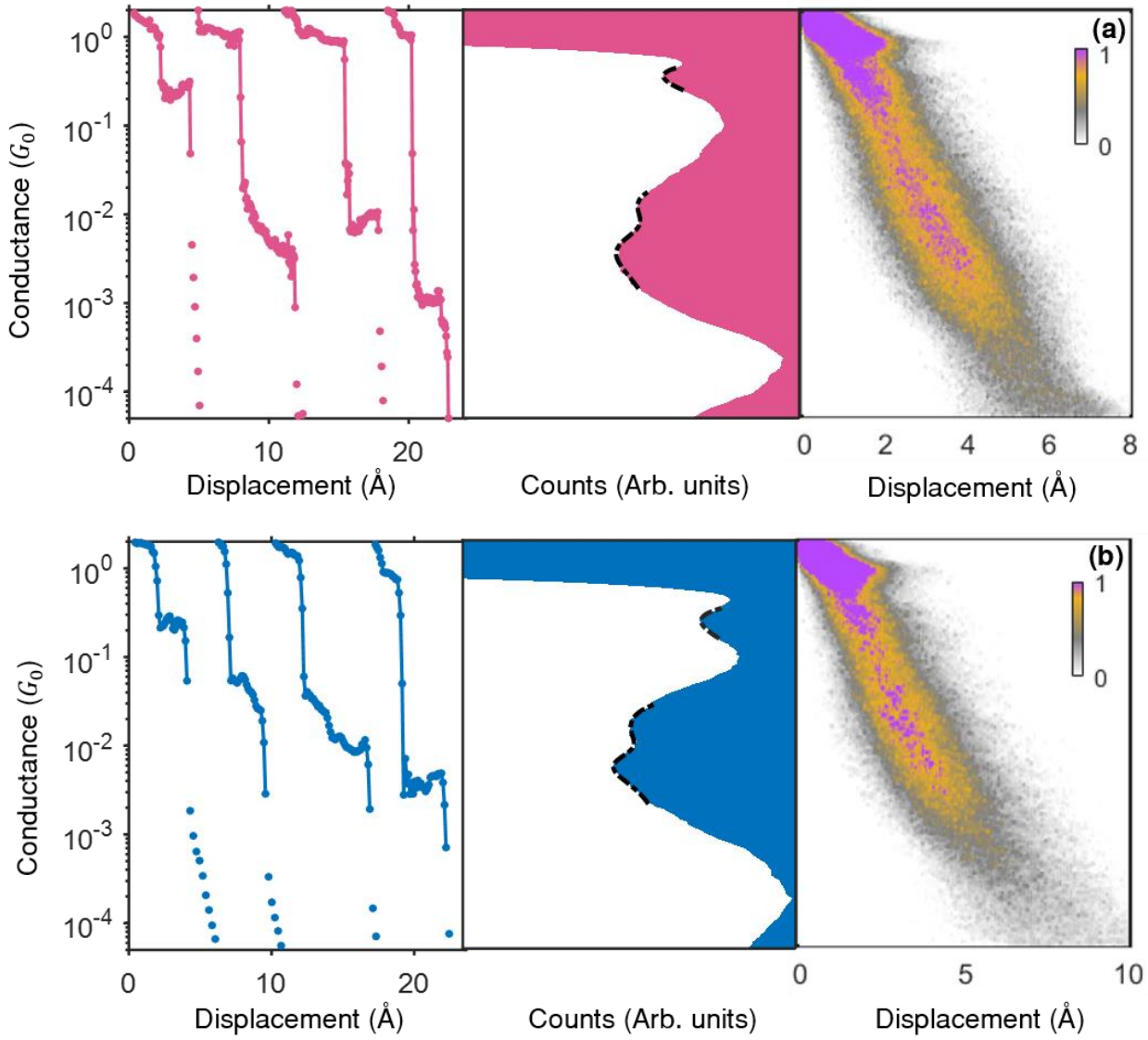

Figure 5.8 (a) *Left panel: representative breaking conductance traces of Au/1,1'-bis(aminomethyl)ferrocene/Au molecular junction in a semi logarithmic scale, with traces shifted horizontally for clarity. Middle panel: Logarithmic conductance histogram, constructed by analyzing* 5000 *individual molecular traces using* 35 *bins per decade. Black dash dotted line depicts the Gaussian fitting to the corresponding conductance peak. Right panel: 2D conductance displacement histogram, generated from the same* 5000 *conductance traces using* 80 *bins per decade. The zero displacement point is assigned here at* 2.0 G_0. ***(b)*** *Similar characterization of Au/1,1'-dicyanoferrocene/Au molecular junction.*

and FC-CN reveal a rather broad conductance feature beneath the high conductance peak (**H**) which can be convoluted into two individual conductance peaks with maxima at $(1.21 \pm 0.11) \times 10^{-2}\, G_0$ and $(2.99 \pm 0.35) \times 10^{-3}\, G_0$ for FC-NH_2 and at $(1.57 \pm 0.09) \times 10^{-2}\, G_0$ and $(5.19 \pm 0.22) \times 10^{-3}\, G_0$ for FC-CN. We refer to these conductance regions as **M** and **L** in descending values of conductance. **M** and **L** configurations show a trend: FC-CN > FC-NH_2 and

their conductance values are distributed over two orders of magnitude between $\sim 10^{-2}$ to $10^{-4}\ G_0$ which hint at the structural variety of geometries due to the easy rotation of FC's cyclopentadiene rings[157]. All the conductance values are summarized in **Table 5.1**. Representative conductance displacement histogram of FC-NH_2 and FC-CN (right panel of **Figure 5.8a-b** respectively) are constructed from the same 5000 traces using 80 bins per decade. A distribution of molecular plateaus over a broad range (as evident from the traces in the left panels of **Figure 5.8a-b**), along with the slanted data cloud (see right panels of **Figure 5.8a-b**) establishes multiple stable configurations appearing due to the chemical anchors[156].

5.2.4. Stretching length histogram and average traces

To compare the evolution of the junction during stretching for the three different types of molecules, characteristic stretching length histograms for each conductance regime (**H**, **M** or **L**) are constructed by considering length from the relative zero position at $0.5\ G_0$ to one order of magnitude below the most probable conductance peak[78,158]. **Figure 5.9a-c** display the typical stretching length histogram of FC, FC-NH_2 and FC-CN for **H** (blue), **M** (red) and **L** (yellow) conductance regimes. The most probable plateau length is determined by the Gaussian fitting of the distribution (shown by the black dashed line), also summarized in **Table 5.1**. Notably, a positive shift in the distribution of **M** and **L** configurations compared to the **H** configuration, suggests that they correspond to a relatively longer conformation. While the larger width of the distribution for **M** and **L** configurations (**Figure 5.9a-c**) illustrates the widespread variation in geometry upon stretching the junction[30,78], larger stretching length indicates higher formation stability. Furthermore, to probe the conductance decay during the elongation of the junction, average conductance displacement traces are shown in **Figure 5.9d-f** for three different molecular junctions in the conductance regimes **H**, **M** or **L**. Almost flat plateau of the high conductance (**H**) region resembles to the atom-like contact[73], compared to the low conductance plateaus which are possibly originating due to the chemical anchors.

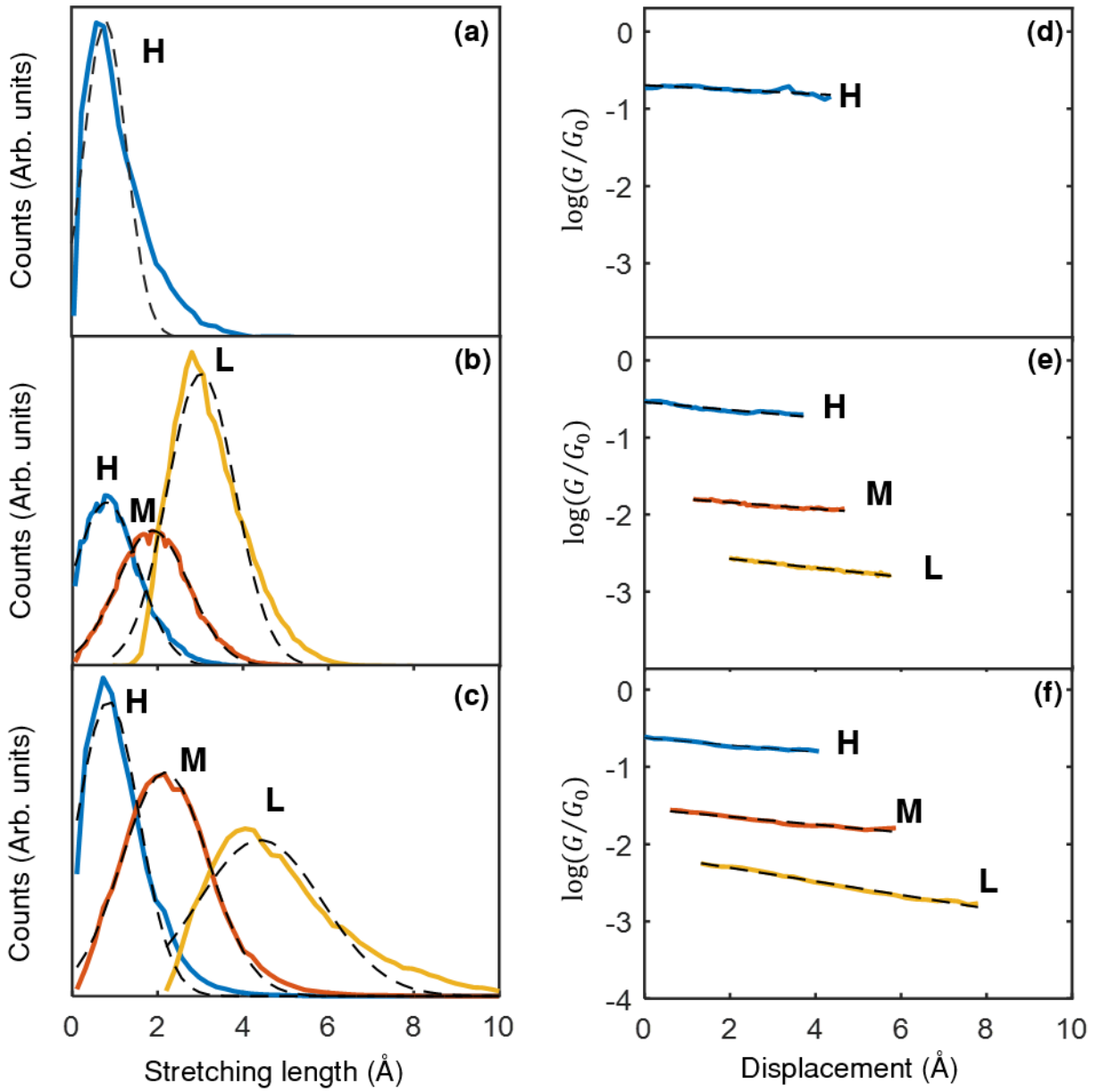

Figure 5.9 (a - c) *Stretching length histogram of ferrocene, 1,1'-bis(aminomethyl)ferrocene and 1,1'-dicyanoferrocene for three different conductance regime (blue-H, red- M and yellow-L). Histogram of a particular conductance region is constructed by considering length from the relative zero position at* $0.5\ G_0$ *to one order of magnitude beneath the most probable conductance value of corresponding regime. Black dashed line depicts the Gaussian fitting of the histogram which yields the most probable stretching length.* ***(d - f)*** *Statistically averaged conductance displacement traces of ferrocene, 1,1'-bis(aminomethyl)ferrocene and 1,1'-dicyanoferrocene . Here blue (red, yellow) color represents average traces of the high conductance regime, H (M, L). Black dashed line represents the linear fitting of the respective average traces to calculate the slope,* $\frac{\partial(log(G/G_0))}{\partial(\Delta x)}$.

Table 5.1 *Conductance parameters of single molecular junctions.*

Parameter	Molecule	Configuration		
		High G (H)	**Mid G (M)**	**Low G (L)**
Conductance (G_0)	FC	$(2.20 \pm 0.03) \times 10^{-1}$	----------	----------
	FC-NH_2	$(3.57 \pm 0.09) \times 10^{-1}$	$(1.21 \pm 0.11) \times 10^{-2}$	$(2.99 \pm 0.35) \times 10^{-3}$
	FC-CN	$(2.47 \pm 0.03) \times 10^{-1}$	$(1.57 \pm 0.09) \times 10^{-2}$	$(5.19 \pm 0.22) \times 10^{-3}$
stretching length (Å)	FC	0.7825 ± 0.0095	----------	----------
	FC-NH_2	0.7949 ± 0.0045	1.871 ± 0.003	3.012 ± 0.009
	FC-CN	0.8486 ± 0.0069	2.174 ± 0.003	4.407 ± 0.017
Slope ($Å^{-1}$)	FC	$-(2.87 \pm 0.75) \times 10^{-2}$	----------	----------
	FC-NH_2	$-(5.05 \pm 0.60) \times 10^{-2}$	$-(4.13 \pm 0.30) \times 10^{-2}$	$-(5.87 \pm 0.21) \times 10^{-2}$
	FC-CN	$-(4.58 \pm 0.57) \times 10^{-2}$	$-(5.03 \pm 0.54) \times 10^{-2}$	$-(8.78 \pm 0.40) \times 10^{-2}$

5.2.5. Transport calculations[2]

(i) High conductance feature

To gain insight into the origin of measured conductance, we now compare experimental results with detailed DFT - based calculations. We first consider two possible geometries (parallel and perpendicular orientation of FC with respect to the electrodes) and for each geometry, energies at

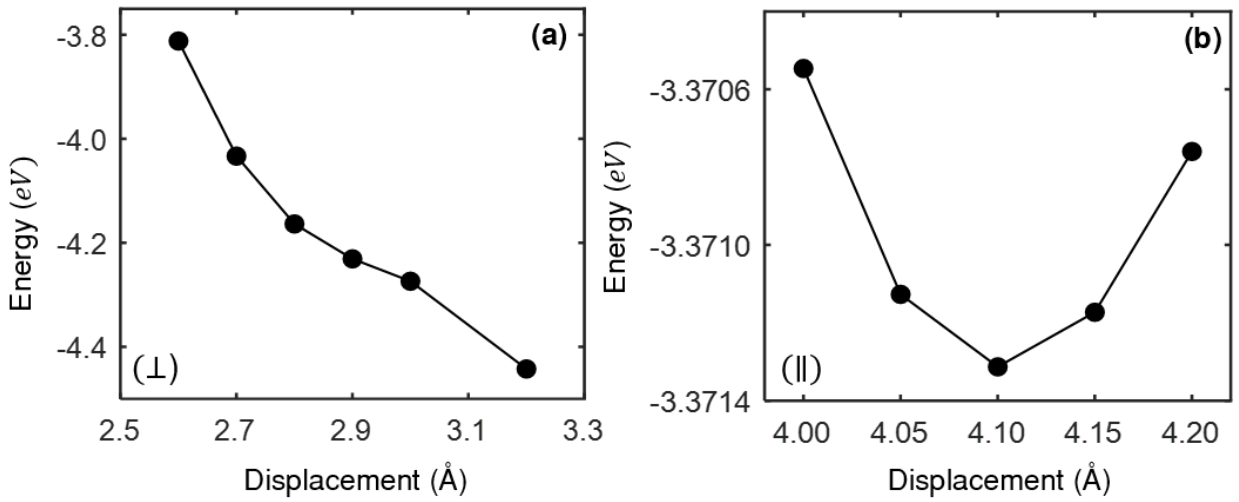

Figure 5.10 (a-b) *Energy of the extended molecule for perpendicular geometry (a) and parallel geometry (b) at different displacement of the electrodes from the molecule.*

[2] Theoretical calculation is performed by Štepán Marek, Puja Kumari, Dr. Soumya Jyoti Ray and Dr. Richard Korytár.

different displacements of the electrodes from the central Fe atom are evaluated. The scale of the energies, shown in **Figure 5.10**, for different displacements is large compared to the thermal energy accessible to the system and hence, each geometry can be considered stable with respect to the thermal fluctuations. Furthermore, we have also investigated the nature of bonding between the Au-Fe and Au-C for perpendicular and parallel geometries, respectively. Note that the incorporation of van der Waals correction seems to have significant impact on the binding energies for both the geometries. The bond energy was found to be significantly higher, $\sim -660\ meV$ for perpendicular and $\sim -1610\ meV$ for the parallel geometries, suggesting formation of covalent bonding. Now, the transmissions for these two geometries are calculated and conductance (G) can be written as,[159]

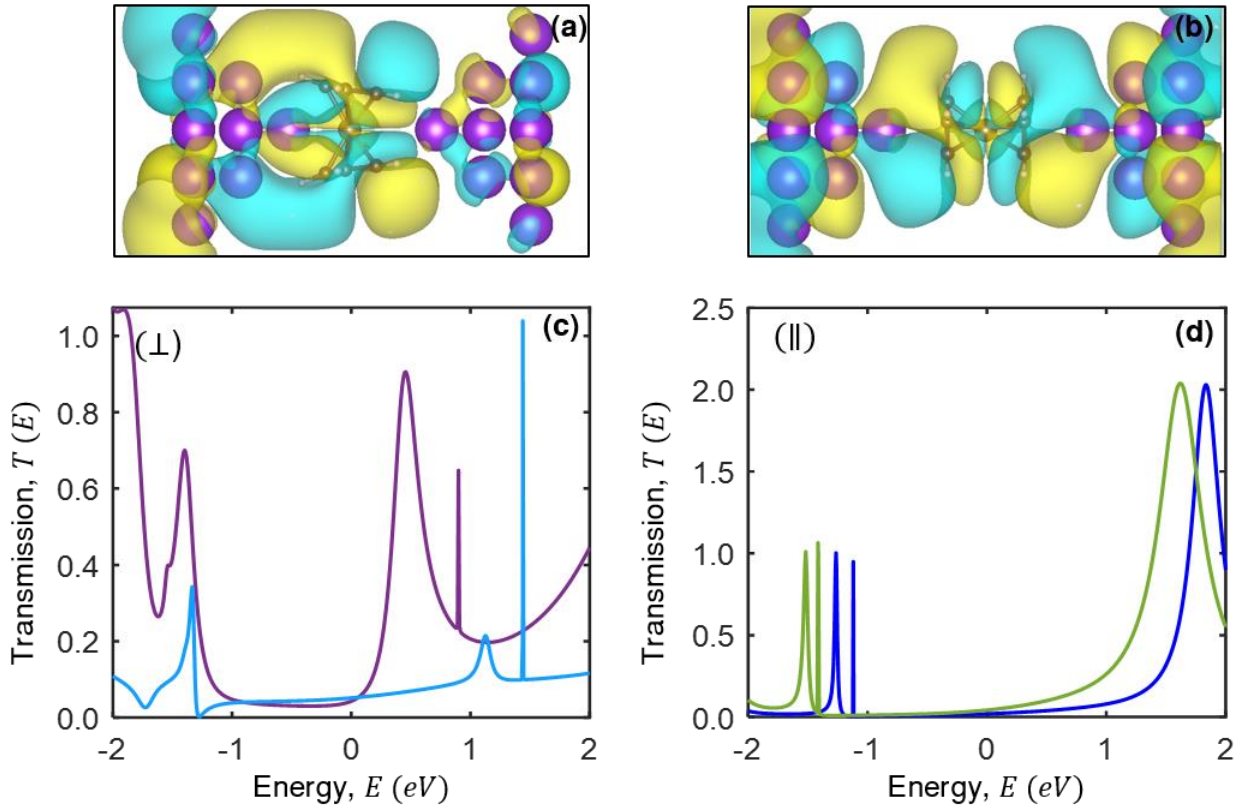

Figure 5.11 (a-b) *Top panels depict perpendicular (a) and parallel (b) geometries and scattering states at equal isosurface levels (yellow is positive, cyan is negative).* ***(c-d)*** *Bottom panels show transmission functions of the corresponding geometries at different electrode displacements from center of the junction. For perpendicular geometry (c), displacements are* 2.6 Å *(violet) and* 3.2 Å *(light blue) and for parallel geometry (d), displacements are* 4.1 Å *(green) and* 4.35 Å *(blue).*

$$G = \frac{I}{V} = \frac{2e^2}{h}\int_{-\infty}^{\infty} T(E)\frac{f_L\left(E;k_BT,E_F+\frac{eV}{2}\right)-f_R\left(E;k_BT,E_F-\frac{eV}{2}\right)}{eV}dE, \quad (5.1)$$

where e is the elementary charge, V is the bias of the junction and $f_{L/R}$ is the Fermi distribution of the left/right reservoir, at temperature $T = 300\ K$. The distribution of the left and right reservoir is shifted symmetrically by the bias of the junction. The difference between the Fermi distributions is called the transport window. For conductance to be significant, the overlap of the transmission function and the transport window must be non-negligible. The transmission functions for both geometries are displayed in **Figure 5.11c-d**. In perpendicular geometry, the transport window overlaps with a resonance for bias of about $1\ V$ but does not overlap significantly for infinitesimal bias. The wave function responsible for this resonance (see **Figure 5.11a**) resembles the LUMO

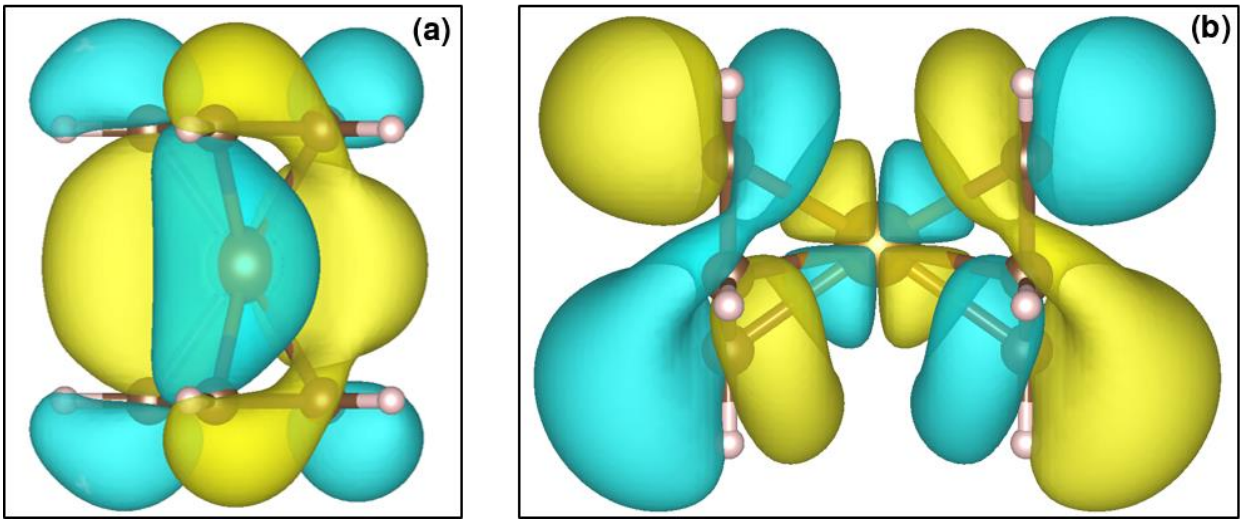

Figure 5.12 (a-b) *The highest occupied molecular orbital (HOMO) for free ferrocene (a) and lowest unoccupied molecular orbital (LUMO) for the same molecule (b).*

orbital of gas-phase FC, shown in **Figure 5.12**. In the parallel geometry (**Figure 5.11b**), the resonance of LUMO orbital is shifted further away from the Fermi energy and the transmission peak does not overlap with transport window even for bias of $1\ V$. The resonant transport in the perpendicular geometry yields relatively high conductance $0.1 - 0.3\ G_0$ and a stronger bias dependence in contrast to the off-resonant parallel geometry having conductance values in the range of $0.02 - 0.09\ G_0$. See **Figure 5.13** for values of conductance at different bias for both the geometries. Comparing the measured conductance along with its strong bias dependence, we suggest that the perpendicular geometry dominates in the ensemble of junctions over the parallel

geometry. The observation of high conductance peak in all three molecules along with similar stretching length (**Figure 5.9a-c**) suggest that it originates primarily from the perpendicular geometry via Au-Fe bond.

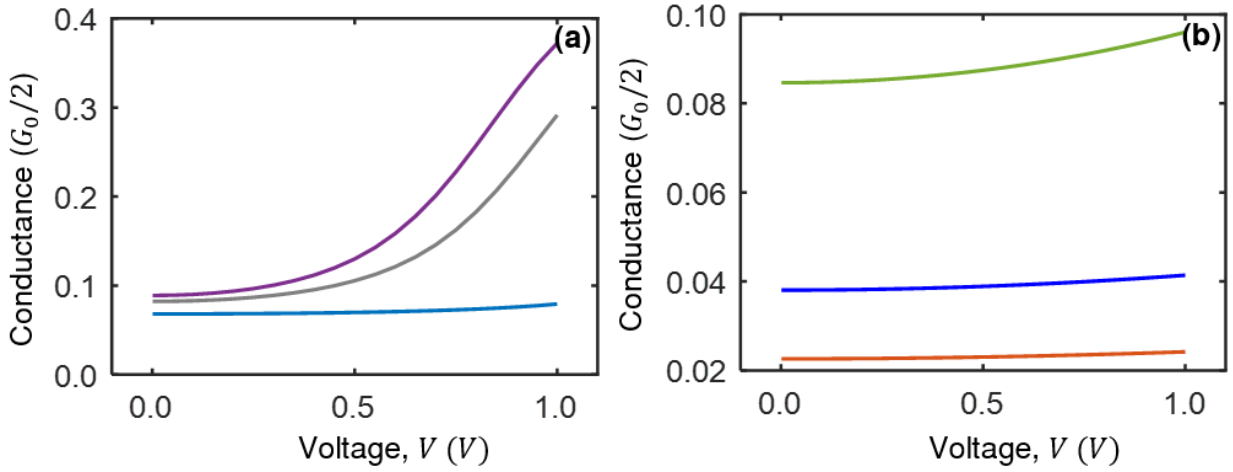

Figure 5.13 (a-b) *Conductance calculated as integral of the transmission function with transport window kernel at different electrode displacements from center of the junction. For perpendicular geometry (a), displacements are* 2.6 Å *(violet),* 2.65 Å *(gray) and* 2.72 Å *(light blue) and for parallel geometry (b), displacements are* 4.1 Å *(green) and* 4.35 Å *(blue) and* 4.5 Å *(orange).*

(ii) Low conductance feature

In this subsection, we explore the conductance behavior of ferrocene molecule coupled to Au electrode via **-NH_2** and **-CN** anchoring groups. Possibility of binding through the chemical anchors of FC-NH_2 and FC-CN-is clearly evident from the calculated negative binding energies for these two configurations (see **Table 5.2**). **Figure 5.14a-b** demonstrate the transmission curves for both the geometries when connected with the chemical anchors (termed as anchoring geometry),

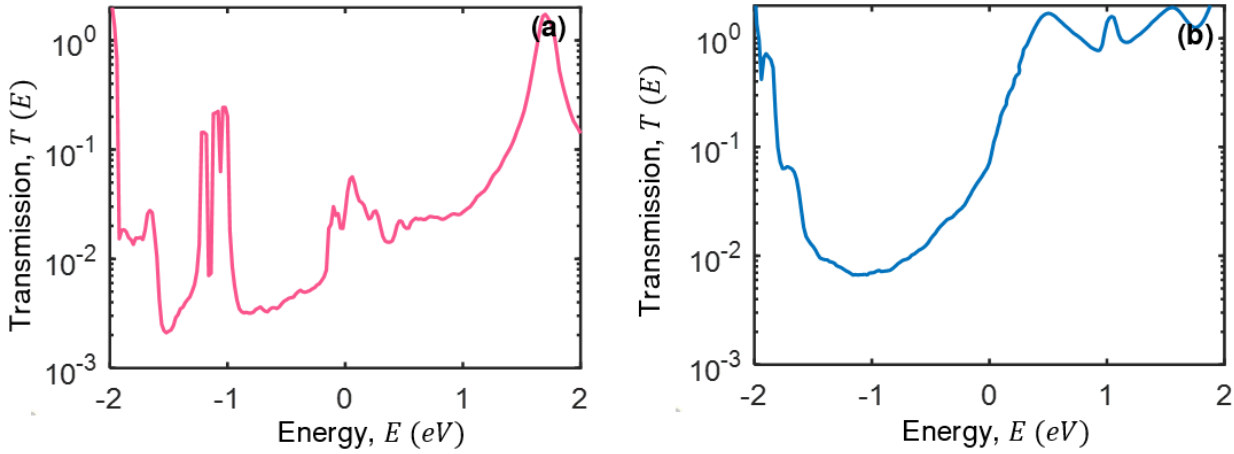

Figure 5.14 (a, b) *Transmission curve of Au/1,1'-bis(aminomethyl)ferrocene/Au and Au/1,1'-dicyanoferrocene/Au junction, coupled via anchoring group (anchoring geometry).*

exhibiting transmission in the range of 10^{-2} to 10^{-3} in the vicinity of metallic Fermi level. Thus, coupling with the anchoring groups may provide multiple conformations of the molecule inside the junction, leading to the broad conductance features with larger stretching length and tilted plateaus. The scattering wave functions indicate that primarily HOMO – 1 orbital is responsible for electron transport of both FC-NH_2 (**Figure 5.15a-b**) and FC-CN junctions (**Figure 5.15c-d**).

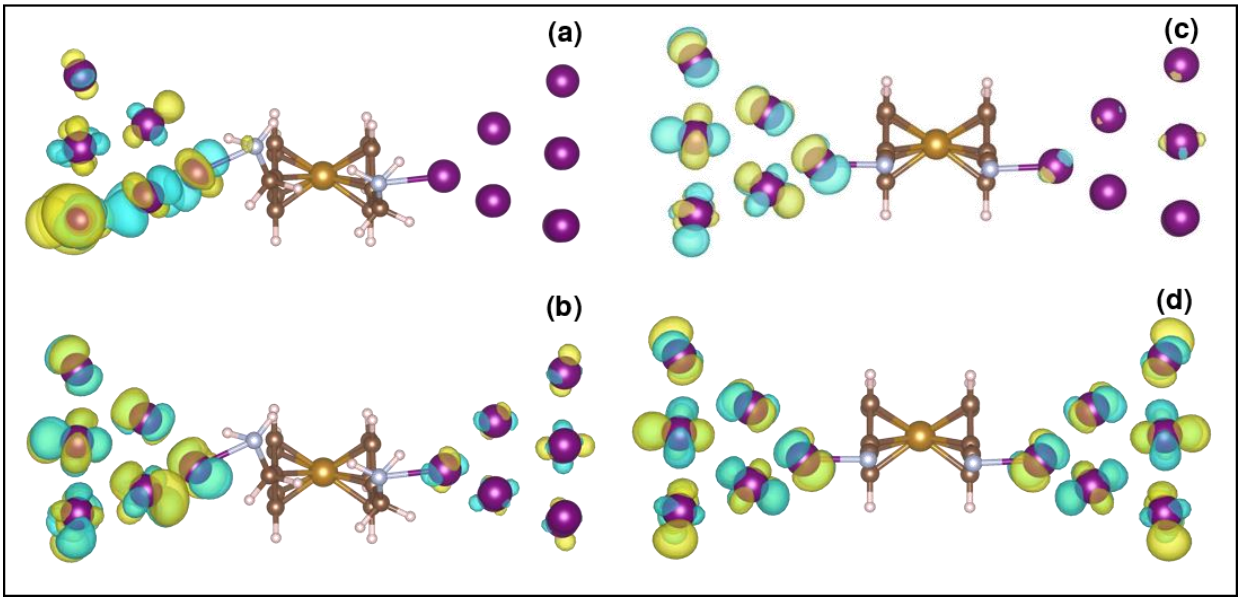

Figure 5.15 (a-b) *Transport states of anchoring geometry of Au/1,1′-bis(aminomethyl)ferrocene/Au : HOMO (a) and HOMO – 1 (b). Yellow isosurfaces have positive values.* ***(c-d)*** *similar transport states of Au/1,1′-dicyanoferrocene/Au junction. Isosurface levels of orbitals are chosen the same for both geometries.*

Table 5.2 *Binding energy of anchoring group coupled FC-NH_2 and FC-CN.*

Molecular system	Binding energy of Anchoring geometry
1,1′-bis(aminomethyl)ferrocene (FC-NH_2)	$-1.20\ eV$
1,1′-dicyanoferrocene (FC-CN)	$-1.13\ eV$

5.3. Conclusion:

In conclusion, we have demonstrated the resonant transport at room temperature by connecting an organometallic molecule between Au electrodes. By measuring conductance displacement traces for thousands of statistically independent junctions using a mechanically controllable break junction set-up, we observe that pristine Ferrocene binds strongly with the Au electrodes and provides a significantly high conductance peak ($\sim 0.1 - 0.3\ G_0$ in the bias range of 20 –

$400\ mV$) in the conductance histogram. The density functional calculations suggest that both perpendicular and parallel orientations of the molecule with respect to electrodes are energetically favorable configurations via covalent bonding. Transmission curve for the perpendicular geometry reveals a sharp peak near metallic Fermi level which leads to a conductance value closed to the experimentally observed conductance as well as a stronger bias dependence. Whereas similar calculations in parallel geometry shows a conductance in the range of $0.01 - 0.09\ G_0$ and having a rather weak bias dependence. We also observed that the inherent rotation of cyclopentadienyl rings of ferrocene has negligible impact on the transmission curves. Furthermore, to understand the effect of chemical anchors, we performed similar experiment on ferrocene terminated with two different anchoring groups (**-NH_2**) and (**-CN**). Both molecules display the high conductance peaks like pristine ferrocene in the conductance histogram, along with additional low conductance features. While the perpendicular geometry with Au facing the Fe atom might be responsible for the high conductance peak, the low conductance feature originate mainly due to the multiple binding geometries with the anchoring groups. Through this study we have not only explored the charge transport mechanism through a single organometallic molecule directly coupled to the metal electrodes via metal-metal chemical bond, but also provide a mechanism to exhibit long-range intra-molecular transport which is important for next generation molecular devices working at ambient condition.

Chapter 6 | Temperature sensitive molecular conformation in Au/ferrocene/Au junction

This chapter discusses the effect of temperature on the formation of Au/ferrocene/Au molecular junction, caused by temperature dependent intramolecular rotation of the Cp rings of ferrocene.

6.1. Introduction:

An important step to actualize the molecular scale devices in real circuitry is to improve our fundamental understanding of charge transport through the molecules, considering all possible factors of influences. Typically, a single molecular junction comprises of three basic components: molecule, metals electrodes and its interface with the molecule. Spatial orientation and electronic coupling between each components profoundly influences the behavior of the junction including its functionality[9]. A possible route to optimize these components towards the desired functionality is the customization of the synthetic molecules[24,75,160–164] and consideration of intrinsic density of states of metal electrodes at the Fermi level[165–167]. On top of that, manipulation of electronic coupling at the metal-molecule interface and its counter response in the characteristics of the junction are implemented to realize the electronic functionality such as rectifier[168] and molecular scale switch[169,170]. Furthermore, significant attention has been given to probe the electronic structure and transport characteristics of metal/molecule/metal junction taking the help of various external stimuli i.e., light, temperature, mechanical force, electric field and environment[142,171–175]. Another important parameter of consideration is the conformation or geometry of the molecule inside the junction which can significantly influence the change transfer to or from the molecule and evolution of the junction, as evident from torsional angle dependent conductance of biphenyl rings[15,28–30], structure assisted contact formation in bipyridine isomers[155]. Recently, enhancement of conductance due to temperature modified conformation of a dynamic molecular structure is reported[176]. Moreover, temperature assisted structural modification of the metallic tips is proposed to make a significant impact on the metal-molecule interface and hence, modify the conductance[177]. Thus, conformation-conductance relationship has already been actively discussed, however, until now, temperature dictated accessibility of molecular conformations has not been reported despite the realization of thermally assisted tunneling[178] and temperature dependent electronic transport mechanism[179].

In the present chapter, we demonstrate that temperature can be a deciding factor to realize the configuration of the dynamic molecular junction based on the single molecular conductance measurement of an organometallic molecule, for that class, a distinct evolution is recently identified due to its unique barrel shape structure[180]. Reported findings is observed for ferrocene molecule which comprises of an iron atom sandwiched between two cyclopentadienyl (Cp) rings[181,182]. One of the interesting aspects of ferrocene is that rotational dynamics of the two

cyclopentadienyl (Cp) rings changes with temperature and especially, reduction of the temperature decelerates the rotational motion due to the finite activation energy barrier (**Figure 6.1**). Combining experimental observations and theoretical calculations, here, we show that reduction of temperature leads to access more conformations of ferrocene to be executed inside the junction. Such unusual behavior is arising due to its temperature modified rotational dynamics of Cp rings which disrupts the metal-molecule coupling with the rise of temperature for those configurations which are coordinated via Cp rings to the metallic electrodes. Thus, existence of a configuration can also be sensitive to the temperature which provides an interplay between the intrinsic characteristics of the dynamic molecule and evolution of that molecular junction. Overall, temperature assisted intra-molecular rotation adds a new degree-of-freedom to understand and control the formation of dynamic molecular junction.

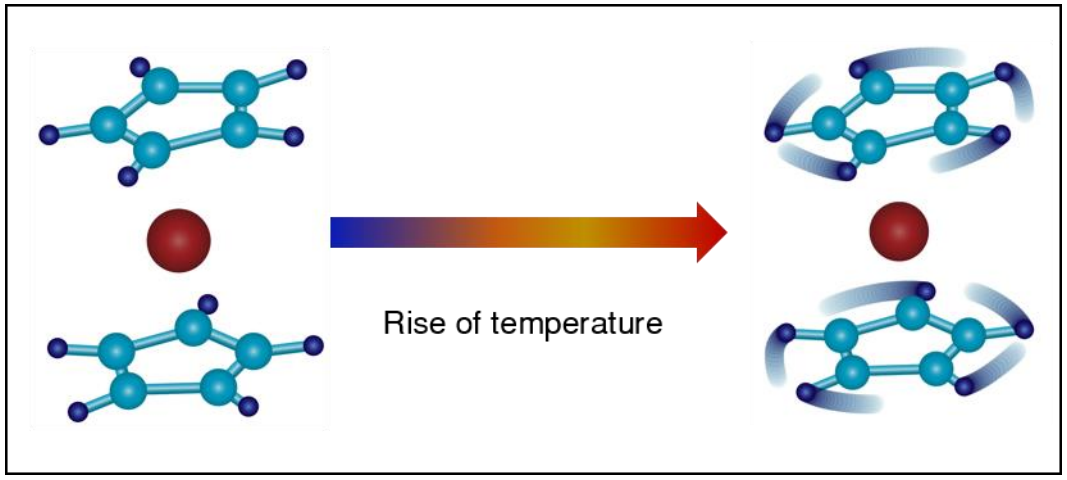

Figure 6.1 *Sketch of ferrocene and graphical demonstration of temperature modified rotational dynamics of its cyclopentadienyl (Cp) rings.*

6.2. Results and discussions:

6.2.1. Conductance traces and histograms

Experiments are performed on ferrocene molecule connected between two atomistic gold tips at three different temperatures 4.2 K, 77 K and 300 K. A mechanically controllable break junction set up is used to form the in situ molecular junction by spreading the molecules from a locally heated molecular source towards the continuously breaking and making atomic junction at cryogenic environments ($\sim$ 4.2 K). Representative breaking conductance traces for three different temperatures, 4.2 K, 77 K, 300 K are shown in the left (blue), middle (orange), right (red) panel of **Figure 6.2**. Observation of flat conductance plateau at 1.0 G_0 followed by plateaus below

1.0 G_0 demonstrate the formation of gold atomic junction followed by the molecular junction suspended between two metallic tips. Influence of temperature on the presence of molecular

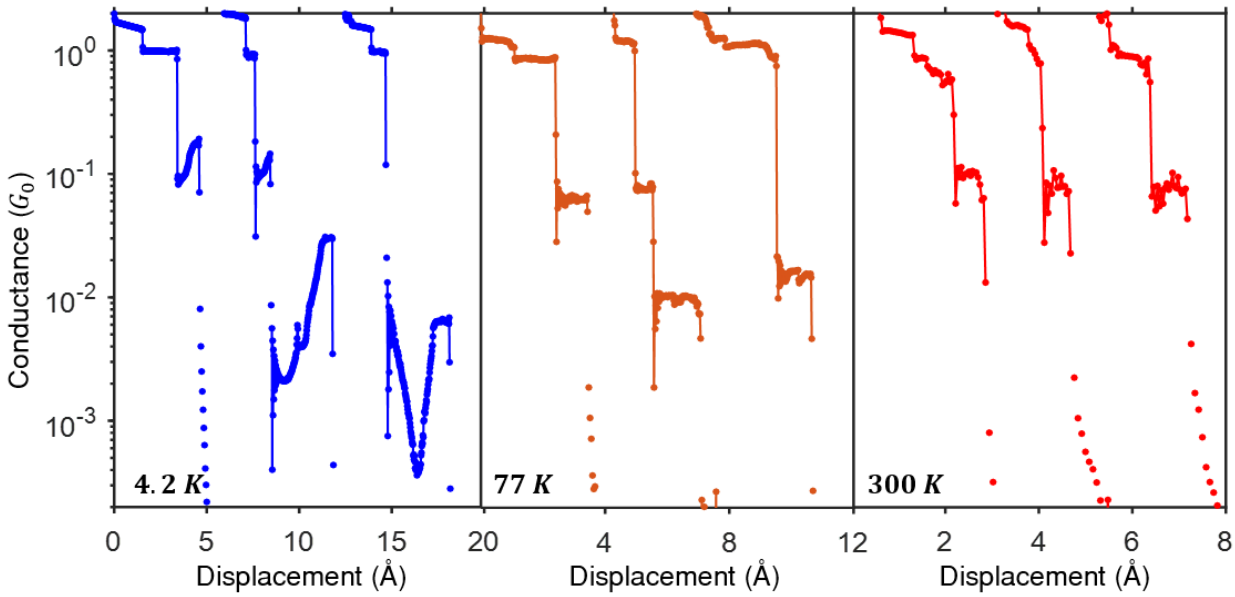

Figure 6.2 *Conductance displacement breaking traces of ferrocene molecular junction attached to gold tips at* 4.2 *K (Left Panel),* 77 *K (Middle panel) and* 300 *K (Right panel). Traces are shifted horizontally for better visualization.*

plateaus (below 1.0 G_0) is clearly evident from **Figure 6.2** and for the sake of presentation, we subdivide the conductance region into two section- High G (~ 0.1 G_0) and Low G (~ 0.01 G_0). At 300 K, plateaus are observed exclusively at the High G region in contrast to 4.2 K and 77 K where combination of both High G and Low G plateaus are observed. In fact at 4.2 K, subsequent plateaus (more than two) can appear in a single trace (see **Figure 6.5c**). Emergence of a plateau typically demonstrate a molecular junction, though its characteristics can vary from trace to trace due to unique evolution of each junction including conformation of the molecules[99,183]. However, to probe the large ensembles of the junction geometries, conductance histogram is prepared. Peaks in the histogram denotes the most prevalent molecular junction conductance's while the width of the conductance distributions indicates the microscopic variations from junction to junction[30]. **Figure 6.3a** displayed the conductance histogram of three different temperatures: 4.2 K (blue), 77 K (orange) and 300 K (red). Interestingly, the number of peaks in the histogram is greatly affected by the temperature. While the High G peak is present at all the three temperatures, the low G peak is absent at 300 K which is not the case for High G peak. This indicates the increase of stable molecular conformations inside the junction while reducing the temperature, being

definitely a new observation. We then move onto the conductance displacement histogram to get

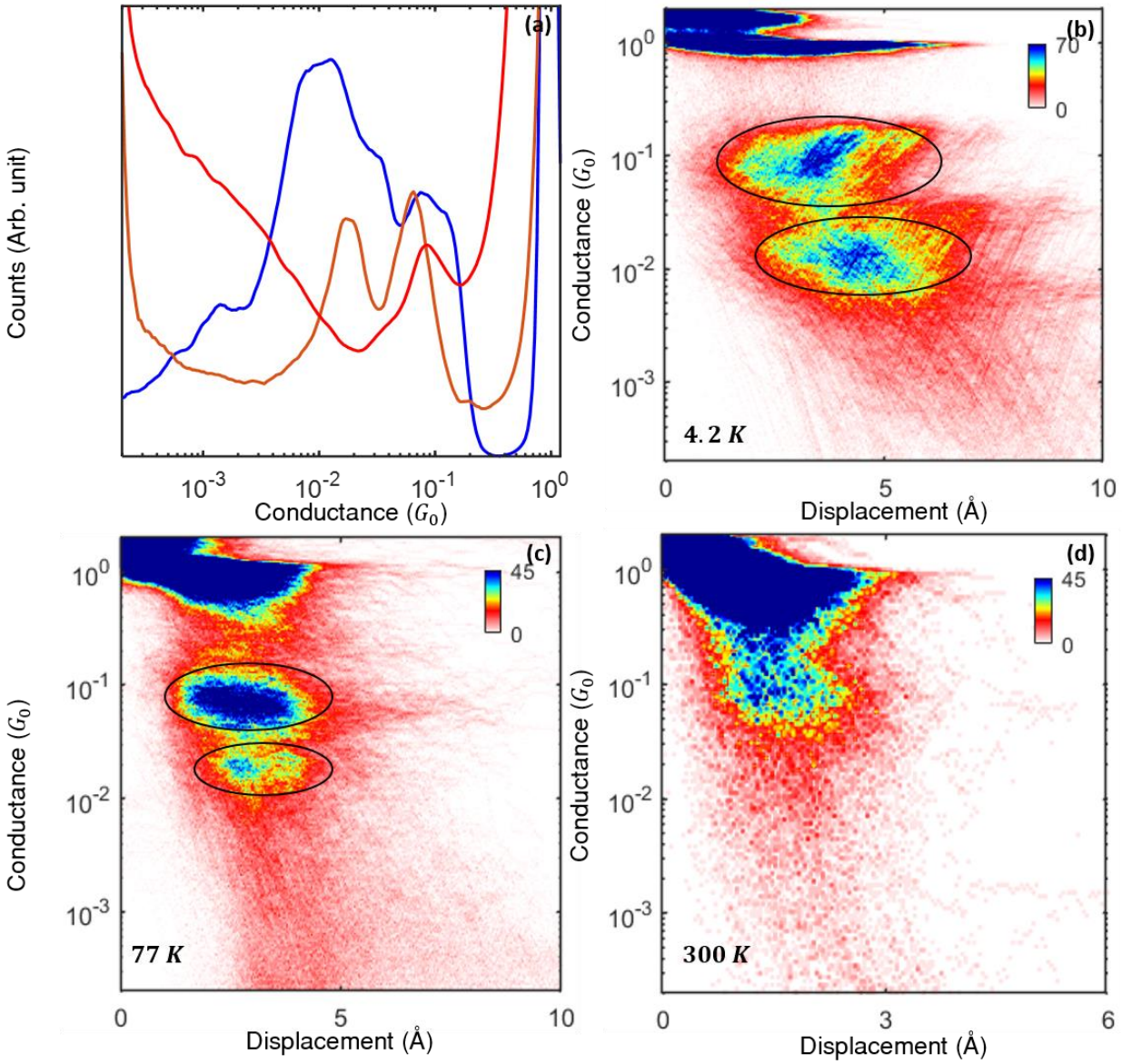

Figure 6.3 (a) *Conductance histogram of the gold/ferrocene/gold junction, following same color for three temperatures.* ***(b-d)*** *Conductance displacement histogram of the same junction at* 4.2 K, 77 K, 300 K. *Top right denotes the color limit and bottom left is the corresponding temperature. Black circle depicts the high density molecular data cloud. Histograms are constructed based on* 7442 *(*4.2 K*),* 9566 *(77*K*) and* 5000 *(*300 K*) conductance displacement traces using* 50 *bins per decade.*

further insight of the dynamical evolution and it is presented in the **Figure 6.3b-d** for 4.2 K, 77 K and 300 K respectively. Two prominent high density data clouds (marked by black circle) at 4.2 K and 77 K are indicative of the two stable configuration of the junction. Whereas at 300K, data clouds are only limited to the High G region, in line with the observation of the conductance traces

and histogram. Moreover, large width along with the fine peaks of the conductance histogram at 4.2 K arises due to rich structures of ferrocene assisted atomic chain formation which is confirmed from the plateau length analysis and will be discussed in the next section. Overall, our findings uncover a new phenomenon for the studied molecule that number of stable conformations of the molecule inside the junction can be modified with respect to the temperature.

6.2.2. Chain formation analysis

Plateau length is defined as the difference between two absolute displacement values, corresponding to two different conductance values containing the conductance plateaus, G_i and G_f, determined from the measured traces. Histogram of these lengths representing the distribution of the plateau lengths, has widely been used to probe the chain formation phenomena of metallic

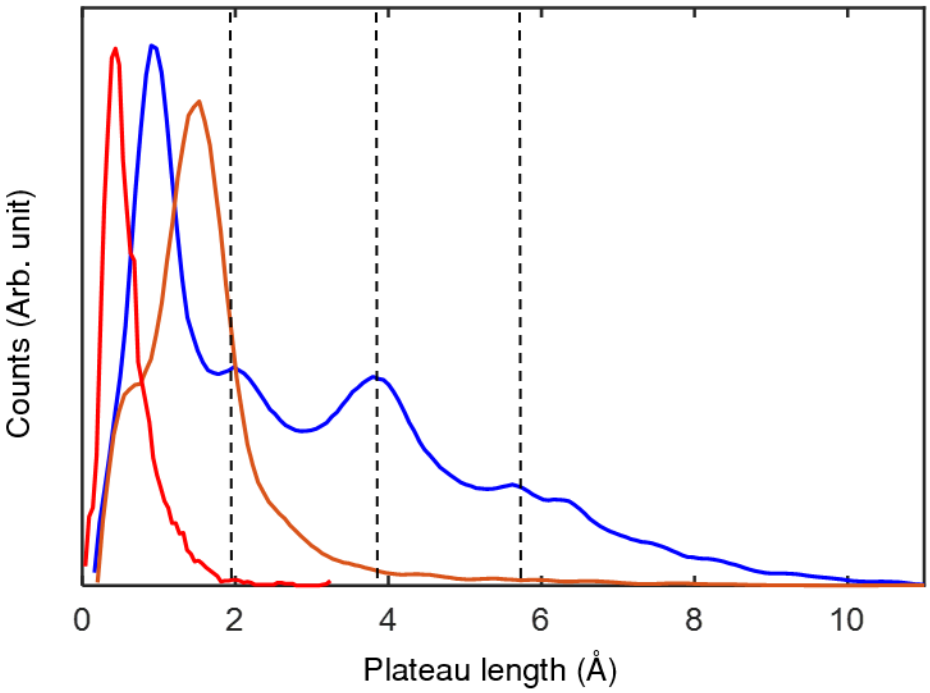

Figure 6.4 *Histogram of molecular plateau length (plateaus below* 1.0 G_0*) of gold/ferrocene/gold junction for the measurements at* 4.2 K *(blue),* 77 K *(orange) and* 300 K *(red). Black dash dotted line is used to denote the equidistant peaks of* 4.2 K *histogram.* 200 *(*4.2 K*,* 77 K*) and* 80 *(*300 K*) bins are considered for histogram generation.*

atomic junction[36,40,45,47,48,69]. **Figure 6.4** shows the plateau length histograms of Au/ferrocene/Au molecular junction at 4.2 K (blue), 77 K (orange) and 300 K (red), respectively. Conductance segments used to prepare the histogram are 0.001 G_0 to 0.5 G_0 for both 4.2 K and 77 K, 0.02 G_0 to 0.5 G_0 for 300 K. Surprisingly, plateau lengths at 4.2 K can extend up to ~ 10 Å in contrast to

77 K and 300 K where it is restricted only within ~ 4 Å and 2 Å respectively. Not only that, histogram of 4.2 K exhibits equidistant peaks (marked by black dashed line) of average separation ~ 2 Å. Length corresponding to each peak structure demonstrates the tendency of the junction to break at that displacement values, in which enough stress is accumulated upon elongation. The relative separation between these peaks is of the order of the interatomic separation of gold (~ 2 Å), which is an indicative of ferrocene assisted gold atomic chain formation. Thus at 4.2 K, broadened peak of conductance histogram corresponds to the microscopic variation of the junction's configuration due to chain mediated structure. Such chain formation is absent at 77 K and 300 K which may lead to sharp conductance peak and in turn, lesser microscopic variation of the possible configurations.

6.2.3. Formation and evolution of junction

Conditional analysis is now taken into account to point out the formational dependency of configurations, found in the junctions at 4.2 K and 77 K. Three different class of traces are identified based on the presence of plateau at the High G ($\sim 0.1\ G_0$) and Low G ($\sim 0.01 G_0$) region, we assign three class of traces-

(a) Type-1: Trace with plateaus at High G.

(b) Type-2: Trace with plateaus at Low G.

(c) Type-3: Trace with plateaus at both High G and Low G.

Representative traces of type-1 (green), type-2 (magenta) and type-3 (light blue) is shown in the **Figure 6.5a-c** (4.2 K) and **Figure 6.6a-c** (77 K). Conditional conductance histogram prepared from each type of traces is shown in **Figure 6.5d** (4.2 K) and **Figure 6.6d** (77 K), following the same colors. Here, blue color denotes the histogram considering traces including all types. Number of traces having characteristics nature like type-1, 2 and 3 out of all types is presented in the form of pie chart (inset of **Figure 6.5d** and **Figure 6.6d**) and details are mentioned in the **Table 6.1**.

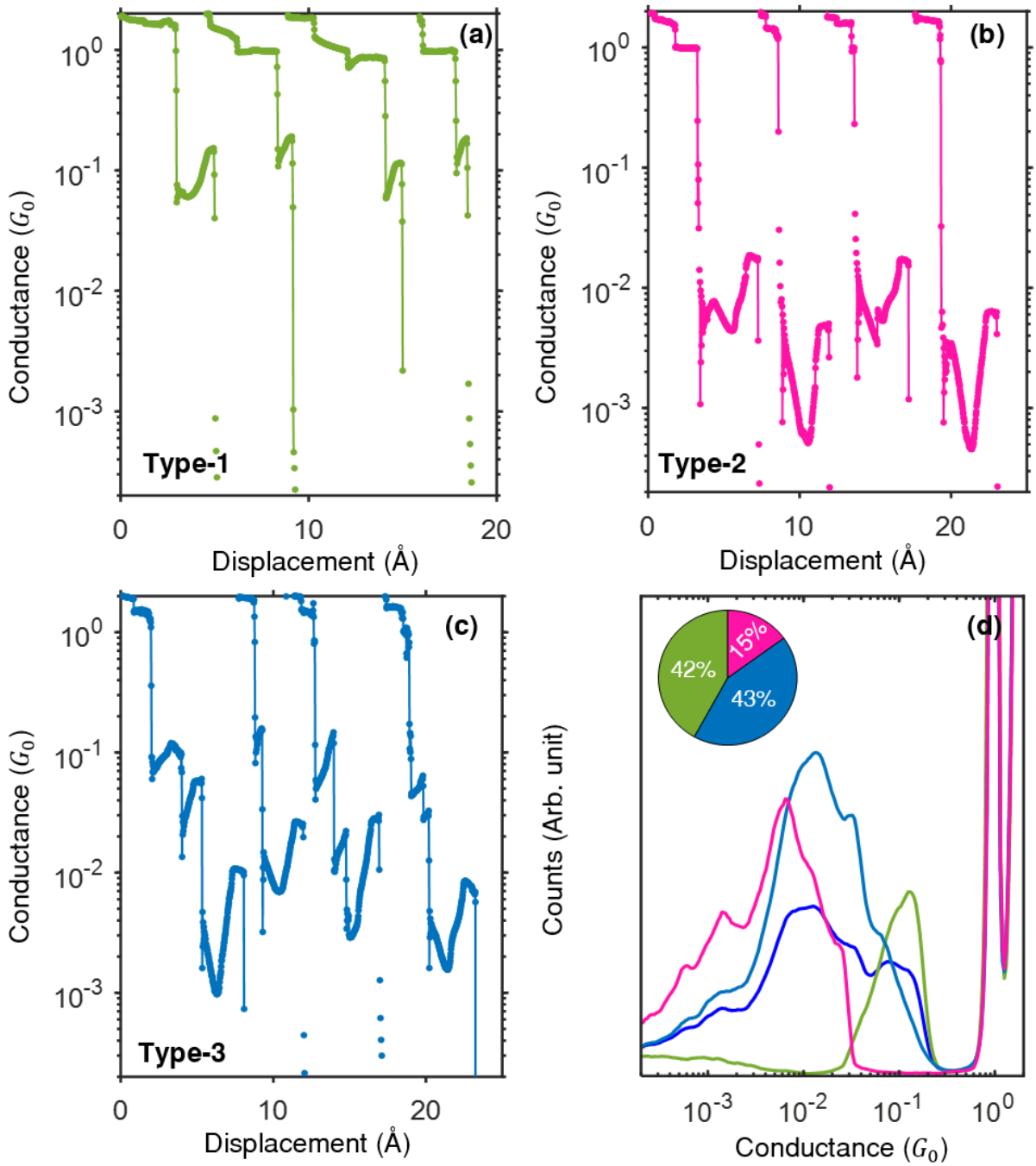

Figure 6.5 (a-c) *Representative traces of type-1 (a), type-2 (b) and type-3 (c) of the ferrocene molecular junction at 4.2 K. Types are defined accordingly the presence of plateaus, see* ***Section 6.3****.* ***(d)*** *Conductance histogram of each types (following same color as the corresponding traces) along with the traces including all types (blue). Histograms are prepared using* 50 *bins per decade. Inset: Pie chart of the percentage of each types out of all types.*

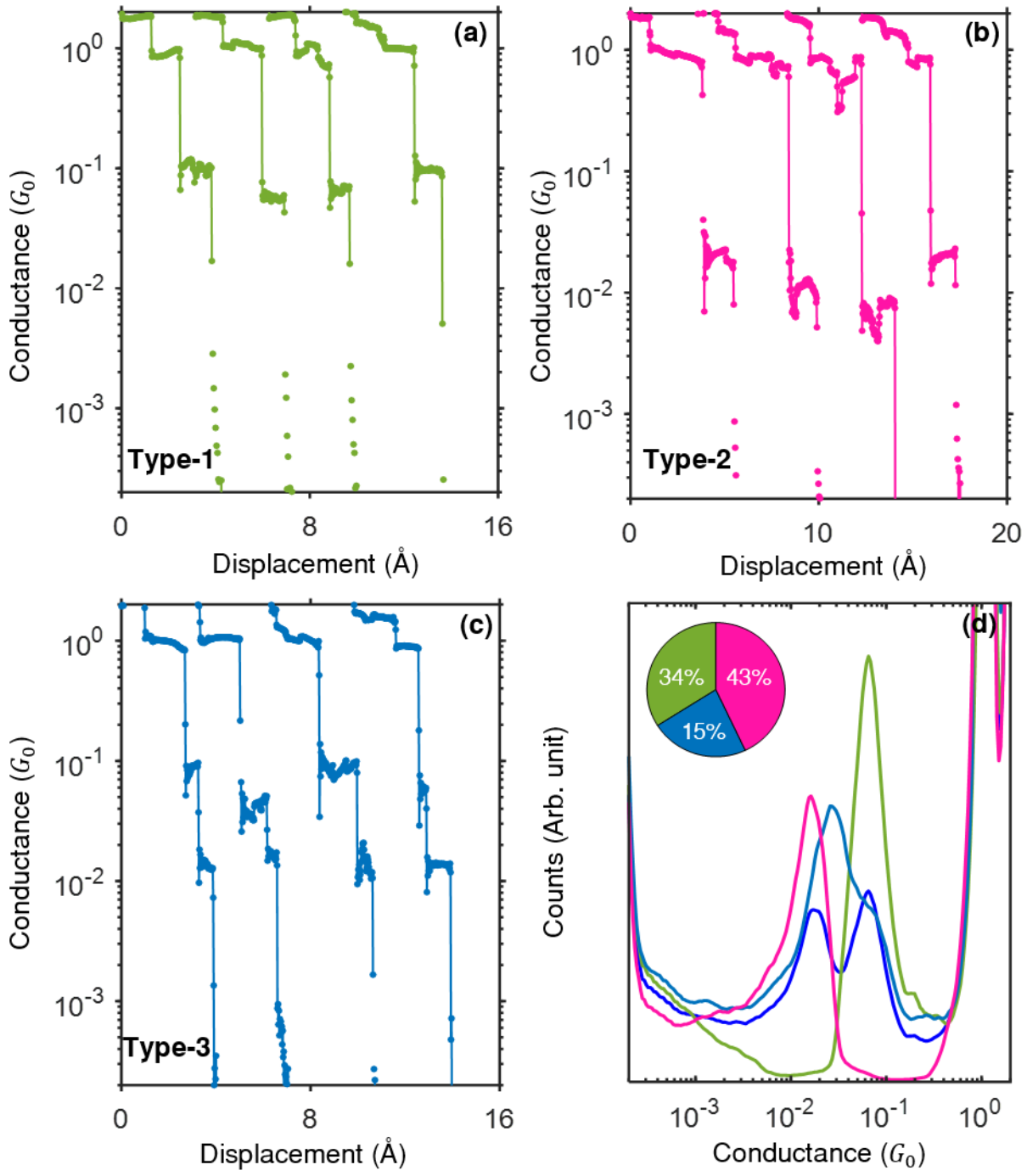

Figure 6.6 *Similar analysis like* ***Figure 6.5*** *for the same junction at* 77 K.

From the relative intensity of the **Figure 6.5d** and **Figure 6.6d**, we can conclude that High G and Low G can be formed independently during stretching (type-1 & type-2). On the other hand, transition from High G to Low G is also possible (type-3). Thus the above mentioned three classes

are possible conformations with different percentage of realization with a maximum possibility of type-3 (both High G and Low G) at 4.2 K and type-2 (only Low G) at 77 K.

Table 6.1 *Number of traces belongs to type-1, 2, 3.*

Temperature	Traces (%)	Type-1 (%)	Type-2(%)	Type-3(%)
4.2 K	7442 (100)	3123 (42)	1136 (15)	3183 (43)
77 K	9566(100)	3276 (34)	4059 (43)	2231 (23)

6.2.4. Molecular dynamics simulations[3]

To shed light on the origin behind the temperature assisted accessibility of more conformations in Au/ferrocene/Au single molecule junction and its impact on conductance, we have performed density functional theory (DFT) calculations based on first-principles. We have taken two pyramidal gold electrodes and placed the ferrocene molecule symmetrically between the electrodes. Two different stable configurations with molecular orientations parallel and perpendicular to the electrode axis can be found in these metal-organometallic junctions, similar to previous reports. The relative stability of the parallel and perpendicular configurations are presented in **Figure 6.7**. In general, it was found that the parallel configuration is energetically

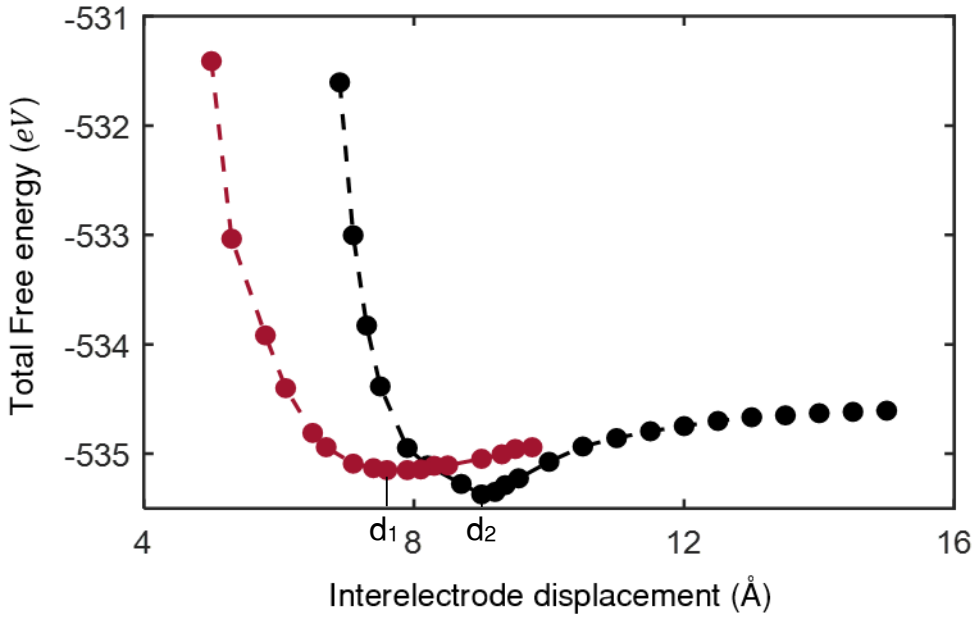

Figure 6.7 *Total energy of Au/ferrocene junction as a function of electrode separation. The calculations are done for perpendicular (red triangles) and parallel (black circles) configurations at different electrode separations.*

[3] Theoretical calculation is performed by Debayan Mondal and Prof. Priya Mahadevan.

more favorable at larger inter-electrode separation ($d_2 = 9.20$ Å,), whereas the perpendicular orientation is stabilized for smaller separation ($d_1 = 7.90$ Å.). We have considered these structures

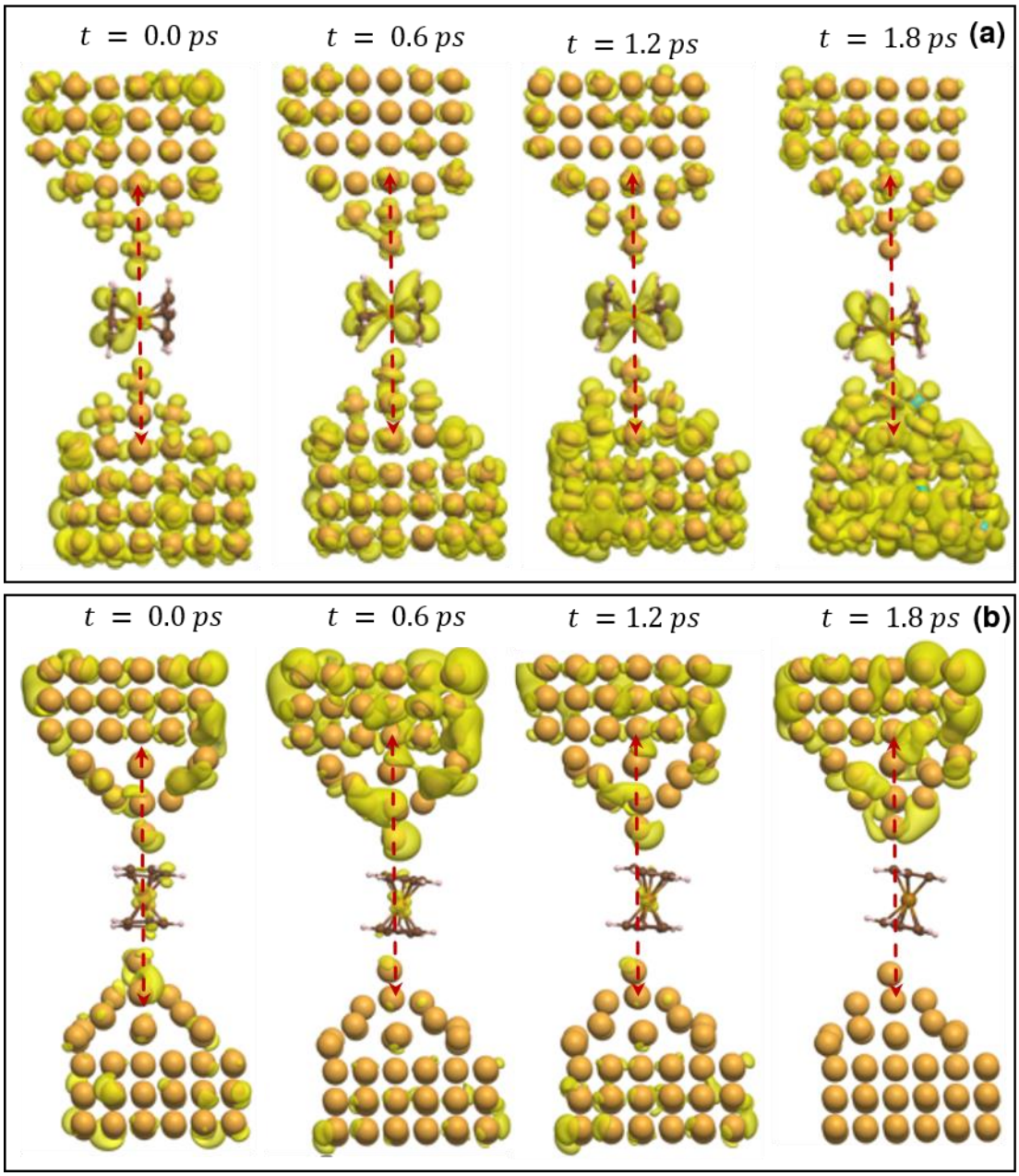

Figure 6.8 (a, b) *MD snapshot of gold molecular junction at* $300\ K$ *with ferrocene molecule perpendicular (a) and parallel (b) to electrode axis (red line) at time* $t = 0\ ps$, $0.6\ ps$, $1.2\ ps$ *and* $1.8\ ps$.

for our further analysis. To discuss the changes in the local geometry with temperature, molecular dynamics simulations were then carried out at temperatures of $300\ K$ and $77\ K$. At $300\ K$, when

the molecule is placed in a perpendicular orientation, the Fe atom of the molecule forms a stable bond with the Au electrodes. Off-centering of the Fe atom from the electrode axis is negligible i.e., 0.03 Å, 0.02 Å and 0.02 Å respectively at $6ps$,$12ps$ and $18ps$ MD timescale (**Figure 6.8a**). But on the other hand, when the molecule is placed in parallel with the electrode axis, a significant off-centering of the Fe atom with the electrode axis can be found i.e., 0.57Å, 0.86Å and 1.07Å

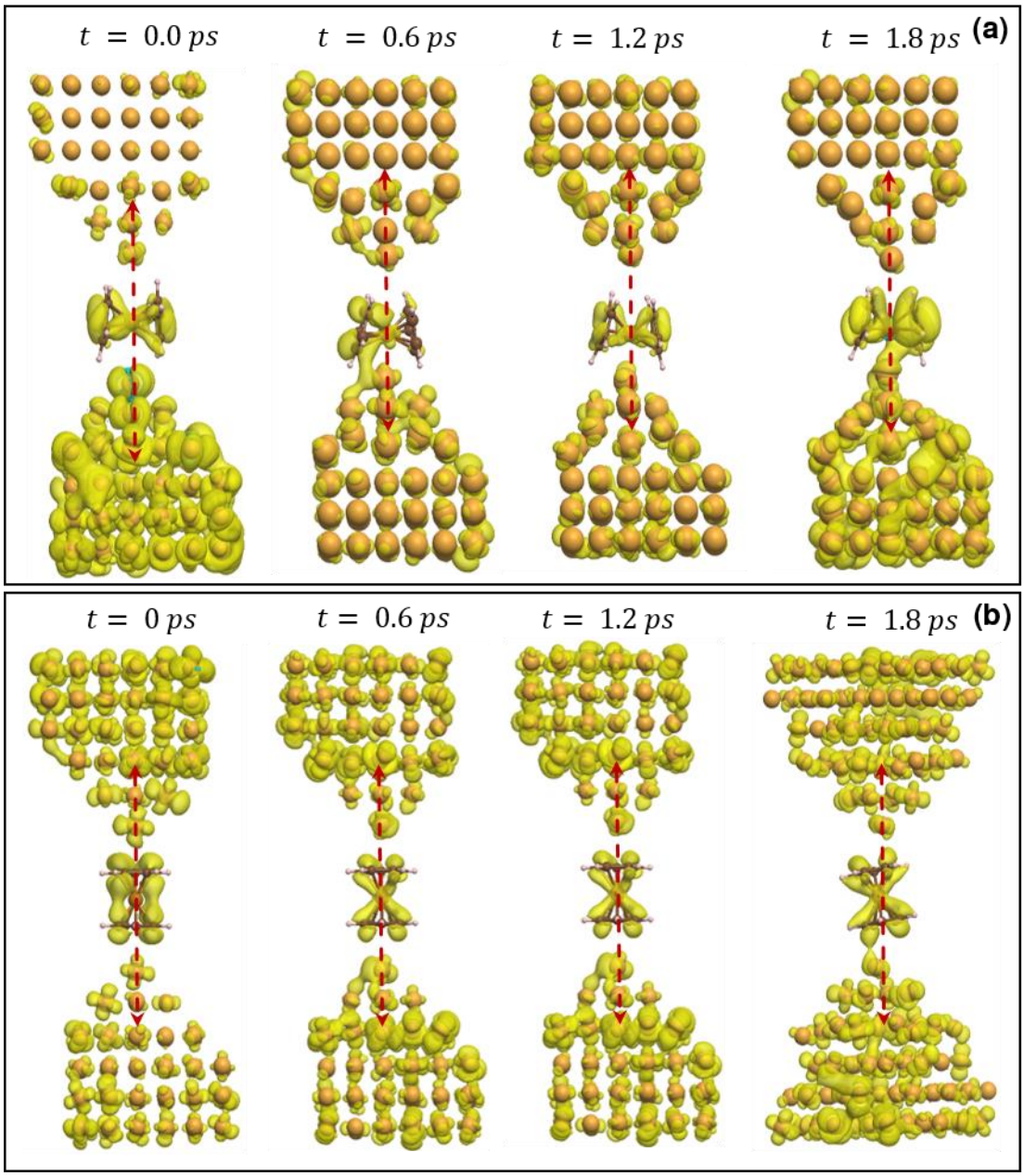

Figure 6.9 (a, b) *MD snapshot of gold molecular junction at* $77\ K$ *with ferrocene molecule perpendicular (a) and parallel (b) to electrode axis (red line) at time* $t = 0\ ps$, $0.6\ ps$, $1.2\ ps$ *and* $1.8\ ps$.

respectively at the previously mentioned MD timescale (**Figure 6.8b**). These observations suggest

that, at room temperature, the molecule can form a stable configuration as a function of time when it is placed perpendicular to the electrode axis but when it is placed parallel, the configuration is no longer stable as a function of time and the molecule is thrown away from the electrode axis in a short time. This is the reason why we see only one conductance peak associated with the molecular junction at $300\,K$. However at low-temperature ($77\,K$), the off-centering of the molecule for both parallel and perpendicular confirmations is negligible (**Figure 6.9**) which implies the stable electrode-molecule bond formation for both the configurations, consistent with the experimentally determined two stable configurations of the junction at $77K$.

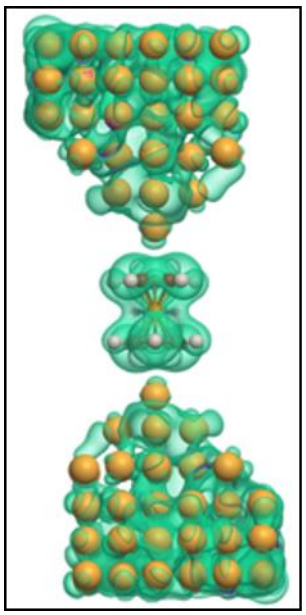

Figure 6.10 *Real-space plot of the charge density around the Fermi energy when the molecule is parallel to the electrode axis at electrode separation* 9.20 Å.

A better understanding of the origin behind the unstable junction formation at room temperature, when the molecule is parallel can be gained by looking at the corresponding real-space plot of the charge density around the Fermi energy (**Figure 6.10**). For the spin-up channel, an efficient hybridization between the frontier orbitals of the Au electrodes and the π-orbitals (p_y) of the molecule is clearly visible. Matrix element for the hopping between the s orbital of the gold tip and the p_y orbital of the carbon atom of the molecule involves a term, $E_{s,y} = m\, V_{pp\sigma}$, Where m is the direction cosine between gold s and carbon p_y orbital and $V_{pp\sigma}$ is the Slater-Koster parameter. For the parallel conformation, Cp rings can rotate freely with a frequency 17° per picosecond, considering one C atom of the Cp ring, this implies that the matrix element would vary as the ring rotates from 0° to 360°, becoming smaller and even zero at some points. As the steric interaction

strength remain almost unchanged, this leads to an off-centering of the molecule from the junction to reduce the effect of steric-repulsion. At low temperature the effect is smaller as the rotation of the Cp ring is small. However for the perpendicular conformation, the coupling between the electrode and the molecule is through the Au-s and d orbital of the stationary Fe atom, which keeps the coupling strength almost constant resulting in a stable junction formation.

6.3. Conclusion:

Overall, we have demonstrated that the formation of chemical bond between a metal and an organic molecule can be dictated by the inherent rotation of the molecule, never observed before to the best of our knowledge. At first, by performing conductance measurements using MCBJ technique at three different temperatures ($300\ K$, $77\ K$ and $4.2\ K$), we observed two stable conformations at low temperature in contrast to the room temperature where only one (high conductance) conformations are seen. Through first principle calculations and MD simulations we try to unravel the underline mechanisms behind these observations. We find that the Cp rings of ferrocene is continuously rotating at room temperature and with decreasing temperature it slows down and almost freezes at low temperature. Two possible conformations are considered: molecule sitting parallel and perpendicular to the electrodes. We have already shown in the previous chapter that both these conformations are energetically favorable if we do not consider the effect of ring rotation. However, we observe here that at room temperature, the dynamic rotation of the Cp rings hinders the formation of stable chemical bond when Au atoms try to couple via the Cp rings, i.e., the parallel conformation. Hence, only vertical conformation, where the coupling is via central Fe atom, is stable providing the high conductance conformation at higher temperature. With the reduction of the temperature, as the rotation of the Cp rings freezes, both these conformations are feasible leading to two different peaks in the histogram. Furthermore, as there is a small change of energy involved with the increase of inter-electrode separation, transition from perpendicular to parallel conformation is possible which explains the experimentally observed traces with plateaus both at High G and Low G simultaneously in a single stretching event (type-3). Thus, we reveal a new aspect in this field where the metal/molecule coupling is controlled by both orientation and intra-molecular dynamics.

Chapter 7 | Molecular orientation dependent mechanical gating in Ag/ferrocene/Ag junction

This chapter highlight the significance of orbital orientation in the overall process of metal-molecule charge transfer and demonstrate that the orientation of the molecule is an inescapable factor to realize the mechanically-gated molecule junctions.

7.1. Introduction:

One of the attractive properties of molecular junctions is their ability to function as electro-mechanical devices. Especially, single-molecule junctions allow the study of coupling between mechanical and electronic degrees of freedom in a structure of a typical single-nanometer size that has a dominant quantum nature, and a pronounced orbital character. This combination has been considered to study diverse phenomena, including electron-phonon interaction[64,66,184–187], quantum interference[127,157] and charge reorganization[188] in the miniaturization limit for electronic conductors. Interestingly, in addition to the more standard electrostatic gating of molecular junctions, these junctions can also be mechanically gated. By changing the interelectrode separation, charge can be transferred from the electrodes to the molecule or vice versa. Consequentially, the molecular energy levels are shifted to a higher or lower energy and the electronic transport characteristics of the junction may change. Mechanically-gated molecular junctions have been extensively studied both experimentally and theoretically[75,127,157,188–193], for example in the context of nanoscale image charge[188], optimization of thermoelectricity[189], and the study of the Kondo effect[193]. However, the influence of the molecule orientation on mechanical gating has not been examined. Such influence can be an attractive route for optimization and regulation of mechanical gating with implications on charge, spin, and heat transport in molecular junctions. Here, our finding demonstrate that mechanical gating of molecular junctions can be dramatically affected by the molecule orientation, where the same molecular junction experiences either a clear mechanical gating or the absence of such an effect, depending on the orientation of the molecule with respect to the electrodes. By comparing experimental observations and theoretical calculations, this behavior can be related to the orbital nature at the metal-molecule interfaces, allowing the identification of the necessary conditions for mechanical gating. The reported findings in this chapter show that the orientation of the molecule is an unavoidable factor to realize the mechanically-gated molecule junctions, and emphasizes the importance of orbital orientation in the general process of metal-molecule charge transfer.

7.2. Results and discussions:

7.2.1. Conductance traces and histograms

Molecular junction (ferrocene, chemical structure is shown in the inset of **Figure 7.1b**) is fabricated between two silver (Ag) electrode tips using a break junction setup. The ferrocene

molecules are introduced from a local heated molecular source towards a cold atomic-scale Ag junction during the repetitive breaking and making cycles to ensure the in-situ formation of

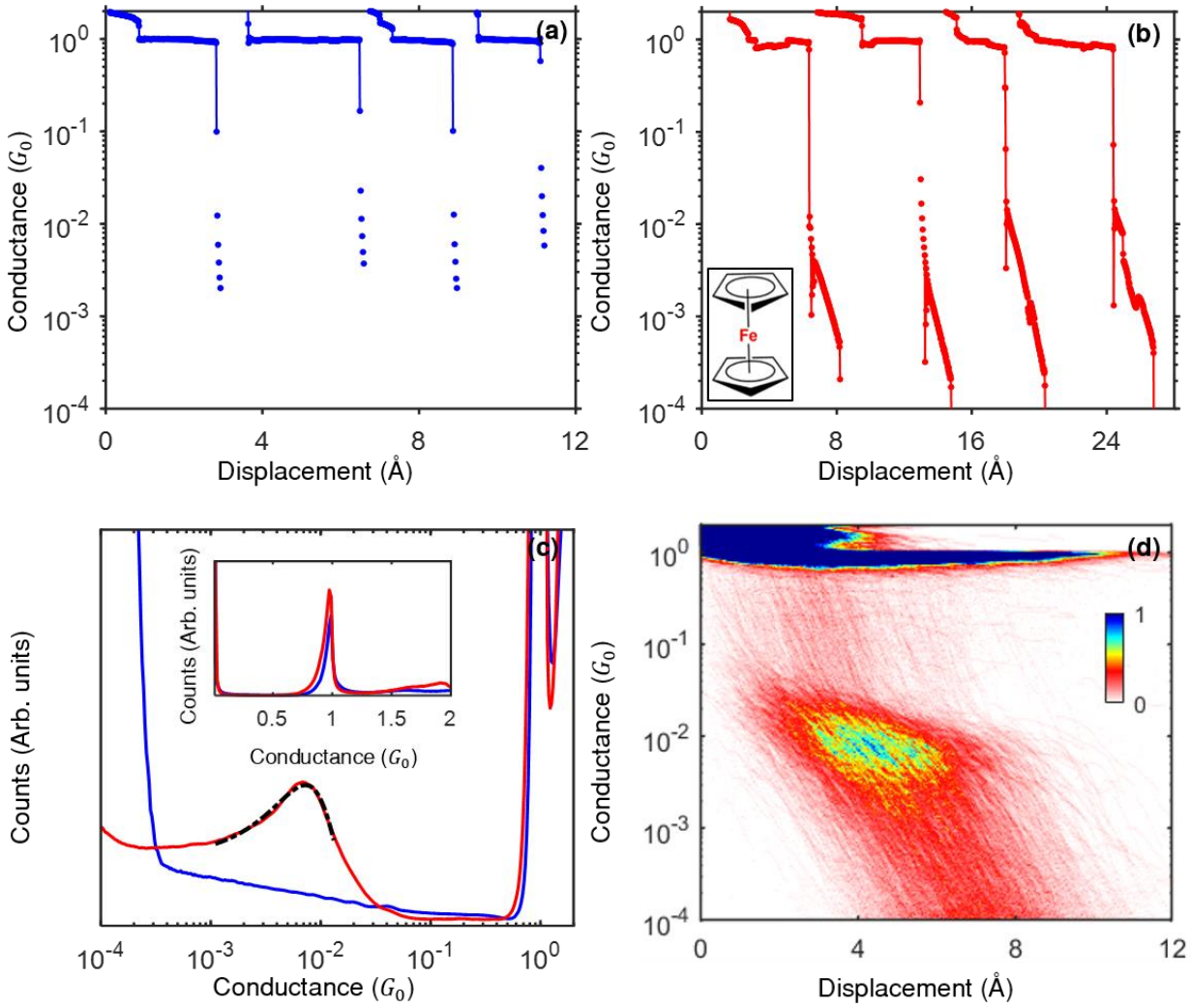

Figure 7.1 (a, b) *Traces of conductance vs. displacement recorded during the breaking of Ag atomic-scale junctions before (a) and after (b) the insertion of ferrocene molecules, recorded at* 50 *mV bias voltage. Traces are shifted horizontally for clarity. Inset of (b): Chemical structure of ferrocene.* ***(c)*** *Conductance histogram for Ag (blue) and Ag/ferrocene (red) junctions, prepared from* 5,000 *and* 10,000 *consecutive conductance traces using* 80 *bins per decade. Black dash dotted line represents a Gaussian fitting to the observed peak. Inset: Conductance histogram of the same junctions, constructed from* 300 *bins in a linear scale.* ***(d)*** *Conductance displacement histogram of Ag/ferrocene junctions prepared from the same traces using* 50 *bins per decade.*

molecular junction in a cryogenic environment ($\sim 4.2\ K$). Successful formation of molecular junction is confirmed from the recorded d.c. conductance (current/voltage) as a function of relative interelectrode separation (namely the displacement) during stretching. First, a bare Ag junction is characterized. **Figure 7.1a** presents in blue examples for conductance traces as a function of

displacement. During the elongation of the Ag junction, the conductance decreases in steps when the contact diameter is reduced. The last conductance plateau at $\sim 1\ G_0$ ($G_0 = (2e^2/h)$, is the conductance quantum, where e is the electron charge and h is the Plank's constant) provides the conductance of a single atom contact between the Ag electrode tips[194]. After the insertion of ferrocene molecules, slanted plateaus below the $\sim 1\ G_0$ step are clearly seen (**Figure 7.1b**). To statistically characterize the most probable conductance features, conductance histograms (**Figure 7.1c**) are prepared from 5,000 and 10,000 consecutive conductance displacement traces for Ag junctions before (blue) and after (red) the introduction of ferrocene, respectively. While the conductance histogram for bare Ag junctions reveals a peak at $\sim 1\ G_0$ (Inset of **Figure 7.1c**) that is associated with the most probable conductance of single Ag atom contacts, after the introduction of ferrocene an additional shallow peak beneath the $1\ G_0$ peak is observed. Consequently, this peak is accumulated as a high density data cloud $\sim\ 1\ \times\ 10^{-2} G_0$ in the corresponding conductance displacement histogram (**Figure 7.1d**), prepared from the same 10,000 traces. Gaussian fitting of the corresponding peak, shown by a black dash dotted line in **Figure 7.1c** yields a most probable conductance value of $7.25\ \pm 0.06\ \times\ 10^{-3} G_0$ for Ag/ferrocene molecular junctions.

7.2.2. Current-voltage and differential conductance spectroscopy

Measurements of current as a function of applied voltage across the junctions ($I - V$ curves) for different junction realizations reveal two distinctive cases, denoted here as type 1 and type 2, (**Figure 7.2a-b**). The presented $I - V$ curves were measured following a repeated reduction in the displacement. Several steps can be observed in the $I - V$ curves, translated in **Figure 7.2c-d** to peaks in the corresponding differential conductance versus voltage ($dI/dV - V$) curves. As will be further discussed below with the aid of ab-initio calculations, the peaks originate from the contributions of molecular orbitals to the conductance. Therefore, shifts in the voltage at which the peaks are observed correspond to shifts in the molecular energy levels with respect to the Fermi level of the electrodes. **Figure 7.2c**, reveals that the peaks of type 1 are shifted to a lower voltage when the displacement is reduced. Namely, the molecular level or levels that dominate transport in type 1 are shifted towards the Fermi level when the junction is squeezed. In contrast, in **Figure 7.2d**, the peaks for type 2 are not shifted in response to a similar mechanical manipulation. Specifically, the inset of **Figure 7.2c**, presents a significant shift from $1.365\ V$ to $0.675\ V$ for a reduction in the displacement of ~ 0.6 Å for type 1, whereas a similar behavior is not seen in the

inset of **Figure 7.2d** for type 2. This is an indication for mechanical induced molecular energy shifts, or mechanical gating, in type 1 and the absence of this effect in type 2 (See **Figure 7.8** and **Figure 7.10** for similar type 1 and 2 behaviors in different realizations of the Ag/ferrocene/Ag molecular junctions).

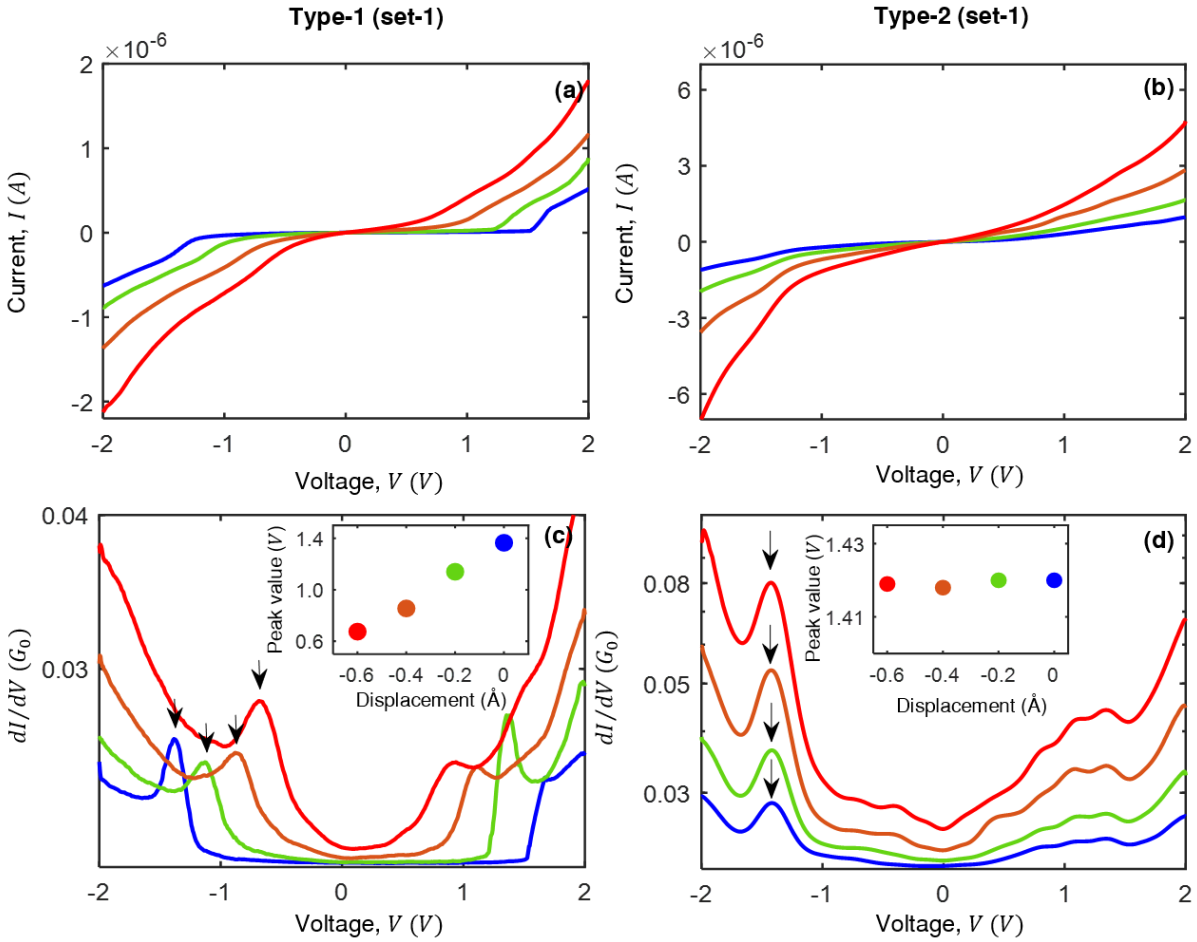

Figure 7.2 (a, b) *Four spectra of current vs. voltage measured at different interelectrode displacements (for color code and displacement see c, d Insets) in Ag/ferrocene molecular junctions with (a, type 1) and without (b, type 2) mechanical gating response.* ***(c)*** *Differential conductance as a function of applied voltage for the junction studied in a.* ***(d)*** *Same as c but with data collected for the molecular junction studied in b. Insets (c, d) Absolute values of peak position (marked with arrows in c, d) as a function of interelectrode displacement.*

7.2.3. Transition voltage spectroscopy

The same effect can also be presented using transition voltage spectroscopy (TVS) plots, where $I-V$ characteristics are re-plotted, in terms of $ln(I/V^2)$ as a function of $1/V$ [195–199]. These plot is also termed as Fowler-Nordheim plot (FN plot) and expected to have a minimum at a

corresponding bias voltage, V_{trans} , at which there is a transition between two different transport regimes. It can be explained by considering an arbitrary tunnel barrier within the Simmons approximation[70] and is described below. Using Simmons approach shown in **Figure 7.3a**, current voltage characteristic of a molecular junction can be modelled as,

$$I(V) = \frac{qA}{4\pi^2\hbar d^2}\left\{\left(\varphi - \frac{qV}{2}\right)\exp\left(-\frac{2d\sqrt{2m_e}}{\hbar}\sqrt{\left(\varphi - \frac{qV}{2}\right)}\right) - \left(\varphi + \frac{qV}{2}\right)\exp\left(-\frac{2d\sqrt{2m_e}}{\hbar}\sqrt{\left(\varphi + \frac{qV}{2}\right)}\right)\right\} \quad (7.1)$$

Where d is the barrier width, A is the junction area, m_e is the electron effective mass, q is the electronic charge and φ is the barrier height. In case of molecular junctions, the barrier height can be approximated by the energy offset between the electrode Fermi level and the nearest molecular orbital and the barrier width corresponds to the molecular length. When the applied bias is smaller than the barrier height, above equation describes a trapezoidal barrier (**Figure 7.3a**, case-2), however, in the zero-bias limit, the barrier is rectangular (**Figure 7.3a**, case-1), and **Equation (7.1)** reduces to

$$I(V) \propto V\exp\left(-\frac{2d\sqrt{2m_e\varphi}}{\hbar}\right) \quad (7.2)$$

On the other hand, when the applied bias exceeds the barrier height, the barrier transitions from trapezoidal to triangular (**Figure 7.3a**, case-2 to 3), and the current-voltage dependence can be described as follows

$$I(V) \propto V^2\exp\left(-\frac{4d\sqrt{2m_e\varphi^3}}{3\hbar qV}\right) \quad (7.3)$$

Rearranging the above equation we get,

$$\ln\left(\frac{I}{V^2}\right) \propto -\frac{4d\sqrt{2m_e\varphi^3}}{3\hbar q} * \frac{1}{V} \quad (7.4)$$

Thus from **Equation (7.4)**, it is clear that $ln(I/V^2)$ as a function of $1/V$ will exhibit a line, the slope of which will depend on the barrier height. To examine the transition of transport mechanism, **Equation (7.2)** should be written in the form of

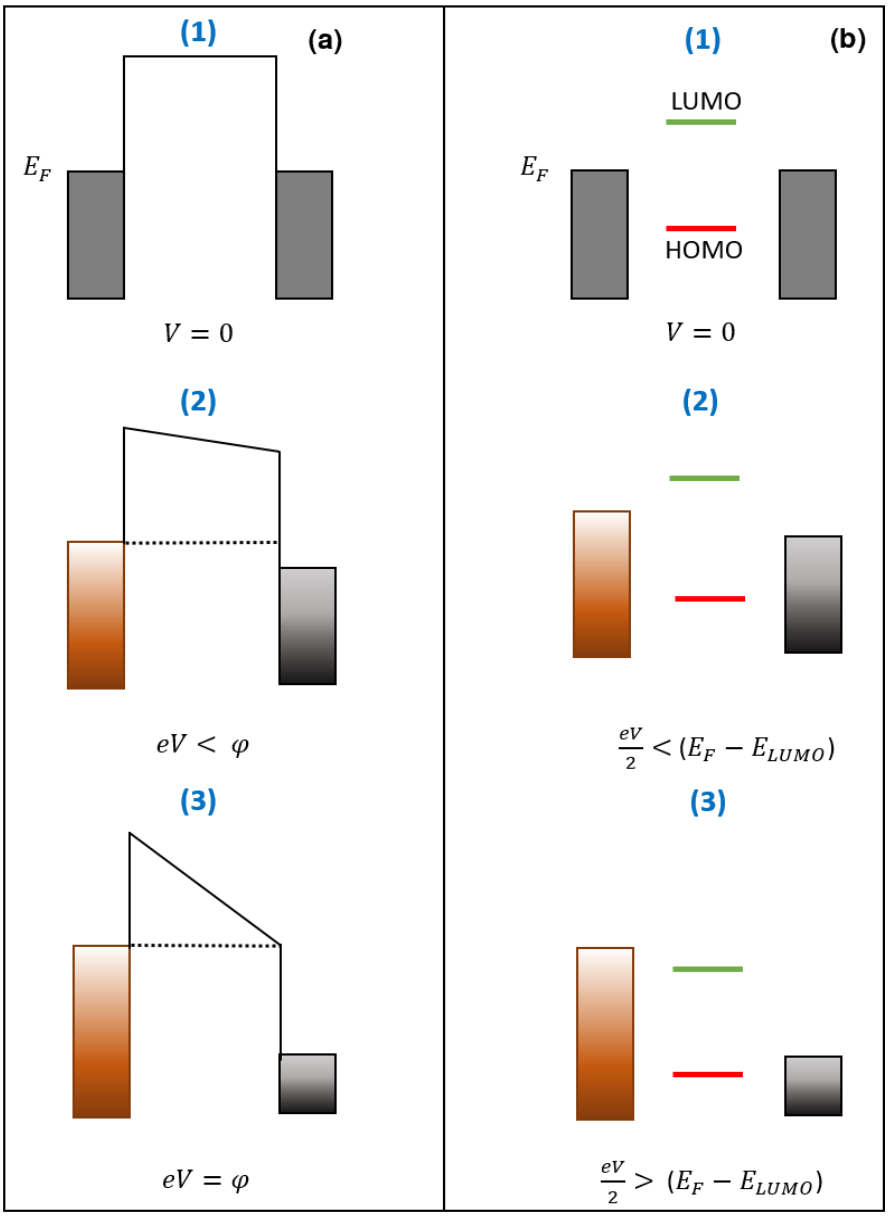

Figure 7.3 (a, 1-3) *Simmons modelling to describe the tunneling transport through the molecule where a molecule is depicted as a tunnel barrier of height φ and length d. Upon application of bias, barrier is tilted, case-2. When applied bias is greater than or equal to φ, barrier is getting triangular, case-3 and electrons are tunneling like field emission.* ***(b, 1-3)*** *Coherent tunneling model for molecular transport where molecular levels are broadened by the interaction with the electrodes. At intermediate biases, the left and right chemical potentials open a path for transport of size eV, case-2. The current increases dramatically when a level is within the bias window (case-3, resonant tunneling).*

$$\ln\left(\frac{I}{V^2}\right) \propto \ln\left(\frac{I}{V}\right) - \frac{2d\sqrt{2m_e\varphi}}{\hbar} \tag{7.5}$$

Here, plot of $ln(I/V^2)$ vs. $1/V$ yield a logarithmic growth in the low-bias regime. When the applied voltage is closer to the barrier height, the mechanisms compete. Hence, a transition from

logarithmic growth to linear decay is occurred and this change of slope leads to a minima in the plot of $\ln(I/V^2)$ as a function of $(1/V)$. The voltage corresponding to the transition of barrier shape from trapezoidal to triangular is referred as V_{trans} and is commonly known as transition voltage. Note that, measurement of V_{trans} is an estimation of height of the original rectangular barrier. It is not the exact height of the barrier as **Equation (7.1)** does not explicitly account for voltage drops at the contacts or the image potential of the tunneling electron. Measurements of V_{trans} for a variety of molecular systems[195] scales linearly with the energetic off set between the metallic Fermi level and nearest molecular orbital. This linearity demonstrate the importance of V_{trans} which is related to the position of nearest molecular orbital from the metallic Fermi level. However, experimentally obtained V_{trans} for alkanethiol molecules with increasing length is found to be independent of molecular length which is inconsistent with Simmons modelling[197]. Incorporation of image potential in the Simmons modelling approach is not helpful to explain it. Then, a most common picture of molecular junctions is considered based on the coherent transport pictures of molecular levels, Lorentz broadened by the coupling at the leads and is located above and below the Fermi level (sketched in **Figure 7.3b**). The fundamental contrast lies in their potential profile. In case of Simmons model, potential decreases linearly with the distance whereas for molecular model, potential drops entirely at the contacts. Within the framework of Landauer formalism of coherent tunneling, transport through the molecular junction is described by a transmission function and can be written as,

$$T(E) = \frac{\eta(1-\eta)\Gamma^2}{\Gamma^2/4 + (E-\varepsilon)^2} \tag{7.6}$$

Where Γ is the total broadening due to coupling between metal and molecules, η is the asymmetry of coupling and ε is the energy of the nearest molecular orbitals (either HOMO or LUMO). Current $I(V)$ can be calculated (also shown in the **Section 2.3**, **Chapter 2**) as,

$$I = \frac{2e}{h}\int_{-\infty}^{+\infty} T(E)\{f_1(E) - f_1(E)\}dE \tag{7.7}$$

Where $f_{1,2}(E) == (\exp(\big(E-\mu_{1,2}\big)/K_BT) + 1)^{-1}$ is the Fermi function for temperature T at the left ($\mu_1 = +eV/2$) and right ($\mu_2 = -eV/2$) electrode respectively. In case of alkanes, zero bias conductance decays exponentially with length and this corresponds to a reduction in the transmission value at the Fermi level and is described by,

$$T(E = E_F) \propto \exp(-\beta d) \tag{7.8}$$

Where β is the decay constant which depends on the conjugation of the considered molecule. This length dependent transmission is expected to happen due to length modified metal-molecule interface because energy level of alkanes is independent of molecular length. Length dependent metal molecule coupling can be written as,

$$\Gamma\,(d) \approx \frac{(E_F - \varepsilon)}{\sqrt{\eta(1-\eta)}} \exp(-{}^{\beta d}/_{2}) \tag{7.9}$$

Now, we have the length dependent transmission,

$$T(E,d) = \frac{1}{\frac{1}{4\eta(1-\eta)} + \left(\frac{E-\varepsilon}{E_F - \varepsilon}\right)^2 \exp(\beta d)} \tag{7.10}$$

Inserting **Equation (7.10)** into **Equation (7.7)** current voltage characteristics and so also, V_{trans} can easily be calculated. Remarkably, calculated V_{trans} is proportional to the energetic off set (i.e., difference between metallic Fermi level and nearest molecular orbital) and also it is independent of molecular length for $d > 8$ Å which is in good agreement with the experimental observation. So, the interpretation of TVS valid within the framework of a coherent tunneling model of molecular junctions instead of Simmons like pictures which are inconsistent with observations on molecular junctions. Overall, this measurement provides an alternative method to determine the apparent height of the tunneling barrier in molecular junctions and shifts in the transition voltage serve as an indication for shifts in the energy of the molecular levels that dominate electron transport and/or systematic variations in their coupling to the continuum states of the electrodes (i.e., electrode-molecules coupling)[141,200].

Thus, we taken into account transition voltage spectroscopy (TVS) analysis to gain further insight about the energy level shifts due to mechanical manipulation. **Figure 7.4a-b** are typical FN plots for Ag/ferrocene junctions for type 1 and 2, respectively at different interelectrode displacements. Focusing on the right side of **Figure 7.4a-b**, in the low bias regime (large$1/V$), a logarithmic dependence with a positive slope is the characteristics of direct tunneling ($V < \varphi/e$; φ being the barrier height between an electrode Fermi level of the electrodes and the closest molecular energy level that dominates electronic transport), as illustrated in **Figure 7.3b**, case-2. Whereas, in the high bias regime (small $1/V$) a linear dependence with a negative slope in **Figure 7.4a-b** implies that the transport is dominated by a Fowler-Nordheim tunneling, for $V > \varphi/e$, illustrated in **Figure 7.3b**, case-(3). **Figure 7.4a-b** show a clear characteristic minima, with a corresponding

transition voltage. The response of the transition voltage to changes in the displacement is observed in the insets of **Figure 7.4a-b** where a shift is seen for type 1 but not for type 2 (see **Figure 7.9** and **Figure 7.11**, similar data for other junction realizations). We can take advantage of the presence of peaks in the dI/dV that correspond to molecular levels to shed light on the relation between transmission voltage shifts and molecular level shifts. When the interelectrode displacement is reduced by 0.6 Å, the transition voltage shifts by $370\ mV$. Assuming for simplicity a symmetric voltage drop on each electrode-molecule contact, which can be justified as a crude approximation by the roughly symmetric locations of the positive and negative peaks in **Figure 7.2c**), the $690\ mV$shift in the examined peak location in **Figure 7.2c** corresponds to a shift of $(690/2) = 345\ mV$ of the molecular levels that dominate the electron transport. Note that for a symmetric voltage drop, the location of the transporting molecular levels with respect to the electrode Fermi level is given by half the voltage at which a peak in the dI/dV curve appears (this is illustrated below with the aid of calculated transmissions and dI/dVcurves). We can conclude that the observed mechanical gating leads to shifts in the transition voltage that are rather similar

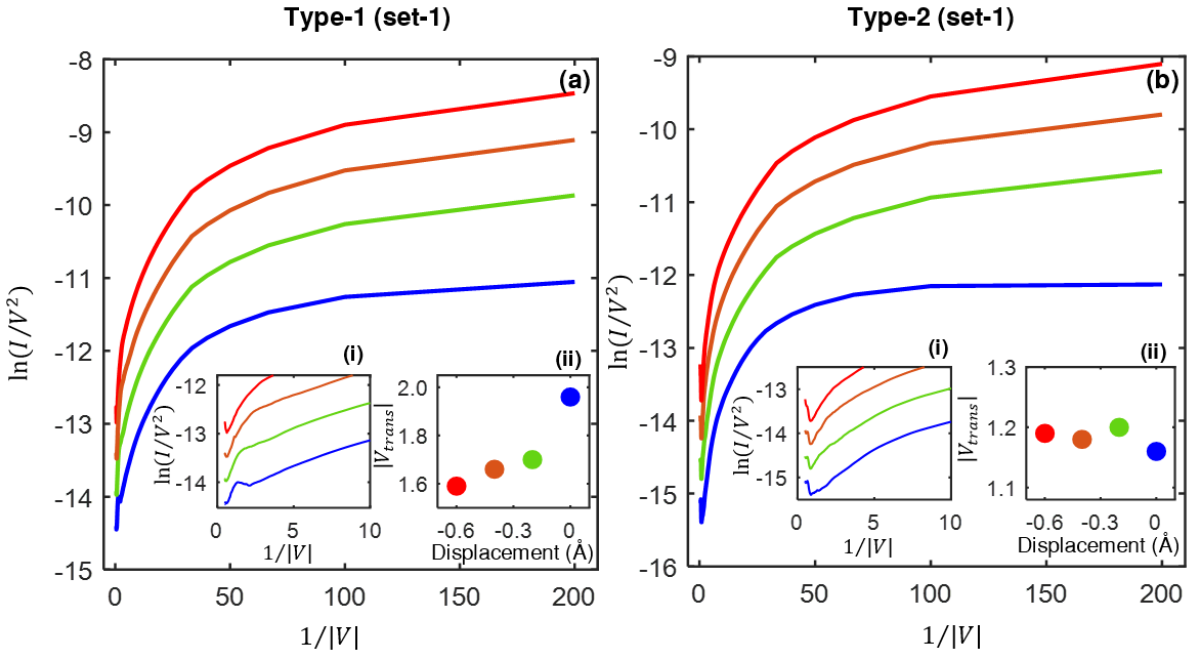

Figure 7.4 (a, b) *Fowler-Nordheim (FN) plots constructed from the same $I-V$ spectra presented in* ***Figure 7.2a-b****, showing $ln(I/V^2)$ versus $1/|V|$ for spectra with (a, type 1) and without (b, type 2) mechanical gating response. For consistency, the negative side of the $I-V$ curves is used for FN plots. Insets (i): Zoomed view of the FN plots to better visualization of the change of transition voltage upon squeezing. Insets (ii): Transition voltage, V_{trans} (absolute values) as a function of interelectrode displacement for type 1 and 2.*

in magnitude to the roughly estimated shifts in the molecular energy levels. Our findings therefore show that TVS is a good indicator for level shifts in the examined junction.

7.2.4. Theoretical calculations[4]

To probe the nature of type 1 and 2, we turn to density functional theory (DFT) and electron transport calculations, as depicted in **Figure 7.6**. For the range of interelectrode displacements that is considered in the experiments the molecular junction can adapt, according to the calculations, two distinct stable configurations with parallel and perpendicular molecular orientations with respect to the electrode axis, as illustrated in the **Figure 7.5a-d**. The calculated total energy as a

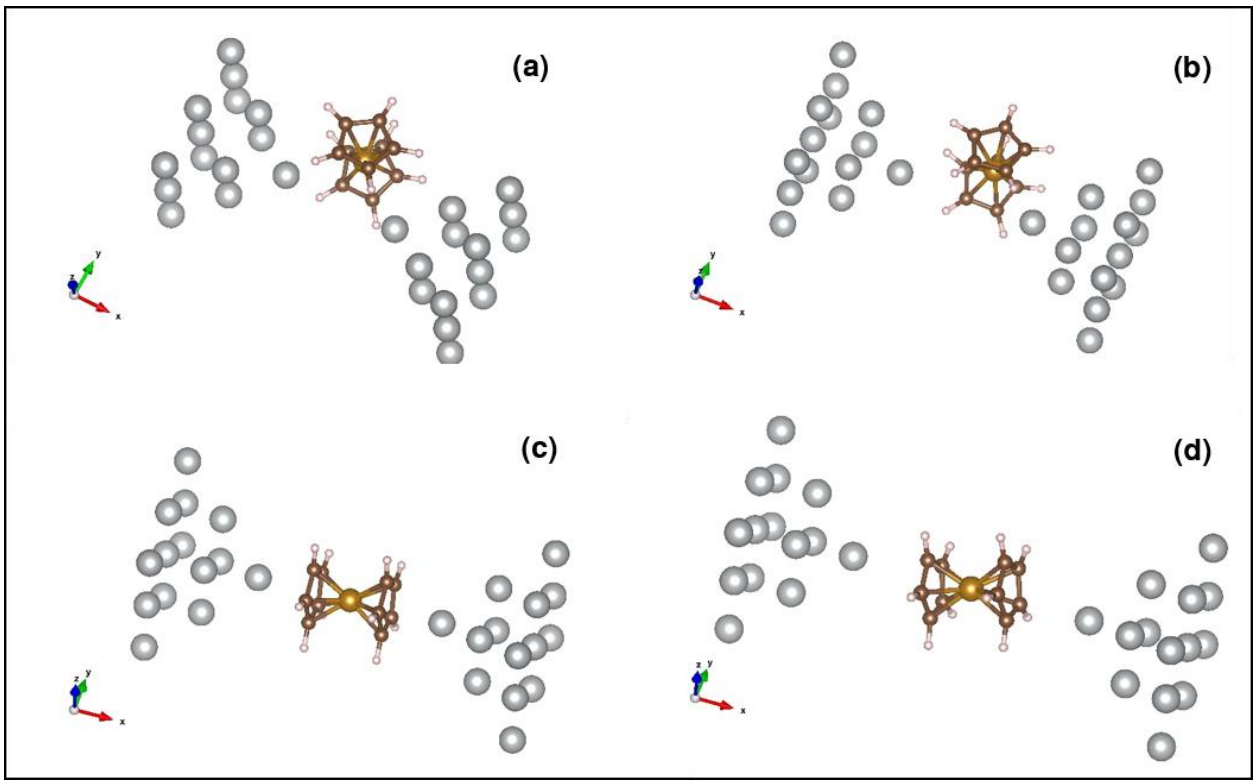

Figure 7.5 (a-d) *Relaxed structures. Perpendicular molecule orientation with respect to the electrode axis: (a) d*=5.2 Å *(b) d*=6.2Å*. Parallel molecule orientation: (c) d*=8.1 Å *(d) d*=9.8Å*.*

function of interelectrode displacement is presented in **Figure 7.6f** for each one of these junction configurations. The two energy curves have a clear minimum at different interelectrode separations. At short interelectrode displacements, the perpendicular configuration is energetically preferred, while for longer displacements the parallel configuration is more stable. A similar behavior was also reported for Ag/Vanadocene/Ag junctions by Pal et al.[84].

[4] Theoretical calculation is performed by Jakub Šebesta and Richard Korytár.

Figure 7.6a-b provide the calculated transmission for various interelectrode displacements for the two configurations. The transmissions for the parallel configuration can essentially be understood as being rigidly shifted toward lower energies upon mechanical squeezing. Namely, a mechanical gating is observed[191]. Below the Fermi energy (taken as zero) pairs of narrow resonances can be seen, while above the Fermi energy a single broad resonance is found. Its peak transmission is 2, pointing to a two-channel or two-orbital origin. The transmissions for the perpendicular configuration have a richer structure, with narrow peaks on both sides of the Fermi energy. Also, the evolution of transmission as a function of stretching is more complex in this case than for the parallel molecular configuration. However, in contrast to the former case, no clear shifts in the transmission peaks are observed when the interelectrode displacement is changed in the given range. Thus, mechanical gating is not found for the perpendicular configuration. We note that in both configurations the transmission resonances are highly asymmetric due to quantum interference[10], similarly to the asymmetries reported for molecular junctions based on a ferrocene derivative[157].

To have a more transparent comparison with the measured data, the described transmission can be directly converted to calculated differential conductance, as presented in **Figure 7.6c-d**, assuming a similar voltage drop across the two electrode-molecule contacts. When the molecule is oriented in parallel to the junction axis, mechanical gating is seen, as was found in the experiments for type 1. However, for the perpendicular molecular orientation a similar effect cannot be found, in agreement with the absence of mechanical gating in the measurements of type 2. Note that the features in **Figure 7.6c-d** are sharper than found in the measured spectra in **Figure 7.2c-d**, since the experimental data is widened by the finite temperature and mainly by the lock-in modulation used for differential conductance measurements.

Figure 7.6e reveals charge transferred from the electrodes to the molecule in equilibrium as a function of interelectrode displacement. The slope is larger in the parallel junction, suggesting that charge reorganization plays an important role in the gating mechanism. The mechanical gating response for the parallel molecule configuration and the absence of this effect for the perpendicular configuration can be ascribed to the orientation of the molecular orbitals that dominate transport with respect to the electrodes, and their coupling to the frontier electrode states. **Figure 7.7** presents calculated isosurfaces of the two degenerate lowest unoccupied molecular orbitals (LUMOs) for an isolated ferrocene, as well as the LUMOs for the parallel and perpendicular junction

configurations (calculations were done for a cluster of a single molecule bridging two metal

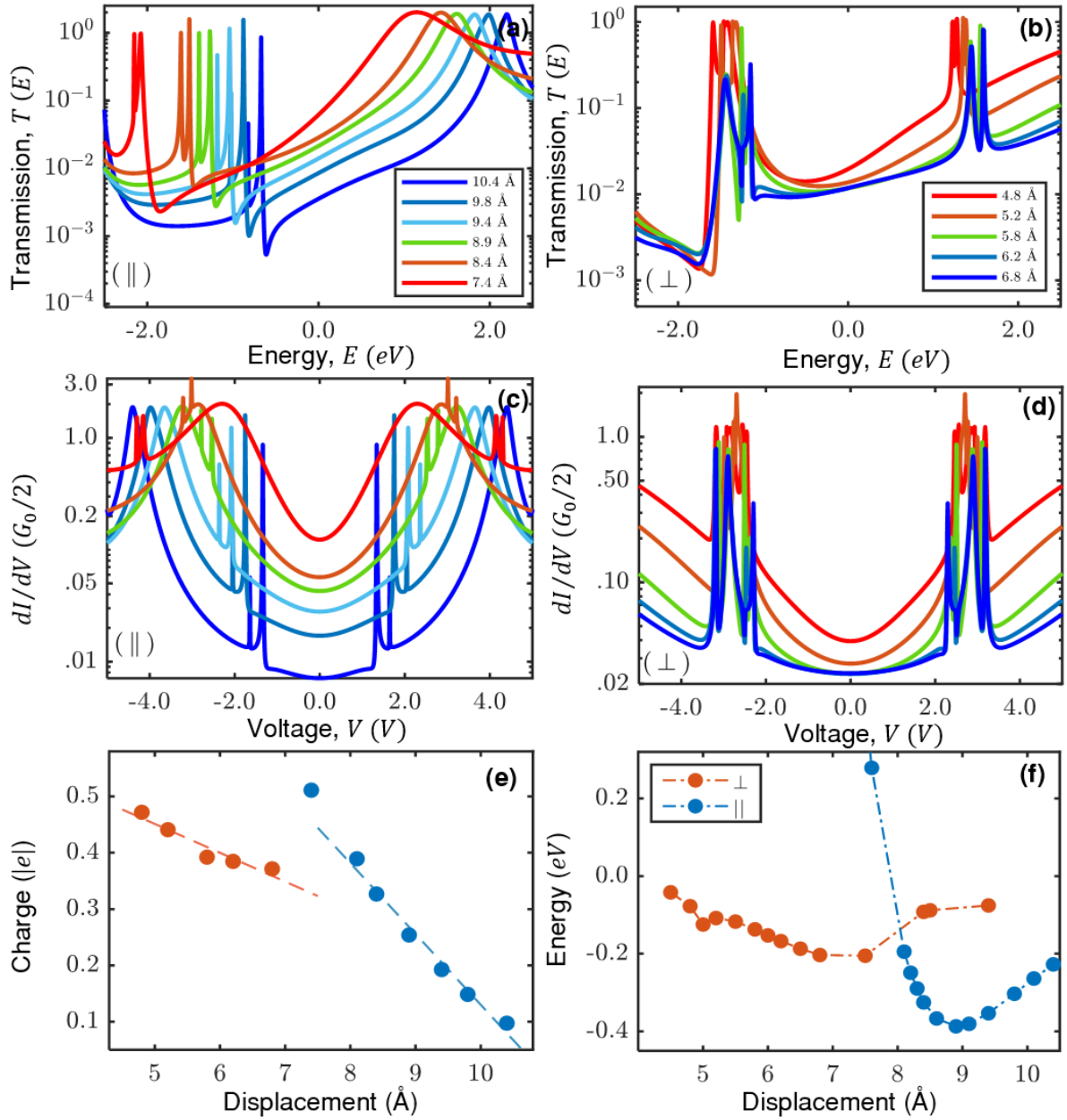

Figure 7.6 (a, b) *Transmission function for parallel (a) and perpendicular (b) molecule orientations in the junction at a varying inter electrode displacement between the electrode tips.* ***(c, d)*** *Differential conductance spectra of the parallel (c) and perpendicular (d) configurations at the same varying inter electrode displacement as in a and b.* ***(e)*** *Charging of the ferrocene molecule in the parallel (blue) and perpendicular configurations (orange).* ***(f)*** *Total energy as a function of interelectrode displacement. (⊥, ∥) denote perpendicular and parallel molecular orientation with respect to the long junction axis.*

apices). As can be seen, the junction LUMOs, which are associated with the broad transmission peak above the Fermi energy in the parallel configuration, and the two narrow peaks above the

Fermi energy in the perpendicular configuration, resemble the LUMOs of the isolated molecule. These orbitals have a significant π-character on the carbon rings, i.e., the wave function spreads away from the ring plane perpendicularly[201]. The remaining contribution to the LUMOs comes from the Fe 3*d* atomic orbitals. Therefore, the molecular LUMOs overlap with the electrodes much more efficiently in the parallel configuration than in the perpendicular configuration. This difference makes the LUMO coupling to the frontier electrode states in the parallel configuration more sensitive to changes in the interelectrode displacement (seen in **Figure 7.6a** as a different width of the broad LUMO peak for different interelectrode displacement) than in the perpendicular case. Thus, the orientation of the LUMO with respect to the electrodes affects the mechanical gating efficiency: When the electrodes are pointing to the less-localized part of the LUMO on the carbon ring, mechanical manipulations likely induce orbital modifications and associated charge transfer. In contrast, when the electrodes are pointing towards the more localized part of the LUMO on the Fe ion, mechanical manipulation has a reduced effect on the local orbital structure and the associated charge redistribution. These findings illustrate that molecular orientation, as well as the distribution of molecular orbitals in space are important parameters for the design and control of mechanical gating in molecular junctions and generally for mechanically-induced charge transfer in metal-molecule interfaces. Interestingly, based on our analysis, efficient mechanical gating is promoted by delocalization of transporting molecular orbitals that point towards the electrodes, while for electrostatic gating in single molecule transistors, efficient gating by a gate electrode is

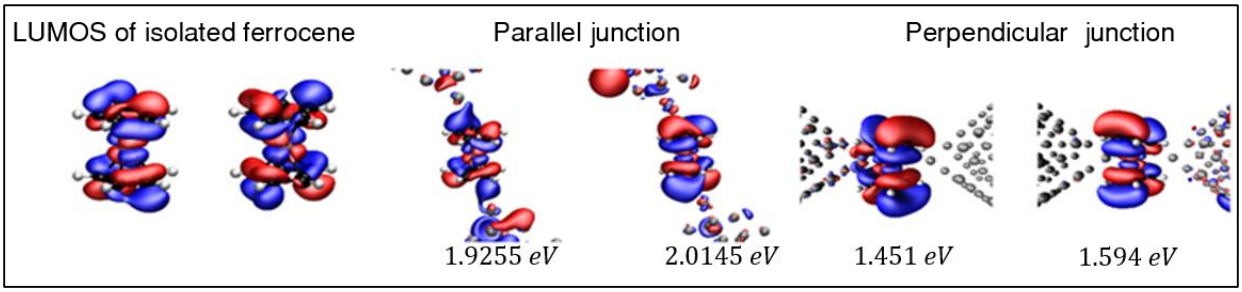

Figure 7.7 *Left: Isosurface plots of the two LUMOs of an isolated ferrocene (degenerate). Center and right, respectively: Isosurface plots of selected electron wave functions of the Ag/ferrocene/Ag junction and their energies (with respect to Fermi energy) for the parallel and perpendicular configurations (at interelectrode separations of* 9.81 Å *and* 6.2 Å*, which correspond to the blue curves in* ***Figure 7.6a-b****). These energies lie in the immediate vicinity of the unoccupied transmission resonances. The plots also contain ball and stick models of the structures (color coding of the atoms: white (H), black (C), pink (Fe) and silver (Ag)). All isosurfaces contains* 93% *of the wavefunction.*

often promoted by more localized orbitals on the molecular bridge, with a rather low coupling to the electrode states.

7.3. Conclusion:

To conclude, we showed by experiments and calculations that mechanical gating of molecular junctions depends on the orientation of the molecule in the junction. In the extreme demonstrated case, the same molecular junction either experience mechanical gating or not, depending on the molecule orientation with respect to the electrodes, as well as on the nature of the interaction between the molecular orbitals and the continuum states of the electrodes. These findings emphasize the importance of geometry and local orbital structure in the context of charge transfer across metal-molecule interfaces and point towards a way to control mechanical gating of charge, spin, and heat transport in molecular junctions.

7.4. Appendix figures:

Current-Voltage characteristics, Differential conductance spectra and Transition Voltage spectroscopy analysis of few other junction realizations with (type-1) or without (type-2) mechanical gating.

(i) Type-1

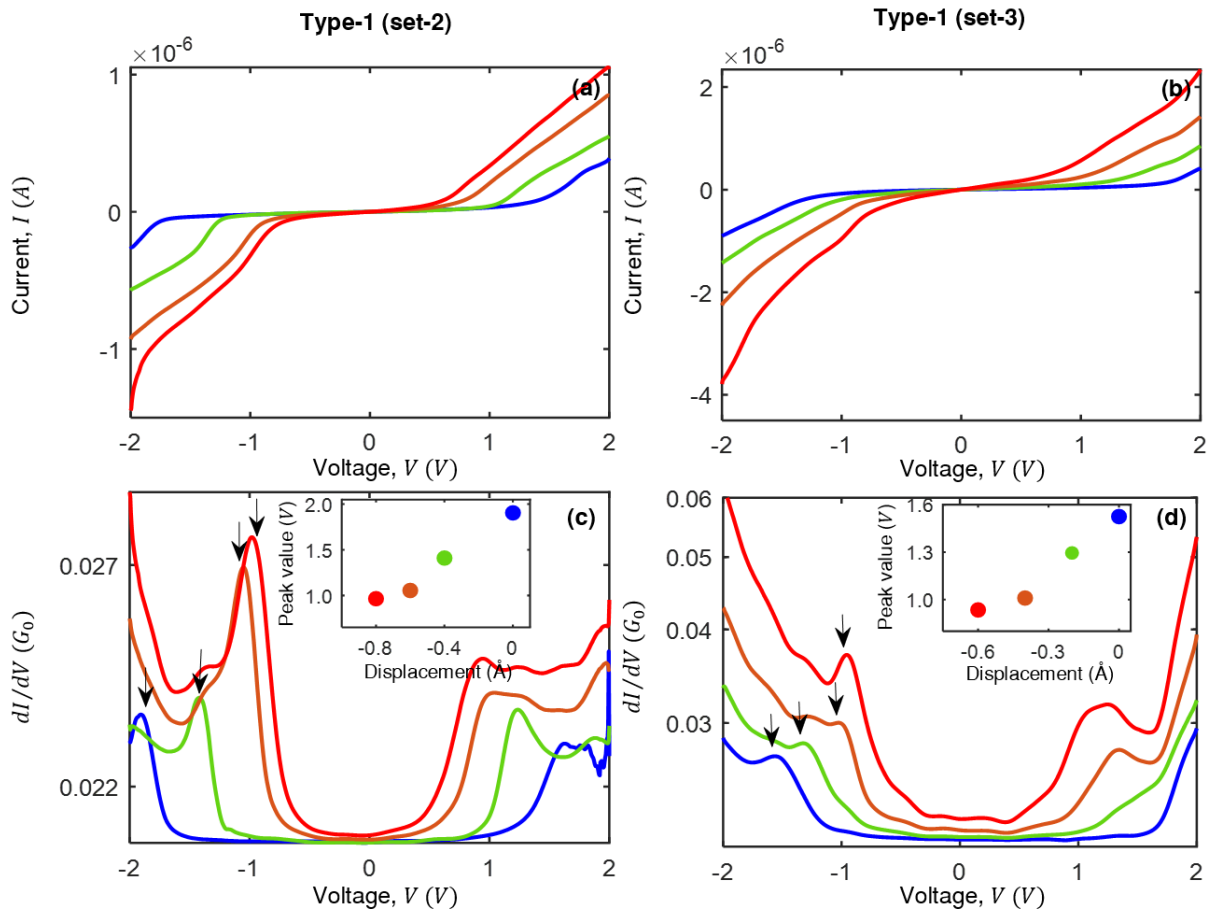

Figure 7.8 (a, b) *Current vs. voltage spectra at different interelectrode displacements in Ag/ferrocene junctions with mechanical gating response (type 1).* ***(c)*** *Differential conductance vs. voltage for the junction studied in a.* ***(d)*** *Same as c but with data collected for the molecular junction studied in b. Insets (c, d) Absolute values of peak position (marked with arrows in c, d) vs. interelectrode displacement.*

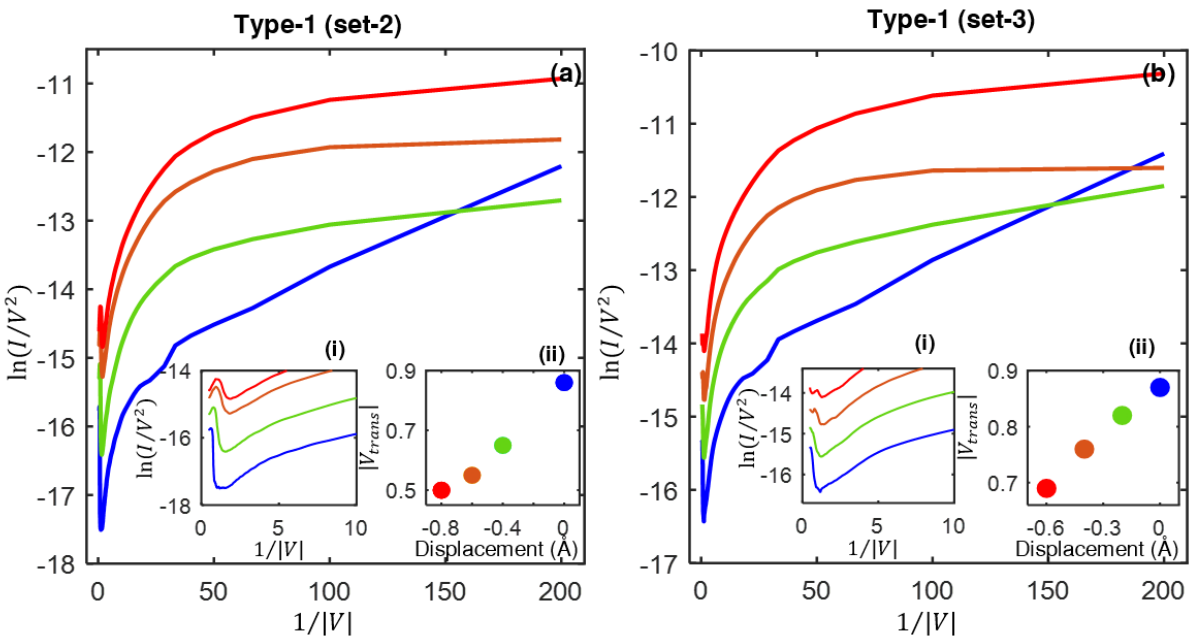

Figure 7.9 (a, b) *FN plots constructed from the same $I-V$ spectra presented in* ***Figure 7.8a-b****. For consistency, the negative side of the $I-V$ curves is considered for TVS analysis. Insets (i): Zoomed view of the TVS plots. Insets (ii): Transition voltage, V_{trans} (absolute values) vs. interelectrode displacement.*

(ii) Type-2

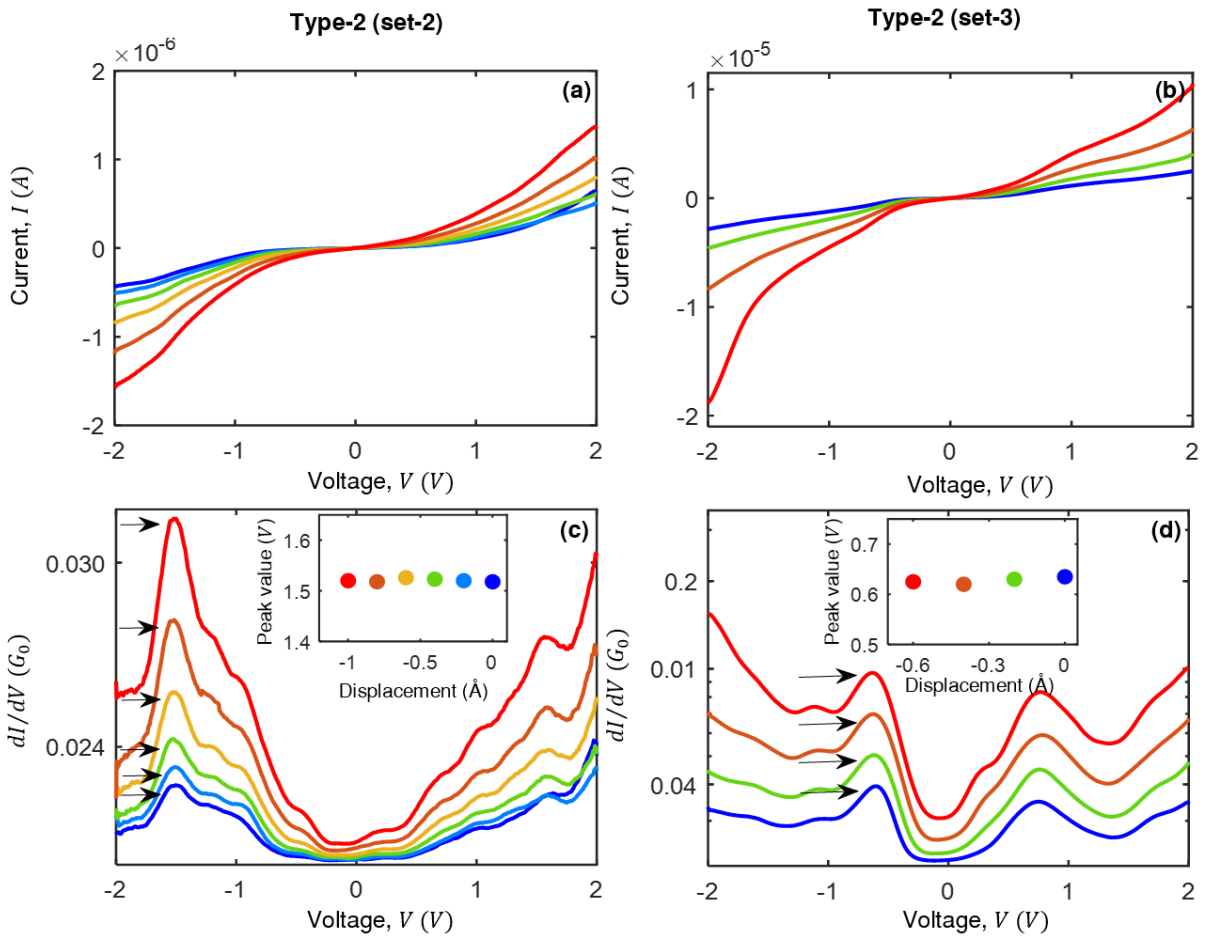

Figure 7.10 (a, b) *Current vs. voltage measured at different interelectrode displacements in Ag/ferrocene junctions without mechanical gating response (type 2).* ***(c)*** *Differential conductance vs. voltage for the junction studied in a.* ***(d)*** *Same as c but with data collected for the molecular junction studied in b. Insets (c, d) Absolute values of peak position (marked with arrows in c, d) vs. interelectrode displacement.*

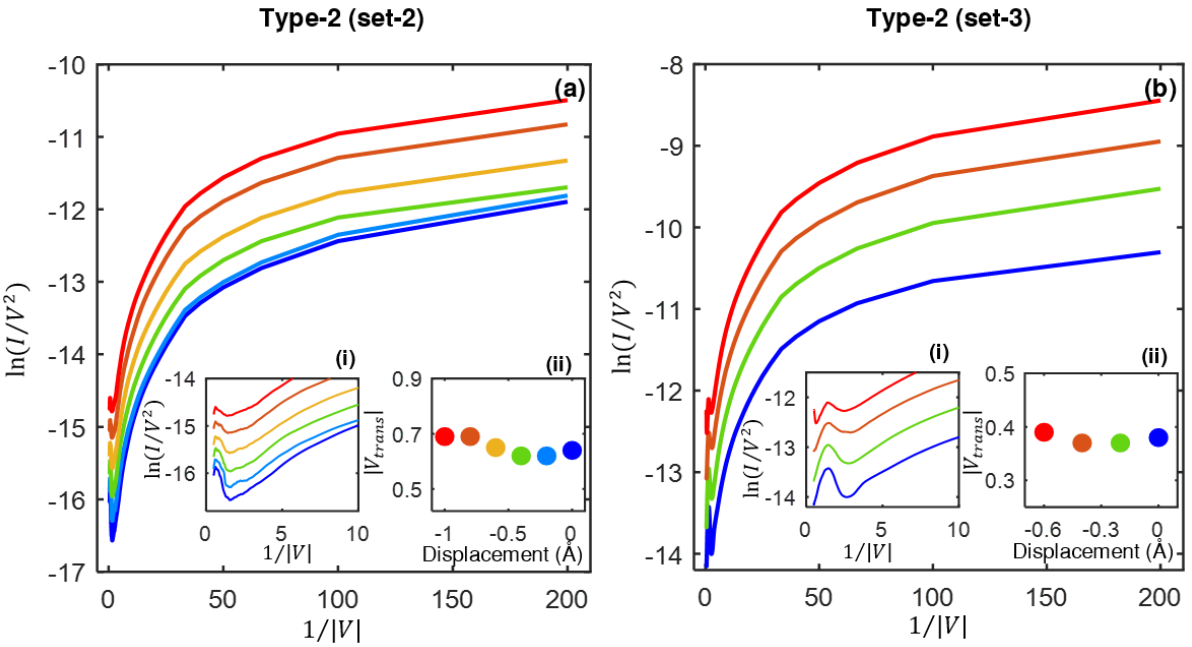

Figure 7.11 (a, b) *FN plots constructed from the same $I-V$ spectra presented in* ***Figure 7.10a-b****. Insets (i): Zoomed view of the FN plots. Insets (ii): Transition voltage, V_{trans} (absolute values) vs. interelectrode displacement.*

Chapter 8 | Formation of copper atomic chain in hydrogen atmosphere

The transport properties of the copper atomic junction following the insertion of hydrogen molecule are the topic of this chapter, which also establishes the creation of a hydrogen-decorated copper atomic chain of more than 1 nm having a conductance as low as $0.001\ G_0$.

8.1. Introduction:

Electrical wire with the smallest possible dimension that one can guess would consist of an array of metallic atoms. Such an array of atoms or in one word chains, being perfect one dimensional system, offers a unique opportunity to understand various fascinating phenomena including atomistic magnetism[202–206], nanoelectromechanics[207,208] and most importantly, quantum mechanical behavior in one dimension[41,73,216,217,92,209–215]. Successful formation of atomic chain is regularly observed in break-junction experiments upon pulling the late 5d metallic contacts such as Au, Pt and Ir[35–37,39,41], in contrary to 3d or 4d metals such as Ag and Cu[38,40]. Theoretical calculation[38,40,218] identifies a common origin to describe the chain formation of metal atoms via reconstruction of low-index surface due to enhanced relativistic effect on electronic structure[104]. On the other hand, systemic investigations reveal an impressive observation that foreign impurities e.g., H_2, O_2, N_2, H_2O, D_2 can stabilize and elongate[103,219–221] the metallic junction and even, atomic chain of 3d and 4d metals can be formed with support of these external molecules[43,47,49]. Extensive study on the impurity induced chain formation establishes the formation of metal atomic chain for Ag/O_2 (0.1 G_0)[43,47,49], Cu/O_2 (0.1 G_0)[49], Cu/N_2 (0.86 G_0)[46], Pd/H_2 (1.0 G_0 and 0.5 G_0)[42], Pd/H_2O (1.0 G_0)[44], Co/H_2 (1.0 $G_0$and 0.2 G_0)[48], Fe/D_2 (1.0 G_0 and 0.25 G_0)[45] and Ni/D_2 (1.0 G_0)[45] systems. Notably, the observed conductance value of these impurity induced chains are limited in the range of 1.0 G_0 – 0.1 G_0 having mostly a single conductance plateau, despite only a mention of stepwise decrease of tunneling conductivity for hydrogen embedded gold nanowires[219]. In addition, due to the presence of the molecules having vibrational degrees of freedom, the conductance of the chains is modified due to electron-vibration interaction. Inelastic electron spectroscopy (IETS) serves as a transport-based probe to determine vibrational modes in the molecular junction and several unusual features or anomalies in the differential conductance were found in these systems. Despite few reports, the complete understanding of formation, evolution and the electron-vibration interaction of these impurity induced chains is still lacking.

In the present chapter, we focus on two different atomic junctions of Cu and Al, in the presence of hydrogen molecules and look for the possibilities of atomic chains based on the experimentally observed transport features. Previous experiments[222–224] with Cu atomic contact in presence of hydrogen molecule confirms that hydrogen molecule can be contacted between the atomistic Cu electrodes. According to the experimental observation[222] , asymmetric contact of $Cu/H_2/Cu$

junction is ensured by theoretical calculation[225,226] with no indication of hydrogen aided copper atomic chain[222,223]. Our findings demonstrate that there are even more possible configurations for

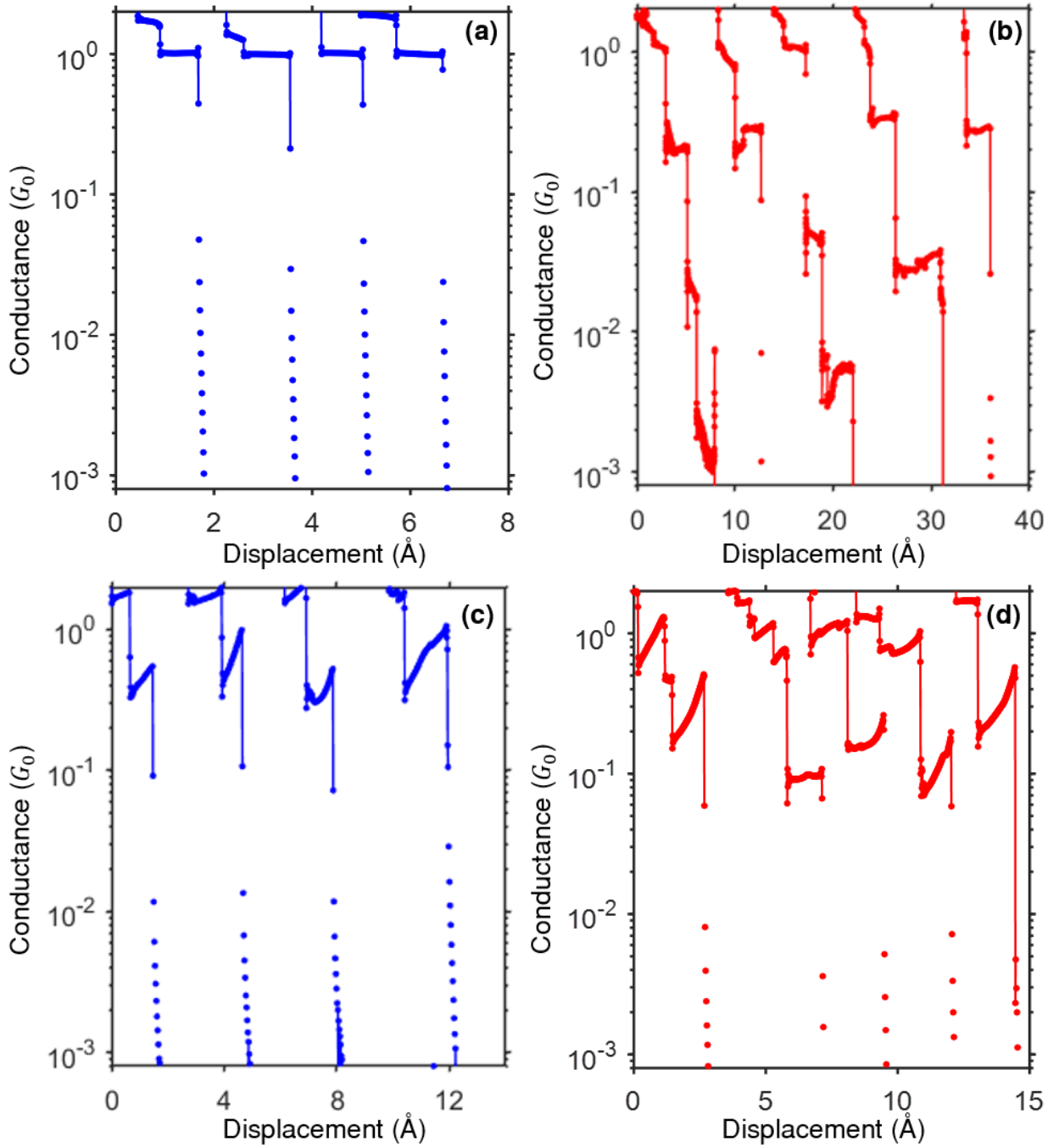

Figure 8.1 (a, b) *Example of conductance displacement breaking traces of copper atomic junction before (a-blue) and after (b-red) introduction of hydrogen molecules, recorded at* 50 *mV bias voltage with traces shifted in the displacement axis for clarity.* ***(c, d)*** *Similar characterization of aluminum atomic junction before (c) and after (d) introduction of hydrogen molecules.*

Cu/H_2 system in the tunneling conductance regime, in addition to the former configuration with

conductance value $\sim 0.2\ G_0$[222–224]. Three stable configurations of hydrogen decorated Cu atomic chains are identified, which is indeed a remarkable observation and may uncover further understanding regarding the phenomena of metal atomic chains in collaboration with external molecules. Moreover, we are herein for the first time reporting the possibility of physically stable structures with extremely low conductance value ($\sim 0.001\ G_0$) in an impurity induced metallic junction. In contrast, we observe only one configuration in Al/H_2/Al junction, without any chain formation. Furthermore, inelastic electron tunneling spectroscopy (IETS) is employed to identify the vibrational signature of Cu/H_2 and Al/H_2 junctions along with its response to the mechanical manipulation.

8.2. Results and discussions:

8.2.1. Conductance traces and histograms

Experiments are performed using a custom designed cryogenic insert based on mechanically controllable break junction technique at cryogenic environments ($\sim 4.2\ K$). Conductance of Copper (Cu) and Aluminum (Al) atomic junctions with or without hydrogen molecule are recorded as a function of inter electrode displacement during each breaking sequences. After each breaking event, junction is recontacted to a conductance $> 100\ G_0$ and this process is repeated several times to address the junction's characteristics statistically. **Figure 8.1a** and **b** display the representative

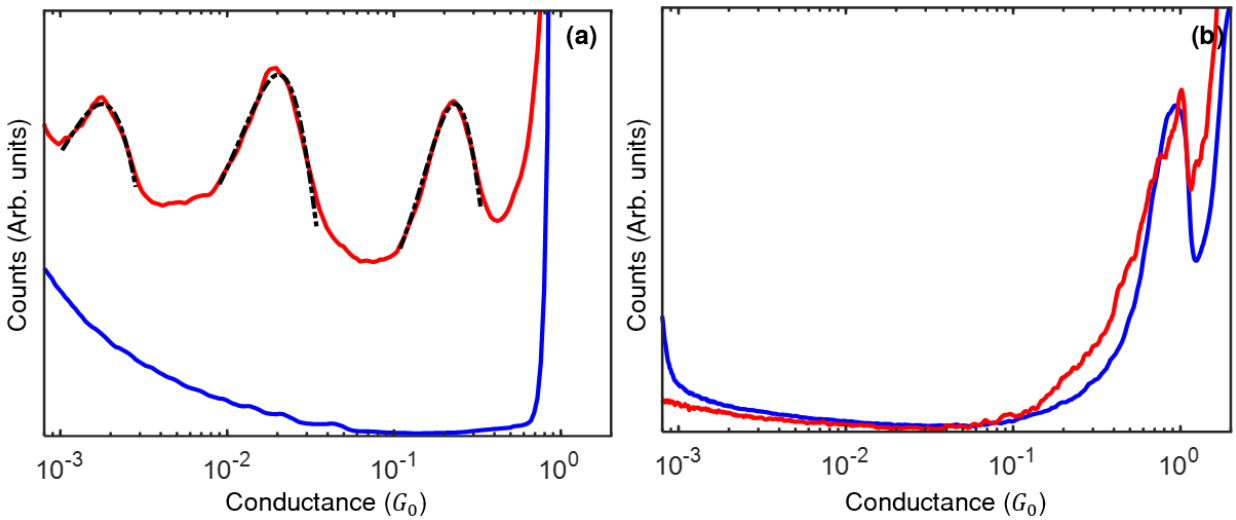

Figure 8.2 (a) *Conductance histogram of copper atomic junction before (blue) and after introduction (red) of hydrogen molecules, prepared from* 5000 *and* 9400 *consecutive conductance displacement traces using* 50 *bins per decade. Black dash dotted line of the histogram presents the Gaussian fitting of the corresponding conductance peak (P-1, P-2 and P-3).* ***(b)*** *Same as a for aluminum junction considering* 20000 *and* 6000 *traces.*

conductance displacement breaking traces of Cu and Al atomic junctions in semi logarithmic scale before (blue) and after (red) insertion of hydrogen molecules, respectively. Flat conductance step i.e., plateau at the quantum of conductance ($G_0 = 2e^2/h$) is evident for Cu atomic junction (**Figure 8.1a**), whereas steps beneath G_0 with positive slopes are observed for Al junction(**Figure 8.1c**)[51,227]. It is important to note that characteristics of this plateaus are determined by the intrinsic chemical valence of respective metals[51]. Distinct evolution of Cu and Al atomic junctions is more pronounced in hydrogen environment as shown in **Figure 8.1b** and **Figure 8.1d**. In presence of hydrogen, subsequent plateaus of conductance value from $\sim 0.3\ G_0$ to $0.001\ G_0$ are appearing in case of Cu junction (**Figure 8.1b**), whereas conductance plateau of Al/H_2 junction (**Figure 8.1d**) can be at lowest$\sim 0.1\ G_0$. Interestingly, unusual plateaus with positive slope for Al junction even persists in presence of hydrogen[228,229]. The presence of molecule, both for Cu and Al junction, is

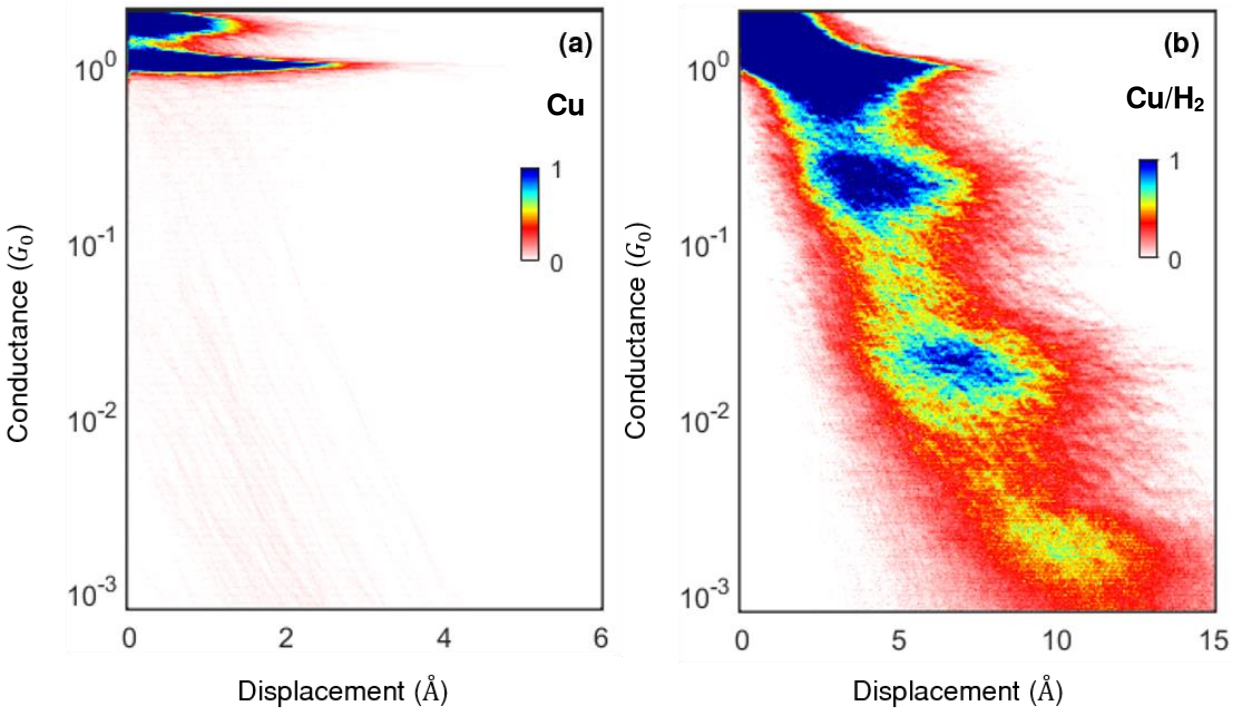

Figure 8.3 (a, b) *Conductance displacement histogram of copper atomic junction before (a) and after (b) insertion of hydrogen molecules, built from the same conductance traces of* ***Figure 8.2a*** *using* 80 *bins per decade. Conductance of the zero displacement is taken at* 2 G_0.

confirmed from the inelastic electron tunneling spectroscopy (IETS) and details of the observations will be discussed in **Section 8.2.4**. Focusing on the statistical analysis of the conductance traces to obtain the most frequently occurring configurations, **Figure 8.2** shows the conductance histograms for Cu (**Figure 8.2a**) and Al (**Figure 8.2b**) with and without hydrogen

molecules. Remarkably, three clear conductance peaks with the most probable values - (P-1): $2.31 \pm 0.02 \times 10^{-1}\, G_0$, (P-2): $2.03 \pm 0.02 \times 10^{-2}\, G_0$ and (P-3): $1.78 \pm 0.02 \times 10^{-3}\, G_0$ emerge as a consequence of hydrogen insertion in case of Cu junction (**Figure 8.2a**). Conductance value of peak, P-1, is in close resembles with the previous reports[222–224]. However, no prominent effect of hydrogen insertion for Al junction is noticed (shown in **Figure 8.2b**), albeit, with a broadening of the atomic peak at $0.78\, G_0$ along with a slight enhancement of data intensity $\sim 0.1\, G_0$ which can be the conductance signature of Al/H_2 junction. Slight enhancement of data intensity $\sim 0.1\, G_0$ can be considered to be the conductance signature of Al/H_2 junction. To get more insight, conductance displacement histogram of Cu and Al atomic junction with (**Figure 8.3b** and **Figure 8.4b**) and without (**Figure 8.3a** and **Figure 8.4a**) hydrogen molecules are considered. For

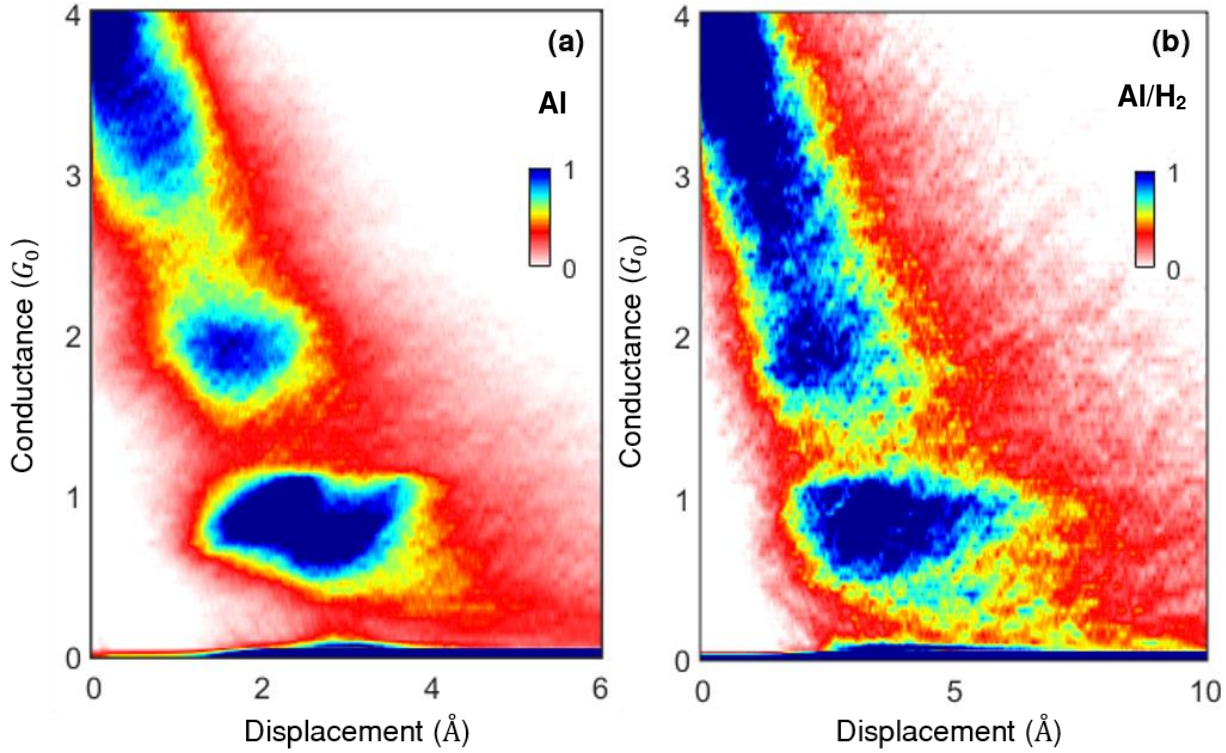

Figure 8.4 (a-b) *Conductance displacement histogram of aluminum atomic junction before (a) and after (b) introduction of hydrogen, based on the same conductance traces used in* ***Figure 8.2b*** *with* 80 *bins in linear scale.* 4 G_0 *is considered as conductance of zero displacement point.*

Al junction, histograms (**Figure 8.4**) are plotted in linear scale since the molecular conductance are high enough for better visualization unlike the Cu/H_2 junctions where order of magnitude lower conductance features are observed.. Three additional high density data clouds with maximum displacement up to ~ 14 Å of **Figure 8.3b** (compared to **Figure 8.3a**) corresponds to the three peaks of the conductance histogram of Cu atomic junction in hydrogen environment. Note that,

appearance of these peaks indicates the formation of multiple nano junctions consisting of Cu atoms and or hydrogen molecule (s) with well-defined configuration. Whereas in case of Al junction, wavy data cloud $\sim 0.8\ G_0$ (**Figure 8.4a**) is clearly observed which arises due to the increase of channel contribution during stretching and in presence of hydrogen molecule, no prominent additional data cloud is seen (**Figure 8.4b**), in line with corresponding conductance histogram.

8.2.2. Chain formation analysis

Length of the plateaus in the form of length histogram is now considered to probe the structural characteristics with stretching for both Cu and Al junction in presence of hydrogen molecules. **Figure 8.5a-b** show the plateau length histogram of Cu and Al atomic junction before (blue) and after (red) insertion of hydrogen molecules. A drastic change in the length histogram of the Cu/H_2 junction is undoubtedly evident, compared to the histogram without hydrogen (**Figure 8.5a**). Whereas, no such obvious effect of hydrogen insertion in the length histogram of Al/H_2 junction is noticed and is shown in the **Figure 8.5b.** Formation of short atomic contacts of Cu atomic

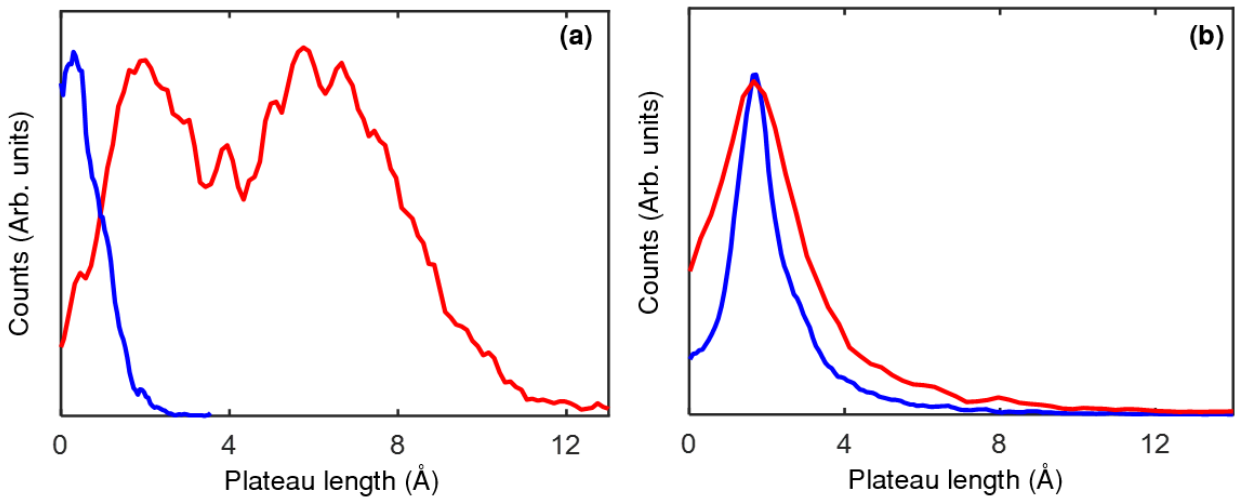

Figure 8.5 (a) *Plateau length histogram of copper atomic junction before (blue) and after (red) insertion of hydrogen molecules considering plateaus of conductance value between* $1.5\ G_0$ *to* $0.7\ G_0$ *and* $1.5\ G_0$ *to* $0.001\ G_0$. ***(b)*** *Similar histogram of aluminum junction considering conductance range* $1.1\ G_0$ *to* $0.1\ G_0$ *, both in presence and absence of molecules.*

junction is well believed, however, in hydrogenic environment Cu junction can be stretched up to 14 Å along with multiple peaks in the length histogram, which indicates the formation of Cu atomic chain in contrast to previous reports[222,223]. Height of these peaks are decreasing

exponentially after ~ 8 Å due to the lower stability of longer plateaus. Hydrogen being one of the smallest atoms, obtaining the exact bond-length from the peaks of the length histogram is not straight-forward. Ample ripples in the length histogram may corresponds to the different adsorption geometry due to uneven distribution of hydrogen and Cu atoms. Further confirmation

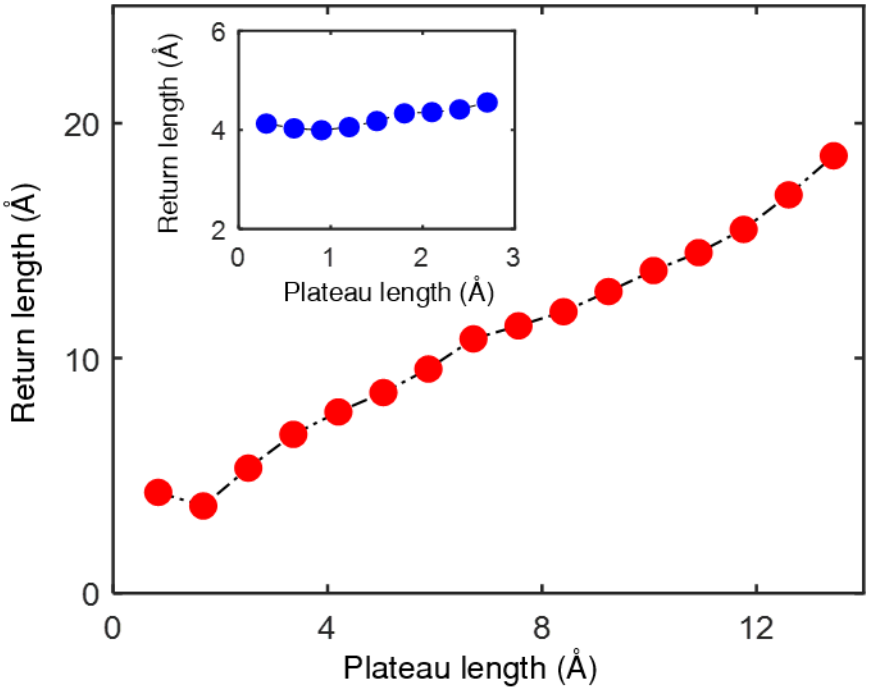

Figure 8.6 *Average return length of copper atomic junction in presence of hydrogen as a function of plateau length. Return length is defined as the amount of length required to retract back to reform the junction after breaking. Inset: Average return length of copper atomic junction as a function of plateau length.*

on the formation of hydrogen assisted Cu atomic chain is established by plotting average return length as a function of plateau length both for with (**Figure 8.6**) and without hydrogen molecule (inset of **Figure 8.6**). Return length is defined as the length over which two electrodes are needed to retract back to reestablish the junction after breaking. Average return length increases almost linearly with the plateau length even up to ~14 Å which gives a strong indication of the formation of atomic chain. An offset of around 4 Å is observed to be present and is independent on the presence of hydrogen molecule which arises due to the elastic response of the atomic banks[36,38]. Furthermore, average conductance displacement breaking trace of Cu/H_2 junction, shown in **Figure 8.7a**, reveals the three sequential steps with conductance value corresponding to the three peaks of the conductance histogram. Small wriggles of these average steps are the signature of structural reconstruction during stretching. From the average traces, it can surely be ensured that

configuration of P-2 and P-3 are responsible for the formation of longer plateaus and configuration of P-1 is limited to short atomic contact. This statement is further supported by considering conditional length histogram as shown in the **Figure 8.7b**. Length histogram taking plateaus from 1.5 G_0 to 0.08 G_0 (black i.e., only P-1) is restricted only within 5 Å, whereas longer plateaus are started to appear whenever plateaus down to P-2 (1.5 G_0 to 0.008 G_0 , light blue) or P-3 (1.5 G_0 to 0.001 G_0 , red) are included.

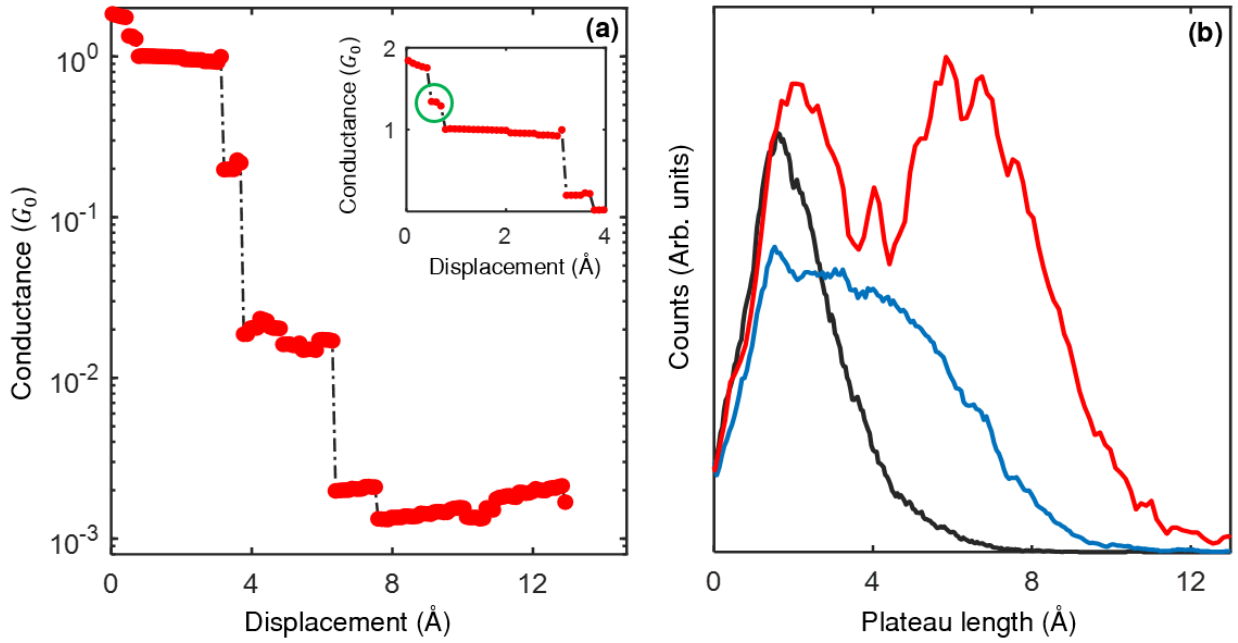

Figure 8.7 (a) *Average conductance displacement breaking trace of copper atomic junction in presence of hydrogen. Inset: Same trace in linear scale to show the precursor plateau at* 1.33 G_0*, marked by green circle.* ***(b)*** *Plateau length histogram of the same junction including plateaus of conductance value in between:* 1.5 G_0 *to* 0.08 G_0 *(black),* 1.5G_0 *to* 0.008 G_0 *(light blue) and* 1.5 G_0 *to* 0.001 G_0 *(Red).*

8.2.3. Formation and evolution of the copper/hydrogen junction

We have further extended our analysis to probe the evolution and mutual correlation among these three peaks (P-1, P-2 and P-3), observed in the conductance histogram of Cu/H_2 junction. Five different sub categories are identified (representative traces of each categories are shown in **Figure 8.8**) and conductance histogram of each categories are presented as the line plot of each block in **Figure 8.9a**, whereas histogram of all traces are shown as grey area plot just as a reference. Different categories are determined by assigning a threshold number of data points to be present in the specific conductance peak, decided from the local minima of P-1, P-2 and P-3. **Figure 8.9b**

illustrates the probability of occurrence of these five different categories in terms of pie chart where color of each sub-chart corresponds to color of the respective line plot. Absolute number of traces belongs to different subcategories with its characteristics definition summarized in **Table 8.1**.

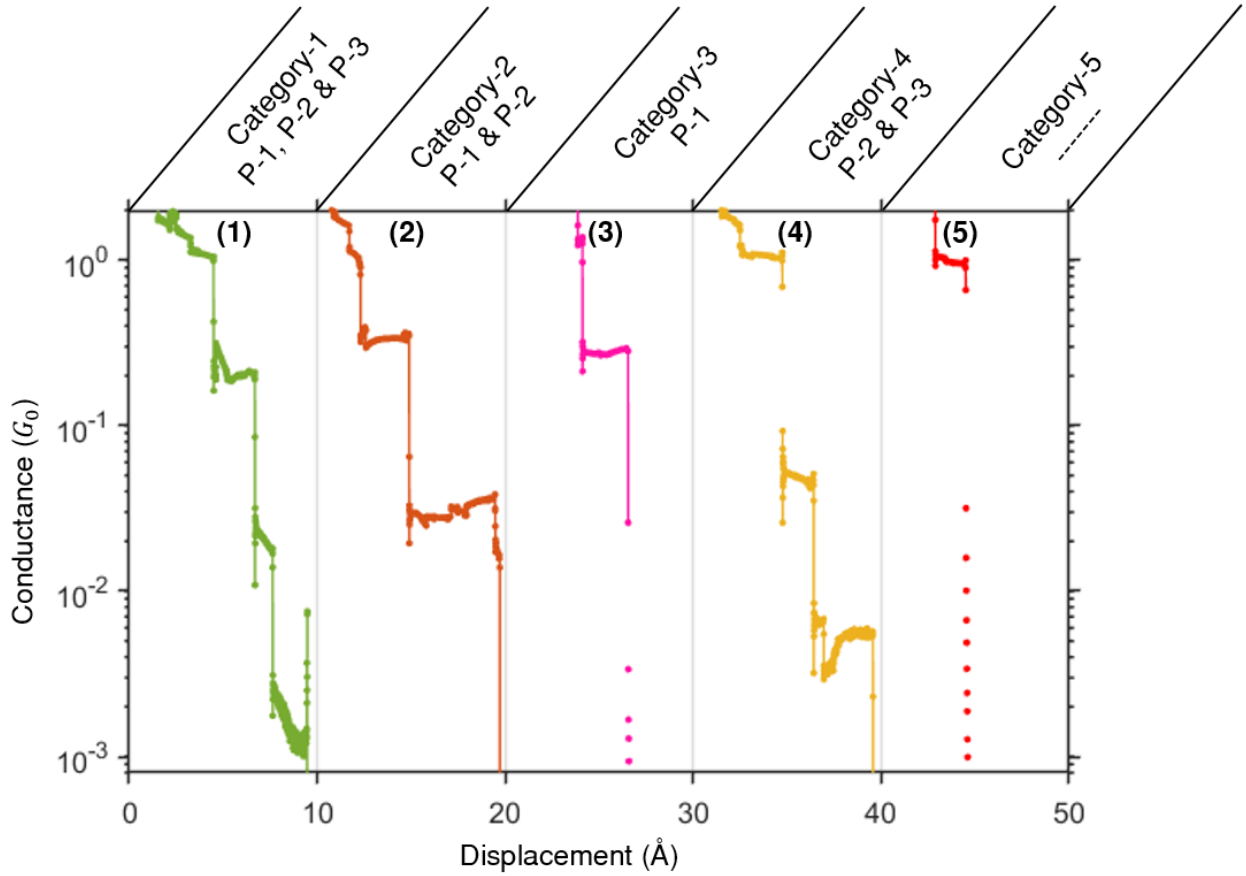

Figure 8.8 *Conductance displacement breaking traces of copper atomic junction in presence of hydrogen, where five different colors denotes the five different sub-categories, mentioned on the respective top. Sub categories are defined based on the presence of plateaus in a particular conductance peak (P-1, P-2 or P-3 on top refers to the presence of plateaus in the corresponding conductance peak). Details regarding the subcategories is summarized in* ***Table*** **8.1**.

Close investigation on the conditional histograms of different subcategories provide the following conclusions regarding the evolution of the junction:

(i) All three plateaus P-1, P-2 and P-3 can occur simultaneously [category **(1)**, 24 %],

(ii) Plateaus of P-2 can be formed as an extension of plateau at P-1 [category **(2)**, 14 %] or plateau at P-2 can be transferred to the steps at P-3 [category **(4)**, 15 %]

(iii) Plateau at P-1 can be formed independently [category **(3)**, 17%]

(iv) There are few traces which don't show any molecular signature in the traces [category **(5)**, 30%].

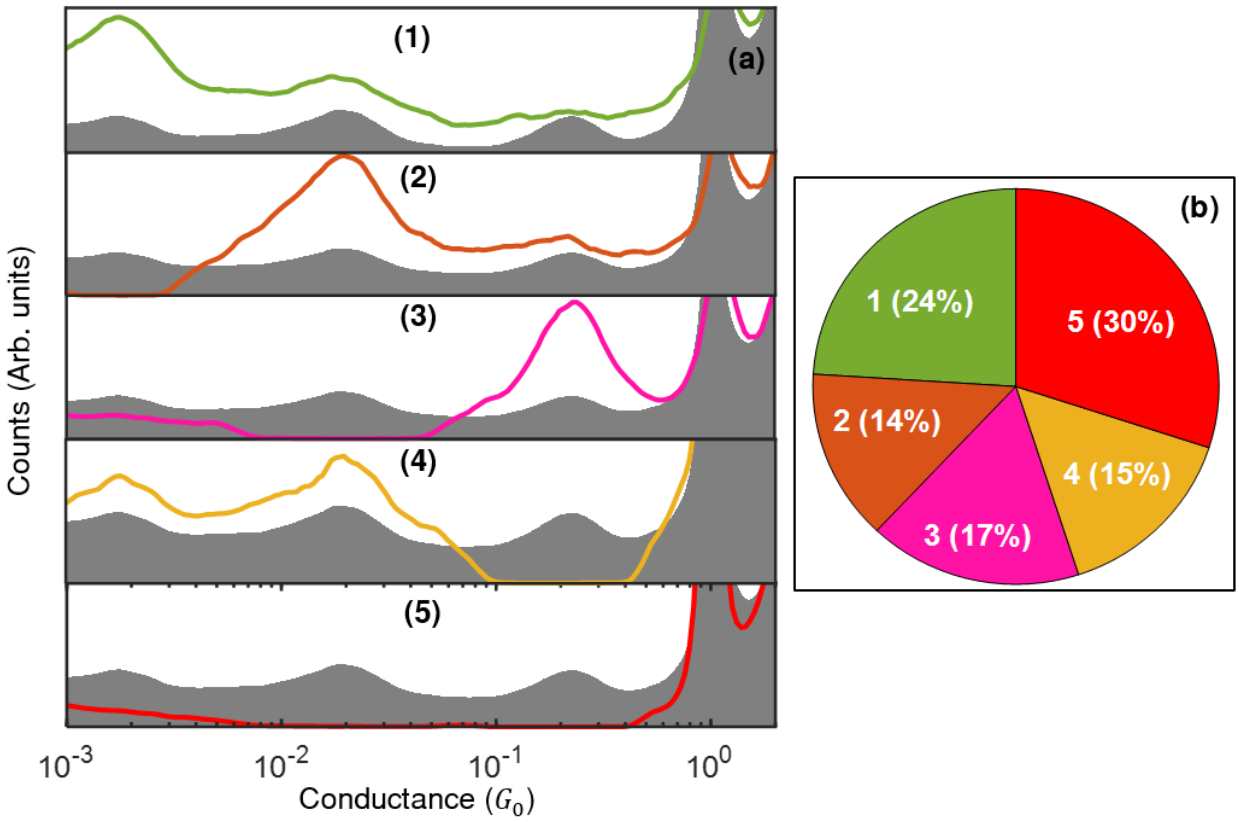

Figure 8.9 (a) *Conditional conductance histogram of copper atomic junction in presence of hydrogen, considering traces of different sub categories. Number in the center of each block denotes the number of the corresponding sub categories where line plot is the histogram of that sub categories and grey area plot is the histogram constructed from entire data set.* ***(b)*** *Pie chart of percentage of traces, belongs to different sub categories. Corresponding number and percentage are mentioned inside the respective color region.*

Table 8.1 *Characteristics of different sub-categories.*

Sub categories	**Plateaus present (denoted by 1) or absent(denoted by 0) at the peak**			**Number of traces (%)**	**Corresponding color in Figure 9**
	P-1	**P-2**	**P-3**		
1	1	1	1	2204(24)	Green
2	1	1	0	1306(14)	Bronze
3	1	0	0	1663(17)	Magenta
4	0	1	1	1408(15)	Yellow

5	0	0	0	2819(30)	Red
Total data	-------			9400(100)	Grey area

Apart from that, formation of premature molecular junction i.e., precursor configuration is also identified from the appearance of a plateau at $\sim 1.33\ G_0$ in average conductance displacement breaking traces of Cu/H_2 junction (marked as a green circle in the inset of **Figure 8.7a**). Similar precursor configuration was observed for diatomic[80] and organometallic[88] molecule-based junction which primarily occurs when the atomic contact lies in parallel to the molecular junction.

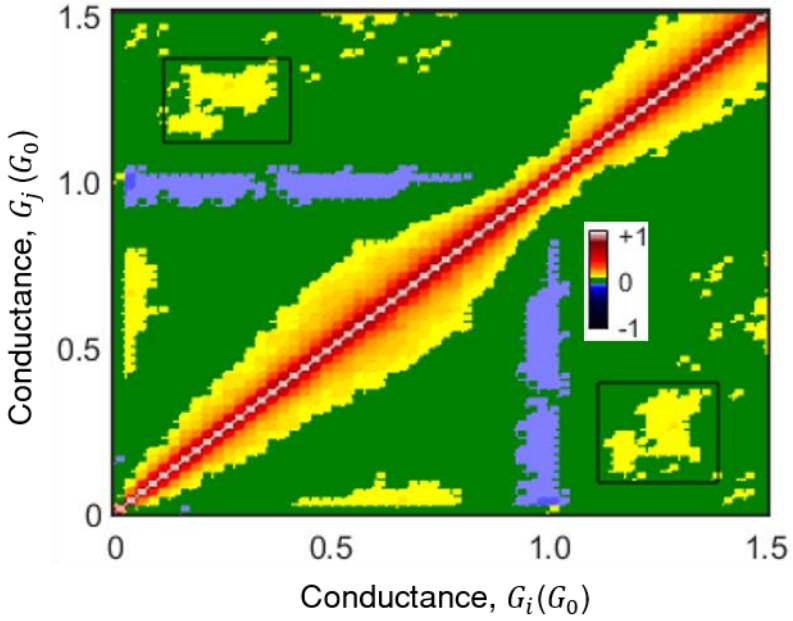

Figure 8.10 *Two dimensional cross correlation histogram (2DCH) of breaking traces of copper atomic junction in presence of hydrogen. Yellow color cloud, marked as black rectangles, reveals the positive correlation which validates the formation of precursor configuration.*

Further validation is given by the two dimensional cross correlation analysis, as described in **Chapter 03**, **Section 3.4**. **Figure 8.10** shows the 2D cross correlation map of Cu/H_2 molecular junctions where horizontal and vertical axes corresponds to the two pull (breaking) conductance, G_i & G_j and yellow (blue) color represents the positive (negative) correlation. An island of positive correlation, marked by black rectangles, between the conductance pairs $0.06\ G_0$ to $0.45\ G_0$ and $1.10\ G_0$ to $1.40\ G_0$, is visible in **Figure 8.10** which corresponds to the formation of precursor configuration. So, this combined analysis establishes the eventual formation of the precursor configuration in which molecule binds alongside to the atomic contact and opens additional channel which results in an increase of the conductance up to $\sim 1.40\ G_0$.

8.2.4. Inelastic electron tunneling spectroscopy

To assure the incorporation of hydrogen into the Cu or Al junction, we adopt inelastic electron tunneling spectroscopy (IETS) as an experimental tool which offers valuable information related to the combined structure of metal and molecule, schematically described in **Figure 8.11a-c**. If the applied bias voltage (V) is sufficient enough to excite certain vibration mode (eV) of the junction, transmitted electrons are then in-elastically scattered either in forward or backward direction. It is manifested as a step up or step down in the differential conductance spectra (dI/dV vs. V). Bias voltage corresponding to these steps are equivalent to the vibrational energy and the sign of these steps (up or down) are determined by the transmission probability of the conduction channels[187,230–232]. However, apart from these step up or step down features, anomalous spikes like peak, dip or peak followed by a dip i.e., S-shaped features are regularly observed in the differential conductance spectra of single molecular junction[233,234]. These anomalies are related to the vibrational mode of the single molecules, which has been modelled by vibrationally induced two level systems (VITLS)[233] or asymmetry coupled two level systems (TLS)[235]. Both models provide an illustration of a physical process that may lead to the appearance of peak or dip like structures in dI/dV curves of the molecular junctions. In our case, asymmetric coupled TLS model is used to fit the experimentally obtained dI/dV curves due to its applicability in a wide range of experimental conditions: using different molecules, metal electrodes and contact size.

General features of the dI/dV spectra include the transition between two conductance plateaus during the sweeping of bias voltage via a characteristic features (step up or down, peak or dip) at the onset of vibrational energy. The switching of the conductance between two discrete levels indicates the consideration of two-level systems (TLS). However, a simple TLS models exhibits only step up or step-down features in contrast to asymmetrically coupled TLS model where step up or step down in the dI/dV can be evolved into the peak or dip depending on the asymmetry in the coupling. TLS model is based on the scattering process on a two-level system located near the center of an atomic sized contact and demonstrated as a double-well potential where energy difference between the two states of the potential well is Δ and the two states are coupled by the tunneling across the barrier with a coupling energy Γ (**Figure 8.11d**). The coupling between the wells causes a hybridization of the two states, resulting into two energy eigenvalues with a splitting of $E = \sqrt{\Delta^2 + \Gamma^2}$. It is further considered that conductance of the lower and upper states of the

TLS is σ_0 and σ_1. Corresponding occupation numbers are n_0 and $n_1 = (1 - n_0)$. Current-Voltage $(I - V)$ characteristics is determined by the voltage dependent occupation numbers as,

$$I(V) = (\sigma_0 n_0 + \sigma_1 n_1)V \tag{8.1}$$

Differential conductance,

$$\frac{dI}{dV} = \sigma_0 + (\sigma_1 - \sigma_0)[n_1 + V\frac{dn_1}{dV}] \tag{8.2}$$

The occupation numbers of the upper state can be calculated from the rate equation as,

$$\frac{dn_1}{dt} = (n_0\nu_0 - n_1\nu_1) \tag{8.3}$$

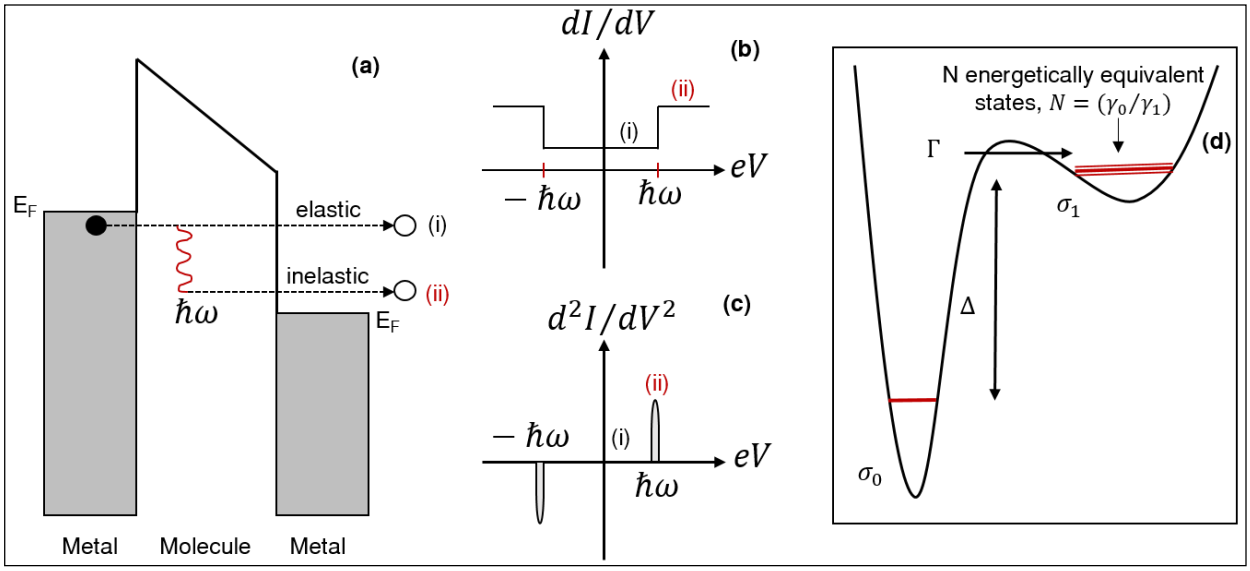

Figure 8.11 (a) *A schematic illustration of electron tunneling through a metal-molecule-metal junction. Electron can lose some of its energy during tunneling to trigger a vibration mode of energy, provided that the bias voltage (eV) crosses the threshold for excitation of the vibrational mode (ħω). Here, '(i)' is the elastic tunneling process; '(ii)' is the inelastic tunneling process.* ***(b, c)*** *The opening of the additional channel leads to an increase in conductance (dI/dV) at $eV = \pm \hbar\omega$ which is manifested as a peak (dip) for the positive (negative) bias of the second derivative of the current (d^2I/dV^2).* ***(d)*** *Asymmetric coupled two level system (TLS) with a degenerate upper level.*

Where ν_0 and ν_1 are the inverse relaxation times of the lower and upper state of the TLS,

$$\nu_0 = \frac{{\rho_F}^2\gamma_0}{4}\left[\frac{eV+E}{2}\left(coth\frac{eV+E}{2KT} - 1\right) + \frac{-eV+E}{2}\left(coth\frac{-eV+E}{2KT} - 1\right) + E(coth\frac{E}{2KT} - 1)\right] \tag{8.4}$$

$$\nu_1 = \frac{{\rho_F}^2 \gamma_1}{4}\left[\frac{eV-E}{2}\left(coth\frac{eV-E}{2KT}-1\right)+\frac{-eV-E}{2}\left(coth\frac{-eV-E}{2KT}-1\right) - E\left(coth\frac{E}{2KT}-1\right)\right] \quad (8.5)$$

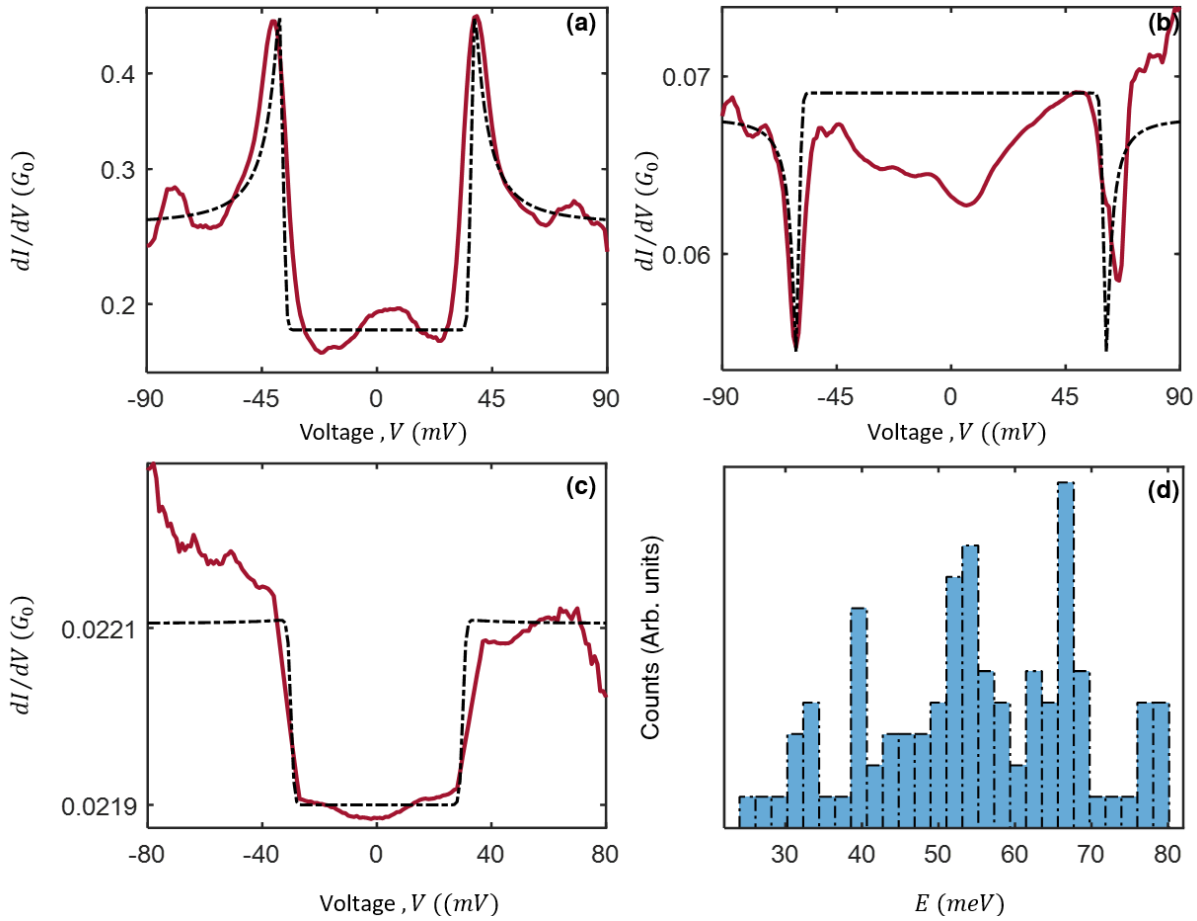

Figure 8.12 (a-c) *Differential conductance vs. applied bias voltage (dI/dV vs.V) spectra of copper atomic junction in presence of hydrogen, measured at zero bias conductance of* $0.19\ G_0$ *(a)* $0.05\ G_0$ *(b) and* $0.002\ G_0$ *(c) . Black dash dotted line is the theoretical fits of asymmetrically coupled TLS model and corresponding parameters are mentioned in the* ***Table 8.2****.* ***(d)*** *Distribution of vibrational energy measured on the different realizations of copper atomic junction in presence of hydrogen.* 98 *different spectra's are analyzed here with the any zero bias conductance value in the range* $0.8\ G_0$*to* $0.001G_0$.

where, ρ_F stands for the density of the states at the Fermi level. γ_0 and γ_1 are the coupling of the lower and upper state of the TLS to the electrons. K, T and e are the Boltzmann constant, temperature and electronic charge respectively. Asymmetry arises due to the difference in phase space between the two levels. For instance, if the ground state is well defined, but the upper state

is not a single level but N energetically equivalent states (**Figure 8.11d**) then the effective coupling constant contains a summation for the final states resulting in parameter, $\gamma_0 = N\gamma_1$.

In the steady state ($\frac{dn_1}{dt} = 0$), occupation number of the lower and upper state is

$$n_0 = \frac{\nu_1}{\nu_0 + \nu_1} \tag{8.6}$$

$$n_1 = \frac{\nu_0}{\nu_0 + \nu_1} \tag{8.7}$$

Putting the values of ν_0 and ν_1 from **Equation (8.4)** and **(8.5)**, occupation numbers is calculated. From this occupation numbers, $I - V$ and dI/dV are calculated and mentioned in the appendix Section. **Equation (8.9)**, shown in appendix section, is used to fit the experimentally recorded dI/dV spectra. Fitting parameters are the energy (E) and asymmetry parameter (N), whereas σ_0 and σ_1 are read from the experimental curves and KT is kept constant at $0.36\ meV$. Note that, finite temperature effect on smearing of the curves is ignored here.

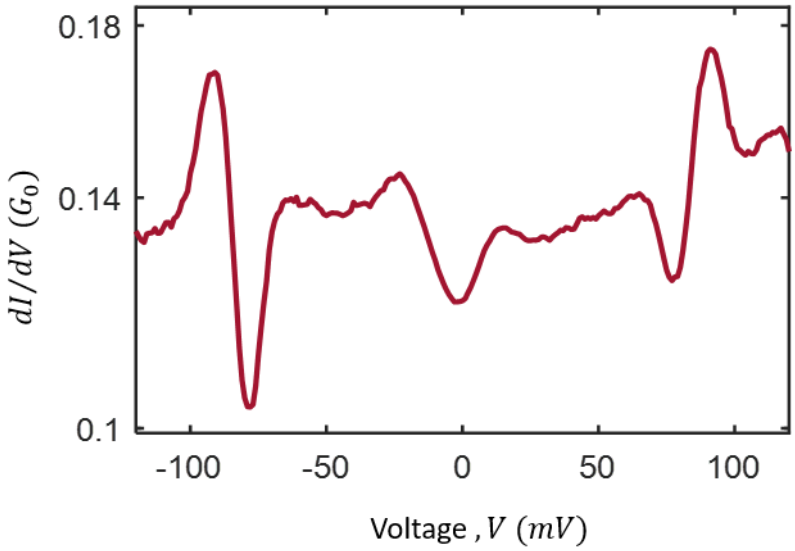

Figure 8.13 *Representative dI/dV vs. V spectra with "**S**" shaped features (peak followed by a dip) of copper atomic junction in presence of hydrogen, measured at zero bias conductance of* $0.11\ G_0$.

Representative anomalous spikes like peak (**Figure 8.12a**), dip (**Figure 8.12b**) along with regular step up (**Figure 8.12c**) features for Cu/H_2 junction are shown in **Figure 8.12a-c**. Corresponding vibrational energies and asymmetry parameters are summarized in **Table 8.2**. Large variation of spectroscopic signatures are noticed from junction to junction which is quite expected as there may be many configurations that atoms or molecules can adopt in the junction. Hence, vibrational

energy determined from 98 independent contacts with any conductance value between 0.8 G_0 to 0.001 G_0 are presented in the form of histogram (**Figure 8.12d**). Vibrational energies are distributed over 20 meV to 80 meV, though, repeatable appearance of certain vibrational energies at specific region ($\sim 33\ meV, 39meV,\ 54\ meV$ and $66\ meV$) are clearly distinguishable. Observed vibrational energies indicates that hydrogen is also participated in the configuration of the Cu atomic chain as vibrational energy of pure metallic contacts can be up to $\sim 20\ meV$. Asymmetry in the coupling can also be easily understood due to the existence of large number of loosely bound configuration where different angles of the molecules with respect to the contact axis have similar binding energies and also molecule can diffuse at different sites of the junction. Furthermore, it is important to mention that peak followed by a dip i.e., S-shaped feature (**Figure 8.13**) is observed in case of Cu/H_2 junction which has been described by the three level model[233].

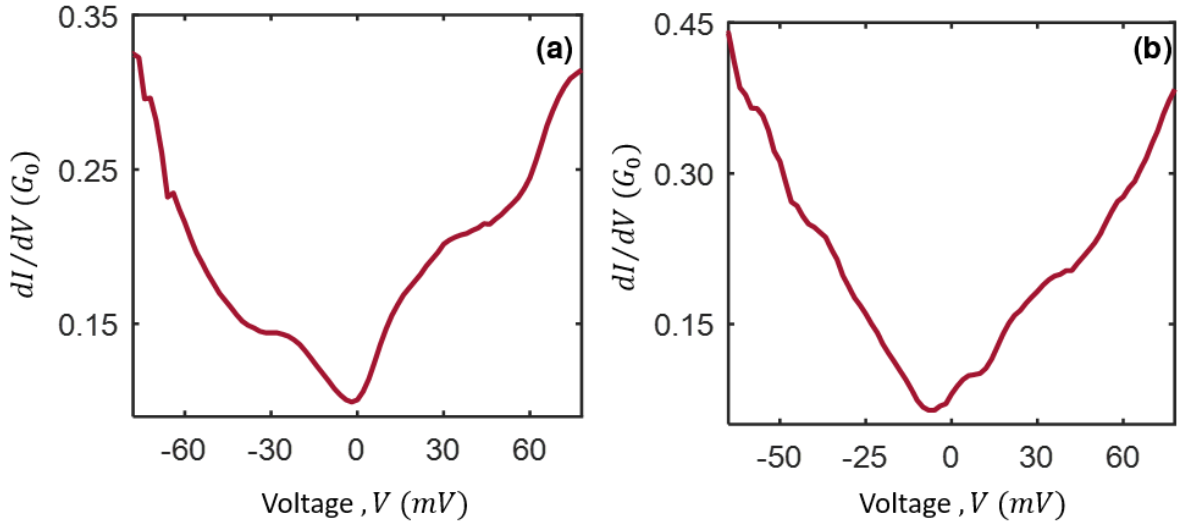

Figure 8.14 (a-b) *dI/dV vs. V spectra of aluminum atomic junction in presence of hydrogen, measured at zero bias conductance of* 0.19 G_0 *(a) and* 0.16 G_0 *(b).*

The fitting of these features using three level model is too complicated and discarded here. Coming back to Al case, two dI/dV spectra of Al/H_2 junction, showing regular step-up feature, is displayed in **Figure 8.14**.

Evolution of vibrational energy with respect to strain could also be extremely useful to classify the vibrational symmetry. Vibrational mode can be longitudinal or transverse describing motion along or perpendicular to the junction's axis. This is performed by checking the response of vibrational energy in the recorded dI/dV spectra of stable contacts upon stretching. Longitudinal symmetry are characterized by the decrease in vibrational energy with increase of stretching and is resulted

from the weakening of metal-molecule bonds[236,237]. Whereas, contrary response i.e., increase of vibrational energy of transverse modes happens due to increasing restoring force like guitar string[236,237]. **Figure 8.15a-c** presents the three sets of dI/dV spectra with prominent vibrational

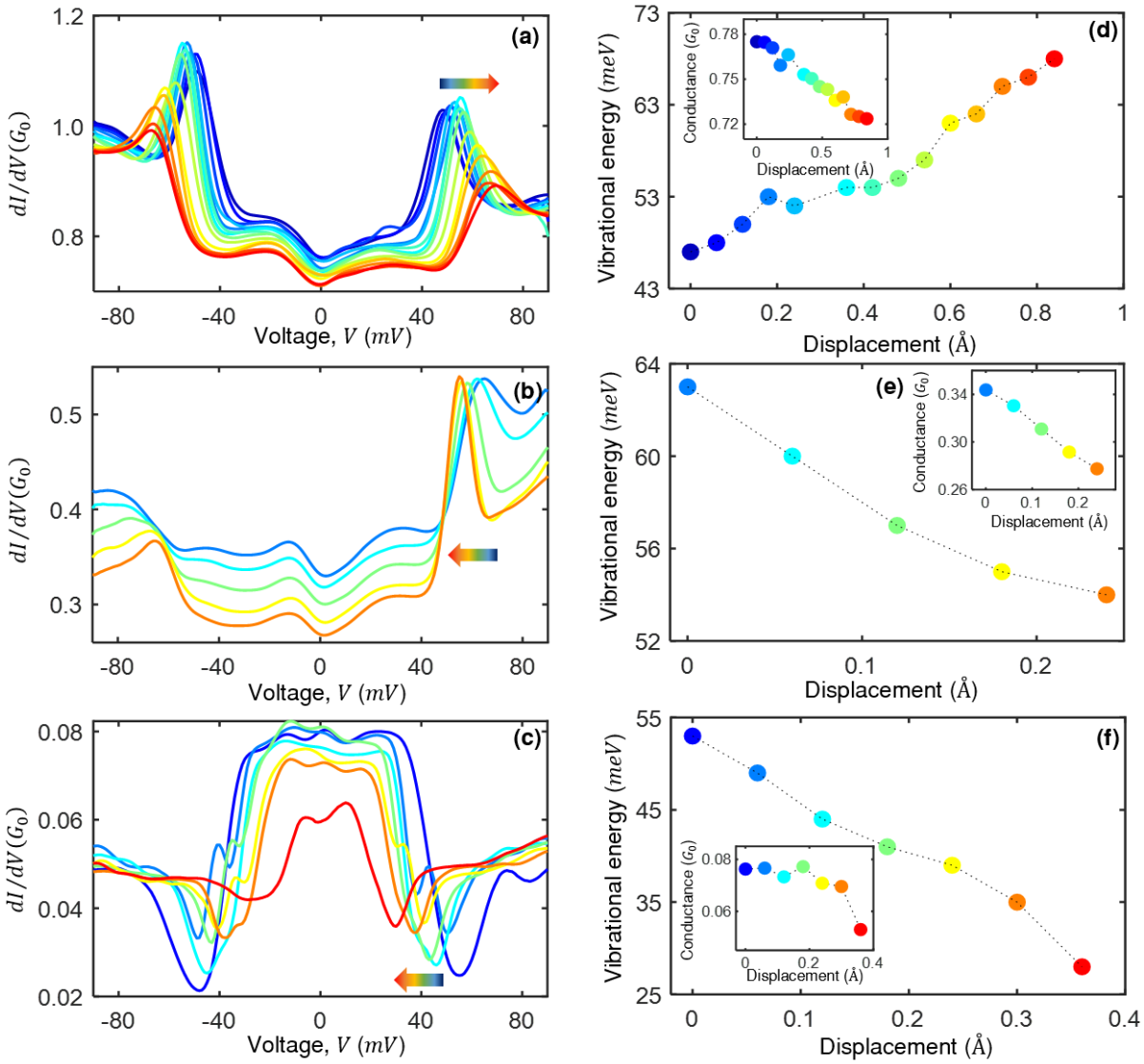

Figure 8.15 (a-c) *dI/dV vs. V spectra of copper atomic junction in presence of hydrogen, recorded upon stretching the junction. Blue color denotes the spectra prior to the start of stretching and red is before the final rupture while intermediate colors are self-explanatory.* ***(d-f)*** *Evolution of vibrational energy upon stretching, obtained from asymmetric coupled TLS model fitting of the spectra's a-c, following same colors. Features appearing at the positive bias voltage are considered for fitting. Inset: Evolution of the zero bias conductance upon stretching for the same spectra's.*

Table 8.2 *dI/dV fitting parameters using asymmetric coupled TLS model.*

Vibrational Features (Figure)	**Fitting Parameters ($KT = 0.36\ meV$)**			
	$\sigma_0(G_0)$	$\sigma_1(G_0)$	$E\ (meV)$	N
Peak (**Figure 8.12a**)	0.185	0.26	37	11
Dip (**Figure 8.12b**)	0.069	0.0675	60	36
Step up (**Figure 8.12c**)	0.0219	0.0223	30	1

signatures where sequences in each set are recorded during the stretching of the junction. Colored arrows dictate the evolution of the features during stretching with blue and red color denotes the start and stop of the stretching fact with intermediate colors are self-explanatory. Energies of the individual vibrational modes of **Figure 8.15a-c** are calculated from the previously explained TLS model and presented as a function of inter electrode displacement in the **Figure 8.15d-f**

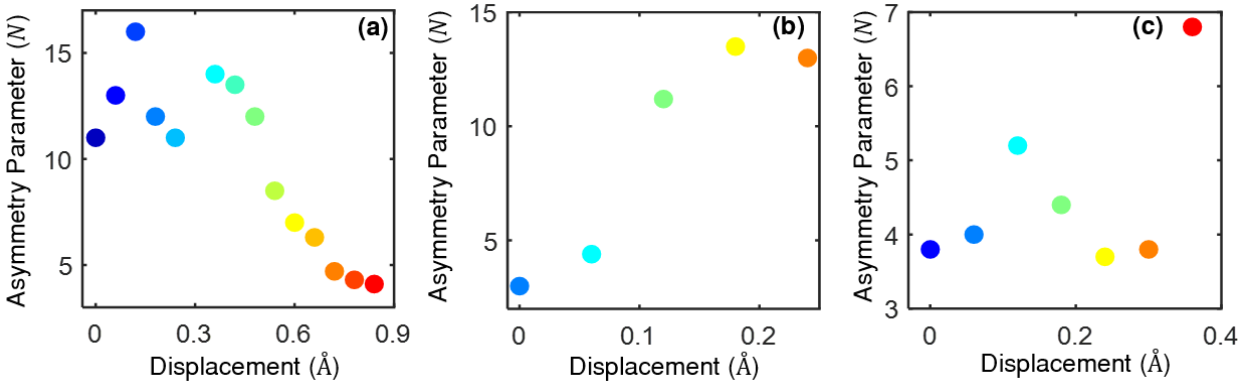

Figure 8.16 (a-c) *Asymmetry parameters (N) of TLS model for the spectra of* ***Figure 8.15a-c*** *as a function of inter electrode displacement, following the same colors.*

respectively. An increase in vibrational energy from 47 meV to 68 meV due to a change in electrode separation of 84 pm is evident from **Figure 8.15d** which is a typical signature of transverse symmetry i.e., motion of molecule perpendicular to the axis of the junction. Opposite to former case, **Figure 8.15e** and **Figure 8.15f** demonstrates a decrease in vibrational energy (63 meV to 54 meV and 53 meV to 28 meV) which renders it as a longitudinal mode i.e., motion along the axis. Corresponding evolution of asymmetry parameter and zero bias conductance with respect to stretching for these three different junctions (**Figure 8.15a-c**) are shown in **Figure 8.16a-c** and in the inset of **Figure 8.15d-f.** Conductance decreases with stretching for these junctions, whereas, no noticeable trend is observed for asymmetry parameters. Note that despite their similar energy, opposite response of vibrational energy with strain could be helpful to distinguish the vibrational symmetry. Correlating vibrational mode with the zero-bias conductance

of the studied junctions, it can be concluded that conductance of transverse symmetry is somehow higher compared to longitudinal one.

8.3. Conclusion:

In conclusion, we have studied the influence of hydrogen in determining the structural and electronic properties of Cu and Al atomic junction. Conductance measurements indicates the formation of multiple stable configurations of Cu/H_2 junctions with most probable conductance values $\sim 0.2\ G_0$, $0.02\ G_0$ and $0.001\ G_0$ and demonstrate the step wise decrease of tunneling conductivity. Whereas no prominent conductance peak was observed for Al/H_2 junction. Plateau length analysis demonstrates the formation of copper atomic chain because of hydrogen insertion. The role of hydrogen to realize the atomic chain is further corroborated from vibrational spectroscopy. In fact, two vibrational modes i.e., longitudinal, and transverse mode of Cu/H_2 junction are identified by their opposite response to strain. Overall, these findings add a new member in the list of impurity induced metal atomic chain formation and helps to improve our knowledge to form a nearly insulating atomic chain. Not only that, but realization of extremely low conducting configuration also suspended between metal atomic segments opens a new question for the theoretician to address.

8.4. Appendix:

$$
\begin{aligned}
I(V) = eV((\sigma_0((E/2 - eV/2)(coth((E - eV)/(2KT)) + 1) \\
- E(coth(E/(2KT)) - 1) + (coth((E + eV)/(2KT)) \\
+ 1)(E/2 + eV/2)))/((E/2 - eV/2)(coth((E \\
- eV)/(2KT)) + 1) - E(coth(E/(2KT)) - 1) \\
+ N((E/2 - eV/2)(coth((E - eV)/(2KT)) - 1) \\
+ E(coth(E/(2KT)) - 1) + (coth((E + eV)/(2KT)) \\
- 1)(E/2 + eV/2)) + (coth((E + eV)/(2KT)) \\
+ 1)(E/2 + eV/2)) + (N\sigma_1((E/2 - eV/2)(coth((E \\
- eV)/(2KT)) - 1) + E(coth(E/(2KT)) - 1) \\
+ (coth((E + eV)/(2KT)) - 1)(E/2 \\
+ eV/2)))/((E/2 - eV/2)(coth((E - eV)/(2KT)) \\
+ 1) - E(coth(E/(2KT)) - 1) + N((E/2 \\
- eV/2)(coth((E - eV)/(2KT)) - 1) \\
+ E(coth(E/(2KT)) - 1) + (coth((E + eV)/(2KT)) \\
- 1)(E/2 + eV/2)) + (coth((E + eV)/(2KT)) \\
+ 1)(E/2 + eV/2)))
\end{aligned}
\tag{8.8}
$$

$$\frac{dI}{dV} = (2\sigma_0((E/2 - eV/2)(coth((E - eV)/(2KT)) + 1) - E(coth(E/(2KT)) - 1) + (coth((E + eV)/(2KT)) + 1)(E/2 + eV/2)))/((E + eV)(coth((E + eV)/(2KT)) + 1) + N((E + eV)(coth((E + eV)/(2KT)) - 1) + 2E(coth(E/(2KT)) - 1) + (E - eV)(coth((E - eV)/(2KT)) - 1)) - 2E(coth(E/(2KT)) - 1) + (E - eV)(coth((E - eV)/(2KT)) + 1)) + (2N\sigma_1((E/2 - eV/2)(coth((E - eV)/(2KT)) - 1) + E(coth(E/(2KT)) - 1) + (coth((E + eV)/(2KT)) - 1)(E/2 + eV/2)))/((E + eV)(coth((E + eV)/(2KT)) + 1) + N((E + eV)(coth((E + eV)/(2KT)) - 1) + 2E(coth(E/(2KT)) - 1) + (E - eV)(coth((E - eV)/(2KT)) - 1)) - 2E(coth(E/(2KT)) - 1) + (E - eV)(coth((E - eV)/(2KT)) + 1)) - (2ENeV(\sigma_0 - \sigma_1)(coth(E/(2KT)) - 2)(Ecoth((E + eV)/(2KT))^2 - 2eV + eVcoth((E + eV)/(2KT))^2 - Ecoth((E - eV)/(2KT))^2 + eVcoth((E - eV)/(2KT))^2 - 2KTcoth((E + eV)/(2KT)) + 2KTcoth((E - eV)/(2KT))))/(KT(4E - 2Ecoth(E/(2KT)) + eVcoth((E + eV)/(2KT)) + Ecoth((E - eV)/(2KT)) - eVcoth((E - eV)/(2KT)) + Ecoth((E + eV)/(2KT)) - 4EN + ENcoth((E + eV)/(2KT)) + 2ENcoth(E/(2KT)) + NeVcoth((E + eV)/(2KT)) + ENcoth((E - eV)/(2KT)) - NeVcoth((E - eV)/(2KT)))^2) \quad (8.9)$$

Chapter 9 | Conclusion and outlook

This chapter serves as the overall conclusion of the current thesis and provides an insight on the range of upcoming research in the topic.

In the present thesis, contribution of molecular orientation to the charge transport characteristics of single molecular junction is investigated along with its impact on contact formation. During the early stage of my doctoral program, significant attention was paid to develop and design the experimental set up based on the MCBJ technique to fabricate the single molecular junction. Successful characterization of our indigenously developed experimental arrangements ensures the capability to conduct the measurements from ambient condition to cryogenic environments. The thesis comprises of studies on 8 different types of junction combining 4 metal electrodes and 6 different molecules: 1. Au/4,4'-bipyridine/Au, 2.Au/2,2'-bipyridine/Au, 3. Au/ferrocene/Au, 4. Au/1,1'-bis(aminomethyl)ferrocene/Au, 5. Au/1,1'-dicyano ferrocene/Au, 6. Ag/ferrocene/Ag, 7. Cu/Hydrogen/Cu, and 8. Al/Hydrogen/Al.

Primarily, the effect of molecular structure to the metal-molecule contact formation is probed by employing two isomers of bipyridine: 4,4'-bipyridine and 2,2'-bipyridine between gold electrodes. Transport measurements during closing the junction indicate the unambiguous formation of 4,4'-bipyridine molecular junction via a jump in conductance value which is completely absent for 2,2'-bipyridine. To explain this observation, two possible mechanisms are identified based on the theoretical calculations which reveal a significant role of geometry of the molecule to the metal-molecule bond formation. Moreover, relation between the evolutions of the junction and its post rupture event is established.

We then intend to explore three-dimensional organometallic molecule-based junction to understand its transport features by tuning the chemical bonding with the electrodes. Based on the experimental results we not only obtain the nature of chemical bond in these junctions, but also find the influence of orientation in determining the transport behavior. Ferrocene is chosen as an organometallic element due to its excellent chemical stability and corresponding single molecular conductance measurements confirms that it can be directly connected to the gold electrodes which exhibits significantly high conductance ($\sim 0.2\ G_0$, one quarter of quantum of conductance). Further experiment considering ferrocene terminated with **–NH_2** and **–CN** anchoring arms provide similar high conductance in conjugation with a broad feature at the low conductance. Theoretical calculations propose the possibility of two stable orientations of ferrocene (perpendicular or parallel to the axis of the electrode) having covalent type of bonding at the metal molecular interface. The perpendicular geometry of ferrocene is coupled via Fe atom of ferrocene to the Au electrodes contrary to parallel geometry which is coordinated by the Cp rings. Transmission

calculation for these two geometries ensures a near resonant transport mechanism of perpendicular geometry with high conductance, whereas it is modified to the low conducting off-resonant mechanism for parallel geometry. Interestingly, this perpendicular geometry can also be realized for anchoring attached molecules and hence, responsible for the generalized high conductance features. Furthermore, coupling with anchoring arms discloses more configurations with low conductance value, in agreement with the experimentally observed broad conductance values because of anchoring group insertion to ferrocene backbone. So, the obvious effect of spatial orientation of ferrocene to the charge transport mechanism is detected. We then extend our study by exploring the effect of temperature on the formation of Au/ferrocene/Au molecular junction. From the conductance measurements at $4.2\ K$, $77\ K$ and $300\ K$, a considerable influence of temperature to the formation of ferrocene molecular junction is noticed. While features due to multiple geometries with conductance value from $0.2\ G_0$ to $0.001\ G_0$ are regularly observed at low temperatures (both $4.2\ K$ and $77\ K$), corresponding features at $300\ K$ are restricted within $0.2\ G_0$ to $0.07\ G_0$. Thus, the number of stable configurations of the junction are enhancing with the reduction of temperature. The possibility of two orientations of ferrocene with different conductance value (perpendicular-high conductance and parallel-low conductance) is already verified from our previous study. Now, to understand this temperature sensitive evolution of the junction, Molecular dynamics (MD) simulation is considered which discloses an important intra-molecular property of ferrocene. Rotational dynamics of the two cyclopentadienyl (Cp) rings of ferrocene differs with temperature and especially, reduction of the temperature decelerates the rotational motion due to the increase of activation energy to reorient the Cp rings. Such temperature dependent rotation prefers only perpendicular geometry to be stable at room temperature in contrast to low temperature where both perpendicular and parallel geometry is favored, in line with the experimentally realized more conformations with the reduction of temperature. The reason is simple to understand- Freely rotating rings at room temperature forbids the bonding between Cp rings and Au electrodes of the parallel geometry whereas static rings at low temperature allows this geometry. Perpendicular geometry is typically unaffected by the temperature as it is coordinated by the Fe atom. Thus, temperature dependent rotation of Cp rings of ferrocene is playing a decisive role to execute the orientation of ferrocene in the form of Au/ferrocene/Au junction. Continuing ferrocene as a molecular component, one more important potential of single molecular junction is explored. Single molecular junction can be mechanically gated in contrast to

the conventional silicon-based transistor and we observed an interesting effect of the structure regulated mechanical gating in Ag/ferrocene/Ag junction. High bias differential conductance spectra along with the transient voltage spectroscopy of ferrocene molecular junction demonstrate that the tunability of the Fermi level of the junction with stretching or squeezing the junction or mechanical gating phenomena is not always observed; can be seen for few realization and in few other cases, it is absent. Theoretical calculations ascribed this presence or absence of mechanical gating to the orientation of molecule inside the junction. Like Au/ferrocene/Au, both parallel and perpendicular geometries are energetically possible conformations for Ag/ferrocene/Ag is recognized with distinctive mechanical gating response. When the molecule is oriented in parallel to the axis of the junction, mechanical gating is seen, however, for the perpendicular molecular orientation, a similar effect is vanished. The emergence of this contrary response is assigned to the difference in orientation of the dominant molecular orbitals with respect to the electrodes, and their coupling to the frontier electrode states. In the extreme demonstrated case, the same molecular junction either experiences mechanical gating or not, depending on the molecule orientation with respect to the electrodes, as well as on the nature of the interaction between the molecular orbitals and the continuum states of the electrodes. These findings point out the importance of geometry and local orbital structure to control the mechanical gating of charge, spin, and heat transport in molecular junctions.

One more important prospect of single molecular junction is the formation of impurity induced metal atomic chain. Realization of impurity assisted atomic chain having conductance value in the tunneling conductance regime ($\sim < 0.1\, G_0$) is established by studying copper and aluminum atomic junction in presence of hydrogen. Three stable configuration of hydrogen decorated copper atomic junction with conductance value $\sim 0.2\, G_0, 0.02\, G_0, 0.002\, G_0$ is ensured from the statistical analysis of the experimental data. Whereas same analysis for aluminum junction reveals its unpretentious behavior in hydrogen environment. Frontier metallic orbitals might play a crucial role for this distinctive response of copper and aluminum junction after insertion of hydrogen. Additional analysis exposes an interesting note. While copper is limited to monoatomic contact in its purest form, hydrogen insertion stabilizes and elongates the junction up to four or five atoms. Involvement of hydrogen to these longer configurations is confirmed from the characteristic vibrational signatures in the inelastic electron tunneling spectroscopy. Furthermore, conductance value of longitudinal and transverse symmetry of the junction, identified from evolution of

vibrational energy with respect to strain, could be extremely useful to propose the possible geometry. Thus, our experimental observations pave the way to fabricate nearly insulating impurity aided atomic chain considering its primary dependence on the frontier metallic orbitals.

Although, influence of molecular orientation to the characteristic response of the single molecular junction including formation and evolution, charge transport mechanism are examined to some extent, optimization towards the desired functionality requires further attention both from experiment and theory perspective.

Few important and immediate possibilities in accordance with the study or observations reported in my thesis are outlined below-

- Jump to molecular contact for 4,4'-bipyridine molecular junction is found to relate to the geometry of the molecule and the interaction at the metal-molecule interface. This can be understood in detail by tuning both the geometry and interface with the help of synthetic chemistry and different electrodes.
- A significant fraction of the present thesis is based on the charge transport phenomena of organometallic molecular junction. Charge transport for this class of molecule is heavily dominated by the spatial orientation due to its unique three-dimensional structure. The importance of this geometry to the other transport characteristics like thermal and spin transport can be a potential problem to address.
- Temperature dictated rotation of Cp rings of ferrocene affects the formation of ferrocene based molecular junction which can be checked with other metallocene to understand and establish a general overview.
- The angle between two Cp rings of ferrocene can modify the hybridization at the metal-molecule interface which is the key factor of a single molecular junction. This angle adds a new degrees of freedom to influence and optimize the functionality of the organometallic based molecular junction.
- Our study on Ag/ferrocene/Ag junction dictates that orientation of molecule inside the single molecule junction is a decisive factor of the mechanical gating response of the corresponding junction. In principle, it is true for other sets of electrodes, however, addressing this problem with the combination of different electrodes and metallocenes can improve our fundamental knowledge regarding the charge transfer at the metal-molecule interface.

- In the case of Ag/ferrocene/Ag junction, a direct correlation between differential conductance spectra and transition voltage spectroscopy (TVS) is evident. Nevertheless, TVS spectroscopy was used to probe the evolution of level alignment due to mechanical manipulation following the previous references, our observation would be helpful for future study, particularly to make a complete interpretation of TVS.
- Formation of low conducting copper atomic chain in presence of hydrogen molecules opens a way to fabricate nearly insulating metallic wire. So far, several metals are employed to form atomic chain in presence of external molecules. Further study focusing on the low conducting regime might be helpful to establish the contribution of frontier metallic and molecular orbitals on the realization of metal atomic chain with negligible conductance. Stabilization of atomic junction in collaboration with foreign molecules is an ongoing interest for the theoretician where our finding adds a new aspect to encounter.

Chapter 10 | Appendix

This chapter contains the experimental results from my doctoral program that were not included in my thesis, along with a statistics of all experiments.

10.1. Additional experimental results:

(i) Experimental details

Single molecular charge transport characteristics of **(1)** ferrocene, **(2)** 1, 1′-dicyanoferrocene, **(3)** 1,1′-bis(aminomethyl)ferrocene and **(4)** 1,1′-dihydroxyferrocene molecular junctions are examined using MCBJ technique at $77\ K$ under high vacuum ($\sim 10^{-6}\ mbar$). Molecules are connected to the atomistic gold electrodes by spreading DCM solution of the target molecules over the notched section of the metallic wire, prior to its breaking.

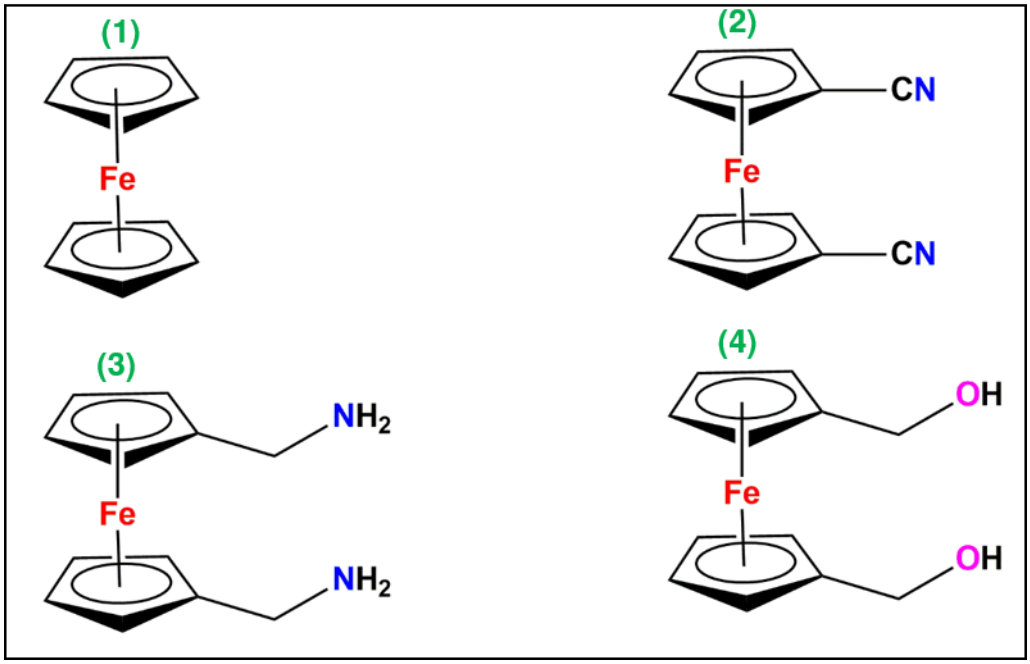

Figure 10.1 *Chemical structure of* ***(1)*** *ferrocene,* ***(2)*** *1, 1′-dicyanoferrocene,* ***(3)*** *1,1′-bis(aminomethyl)ferrocene and* ***(4)*** *1,1′-dihydroxyferrocene.*

(ii) Results

(a) Conductance traces and histograms

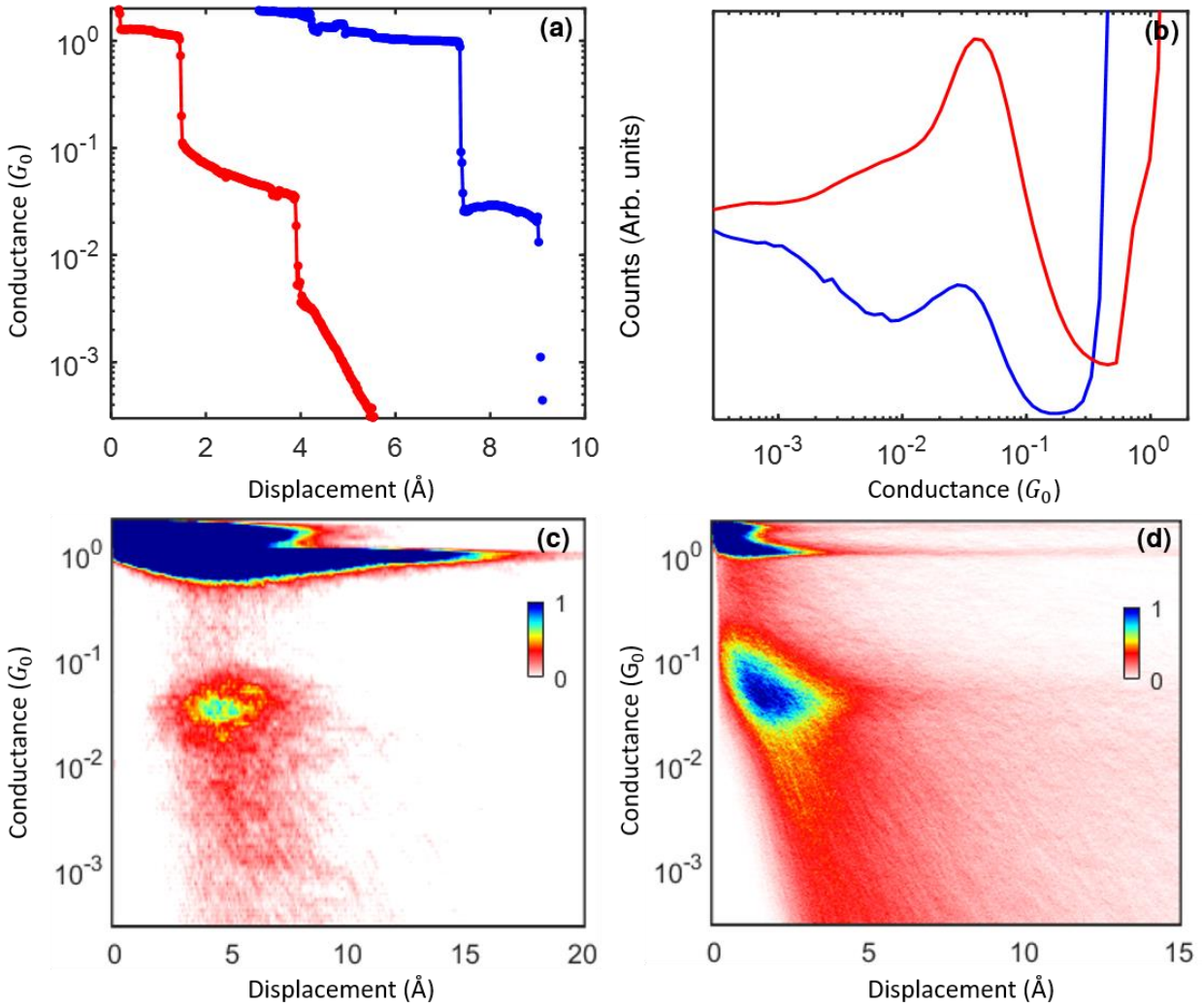

Figure 10.2 (a, b) *Conductance displacement traces and conductance histogram of gold/ferrocene junction where blue and red color denotes the breaking (pull) and making (push) traces.* 20 *bins per decade are considered for histogram generation.* ***(c-d)*** *Conductance displacement histogram of pull (c) and push (d) traces of the same junction, constructed by using* 30 *and* 100 *bins per decade respectively. Histograms are built from* 20,000 *consecutive conductance displacement traces.*

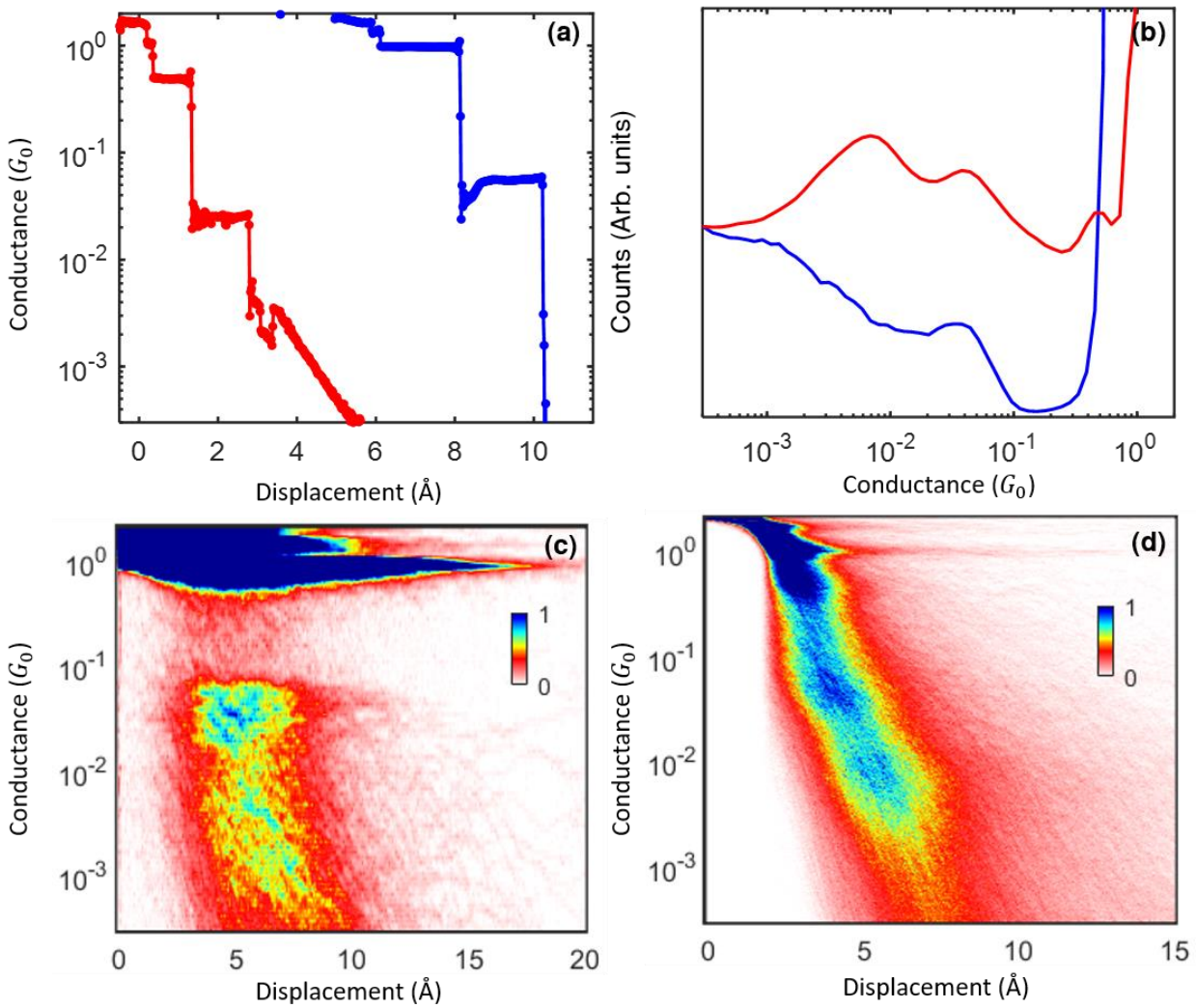

Figure 10.3 *Similar analysis like* ***Figure 10.2*** *for 1, 1'-dicyanoferrocene molecular junction considering* 18,000 *number of traces.*

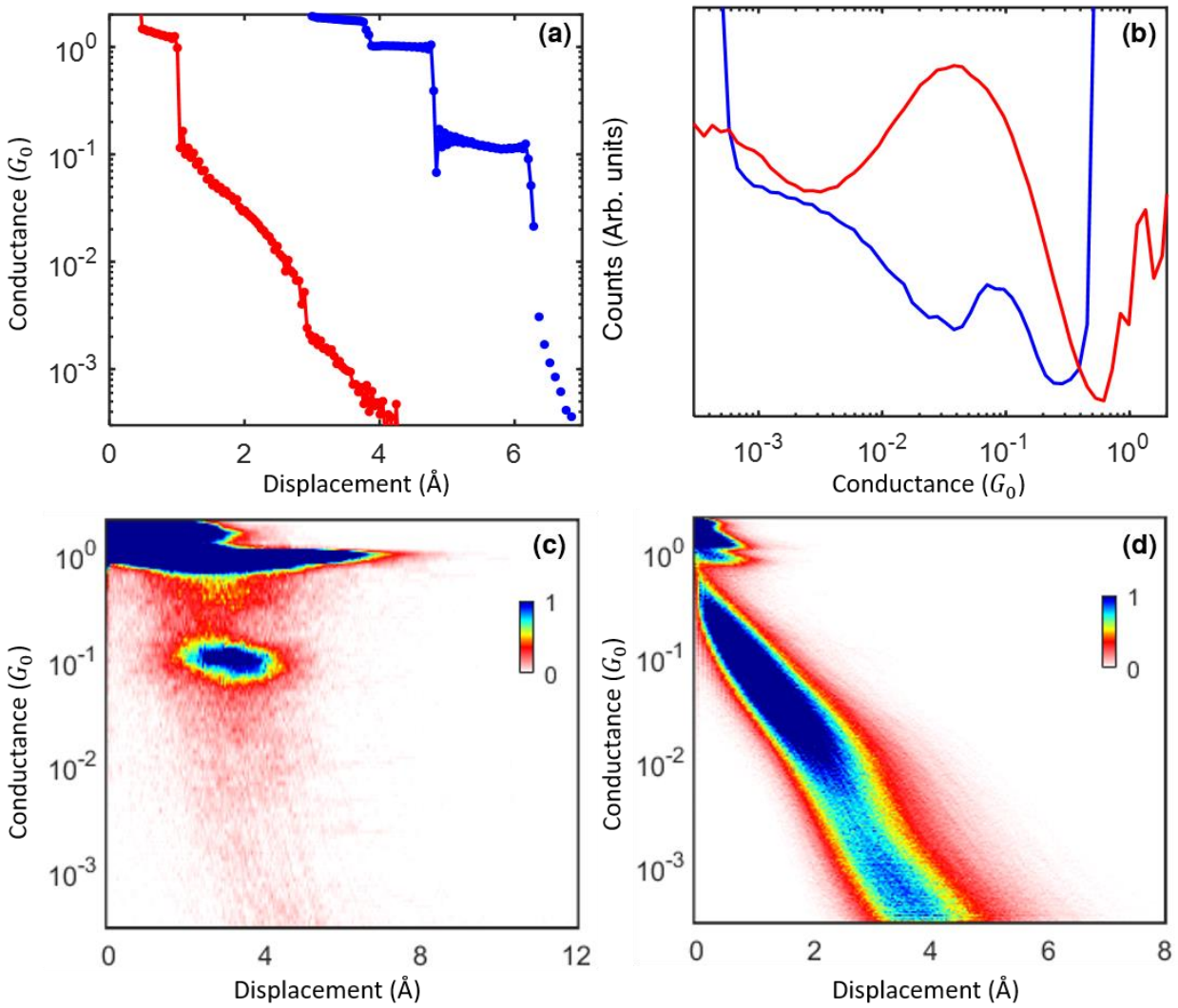

Figure 10.4 *Similar analysis like* ***Figure 10.2*** *for 1,1'-bis(aminomethyl)ferrocene molecular junction.*

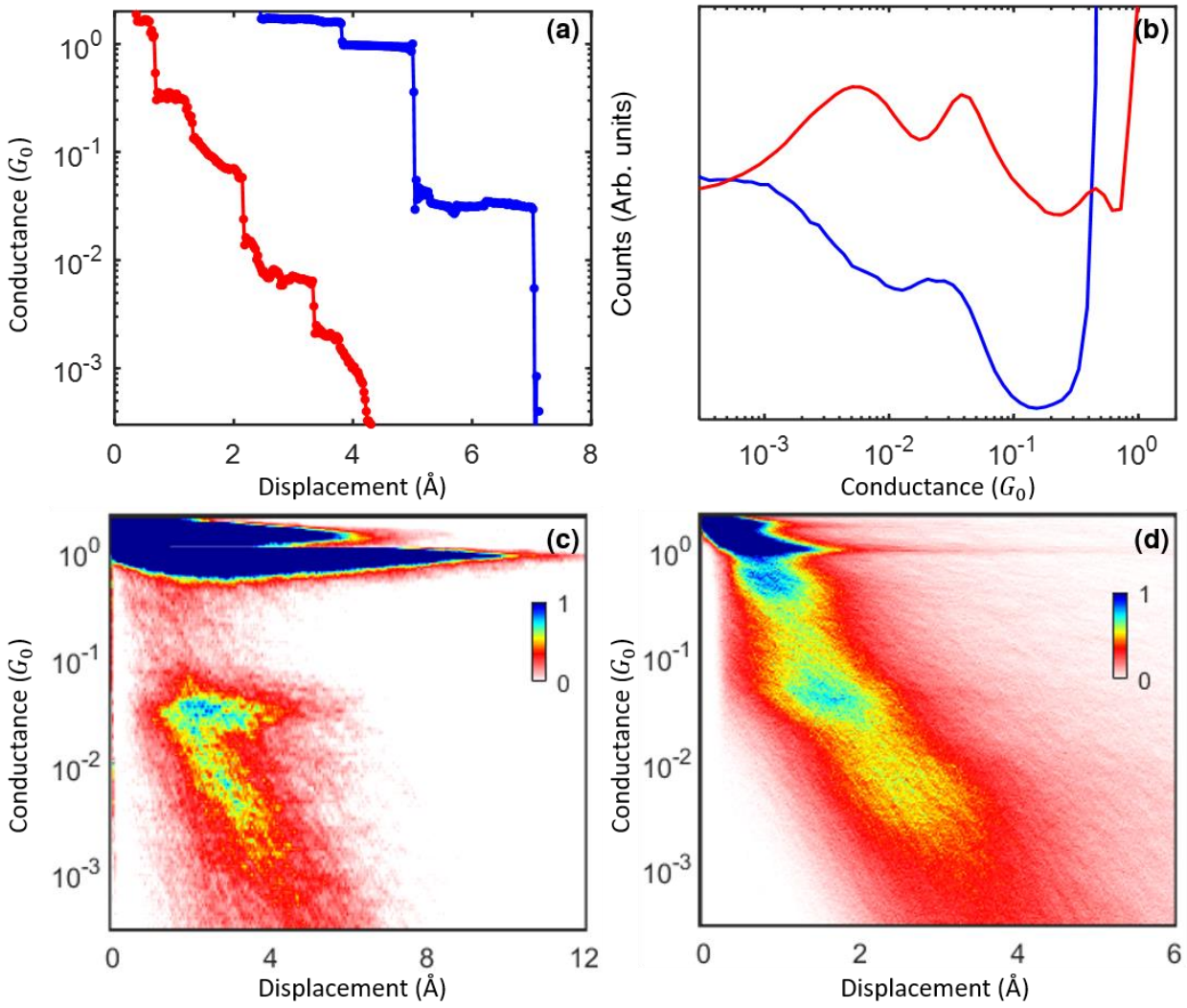

Figure 10.5 *Similar analysis like* ***Figure 10.2*** *for 1,1'-dihydroxyferrocene molecular junction.*

(b) Plateau length histogram

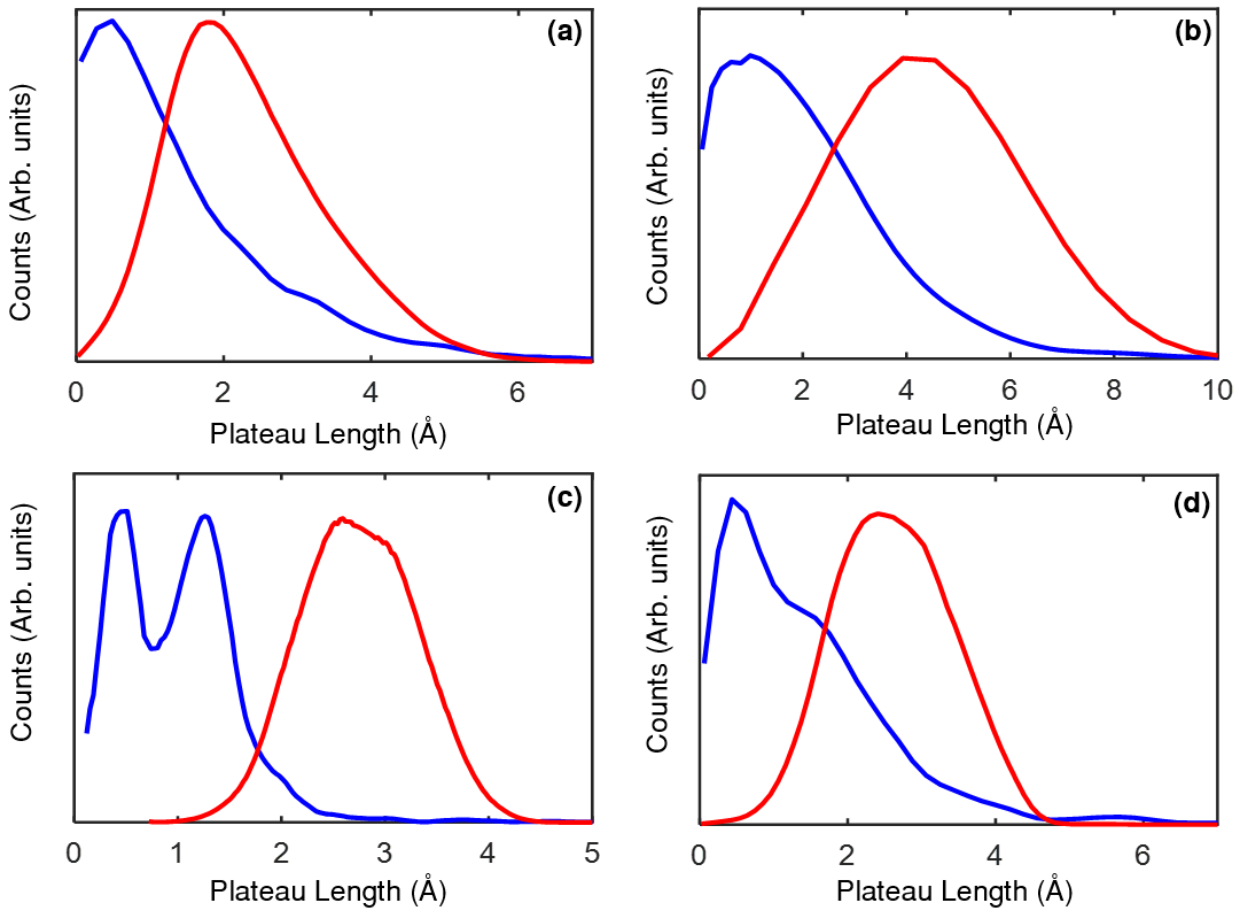

Figure 10.6 (a-d) *Plateau length histogram of ferrocene, 1,1′-dicyanoferrocene, 1,1′-bis(aminomethyl)ferrocene and 1,1′-dihydroxyferrocene molecular junction respectively where blue and red color implies the histogram of pull and push traces. Traces with prominent molecular features are considered for length analysis and details are documented in* ***Table 10.1****.*

Table 10.1 *Details of Plateau length histogram.*

Molecular junction	**Number of data**		**Lowest conductance (G_0) considered for length analysis (Highest is $0.3\ G_0$)**		**Number of bins (Pull and Push)**
	Pull	**Push**	**Pull**	**Push**	
Ferrocene	2003	15873	0.005		800
1, 1′-dicyanoferrocene	2089	15304	0.002	0.0005	300
1,1′-bis(aminomethyl)ferrocene	2334	16915	0.01	0.001	200
1,1′-dihydroxyferrocene	3090	15604	0.002	0.0005	1000

10.2. Summary of experiments during the tenure of my PhD:

During my doctoral tenure, I have completed 55 experiments with the help of three experimental set ups. Total five metal electrodes and ten molecules were tried to probe the characteristics of single molecular devices by fabricating metal/molecule/metal junction using MCBJ technique. However, I was not always succeeded to form the junction or to achieve the desirable results. Here, statistics of the measurements is presented in the form of bar diagram and details are mentioned in the **Table 10.2**.

Metal electrodes-

(i) Gold (Au), (ii) Silver (Ag), (iii) Copper (Cu), (iv) Platinum (Pt) and (v) Aluminum (Al).

Molecules-

(i) 1,4-benzenedithiol, (ii) 2-Aminothiophenol, (iii) 2,2′-bipyridine, (iv) 4,4′-bipyridine, (v) Ferrocene, (vi) 1,1′-dicyanoferrocene, (vii) 1,1′-bis(aminomethyl)ferrocene, (viii) 1,1′-dihydroxyferrocene, (ix) Biferrocene, (x) Hydrogen.

Table 10.2 *Statistics of the experiments.*

Set up	**No. of Experiments**	**Type of junction**		**Temperature (*K*)**			**Yield**	
		Metallic (Me)	**Molecular (Mo)**	**300**	**77**	**4.2**	**Succeed (Su)**	**Failed (Fa)**
Room temperature (1)	23	3	20	23	0	0	14	9
Israel stick (2)	20	8	12	2	15	3	12	8
SNB stick (3)	12	7	5	3	8	1	7	5
Total	55	18	37	28	23	4	33	22
		55		55			55	

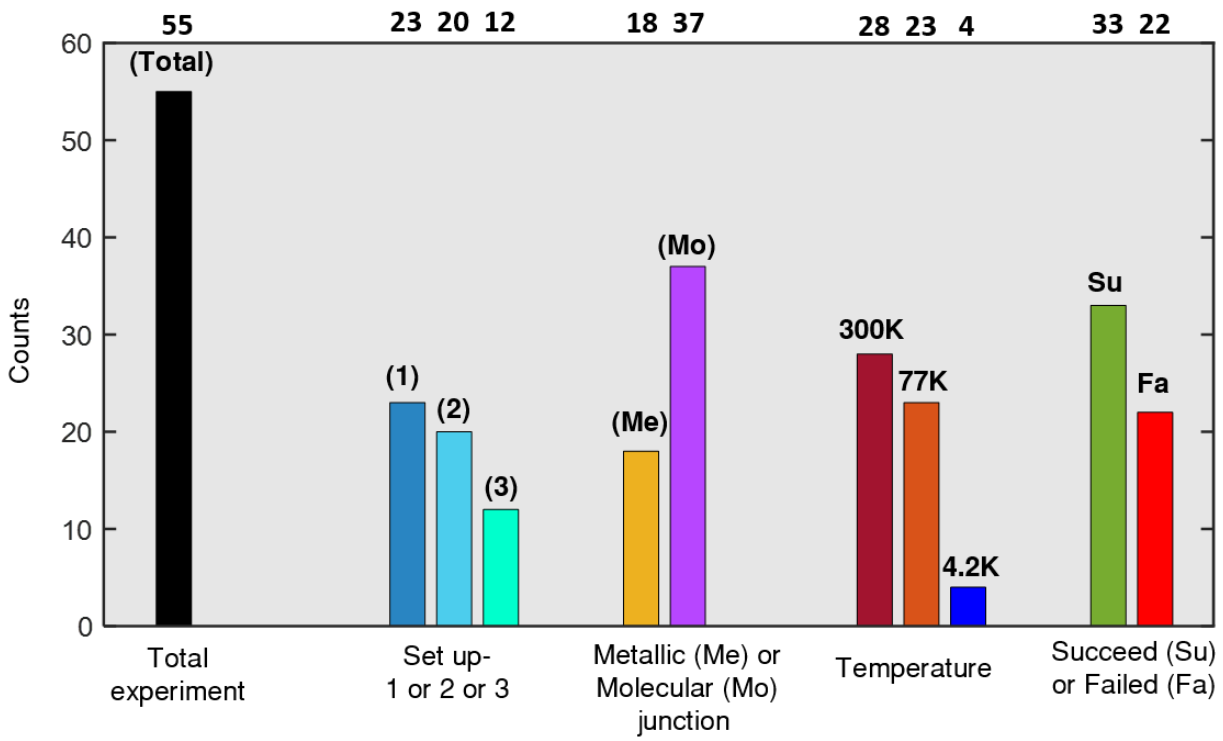

Figure 10.7 *Statistics of the experiments where number on the top demonstrates the y value of the corresponding parameter, mentioned in the x axis.*

References

1. Richard P. Feynman. There's a Plenty of Room At the bottom. *Engineering and Science* vol. 23 22–35 (1960).
2. Aviram, A. & Ratner, M. A. Molecular rectifiers. *Chem Phys Lett* **29**, 277–283 (1974).
3. Lonsdale, K. The Structure of the Benzene Ring in C6(CH3)6. *Proc R Soc London* 494–215 (1929).
4. Van Ruitenbeek, J. M. *et al.* Adjustable nanofabricated atomic size contacts. *Rev Sci Instrum* **67**, 108–111 (1996).
5. C. J. Muller, J. M. van Ruitenbeek, and L. J. de J. Conductance and Supercurrent Discontinuities in Atomic-Scale Metallic Constrictions of Variable Width C. *Phys Rev Lett* **69**, 140–143 (1992).
6. Reed, M. A., Zhou, C., Muller, C. J., Burgin, T. P. & Tour, J. M. Conductance of a Molecular Junction. *Science (80-)* **278**, 1–3 (1997).
7. Nikiforov, M. Single-Molecule Resistance Measured by Repeated Formation of Molecular Junctions. *MRS Bull* **28**, 790–792 (2003).
8. Venkataraman, L. *et al.* Single-molecule circuits with well-defined molecular conductance. *Nano Lett* **6**, 458–462 (2006).
9. Su, T. A., Neupane, M., Steigerwald, M. L., Venkataraman, L. & Nuckolls, C. Chemical principles of single-molecule electronics. *Nat Rev Mater* **1**, (2016).
10. Evers, F., Korytár, R., Tewari, S. & Van Ruitenbeek, J. M. Advances and challenges in single-molecule electron transport. *Rev Mod Phys* **92**, 35001 (2020).
11. Wang, L., Wang, L., Zhang, L. & Xiang, D. Advance of Mechanically Controllable Break Junction for Molecular Electronics. *Top Curr Chem* **375**, 1–42 (2017).
12. Kiguchi, M. & Murakoshi, K. Highly conductive single molecular junctions by direct binding of π-conjugated molecule to metal electrodes. *Thin Solid Films* **518**, 466–469 (2009).
13. Tada, T. & Yoshizawa, K. Quantum transport effects in nanosized graphite sheets. II. Enhanced transport effects by heteroatoms. *J Phys Chem B* **107**, 8789–8793 (2003).
14. Kim, B., Beebe, J. M., Jun, Y., Zhu, X. Y. & Frisbie, G. D. Correlation between HOMO alignment and contact resistance in molecular junctions: Aromatic thiols versus aromatic isocyanides. *J Am Chem Soc* **128**, 4970–4971 (2006).
15. Mishchenko, A. *et al.* Single-molecule junctions based on nitrile-terminated biphenyls: A promising new anchoring group. *J Am Chem Soc* **133**, 184–187 (2011).
16. Martin, C. A. *et al.* Fullerene-based anchoring groups for molecular electronics. *J Am Chem Soc* **130**, 13198–13199 (2008).

17. Chen, F., Li, X., Hihath, J., Huang, Z. & Tao, N. Effect of anchoring groups on single-molecule conductance: Comparative study of thiol-, amine-, and carboxylic-acid-terminated molecules. *J Am Chem Soc* **128**, 15874–15881 (2006).

18. Lörtscher, E. *et al.* Influence of the anchor group on charge transport through single-molecule junctions. *ChemPhysChem* **12**, 1677–1682 (2011).

19. Schull, G., Frederiksen, T., Arnau, A., Sánchez-Portal, D. & Berndt, R. Atomic-scale engineering of electrodes for single-molecule contacts. *Nat Nanotechnol* **6**, 23–27 (2011).

20. Quek, S. Y. *et al.* Amine - Gold linked single-molecule circuits: Experiment and theory. *Nano Lett* **7**, 3477–3482 (2007).

21. Ulrich, J. *et al.* Variability of conductance in molecular junctions. *J Phys Chem B* **110**, 2462–2466 (2006).

22. Li, L. *et al.* Highly conducting single-molecule topological insulators based on mono- and di-radical cations. *Nat Chem* **14**, 1061–1067 (2022).

23. Kaneko, S., Nakazumi, T. & Kiguchi, M. Fabrication of a well-defined single benzene molecule junction using Ag electrodes. *J Phys Chem Lett* **1**, 3520–3523 (2010).

24. Yelin, T. *et al.* Conductance saturation in a series of highly transmitting molecular junctions. *Nat Mater* **15**, 444–449 (2016).

25. Schneebeli, S. T. *et al.* Single-molecule conductance through multiple π-π-stacked benzene rings determined with direct electrode-to-benzene ring connections. *J Am Chem Soc* **133**, 2136–2139 (2011).

26. Kiguchi, M. *et al.* Highly conductive molecular junctions based on direct binding of benzene to platinum electrodes. *Phys Rev Lett* **101**, 1–4 (2008).

27. Tal, O. *et al.* Molecular signature of highly conductive metal-molecule-metal junctions. *Phys Rev B - Condens Matter Mater Phys* **80**, 1–8 (2009).

28. Mishchenko, A. *et al.* Influence of conformation on conductance of biphenyl-dithiol single-molecule contacts. *Nano Lett* **10**, 156–163 (2010).

29. Vonlanthen, D. *et al.* Chemically controlled conductivity: torsion-angle dependence in a single-molecule biphenyldithiol junction. *Angew Chemie - Int Ed* **48**, 8886–8890 (2009).

30. Venkataraman, L., Klare, J. E., Nuckolls, C., Hybertsen, M. S. & Steigerwald, M. L. Dependence of single-molecule junction conductance on molecular conformation. *Nature* **442**, 904–907 (2006).

31. Büttiker, M. Scattering theory of current and intensity noise correlations in conductors and wave guides. *Phys Rev B* **46**, 12485–12507 (1992).

32. Blanter, Y. M. & Büttiker, M. Shot noise in mesoscopic conductors. *Phys Rep* **336**, 1–166 (2000).

33. Landauer, R. Spatial variation of currents and fields due to localized scatterers in metallic conduction. *IBM J Res Dev* **1**, 223–231 (1957).

34. Vrouwe, S. A. G. *et al.* Mechanics of lithographically defined break junctions. *Phys Rev B - Condens Matter Mater Phys* **71**, 1–7 (2005).

35. Kizuka, T. & Monna, K. Atomic configuration, conductance, and tensile force of platinum wires of single-atom width. *Phys Rev B - Condens Matter Mater Phys* **80**, 1–9 (2009).

36. Yanson, A. I., Rubio Bollinger, G., Van Den Brom, H. E., Agraït, N. & Van Ruitenbeek, J. M. Formation and manipulation of a metallic wire of single gold atoms. *Nature* **395**, 783–785 (1998).

37. Hideaki Ohnishi, Yukihito, K. T. Quantized Conductance Through Individual Rows of Suspends gold atoms. *Nature* **246**, 170 (1973).

38. Bahn, S. R. & Jacobsen, K. W. Chain formation of metal atoms. *Phys Rev Lett* **87**, 266101-1-266101–2 (2001).

39. Takai, Y., Kawasaki, T., Kimura, Y., Ikuta, T. & Shimizu, R. Dynamic observation of an atom-sized gold wire by phase electron microscopy. *Phys Rev Lett* **87**, 1–4 (2001).

40. Smit, R. H. M., Untiedt, C., Yanson, A. I. & Van Ruitenbeek, J. M. Common origin for surface reconstruction and the formation of chains of metal atoms. *Phys Rev Lett* **87**, 266102-1-266102–4 (2001).

41. Smit, R. H. M., Untiedt, C. & Van Ruitenbeek, J. M. The high-bias stability of monatomic chains. *Nanotechnology* **15**, (2004).

42. Kiguchi, M., Hashimoto, K., Ono, Y., Taketsugu, T. & Murakoshi, K. Formation of a Pd atomic chain in a hydrogen atmosphere. *Phys Rev B - Condens Matter Mater Phys* **81**, 1–5 (2010).

43. Li, Y. *et al.* Atomic and Electronic Structures of a Single Oxygen Molecular Junction with Au, Ag, and Cu Electrodes. *J Phys Chem C* **120**, 16254–16258 (2016).

44. Fukuzumi, R., Kaneko, S., Fujii, S., Nishino, T. & Kiguchi, M. Formation of a Chain-like Water Single Molecule Junction with Pd Electrodes. *J Phys Chem C* **122**, 4698–4703 (2018).

45. Kumar, M., Sethu, K. K. V. & Van Ruitenbeek, J. M. Molecule-assisted ferromagnetic atomic chain formation. *Phys Rev B - Condens Matter Mater Phys* **91**, 1–7 (2015).

46. Kaneko, S. *et al.* Formation of single Cu atomic chain in nitrogen atmosphere. *J Phys Chem C* **119**, 862–866 (2015).

47. Thijssen, W. H. A., Marjenburgh, D., Bremmer, R. H. & Van Ruitenbeek, J. M. Oxygen-enhanced atomic chain formation. *Phys Rev Lett* **96**, 2–5 (2006).

48. Nakazumi, T. & Kiguchi, M. Formation of Co atomic wire in hydrogen atmosphere. *J Phys Chem Lett* **1**, 923–926 (2010).

49. Thijssen, W. H. A., Strange, M., De Jaan Brugh, J. M. & Van Ruitenbeek, J. M. Formation and properties of metal-oxygen atomic chains. *New J Phys* **10**, (2008).

50. Cuevas, J. C. & Scheer, E. *Molecular Electronics: An Introduction to Theory and*

Experiment. *World Scienti c Pub Co Inc* (World Scienti c Pub Co Inc, 2010).

51. Snoke, D., Denev, S., Liu, Y., Pfeiffer, L. N. & West, K. *The signature of chemical valence in the electrical conduction through asingle-atomcontact*. *Nature* vol. 418 (2002).

52. Grigoriev, A., Sköldberg, J., Wendin, G. & Crljen, Ž. Critical roles of metal-molecule contacts in electron transport through molecular-wire junctions. *Phys Rev B - Condens Matter Mater Phys* **74**, 1–16 (2006).

53. Collepardo-Guevara, R., Walter, D., Neuhauser, D. & Baer, R. A Hückel study of the effect of a molecular resonance cavity on the quantum conductance of an alkene wire. *Chem Phys Lett* **393**, 367–371 (2004).

54. Finch, C. M., García-Suárez, V. M. & Lambert, C. J. Giant thermopower and figure of merit in single-molecule devices. *Phys Rev B - Condens Matter Mater Phys* **79**, 2–5 (2009).

55. Kemp, M., Roitberg, A., Mujica, V., Wanta, T. & Ratner, M. A. Molecular wires: Extended coupling and disorder effects. *J Phys Chem* **100**, 8349–8355 (1996).

56. Papadopoulos, T. A., Grace, I. M. & Lambert, C. J. Control of electron transport through Fano resonances in molecular wires. *Phys Rev B - Condens Matter Mater Phys* **74**, 1–4 (2006).

57. Zotti, L. A. Molecular electronics. *Appl Sci* **11**, (2021).

58. Ernzerhof, M. A simple model of molecular electronic devices and its analytical solution. *J Chem Phys* **127**, (2007).

59. Cardamone, D. M., Stafford, C. A. & Mazumdar, S. Controlling quantum transport through a single molecule. *Nano Lett* **6**, 2422–2426 (2006).

60. Emberly, E. G. & Kirczenow, G. Theoretical study of electrical conduction through a molecule connected to metallic nanocontacts. *Phys Rev B - Condens Matter Mater Phys* **58**, 10911–10920 (1998).

61. Shi, X., Dai, Z. & Zeng, Z. Electron transport in self-assembled monolayers of thiolalkane: Symmetric I-V curves and Fano resonance. *Phys Rev B - Condens Matter Mater Phys* **76**, 1–5 (2007).

62. Moreland, J. & Ekin, J. W. Electron tunneling experiments using Nb-Sn 'break' junctions. *J Appl Phys* **58**, 3888–3895 (1985).

63. Reed, M. A., Zhou, C., Muller, C. J., Burgin, T. P. & Tour, J. M. Conductance of a molecular junction. *Science (80-)* **278**, 252–254 (1997).

64. Smit, R. H. M. *et al.* Measurement of the conductance of a hydrogen molecule. *Nature* **419**, 906–909 (2002).

65. Kaneko, S., Motta, C., Brivio, G. P. & Kiguchi, M. Mechanically controllable bi-stable states in a highly conductive single pyrazine molecular junction. *Nanotechnology* **24**, (2013).

66. Rakhmilevitch, D., Korytár, R., Bagrets, A., Evers, F. & Tal, O. Electron-vibration

interaction in the presence of a switchable kondo resonance realized in a molecular junction. *Phys Rev Lett* **113**, 1–6 (2014).

67. Perrin, M. L. *et al.* Charge transport in a zinc-porphyrin single-molecule junction. *Beilstein J Nanotechnol* **2**, 714–719 (2011).

68. Kamenetska, M. *Single molecule junction conductance and binding geometry, PhD Thesis, Columbia University*. *Phd thesis* (2012).

69. Untiedt, C. *et al.* Calibration of the length of a chain of single gold atoms. *Phys Rev B - Condens Matter Mater Phys* **66**, 854181–854186 (2002).

70. Simmons, J. G. Generalized Formula for the Electric Tunnel Effect between Similar Electrodes Separated by a Thin Insulating Film. *J Appl Phys* **34**, 1793–1803 (1963).

71. Michaelson, H. B. The work function of the elements and its periodicity. *J Appl Phys* **48**, 4729–4733 (1977).

72. Kolesnychenko, O. Y., Shklyarevskii, O. I. & van Kempen, H. Giant influence of adsorbed helium on field emission resonance measurements. *Phys Rev Lett* **83**, 2242–2245 (1999).

73. Agraït, N., Yeyati, A. L. & van Ruitenbeek, J. M. Quantum properties of atomic-sized conductors. *Phys Rep* **377**, 81–279 (2003).

74. Teresa González, M. *et al.* Electrical conductance of molecular junctions by a robust statistical analysis. *Nano Lett* **6**, 2238–2242 (2006).

75. Quek, S. Y. *et al.* Mechanically controlled binary conductance switching of a single-molecule junction. *Nat Nanotechnol* **4**, 230–234 (2009).

76. Greenwald, J. E. *et al.* Highly nonlinear transport across single-molecule junctions via destructive quantum interference. *Nat Nanotechnol* **16**, 313–317 (2021).

77. Konishi, T. *et al.* Single molecule dynamics at a mechanically controllable break junction in solution at room temperature. *J Am Chem Soc* **135**, 1009–1014 (2013).

78. Hong, W. *et al.* Single molecular conductance of tolanes: Experimental and theoretical study on the junction evolution dependent on the anchoring group. *J Am Chem Soc* **134**, 2292–2304 (2012).

79. Makk, P. *et al.* Correlation analysis of atomic and single-molecule junction conductance. *ACS Nano* **6**, 3411–3423 (2012).

80. Balogh, Z. *et al.* Precursor configurations and post-rupture evolution of Ag-CO-Ag single-molecule junctions. *Nanoscale* **6**, 14784–14791 (2014).

81. Hayakawa, R. *et al.* Large Magnetoresistance in Single-Radical Molecular Junctions. *Nano Lett* **16**, 4960–4967 (2016).

82. Capozzi, B. *et al.* Single-molecule diodes with high rectification ratios through environmental control. *Nat Nanotechnol* **10**, 522–527 (2015).

83. Cui, L. *et al.* Thermal conductance of single-molecule junctions. *Nature* **572**, 628–633 (2019).

84. Pal, A. N. *et al.* Nonmagnetic single-molecule spin-filter based on quantum interference. *Nat Commun* **10**, 5565 (2019).

85. Untiedt, C. *et al.* Formation of a metallic contact: Jump to contact revisited. *Phys Rev Lett* **98**, 1–4 (2007).

86. Gerhard, L. & Wulfhekel, W. Conductance and adhesion in an atomically precise Au-Au point contact. *Phys Rev B* **101**, 1–7 (2020).

87. Trouwborst, M. L., Huisman, E. H., Bakker, F. L., Van Der Molen, S. J. & Van Wees, B. J. Single atom adhesion in optimized gold nanojunctions. *Phys Rev Lett* **100**, 1–4 (2008).

88. Pal, A. N., Klein, T., Vilan, A. & Tal, O. Electronic conduction during the formation stages of a single-molecule junction. *Beilstein J Nanotechnol* **9**, 1471–1477 (2018).

89. Kamenetska, M. *et al.* Formation and evolution of single-molecule junctions. *Phys Rev Lett* **102**, 2–5 (2009).

90. Park, Y. S. *et al.* Contact chemistry and single-molecule conductance: A comparison of phosphines, methyl sulfides, and amines. *J Am Chem Soc* **129**, 15768–15769 (2007).

91. Pera, G. *et al.* Metal-molecule-metal junctions in langmuir-blodgett films using a new linker: Trimethylsilane. *Chem - A Eur J* **16**, 13398–13405 (2010).

92. Vardimon, R. *et al.* Probing the orbital origin of conductance oscillations in atomic chains. *Nano Lett* **14**, 2988–2993 (2014).

93. Kaneko, S., Takahashi, R., Fujii, S., Nishino, T. & Kiguchi, M. Controlling the formation process and atomic structures of single pyrazine molecular junction by tuning the strength of the metal-molecule interaction. *Phys Chem Chem Phys* **19**, 9843–9848 (2017).

94. Haiss, W. *et al.* Precision control of single-molecule electrical junctions. *Nat Mater* **5**, 995–1002 (2006).

95. Takács, A. F. *et al.* Electron transport through single phthalocyanine molecules studied using scanning tunneling microscopy. *Phys Rev B - Condens Matter Mater Phys* **78**, 3–6 (2008).

96. Schmaus, S. *et al.* Giant magnetoresistance through a single molecule. *Nat Nanotechnol* **6**, 185–189 (2011).

97. Bagrets, A. *et al.* Single molecule magnetoresistance with combined antiferromagnetic and ferromagnetic electrodes. *Nano Lett* **12**, 5131–5136 (2012).

98. Isshiki, Y., Fujii, S., Nishino, T. & Kiguchi, M. Impact of junction formation processes on single molecular conductance. *Phys Chem Chem Phys* **20**, 7947–7952 (2018).

99. Vladyka, A. *et al.* In-situ formation of one-dimensional coordination polymers in molecular junctions. *Nat Commun* **10**, 1–9 (2019).

100. Hou, S. *et al.* First-principles calculation of the conductance of a single 4,4 bipyridine molecule. *Nanotechnology* **16**, 239–244 (2005).

101. Liu, J. *et al.* Transition from Tunneling Leakage Current to Molecular Tunneling in Single-

Molecule Junctions. *Chem* **5**, 390–401 (2019).

102. Magyarkuti, A. *et al.* Temporal correlations and structural memory effects in break junction measurements. *J Chem Phys* **146**, (2017).

103. Balogh, Z., Makk, P. & Halbritter, A. Alternative types of molecule-decorated atomic chains in Au-CO-Au single-molecule junctions. *Beilstein J Nanotechnol* **6**, 1369–1376 (2015).

104. Calvo, M. R. *et al.* Influence of Relativistic Effects on the Contact Formation of Transition Metals. *Phys Rev Lett* **120**, 76802 (2018).

105. Fernández, M. A. *et al.* Dynamic bonding of metallic nanocontacts: Insights from experiments and atomistic simulations. *Phys Rev B* **93**, 1–10 (2016).

106. Reichert, J. *et al.* Driving Current through Single Organic Molecules. *Phys Rev Lett* **88**, 4 (2002).

107. Seferos, D. S., Blum, A. S., Kushmerick, J. G. & Bazan, G. C. Single-molecule charge-transport measurements that reveal technique-dependent perturbations. *J Am Chem Soc* **128**, 11260–11267 (2006).

108. Fan, F. R. F. *et al.* Charge transport through self-assembled monolayers of compounds of interest in molecular electronics. *J Am Chem Soc* **124**, 5550–5560 (2002).

109. Andres, R. P. *et al.* 'Coulomb staircase' at room temperature in a self-assembled molecular nanostructure. *Science (80-)* **272**, 1323–1325 (1996).

110. Slowinski, K., Fong, H. K. Y. & Majda, M. Mercury-mercury tunneling junctions. 1. Electron tunneling across symmetric and asymmetric alkanethiolate bilayers. *J Am Chem Soc* **121**, 7257–7261 (1999).

111. Li, C. *et al.* Charge transport in single Au | alkanedithiol | Au junctions: Coordination geometries and conformational degrees of freedom. *J Am Chem Soc* **130**, 318–326 (2008).

112. Osorio, E. A., Bjørnholm, T., Lehn, J. M., Ruben, M. & Van Der Zant, H. S. J. Single-molecule transport in three-terminal devices. *J Phys Condens Matter* **20**, (2008).

113. Chen, J., Reed, M. A., Rawlett, A. M. & Tour, J. M. Large on-off ratios and negative differential resistance in a molecular electronic device. *Science (80-)* **286**, 1550–1552 (1999).

114. Haag, R., Rampi, M. A., Holmlin, R. E. & Whitesides, G. M. Electrical breakdown of aliphatic and aromatic self-assembled monolayers used as nanometer-thick organic dielectrics. *J Am Chem Soc* **121**, 7895–7906 (1999).

115. Kergueris, C. *et al.* Electron transport through a metal-molecule-metal junction. *Phys Rev B - Condens Matter Mater Phys* **59**, 12505–12513 (1999).

116. Donhauser, Z. J. *et al.* Conductance switching in single molecules through conformational changes. *Science (80-)* **292**, 2303–2307 (2001).

117. Cui, X. D. *et al.* Reproducible measurement of single-molecule conductivity. *Science (80-*

) **294**, 571–574 (2001).

118. Dadosh, T. *et al.* Measurement of the conductance of single conjugated molecules. *Nature* **436**, 677–680 (2005).

119. Park, J. *et al.* Coulomb blockade and the kondo effect in single-atom transistors. *Nature* **417**, 722–725 (2002).

120. Lo, E. Transport Properties of a Single-Molecule Diode. 4931–4939 (2012).

121. Zang, Y. *et al.* Resonant Transport in Single Diketopyrrolopyrrole Junctions. *J Am Chem Soc* **140**, 13167–13170 (2018).

122. Luka-Guth, K. *et al.* Role of solvents in the electronic transport properties of single-molecule junctions. *Beilstein J Nanotechnol* **7**, 1055–1067 (2016).

123. Bai, J., Li, X., Zhu, Z., Zheng, Y. & Hong, W. Single-Molecule Electrochemical Transistors. *Adv Mater* **33**, (2021).

124. Choi, B. *et al.* Solvent-dependent conductance decay constants in single cluster junctions. *Chem Sci* **7**, 2701–2705 (2016).

125. Hu, Y. *et al.* Single Dynamic Covalent Bond Tailored Responsive Molecular Junctions. *Angew Chemie - Int Ed* **60**, 20872–20878 (2021).

126. Zang, Y. *et al.* Directing isomerization reactions of cumulenes with electric fields. *Nat Commun* **10**, 1–7 (2019).

127. Stefani, D. *et al.* Large Conductance Variations in a Mechanosensitive Single-Molecule Junction. *Nano Lett* **18**, 5981–5988 (2018).

128. Schosser, W. M. *et al.* Mechanical conductance tunability of a porphyrin-cyclophane single-molecule junction. *Nanoscale* **14**, 984–992 (2022).

129. Caneva, S. *et al.* A Mechanically Tunable Quantum Dot in a Graphene Break Junction. *Nano Lett* **20**, 4924–4931 (2020).

130. Cui, L. *et al.* Quantized thermal transport in single-atom junctions. *Science (80-)* **355**, 1192–1195 (2017).

131. Reddy, P., Jang, S. Y., Segalman, R. A. & Majumdar, A. Thermoelectricity in molecular junctions. *Science (80-)* **315**, 1568–1571 (2007).

132. Kim, T. *et al.* Determination of energy level alignment and coupling strength in 4,4′-bipyridine single-molecule junctions. *Nano Lett* **14**, 794–798 (2014).

133. Paoletta, A. L., Fung, E. D. & Venkataraman, L. Gap Size-Dependent Plasmonic Enhancement in Electroluminescent Tunnel Junctions. *ACS Photonics* **9**, 688–693 (2022).

134. Marqués-González, S., Matsushita, R. & Kiguchi, M. Surface enhanced Raman scattering of molecules in metallic nanogaps. *J Opt (United Kingdom)* **17**, (2015).

135. Zotti, L. A. *et al.* Revealing the role of anchoring groups in the electrical conduction through single-molecule junctions. *Small* **6**, 1529–1535 (2010).

136. Cheng, Z. L. *et al.* In situ formation of highly conducting covalent Au-C contacts for single-molecule junctions. *Nat Nanotechnol* **6**, 353–357 (2011).

137. Li, L. *et al.* insulators based on mono- and di-radical cations. *Nat Chem* (2022) doi:10.1038/s41557-022-00978-1.

138. Diez-Perez, I. *et al.* Controlling single-molecule conductance through lateral coupling of φ orbitals. *Nat Nanotechnol* **6**, 226–231 (2011).

139. Kuang, G. *et al.* Resonant Charge Transport in Conjugated Molecular Wires beyond 10 nm Range. *J Am Chem Soc* **138**, 11140–11143 (2016).

140. Li, S. *et al.* Transition between Nonresonant and Resonant Charge Transport in Molecular Junctions. *Nano Lett* **21**, 8340–8347 (2021).

141. Song, H. *et al.* Observation of molecular orbital gating. *Nature* **462**, 1039–1043 (2009).

142. Zang, Y. *et al.* Voltage-Induced Single-Molecule Junction Planarization. *Nano Lett* **21**, 673–679 (2021).

143. Zang, Y. *et al.* Electronically Transparent Au-N Bonds for Molecular Junctions. *J Am Chem Soc* **139**, 14845–14848 (2017).

144. Bredow, T. *et al.* Ferrocene-1,1′-dithiol as molecular wire between Ag electrodes: The role of surface defects. *J Chem Phys* **128**, (2008).

145. Zhou, L. *et al.* One-dimensional iron-cyclopentadienyl sandwich molecular wire with half metallic, negative differential resistance and high-spin filter efficiency properties. *J Am Chem Soc* **130**, 4023–4027 (2008).

146. Zhao, X. & Stadler, R. DFT-based study of electron transport through ferrocene compounds with different anchor groups in different adsorption configurations of an STM setup. *Phys Rev B* **99**, 1–10 (2019).

147. Zhao, X., Kastlunger, G. & Stadler, R. Quantum interference in coherent tunneling through branched molecular junctions containing ferrocene centers. *Phys Rev B* **96**, 1–12 (2017).

148. Kanthasamy, K. *et al.* Charge Transport through Ferrocene 1,1′-Diamine Single-Molecule Junctions. *Small* **12**, 4849–4856 (2016).

149. Cristian Morari, Ivan Rungger, Alexandre R. Rocha, Stefano Sanvito, Sorin Melinte, A. & Rignanese, G.-M. Electronic Transport Properties of 1,1=-Ferrocene Dicarboxylic Acid Linked to Al(111) Electrodes. *ACS Nano* **3**, 4147–4143 (209AD).

150. Aragonès, A. C. *et al.* Control over Near-Ballistic Electron Transport through Formation of Parallel Pathways in a Single-Molecule Wire. *J Am Chem Soc* **141**, 240–250 (2019).

151. Getty, S. A. *et al.* Near-perfect conduction through a ferrocene-based molecular wire. *Phys Rev B - Condens Matter Mater Phys* **71**, 2–5 (2005).

152. Lawson, B., Zahl, P., Hybertsen, M. S. & Kamenetska, M. Formation and Evolution of Metallocene Single-Molecule Circuits with Direct Gold-π Links. *J Am Chem Soc* **144**, 6504–6515 (2022).

153. Liu, R. *et al.* Stable Universal 1- and 2-Input Single-Molecule Logic Gates. doi:10.1002/adma.202202135.

154. Trouwborst, M. L., Huisman, E. H., Bakker, F. L., Van Der Molen, S. J. & Van Wees, B. J. Single atom adhesion in optimized gold nanojunctions. *Phys Rev Lett* **100**, (2008).

155. Pabi, B., Mondal, D., Mahadevan, P. & Pal, A. N. Probing metal-molecule contact at the atomic scale via conductance jumps. *Phys Rev B* **104**, 1–8 (2021).

156. Perrin, M. L. *et al.* Charge transport in a zinc-porphyrin single-molecule junction. *Beilstein J Nanotechnol* **2**, 714–719 (2011).

157. Camarasa-Gómez, M. *et al.* Mechanically Tunable Quantum Interference in Ferrocene-Based Single-Molecule Junctions. *Nano Lett* **20**, 6381–6386 (2020).

158. Moreno-garc, P. *et al.* Single-Molecule Conductance of Functionalized Oligoynes: Length Dependence and Junction Evolution. (2013).

159. Arnold, A., Weigend, F. & Evers, F. Quantum chemistry calculations for molecules coupled to reservoirs: Formalism, implementation, and application to benzenedithiol. *J Chem Phys* **126**, (2007).

160. Garner, M. H. *et al.* Comprehensive suppression of single-molecule conductance using destructive σ-interference. *Nature* **558**, 416–419 (2018).

161. Lafferentz, A. *et al.* Conductance of a Single Conjugated Polymer as a Continuous Function of Its Length. *Science (80-)* **323**, 1190–1193 (2009).

162. Moreno-García, P. *et al.* Charge transport in C60-based dumbbell-type molecules: Mechanically induced switching between two distinct conductance states. *J Am Chem Soc* **137**, 2318–2327 (2015).

163. Venkataraman, L. *et al.* Electronics and chemistry: Varying single-molecule junction conductance using chemical substituents. *Nano Lett* **7**, 502–506 (2007).

164. Kiguchi, M. *et al.* Single molecular resistive switch obtained via sliding multiple anchoring points and varying effective wire length. *J Am Chem Soc* **136**, 7327–7332 (2014).

165. Ko, C. H., Huang, M. J., Fu, M. D. & Chen, C. H. Superior contact for single-molecule conductance: Electronic coupling of thiolate and isothiocyanate on Pt, Pd, and Au. *J Am Chem Soc* **132**, 756–764 (2010).

166. Seminario, J. M., Cruz, C. E. D. La, Derosa, P. A. & Carolina, S. A Theoretical Analysis of Metal - Molecule Contacts. *J Am Chem Soc* **123**, 5616–5617 (2001).

167. Adak, O., Korytár, R., Joe, A. Y., Evers, F. & Venkataraman, L. Impact of Electrode Density of States on Transport through Pyridine-Linked Single Molecule Junctions. *Nano Lett* **15**, 3716–3722 (2015).

168. Batra, A. *et al.* Tuning Recti fi cation in Single-Molecular Diodes. **22**, (2013).

169. Su, T. A., Li, H., Steigerwald, M. L., Venkataraman, L. & Nuckolls, C. Stereoelectronic switching in single-molecule junctions. *Nat Chem* **7**, 215–220 (2015).

170. Su, T. A. *et al.* Single-Molecule Conductance in Atomically Precise Germanium Wires. *J Am Chem Soc* **137**, 12400–12405 (2015).

171. Aradhya, S. V. & Venkataraman, L. Single-molecule junctions beyond electronic transport. *Nat Nanotechnol* **8**, 399–410 (2013).

172. Zyazin, A. S. *et al.* Electric field controlled magnetic anisotropy in a single molecule. *Nano Lett* **10**, 3307–3311 (2010).

173. Nakashima, S., Takahashi, Y. & Kiguchi, M. Effect of the environment on the electrical conductance of the single benzene-1,4-diamine molecule junction. *Beilstein J Nanotechnol* **2**, 755–759 (2011).

174. Darwish, T. & Ciampi, S. Multi-Responsive Photo- and Chemo-Electrical Single-Molecule Switches. (2014).

175. Reddy, H. *et al.* Determining plasmonic hot-carrier energy distributions via single-molecule transport measurements. *Science (80-)* **369**, 423–426 (2020).

176. Lee, W. *et al.* Increased Molecular Conductance in Oligo[n]phenylene Wires by Thermally Enhanced Dihedral Planarization. *Nano Lett* **22**, 4919–4924 (2022).

177. Kamenetska, M., Widawsky, J. R., Dell'Angela, M., Frei, M. & Venkataraman, L. Temperature dependent tunneling conductance of single molecule junctions. *J Chem Phys* **146**, (2017).

178. Li, H. B. *et al.* Temperature-Dependent Tunneling in Furan Oligomer Single-Molecule Junctions. *ACS Sensors* **6**, 565–572 (2021).

179. Grellmann, T., Mayer, D., Offenhäusser, A. & Wördenweber, R. Temperature-Dependent Electron Transport in Single Terphenyldithiol Molecules. *J Phys Chem A* **121**, 2911–2917 (2017).

180. Lawson, B., Zahl, P., Hybertsen, M. S. & Kamenetska, M. Formation and Evolution of Metallocene Single-Molecule Circuits with Direct Gold-πLinks. *J Am Chem Soc* **144**, 6504–6515 (2022).

181. Samuel A. Miller, J. A. T. and J. F. T. 114. Dicyclopentadienyliron. *J Chem Soc* 1–4 (1952).

182. Kealy, T. J. & Pauson, P. L. Nature 1039. *Nature* **168**, 1039–1040 (1951).

183. Meisner, J. S. *et al.* Importance of direct metal-π coupling in electronic transport through conjugated single-molecule junctions. *J Am Chem Soc* **134**, 20440–20445 (2012).

184. Stipe, B. C., Rezaei, M. A. & Ho, W. Single-molecule vibrational spectroscopy and microscopy. *Science (80-)* **280**, 1732–1735 (1998).

185. Hongkun Park *et al.* Nanomechanical oscillationsinasingle-C60transistor. *Nature* **407**, 57 (2000).

186. Hihath, J., Arroyo, C. R., Rubio-Bollinger, G., Tao, N. & Agraït, N. Study of electron-phonon interactions in a single molecule covalently connected to two electrodes. *Nano Lett* **8**, 1673–1678 (2008).

187. Tal, O., Krieger, M., Leerink, B. & Van Ruitenbeek, J. M. Electron-vibration interaction in single-molecule junctions: From contact to tunneling regimes. *Phys Rev Lett* **100**, 1–4 (2008).

188. Perrin, M. L. *et al.* Large tunable image-charge effects in single-molecule junctions. *Nat Nanotechnol* **8**, 282–287 (2013).

189. Rincón-García, L. *et al.* Molecular design and control of fullerene-based bi-thermoelectric materials. *Nat Mater* **15**, 289–293 (2016).

190. Pump, F. *et al.* Quantum transport through STM-lifted single PTCDA molecules. *Appl Phys A Mater Sci Process* **93**, 335–343 (2008).

191. Toher, C. *et al.* Electrical transport through a mechanically gated molecular wire. *Phys Rev B - Condens Matter Mater Phys* **83**, 1–12 (2011).

192. Walkey, M. C. *et al.* Chemically and Mechanically Controlled Single-Molecule Switches Using Spiropyrans. *ACS Appl Mater Interfaces* **11**, 36886–36894 (2019).

193. Scott, G. D. & Natelson, D. Kondo resonances in molecular devices. *ACS Nano* **4**, 3560–3579 (2010).

194. Rodrigues, V., Bettini, J., Rocha, A. R., Rego, L. G. C. & Ugarte, D. Quantum conductance in silver nanowires: Correlation between atomic structure and transport properties. *Phys Rev B - Condens Matter Mater Phys* **65**, 1–4 (2002).

195. Beebe, J. M., Kim, B., Gadzuk, J. W., Frisbie, C. D. & Kushmerick, J. G. Transition from direct tunneling to field emission in metal-molecule-metal junctions. *Phys Rev Lett* **97**, 1–4 (2006).

196. Beebe, J. M., Kim, B. S., Frisbei, C. D. & Kushmerick, J. G. Measuring relative barrier heights in molecular electronic junctions with transition voltage spectroscopy. *ACS Nano* **2**, 827–832 (2008).

197. Huisman, E. H., Guédon, C. M., Van Wees, B. J. & Van Der Molen, S. J. Interpretation of transition voltage spectroscopy. *Nano Lett* **9**, 3909–3913 (2009).

198. Trouwborst, M. L. *et al.* Transition voltage spectroscopy and the nature of vacuum tunneling. *Nano Lett* **11**, 614–617 (2011).

199. Vilan, A., Cahen, D. & Kraisler, E. Rethinking transition voltage spectroscopy within a generic taylor expansion view. *ACS Nano* **7**, 695–706 (2013).

200. Bruot, C., Hihath, J. & Tao, N. Mechanically controlled molecular orbital alignment in single molecule junctions. *Nat Nanotechnol* **7**, 35–40 (2012).

201. Schreckenbach, G. The 57Fe nuclear magnetic resonance shielding in ferrocene revisited. A density-functional study of orbital energies, shielding mechanisms, and the influence of the exchange-correlation functional. *J Chem Phys* **110**, 11936–11949 (1999).

202. Toskovic, R. *et al.* Atomic spin-chain realization of a model for quantum criticality. *Nat Phys* **12**, 656–660 (2016).

203. Chen, B. *et al.* All-oxide–based synthetic antiferromagnets exhibiting layer-resolved magnetization reversal. *Science (80-)* **357**, 191–194 (2017).

204. Hirjibehedin, C. F., Lutz, C. P. & Heinrich, A. J. Spin coupling in engineered atomic structures. *Science (80-)* **312**, 1021–1024 (2006).

205. Chakrabarti, S., Vilan, A. & Peralta, J. E. Magnetic control over the fundamental structure of atomic wires. *Nat Commun* **13**, 1–12 (2022).

206. Kumar, M. *et al.* Shot noise and magnetism of Pt atomic chains: Accumulation of points at the boundary. *Phys Rev B - Condens Matter Mater Phys* **88**, 1–8 (2013).

207. Shiota, T., Mares, A. I., Valkering, A. M. C., Oosterkamp, T. H. & Van Ruitenbeek, J. M. Mechanical properties of Pt monatomic chains. *Phys Rev B - Condens Matter Mater Phys* **77**, 1–5 (2008).

208. Rubio-Bollinger, G., Bahn, S. R., Agraït, N., Jacobsen, K. W. & Vieira, S. Mechanical properties and formation mechanisms of a wire of single gold atoms. *Phys Rev Lett* **87**, 1–4 (2001).

209. Yanson, I. K. *et al.* Atomic-size oscillations in conductance histograms for gold nanowires and the influence of work hardening. *Phys Rev Lett* **95**, 1–4 (2005).

210. Smit, R. H. M., Untiedt, C., Rubio-Bollinger, G., Segers, R. C. & van Ruitenbeek, J. M. Observation of a Parity Oscillation in the Conductance of Atomic Wires. *Phys Rev Lett* **91**, 1–4 (2003).

211. Segovia, P., Purdle, D., Hengsberger, M. & Baer, Y. Observation of spin and charge collective modes in one-dimensional metallic chains. *Nature* **402**, 504–507 (1999).

212. Ahn, J. R., Yeom, H. W., Yoon, H. S. & Lyo, I. W. Metal-insulator transition in au atomic chains on si with two proximal bands. *Phys Rev Lett* **91**, 10–13 (2003).

213. Fölsch, S., Hyldgaard, P., Koch, R. & Ploog, K. H. Quantum Confinement in Monatomic Cu Chains on Cu(111). *Phys Rev Lett* **92**, 4 (2004).

214. Ludoph, B. & Ruitenbeek, J. M. Thermopower of atomic-size metallic contacts. *Phys Rev B - Condens Matter Mater Phys* **59**, 12290–12293 (1999).

215. Mares, A. I., Otte, A. F., Soukiassian, L. G., Smit, R. H. M. & Van Ruitenbeek, J. M. Observation of electronic and atomic shell effects in gold nanowires. *Phys Rev B - Condens Matter Mater Phys* **70**, 1–4 (2004).

216. Yanson, A. I., Yanson, I. K. & Van Rultenbeek, J. M. Observation of shell structure in sodium nanowires. *Nature* **400**, 144–146 (1999).

217. Mares, A. I. & Van Ruitenbeek, J. M. Observation of shell effects in nanowires for the noble metals Cu, Ag, and Au. *Phys Rev B - Condens Matter Mater Phys* **72**, 1–7 (2005).

218. Thiess, A., Mokrousov, Y., Blügel, S. & Heinze, S. Theory and application of chain formation in break junctions. *Nano Lett* **8**, 2144–2149 (2008).

219. Csonka, S., Halbritter, A. & Mihály, G. Pulling gold nanowires with a hydrogen clamp:

Strong interactions of hydrogen molecules with gold nanojunctions. *Phys Rev B - Condens Matter Mater Phys* **73**, 1–6 (2006).

220. Kaneko, S., Zhang, J., Zhao, J. & Kiguchi, M. Electronic conductance of platinum atomic contact in a nitrogen atmosphere. *J Phys Chem C* **117**, 9903–9907 (2013).

221. Makk, P., Balogh, Z., Csonka, S. & Halbritter, A. Pulling platinum atomic chains by carbon monoxide molecules. *Nanoscale* **4**, 4739–4745 (2012).

222. Li, Y., Kaneko, S., Fujii, S. & Kiguchi, M. Symmetry of Single Hydrogen Molecular Junction with Au, Ag, and Cu Electrodes. *J Phys Chem C* **119**, 19143–19148 (2015).

223. Nakazumi, T., Kaneko, S. & Kiguchi, M. Electron transport properties of Au, Ag, and Cu atomic contacts in a hydrogen environment. *J Phys Chem C* **118**, 7489–7493 (2014).

224. Matsushita, R., Kaneko, S., Nakazumi, T. & Kiguchi, M. Effect of metal-molecule contact on electron-vibration interaction in single hydrogen molecule junction. *Phys Rev B - Condens Matter Mater Phys* **84**, 1–5 (2011).

225. Motta, C., Fratesi, G. & Trioni, M. I. Conductance calculation of hydrogen molecular junctions between Cu electrodes. *Phys Rev B - Condens Matter Mater Phys* **87**, 1–6 (2013).

226. Jiang, Z., Wang, H., Shen, Z., Sanvito, S. & Hou, S. Effects of the molecule-electrode interface on the low-bias conductance of Cu-H2-Cu single-molecule junctions. *J Chem Phys* **145**, (2016).

227. Scheer, E., Joyez, P., Esteve, D., Urbina, C. & Devoret, M. H. Conduction Channel Transmissions of Atomic-Size Aluminum Contacts. *Phys Rev Lett* **78**, 3535–3538 (1997).

228. Halbritter, A., Csonka, S., Makk, P. & Mihály, G. Interaction of hydrogen with metallic nanojunctions. *J Phys Conf Ser* **61**, 214–218 (2007).

229. Makk, P., Csonka, S. & Halbritter, A. Effect of hydrogen molecules on the electronic transport through atomic-sized metallic junctions in the superconducting state. *Phys Rev B - Condens Matter Mater Phys* **78**, 1–6 (2008).

230. Galperin, M., Ratner, M. A. & Nitzan, A. Inelastic electron tunneling spectroscopy in molecular junctions: Peaks and dips. *J Chem Phys* **121**, 11965–11979 (2004).

231. De La Vega, L., Martín-Rodero, A., Agraït, N. & Yeyati, A. L. Universal features of electron-phonon interactions in atomic wires. *Phys Rev B - Condens Matter Mater Phys* **73**, 1–5 (2006).

232. Viljas, J. K., Cuevas, J. C., Pauly, F. & Häfner, M. Electron-vibration interaction in transport through atomic gold wires. *Phys Rev B - Condens Matter Mater Phys* **72**, 1–18 (2005).

233. Thijssen, W. H. A., Djukic, D., Otte, A. F., Bremmer, R. H. & Van Ruitenbeek, J. M. Vibrationally induced two-level systems in single-molecule junctions. *Phys Rev Lett* **97**, 1–4 (2006).

234. Thijssen, W. H. A. (Robert). *Molecule-assisted atomic chain formation, Phd thesis*. (2007).

235. Halbritter, A., Makk, P., Csonka, S. & Mihály, G. Huge negative differential conductance in Au- H2 molecular nanojunctions. *Phys Rev B - Condens Matter Mater Phys* **77**, (2008).

236. Djukic, D. *et al.* Stretching dependence of the vibration modes of a single-molecule Pt- H2 -Pt bridge. *Phys Rev B - Condens Matter Mater Phys* **71**, 1–4 (2005).

237. Regev Ben-Zvi, Ran Vardimon, Tamar Yelin, and O. T. Electron-Vibration Interaction in Multichannel Single-Molecule Junctions Regev. *ACS Nano* **7**, 11147–11155 (2013).